



ISSN 2518-7198 (Print)
ISSN 2663-5089 (Online)

BULLETIN

OF THE KARAGANDA UNIVERSITY

PHYSICS

Series

№ 3(99)/2020

ISSN 2518-7198 (Print)
ISSN 2663-5089 (Online)
Индексі 74616
Индекс 74616

**ҚАРАҒАНДЫ
УНИВЕРСИТЕТІНІҢ
ХАБАРШЫСЫ**

ВЕСТНИК
КАРАГАНДИНСКОГО
УНИВЕРСИТЕТА

BULLETIN
OF THE KARAGANDA
UNIVERSITY

ФИЗИКА сериясы

Серия ФИЗИКА

PHYSICS Series

№ 3(99)/2020

Шілде–тамыз–қыркүйек
30 қыркүйек 2020 ж.

Июль–август–сентябрь
30 сентября 2020 г.

July–August–September
September 30th, 2020

1996 жылдан бастап шығады
Издается с 1996 года
Founded in 1996

Жылына 4 рет шығады
Выходит 4 раза в год
Published 4 times a year

Қарағанды, 2020
Караганда, 2020
Karaganda, 2020

Бас редакторы

PhD д-ры
А.К. Хасенов

Жауапты хатшы

PhD д-ры
Д.Ж. Қарабекова

Редакция алқасы

Б.Р. Нүсіпбеков,	техн. ғыл. канд., Акад. Е.А. Бөкетов ат. Қарағанды университеті (Қазақстан);
Т.Ә. Көкетайтегі,	физ.-мат. ғыл. д-ры, Акад. Е.А. Бөкетов ат. Қарағанды университеті (Қазақстан);
Н.Х. Ибраев,	физ.-мат. ғыл. д-ры, Акад. Е.А. Бөкетов ат. Қарағанды университеті (Қазақстан);
А.О. Сәулебеков,	физ.-мат. ғыл. д-ры, М.В. Ломоносов атындағы ММУ-нің Қазақстан филиалы, Нұр-Сұлтан (Қазақстан);
И.В. Брейдо,	техн. ғыл. д-ры, Қарағанды мемлекеттік техникалық университеті (Қазақстан);
И.П. Курытник,	техн. ғыл. д-ры, Освенцимдегі В. Пилецкий атындағы Мемлекеттік жоғары кәсіптік мектебі (Польша);
М. Стоев,	PhD д-ры, инженерия докторы, «Неофит-Рилски» Оңтүстік-Батыс университеті (Болгария);
М.М. Кидибаев,	физ.-мат. ғыл. д-ры, Қырғызстан Ұлттық ғылым академиясының Физика институты, Бішкек (Қырғызстан);
З.Ж. Жаңабаев,	физ.-мат. ғыл. д-ры, Әл-Фараби атындағы Қазақ ұлттық университеті (Қазақстан);
Г.В. Климушева,	физ.-мат. ғыл. д-ры, Украина Ғылым академиясының Физика институты, Киев (Украина);
С.Е. Көмеков,	физ.-мат. ғыл. д-ры, Қ.И.Сәтбаев атындағы Қазақ ұлттық техникалық университеті, Алматы (Қазақстан);
В.М. Лисицын,	физ.-мат. ғыл. д-ры, Томск политехникалық университеті (Ресей);
И.Н. Огородников,	физ.-мат. ғыл. д-ры, Ресейдің Тұңғыш Президенті Б.Н. Ельцин атындағы Орал федералдық университеті, Екатеринбург (Ресей);
О.П. Пчеляков,	физ.-мат. ғыл. д-ры, РФА Сібір бөлімшесінің А.В. Ржанов атындағы Жартылай өткізгіштер физикасы институты, Новосибирск (Ресей);
А.Т. Акылбеков,	физ.-мат. ғыл. д-ры, Л.Н.Гумилев атындағы Еуразия ұлттық университеті, Нұр-Сұлтан (Қазақстан);
А.Ж. Тұрмұхамбетов,	физ.-мат. ғыл. д-ры, Қ.И. Сәтбаев атындағы Қазақ ұлттық техникалық университеті, Алматы (Қазақстан);
К.Ш. Шүңкеев,	физ.-мат. ғыл. д-ры, Ақтөбе мемлекеттік педагогикалық институты (Қазақстан);
В.Ю. Кучерук,	техн. ғыл. д-ры, Винница ұлттық техникалық университеті (Украина);
В.А. Кульбачинский,	физ.-мат. ғыл. д-ры, М.В. Ломоносов атындағы Москва мемлекеттік университеті (Ресей);
А.Д. Погребняк,	физ.-мат. ғыл. д-ры, Сумск мемлекеттік университеті (Украина);
А.П. Суржиков,	физ.-мат. ғыл. д-ры, Томск политехникалық университеті (Ресей)

Редакцияның мекенжайы: 100024, Қазақстан, Қарағанды қ., Университет к-сі, 28
Тел.: (7212) 77-04-38; факс: (7212) 35-63-98.
E-mail: vestnikku@gmail.com; Сайты: physics-vestnik.ksu.kz

Редакторлары

Ж.Т. Нурмуханова, С.С. Балкеева, Т.А. Кохановер

Компьютерде беттеген

В.В. Бутяйкин

Қарағанды университетінің хабаршысы. «Физика» сериясы.

ISSN 2518-7198 (Print). ISSN 2663-5089 (Online).

Меншік иесі: «Академик Е.А. Бөкетов атындағы Қарағанды университеті» КЕАҚ.

Қазақстан Республикасы Ақпарат және қоғамдық даму министрлігімен тіркелген. 30.09.2020 ж. № KZ38VPY00027378 қайта есепке қою туралы куәлігі.

Басуға 29.09.2020 ж. қол қойылды. Пішімі 60×84 1/8. Қағазы офсеттік. Көлемі 12,37 б.т. Таралымы 200 дана. Бағасы келісім бойынша. Тапсырыс № 57.

«Акад. Е.А. Бөкетов ат. Қарағанды ун-ті» КЕАҚ-ның баспасының баспаханасында басылып шықты. 100012, Қазақстан, Қарағанды қ., Гоголь к-сі, 38. Тел. 51-38-20. E-mail: izd_kargu@mail.ru

© Академик Е.А. Бөкетов атындағы Қарағанды университеті, 2020

Главный редактор

д-р PhD

А.К. Хасенов

Ответственный секретарь

д-р PhD

Д.Ж. Карабекова

Редакционная коллегия

Б.Р. Нусупбеков,	канд. техн. наук, Карагандинский университет им. акад. Е.А. Букетова (Казахстан);
Т.А. Кокетайтеги,	д-р физ.-мат. наук, Карагандинский университет им. акад. Е.А. Букетова (Казахстан);
Н.Х. Ибраев,	д-р физ.-мат. наук, Карагандинский университет им. акад. Е.А. Букетова (Казахстан);
А.О. Саулебеков,	д-р физ.-мат. наук, Казахстанский филиал МГУ им. М.В. Ломоносова, Нур-Султан (Казахстан);
И.В. Брейдо,	д-р техн. наук, Карагандинский государственный технический университет (Казахстан);
И.П. Курятник,	д-р техн. наук, Государственная высшая профессиональная школа им. В. Пилецкого в Освенциме (Польша);
М. Стоев,	д-р PhD, доктор инженерии, Юго-Западный университет им. Неофита Рильского, Благоевград (Болгария);
М.М. Кидибаев,	д-р физ.-мат. наук, Институт физики Национальной академии наук Кыргызстана, Бишкек (Кыргызстан);
З.Ж. Жанабаев,	д-р физ.-мат. наук, Казахский национальный университет им. аль-Фараби, Алматы (Казахстан);
Г.В. Климушева,	д-р физ.-мат. наук, Институт физики Академии наук Украины, Киев (Украина);
С.Е. Кумеков,	д-р физ.-мат. наук, Казахский национальный технический университет им. К. Сатпаева, Алматы (Казахстан);
В.М. Лисицын,	д-р физ.-мат. наук, Томский политехнический университет (Россия);
И.Н. Огородников,	д-р физ.-мат. наук, Уральский федеральный университет им. Первого Президента России Б.Н. Ельцина, Екатеринбург (Россия);
О.П. Пчеляков,	д-р физ.-мат. наук, Институт физики полупроводников им. А.В. Ржанова Сибирского отделения РАН, Новосибирск (Россия);
А.Т. Акылбеков,	д-р физ.-мат. наук, Евразийский национальный университет им. Л.Н. Гумилева, Нур-Султан (Казахстан);
А.Ж. Турмухамбетов,	д-р физ.-мат. наук, Казахский национальный технический университет им. К. Сатпаева, Алматы (Казахстан);
К.Ш. Шункеев,	д-р физ.-мат. наук, Актюбинский государственный педагогический институт (Казахстан);
В.Ю. Кучерук,	д-р техн. наук, Винницкий национальный технический университет (Украина);
В.А. Кульбачинский,	д-р физ.-мат. наук, Московский государственный университет им. М.В. Ломоносова (Россия);
А.Д. Погребняк,	д-р физ.-мат. наук, Сумский государственный университет (Украина);
А.П. Суржиков,	д-р физ.-мат. наук, Томский политехнический университет (Россия)

Адрес редакции: 100024, Казахстан, г. Караганда, ул. Университетская, 28

Тел.: (7212) 77-04-38; факс: (7212) 35-63-98.

E-mail: vestnikku@gmail.com; Сайт: physics-vestnik.ksu.kz

Редакторы

Ж.Т. Нурмуханова, С.С. Балкеева, Т.А. Кохановер

Компьютерная верстка

В.В. Бутяйкин

Вестник Карагандинского университета. Серия «Физика».

ISSN 2518-7198 (Print). ISSN 2663-5089 (Online).

Собственник: НАО «Карагандинский университет имени академика Е.А. Букетова».

Зарегистрирован Министерством информации и общественного развития Республики Казахстан.

Свидетельство о постановке на переучет № KZ38VPY00027378 от 30.09.2020 г.

Подписано в печать 29.09.2020 г. Формат 60×84 1/8. Бумага офсетная. Объем 12,37 п.л. Тираж 200 экз.

Цена договорная. Заказ № 57.

Отпечатано в типографии издательства НАО «Карагандинский ун-т им. акад. Е.А. Букетова».

100012, Казахстан, г. Караганда, ул. Гоголя, 38, тел.: (7212) 51-38-20. E-mail: izd_kargu@mail.ru

© Карагандинский университет им. академика Е.А. Букетова, 2020

Main Editor

PhD

A.K. Khassenov

Responsible secretary

PhD

D.Zh. Karabekova

Editorial board

- B.R. Nussupbekov**, Cand. of techn. sciences, Karagandy University of the name of acad. E.A. Buketov (Kazakhstan);
T.A. Kuketaev, Doctor of phys.-math. sciences, Karagandy University of the name of acad. E.A. Buketov (Kazakhstan);
N.Kh. Ibrayev, Doctor of phys.-math. sciences, Karagandy University of the name of acad. E.A. Buketov (Kazakhstan);
A.O. Saulebekov, Doctor of phys.-math. sciences, Kazakhstan branch of Lomonosov Moscow State University, Nur-Sultan (Kazakhstan);
- I.V. Breido**, Doctor of techn. sciences, Karaganda State Technical University (Kazakhstan);
I.P. Kurytnik, Doctor of techn. sciences, The State School of Higher Education in Oświęcim (Auschwitz) (Poland);
- M. Stoev**, PhD, doctor of engineering, South-West University «Neofit Rilski» (Bulgaria);
M.M. Kidibaev, Doctor of phys.-math. sciences, Institute of Physics of the National Academy of Sciences of the Kyrgyzstan, Bishkek (Kyrgyzstan);
- Z.Zh. Zhanabaev**, Doctor of phys.-math. sciences, Al-Farabi Kazakh National University, Almaty (Kazakhstan);
- G.V. Klimusheva**, Doctor of phys.-math. sciences, Institute of Physics of the National Academy of Science of Ukraine, Kiev (Ukraine);
- S.E. Kumekov**, Doctor of phys.-math. sciences, Kazakh National Technical University named after K. Satpayev, Almaty (Kazakhstan);
- V.M. Lisitsyn**, Doctor of phys.-math. sciences, Tomsk Polytechnic University (Russia);
I.N. Ogorodnikov, Doctor of phys.-math. sciences, Ural Federal University named after the first President of Russia B.N. Yeltsin, Yekaterinburg (Russia);
- O.P. Pchelyakov**, Doctor of phys.-math. sciences, Rzhanov Institute of Semiconductor Physics of Siberian branch of Russian Academy of Sciences, Novosibirsk (Russia);
- A.T. Akylbekov**, Doctor of phys.-math. sciences, L.N. Gumilyov Eurasian National University, Nur-Sultan (Kazakhstan);
A.Zh. Turmuhambetov, Doctor of phys.-math. sciences, Satbayev Kazakh National Technical University, Almaty (Kazakhstan);
K.Sh. Shunkeyev, Doctor of phys.-math. sciences, Aktobe State Pedagogical Institute (Kazakhstan);
V.Yu. Kucheruk, Doctor of techn. sciences, Vinnytsia National Technical University, Vinnitsa (Ukraine);
V.A. Kulbachinskii, Doctor of phys.-math. sciences, Lomonosov Moscow State University (Russia);
A.D. Pogrebnyak, Doctor of phys.-math. sciences, Sumy state University (Ukraine);
A.P. Surzhikov, Doctor of phys.-math. sciences, Tomsk Polytechnic University (Russia)

Postal address: 28, University Str., 100024, Karaganda, Kazakhstan

Tel.: (7212) 77-04-38; fax: (7212) 35-63-98.

E-mail: vestnikku@gmail.com; Web-site: physics-vestnik.ksu.kz

Editors

Zh.T. Nurmukhanova, S.S. Balkeyeva, T.A. Kokhanover

Computer layout

V.V. Butyaikin

Bulletin of the Karaganda University. «Physics» series.

ISSN 2518-7198 (Print). ISSN 2663-5089 (Online).

Proprietary: NLC «Karagandy University of the name of academician E.A. Buketov».

Registered by the Ministry of Information and Social Development of the Republic of Kazakhstan. Rediscount certificate No. KZ38VPY00027378 dated 30.09.2020.

Signed in print 29.09.2020. Format 60×84 1/8. Offset paper. Volume 12,37 p.sh. Circulation 200 copies. Price upon request. Order № 57.

Printed in the Publishing house of NLC «Karagandy University of the name of acad. E.A. Buketov». 100012, Kazakhstan, Karaganda, Gogol Str., 38, Tel.: (7212) 51-38-20. E-mail: izd_kargu@mail.ru

МАЗМУНЫ — СОДЕРЖАНИЕ — CONTENTS

КОНДЕНСАЦИЯ ЛАНҒАН КҮЙДІҢ ФИЗИКАСЫ ФИЗИКА КОНДЕНСИРОВАННОГО СОСТОЯНИЯ PHYSICS OF THE CONDENSED MATTER

<i>Seliverstova E.V., Ibrayev N.Kh., Temirbayeva D.A., Omarova G.S.</i> Optical properties of ablated graphene oxide in aqueous dispersions	6
<i>Serikov T.M.</i> The effect of electric transport properties of titanium dioxide nanostructures on their photocatalytic activity	13
<i>Rudnikov A.S., Yarmolenko M.A., Rogachev A.A., Surzhikov A.P., Luchnikov A.P., Frolova O.A.</i> Phase composition and morphology of nanostructured coatings deposited by laser dispersion of a mixture of polyethylene with iron oxalate.....	22
<i>Piliptsov D.G., Rudnikov A.S., Rogachev A.V., Jiang Xiao Hong, Kulesh E.A., Surzhikov A.P., Luchnikov A.P., Frolova O.A.</i> Structural properties of carbon composites doped with boron.....	31
<i>Dmitriyeva E.A., Lebedev I.A., Grushevskaya E.A., Murzalinov D.O., Serikkanov A.S., Tompakova N.M., Fedosimova A.I., Temiraliyev A.T.</i> The effect of three-minute exposure of oxygen plasma on the properties of tin oxide films.....	38
<i>Borodin Y.V., Sysolov K.V., Rande V.R., Vavilova G.V., Starý O.</i> Spectroscopy of nanoscale crystalline structural elements	46

ТЕХНИКАЛЫҚ ФИЗИКА ТЕХНИЧЕСКАЯ ФИЗИКА TECHNICAL PHYSICS

<i>Perminov V.A., Fryanova K.O.</i> Mathematical modeling of the initiation and spread of forest fires and their impact on buildings and structures	54
<i>Kovbasa V.P., Solomka A.V., Spirin A.V., Kucheruk V.Yu., Karabekova D.Zh., Khassenov A.K.</i> Theoretical determination of the distribution of forces and the size of the boundaries of the contact in the interaction of the deformable drive wheel with the soil	62

ЖЫЛУ ФИЗИКАСЫ ЖӘНЕ ТЕОРИЯЛЫҚ ЖЫЛУ ТЕХНИКАСЫ ТЕПЛОФИЗИКА И ТЕОРЕТИЧЕСКАЯ ТЕПЛОТЕХНИКА THERMOPHYSICS AND THEORETICAL THERMOENGINEERING

<i>Sarode A.P., Mahajan O.H.</i> Theoretical aspects of transient temperature on cubic crystal surface in a photoacoustic effect	73
--	----

АСПАПТАР МЕН ЭКСПЕРИМЕНТ ТЕХНИКАСЫ ПРИБОРЫ И ТЕХНИКА ЭКСПЕРИМЕНТА INSTRUMENTS AND EXPERIMENTAL TECHNIQUES

<i>Udovytska Yu.A., Luniov S.V., Maslyuk V.T., Megela I.G.</i> Influence of electron irradiation on mechanical properties of epoxy polymers	80
<i>Zinchenko S., Ben A., Nosov P., Popovych I., Mateichuk V., Grosheva O.</i> The vessel movement optimisation with excessive control	86

АВТОРЛАР ТУРАЛЫ МӘЛІМЕТТЕР — СВЕДЕНИЯ ОБ АВТОРАХ — INFORMATION ABOUT AUTHORS	97
--	----

E.V. Seliverstova*, N.Kh. Ibrayev, D.A. Temirbayeva, G.S. Omarova

Institute of Molecular Nanophotonics, Karagandy University of the name of academician E.A. Buketov, Kazakhstan
(*E-mail: genia_sv@mail.ru)

Optical properties of ablated graphene oxide in aqueous dispersions

The effect of laser radiation on the structural and optical properties of graphene oxide dispersed in water was studied. It was shown that under laser ablation a significant reduction in the size of graphene oxide sheets can be achieved. In this case, the resulting main parts of particles have a size of about 110–120 nm, and are similar to graphene quantum dots. The Raman spectra indicate the reduction of graphene oxide during laser radiation. The thickness of the formed particles practically was not changed, since the I_D/I_G ratio has close values. The prepared dispersions of graphene oxide exhibit wide luminescence bands in the region of 400–600 nm with a maximum of about 450 nm and a lifetime of 1.6 ns. It was shown that by laser ablation it is possible to achieve a significant increasing in the luminescent ability of graphene oxide in an aqueous solution. In this case, the luminescence intensity increased by almost 2 times, while the optical density of the solution was increased by only 5 % relative to the initial dispersion. The results can be used to create organic luminescent materials, in optical nanotechnology, as well as in photovoltaics, biophysics and bioimaging.

Keywords: graphene oxide, laser ablation, dispersion, size distribution, structure, absorbance, luminescence, lifetime kinetics.

Introduction

Carbon is one of the most common chemical elements. Carbon materials that include graphite, diamonds, fullerenes, carbon nanotubes and graphene have been well known for a long time.

Graphene is widely used in energy and environmental materials [1], such as energy storage [2], photovoltaics [3], photoelectrochemical [4] and photocatalytic [5–8] generation of hydrogen/hydrocarbon fuels and photocatalysis of organic pollutants.

It is known that graphene is a superconducting material with zero band gap. In this case, graphene oxides are semiconductors with a controlled band gap width by resizing sheets and the degree of its oxidation. Graphene oxide and its modifications, unlike graphene, is a more convenient material for researchers, since it is easy to obtain and also used for practical purposes.

The quantum confinement effect is applicable not only to graphene, but also to graphene oxide. This led to the emergence of a new type of carbon nanostructures — graphene quantum dots. Such quantum dots have a discrete band gap and exhibit photoluminescent properties. Graphene quantum dots of various shapes and sizes exhibit unusual photoluminescence, which is associated with a circular polygonal shape and the corresponding edge effects of graphene quantum dots [8].

Compared to traditional semiconductor quantum dots and organic dyes, photoluminescent carbon-based quantum dots have high solubility in aqueous solutions, chemical inertness, and resistance to photobleaching. For example, electron generation and transport at graphene dots were used for solar cells [9–11], organic light emitting diodes (OLED) [12], photodetectors, photocatalysts [13] and supercapacitors [14]. Extinction-

controlled fluorescence was developed for sensors of biomolecules, metal ions, and toxic/hazardous substances [15, 16].

Also, an its advantage is low toxicity and high biocompatibility compared to semiconductor quantum dots, which makes them very promising for biophysical and medical applications, for example, for bioimages, biosensors, drug delivery, and medical diagnostics [17, 18]. In addition, graphene dots can be easily modified both by the addition of functional groups and by doping with heteroatoms. It may be useful for fluorescent nanocomposites, functional hybrids, and materials with a high refractive index [18].

Over the past few years, significant progress has been made in the synthesis, study of the properties and practical applications of carbon-based and graphene quantum dots. There is two approaches are distinguished among the methods for the obtaining of graphene dots: «bottom-up» and «top-down». However, the synthesis used in these approaches often require the usage of aggressive reagents, critical reaction conditions, are time-consuming and, often, expensive procedures, since they involve several stages.

Pulse laser ablation in a liquid can be used as a one-step, low-cost and fast method for preparing graphene dots with controlled parameters. Currently, very few papers have been published on the preparation of graphene quantum dots by laser ablation [19, 20].

In particular, this method was used in Ref. [19] to obtain graphene oxide nanostructures. It was shown that in the process of ablation, occurs the formation of graphene oxide nanostructures with various shapes: ribbons, flakes and quantum dots with simultaneous photoreduction of graphene oxide. The quantum dots of graphene oxide have blue photoluminescence, which is the result of recombination of charge carriers localized on zigzag edges. The luminescence intensity varies for dots obtained at different irradiation times.

Also, this method was used for the synthesis of graphene oxide dots in Ref. [20]. The diameter of the resulting structures varies from 5 to 30 nm, and they have good stability and crystallinity. The luminescence spectrum of the resulting nanostructures is located in the yellow-green region, which is atypical for graphene quantum dots. The authors showed that these dots have high optoelectronic properties and were used as markers for displaying cancer cells.

In this work, we studied the effect of laser radiation on the structural and optical properties of graphene oxide dispersed in water.

Experimental

For the preparation of dispersions, a single-layer graphene oxide (GO, Cheaptubes) was used. Since it was shown earlier in our work [21], GO dispersed into particles of various sizes and stability in various organic solvents. Here we selected water. Deionized water was purified using the AquaMax system. The specific resistance of water was equal to 18.2 M Ω /cm. The surface tension of water was equal to 72.8 mN/m at pH=5.6 and a temperature of 22 °C.

The GO concentration in the solution was equal to 0.25 mg/ml. To obtain dispersion, it was treated with ultrasound for 30 minutes. The GO dispersion was undergo to laser ablation with the second harmonic of a solid-state Nd:YAG laser with a generation wavelength at 532.0 nm, a pulse duration of 10 ns, and an pulse energy of ~ 16 J/cm². The height of the ablated liquid was 0.8 cm. The particle size of graphene oxide in the solutions was determined by dynamic light scattering method using a Zetasizer nano analyzer (Malvern).

The absorption and fluorescence spectra of the samples were measured on Cary and Eclipse (Agilent) spectrometers, respectively. Raman spectra of the prepared samples were recorded using Confotec MR520 (3D Scanning Raman Confocal Microscope, Sol Instruments) with laser excitation at a wavelength of 532 nm.

The fluorescence lifetimes of dispersions were determined using the TCSPC system (Becker&Hickl) at an excitation wavelength of $\lambda_{\text{ex}} = 488$ nm. The fluorescence lifetimes were determined from decay kinetics processing with SPCImage software (Becker&Hickl). All measurements were performed in 1 cm quartz cuvettes at room temperature.

Results and discussion

Measurements showed that after dispersing of GO in water and before laser irradiation, about half of the particles have an average size of 4900 nm, and the second half of sizes are in the order of 2300 nm (Fig. 1a).

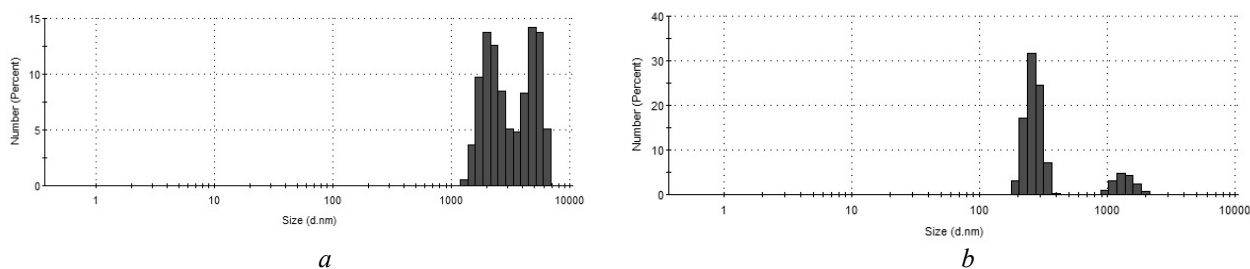


Figure 1. Size distribution of GO particles in water before (a) and after (b) laser irradiation

After ablation (Fig. 1b), a darkening of the GO solution was registered and a decrease in the average particle size to 200–250 nm were observed. And about 13 % of the particles have a diameter of about 1400 nm.

Measurements of the optical characteristics showed (Fig. 2) a wide absorption band with a maximum of about 230 nm of the prepared dispersion, which is formed by transitions between orbitals of $\pi\pi^*$ -nature in C–C aromatic bonds [22, 23]. A shoulder of about 300 nm is associated with $n\rightarrow\pi^*$ transitions in C=O bonds, and it is almost indistinguishable in the absorption spectra.

It can be seen from the spectrum that the optical density of the dispersion of graphene oxide in water after ablation is higher than before irradiation. It is a result of uniform distribution and increase in the concentration of GO particles after laser treatment. As well as the fact that prior to ablation, graphene oxide flakes were clearly distinguishable in solution. After laser treatment, the solution became more transparent and intensely colored due to the uniform distribution of graphene oxide particles.

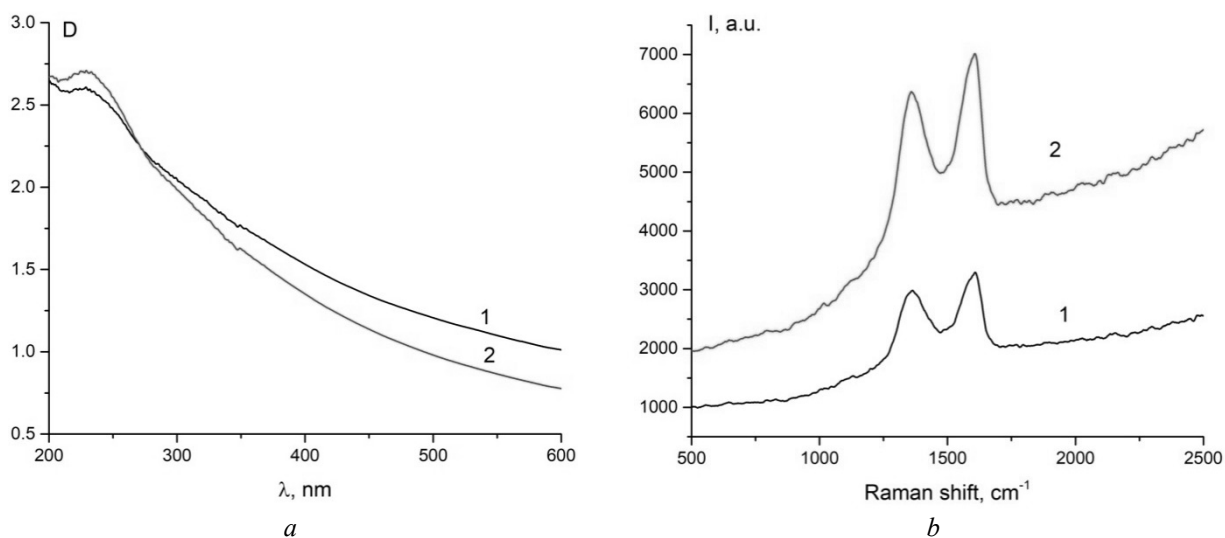


Figure 2. Absorption (a) and Raman (b) spectra of GO dispersion before (1) and after (2) ablation

The effect of laser ablation on the structural properties of graphene oxide is shown in Figure 2b. Two intense bands in the region of 1300 and 1600 cm^{-1} were registered in the Raman spectrum of GO. The G-band of GO is located at 1605 cm^{-1} and is shifted to higher frequencies compared to the position of this band in graphite (1581 cm^{-1}) due to the presence of separate double bonds that resonate at higher frequencies [24, 25]. After complete reduction of graphene oxide to graphene, a bathochromic shift usually occurs. As can be seen from the figure, it was not occurred after laser ablation.

Also, in the Raman spectrum of GO, there is exhibits a D band of about 1360 cm^{-1} , which characterizes the defectness of graphene and is active only if defects participate in double resonance scattering near the Brillouin zone [24]. Therefore, the I_D/I_G intensities ratio is often used to determine the size of domains with sp^2 hybridization in carbon materials. The data obtained showed that the ratio of the intensities of the G and D bands was changed from 1.10 to 1.05, which indicates a partial reduction of graphene oxide during laser ablation.

Under the studying the luminescent properties of the prepared dispersions, the spectra shown in Figure 3 were obtained.

A wide band with a maximum of about 450 nm was registered in the GO luminescence spectrum. When the luminescence excitation wavelength was changed from 320 nm to 350 nm, the position and shape of the fluorescence band was not changed. The fluorescence intensity in this case was increased by ~20 %.

After ablation, the luminescence spectrum also practically was not changed in its shape, however, the luminescence intensity was increased almost in 2 times for both excitation wavelengths. This fact could be explained by growth in the optical density D of the solution after ablation. However, the D value was increased by only 5 %. Therefore, growth in the luminescence intensity is associated with other processes. As shown by the measured fluorescence excitation spectra (on the inset in Fig. 3a), the main contribution to the GO fluorescence is made by the centers actively absorbing light in the region of 320–340 nm. After laser ablation, their changes practically do not occur. When the excitation spectrum was recorded at the long-wavelength edge of the luminescence (at ~580 nm), a spectrum that was similar in shape to the absorption spectrum of GO was obtained. At present, the mechanism of the occurrence of fluorescence in graphene nanostructures remains incompletely studied, but most authors [24, 25] believe that it can be assigned to different emitting groups or localized electron–hole pairs due to the isolation of sp^2 clusters inside the sp^3 matrix. In any case, this will be the basis for our further studies.

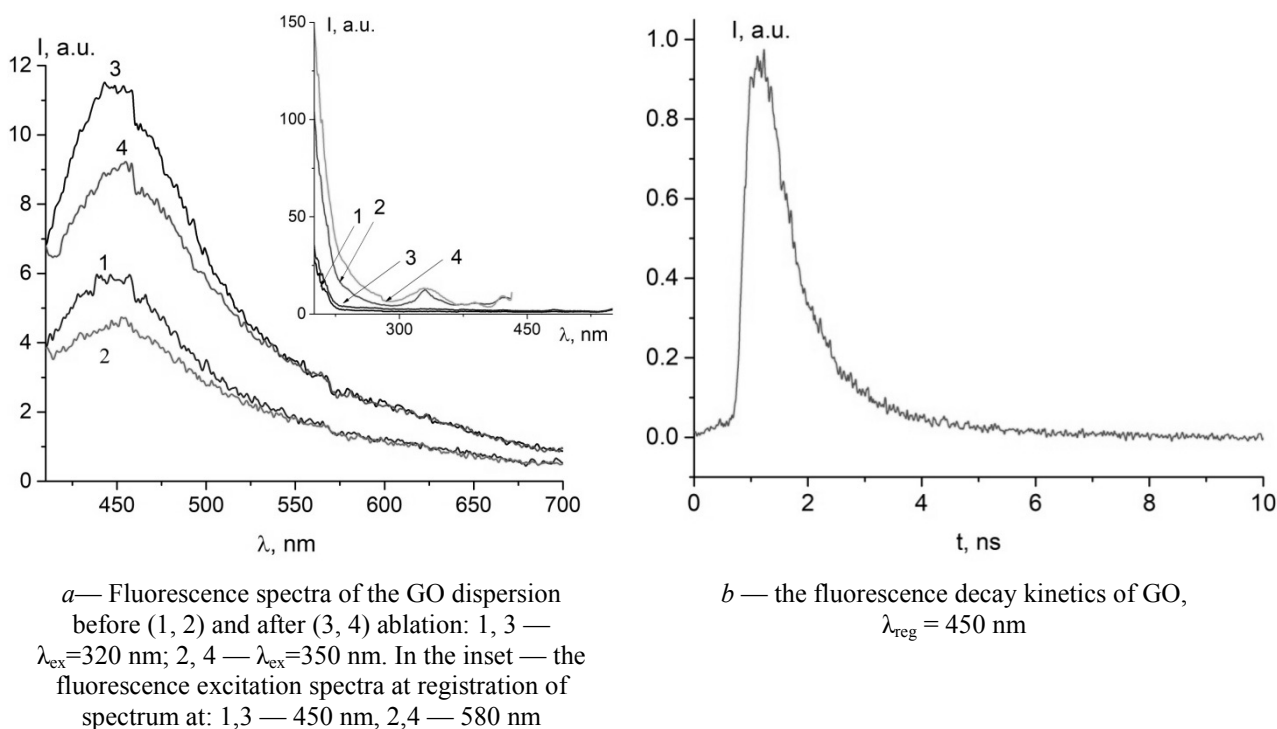


Figure 3

When measuring the lifetime of GO luminescence in solutions, the excitation was carried out at a wavelength of 375 nm (Figure 3b). The decay kinetics of GO is described by a bi-exponential equation. The average fluorescence lifetime of GO at $\lambda = 455$ nm is equal to $\tau_{\text{fl}} = 1.6$ ns for the initial dispersion. After ablation, τ_{fl} has changed little and it was equal to 1.57 ns. This indicates a similar nature of luminescence before and after laser ablation of a graphene oxide dispersion.

Conclusion

Thus, it has been shown that by laser ablation of graphene oxide in water, a significant reduction in the size of GO sheets can be achieved. In this case, the resulting particles have a size mainly of about 110–120 nm, and are similar to graphene quantum dots. The measured Raman spectra indicate the reduction of graphene oxide during laser ablation. In this case, the thickness of the formed particles practically does not change, since the $I_{\text{D}}/I_{\text{G}}$ ratio has close values.

It was shown that by laser ablation it is possible to achieve a significant increase in the luminescent ability of GO in an aqueous solution. In this case, the luminescence intensity was increased by almost 2 times, while the optical density of the solution was increased by only 5 % relative to the initial solution. The recorded fluorescence excitation spectra indicate that the main contribution to the GO luminescence is made by the centers actively absorbing light in the region of 320–340 nm. After laser ablation, changes in the fluorescence excitation spectra practically do not occur.

The results can be used to create organic luminescent materials, in optical nanotechnologies, as well as in photovoltaics, biophysics and bioimaging.

This work was carried out as part of the research project AP08052672, funded by the Ministry of Education and Science of the Republic of Kazakhstan.

References

- 1 Kamat P.V. Graphene-based nanoassemblies for energy conversion / P.V. Kamat // *J. Phys. Chem. Lett.* — 2011. — Vol. 2. — P. 242–251. DOI: 10.1021/jz101639v
- 2 Wang D.H. Self-assembled TiO₂-graphene hybrid nanostructures for enhanced Li-Ion insertion / D.H. Wang, D.W. Choi, J. Li, Z.G. Yang, Z.M. Nie, R. Kou // *ACS Nano.* — 2009. — Vol. 3. — P. 907–914. DOI: 10.1021/nn900150y
- 3 Wang X., Zhi L., Muellen K. Transparent, Conductive graphene electrodes for dye-sensitized solar cells / X. Wang, L. Zhi, K. Muellen // *Nano Lett.* — 2008. — Vol. 8. — P. 323–327. DOI: 10.1021/nl072838r
- 4 Ng Y.H. To what extent do graphene scaffolds improve the photovoltaic and photocatalytic response of TiO₂ nanostructured films / Y.H. Ng, I.V. Lightcap, K. Goodwin, M. Matsumura, P.V. Kamat // *J. Phys. Chem. Lett.* — 2010. — Vol. 15 — P. 2222–2227. DOI:10.1021/jz100728z
- 5 Li Q. Highly efficient visible-light-driven photocatalytic hydrogen production of CdS-cluster-decorated graphene nanosheets / Q. Li, B.D. Guo, J.G. Yu, J.R. Ran, B.H. Zhang, H.J. Yan, et al. // *J. Am. Chem. Soc.* — 2011. — Vol. 133. — P. 10878–10884. DOI: 10.1021/ja2025454
- 6 Ozer L.Y. Inorganic semiconductors-graphene composites in photo(electro)catalysis: synthetic strategies, interaction mechanisms and applications / L.Y. Ozer, C. Garlisi, H. Oladipo, M. Pagliaro, S.A. Sharief, A. Yusuf, et al. // *J. Photochem. and Photobiol. C: Photochem. Rev.* — 2007. — Vol. 33. — P. 132–164. DOI: 10.1016/j.jphotochemrev.2017.06.003
- 7 Zhang Z. Role of particle size in nanocrystalline TiO₂-based photocatalysts / Z. Zhang, C. Wang, R. Zakaria, Y. Ying // *J. Phys. Chem.: B.* — 1998. — Vol. 102. — P. 10871–10878. <https://doi.org/10.1021/jp982948>
- 8 Kim S. Anomalous behaviors of visible luminescence from graphene quantum dots: interplay between size and shape / S. Kim, S.W. Hwang, M. Kim, D.Y. Shin, D.H. Shin // *ACS Nano.* — 2012. — Vol. 6. — P. 8203. DOI: 10.1021/nn302878r
- 9 Tang Q. Rapid conversion from carbohydrates to large-scale carbon quantum dots for all-weather solar cells / Q. Tang, W. Zhu, B. He, P. Yang // *ACS Nano.* — 2017. — Vol. 11. — P. 1540–1547. DOI: 10.1021/acsnano.6b06867
- 10 Ryu J. Correction: size effects of a graphene quantum dot modified-blocking TiO₂ layer for efficient planar perovskite solar cells / J. Ryu, J.W. Lee, H. Yu, J. Yun, K. Lee, J. Lee // *J. Mater. Chem. A.* — 2017. — Vol. 34. — P. 18276. DOI: 10.1039/C7TA90183F
- 11 Tsai M.-L. Si Hybrid solar cells with 13 % efficiency via concurrent improvement in optical and electrical properties by employing graphene quantum dots / M.-L. Tsai, W.-R. Wei, L. Tang, H.-C. Chang, S.-H. Tai, P.-K. Yang, et al. // *ACS Nano.* — 2015. — Vol. 1. — P. 815–821. DOI: 10.1021/acsnano.5b05928
- 12 Song S.H. Highly efficient light-emitting diode of graphene quantum dots fabricated from graphite intercalation compounds / S.H. Song, M.-H. Jang, J. Chung, S.H. Jin, B.H. Kim, S.-H. Hur, et al. // *Adv. Opt. Mater.* — 2014. — Vol. 11. — P. 1016–1023. DOI: 10.1002/adom.201400184
- 13 Arvand M. Analytical methodology for the electro-catalytic determination of estradiol and progesterone based on graphene quantum dots and poly(sulfosalicylic acid) co-modified electrode / M. Arvand, S. Hemmati // *Talanta.* — 2017. — Vol. 174. — P. 243–255. DOI: 10.1016/j.talanta.2017.05.083
- 14 Niu Y. Graphene quantum dots as a novel conductive additive to improve the capacitive performance for supercapacitors / Y. Niu, J. Wang, J. Zhang, Zh. Shi // *Journal of Electroanalytical Chemistry.* — 2018. — Vol. 828. — P. 1–10. DOI: 10.1016/j.jelechem.2018.09.003
- 15 Li K. Technical synthesis and biomedical applications of graphene quantum dots / K. Li, W. Liu, Y. Ni, D. Li, D. Lin, Z. Su, et al. // *J. Mater. Chem. B.* — 2017. — Vol. 5. — P. 4811–4826. DOI: 10.1039/C7TB01073G
- 16 Xu Q. Singleparticle spectroscopic measurements of fluorescent graphene quantum dots / Q. Xu, Q. Zhou, Z. Hua, Q. Xue, C. Zhang, X. Wang, et al. // *ACS Nano.* — 2013. — Vol. 12. — P. 10654–10661. DOI: 10.1021/nn4053342
- 17 Nuengmatcha P. The use of S₂O₈²⁻ and H₂O₂ as novel specific masking agents for highly selective «turn-on» fluorescent switching recognition of CN and I based on Hg₂ graphene quantum dots / P. Nuengmatcha, P. Sricharoen, N. Limchoowong, R. Mahachai, S. Chanthai // *RSC Adv.* — 2018. — Vol. 8. — P. 1407–1417. DOI: 10.1039/C7RA12327B
- 18 Wang D. Recent advances in graphene quantum dots for fluorescence bioimaging from cells through tissues to animals / D. Wang, J.-F. Chen, L. Dai // *Part. Syst. Charact.* — 2014. — Vol. 32. — P. 515–523. DOI: 10.1002/ppsc.201400219
- 19 Lin T.N. Laser-ablation production of graphene oxide nanostructures: from ribbons to quantum dots / T.N. Lin, K.H. Chih, C.T. Yuan, J.L. Shen, C.A.J. Lince, W.R. Liud // *Nanoscale.* — 2015. — Vol. 7. — P. 2708–2715. DOI: 10.1039/C4NR05737F

- 20 Kang S. Graphene oxide quantum dots derived from coal for bioimaging: facile and green approach / S. Kang, K.M. Kim, K. Jung, Y. Son, S. Mhin, J.H. Ryu, et al. // *Scientific Reports*. — 2019. — Vol. 9. — P. 4101. DOI: 10.1038/s41598-018-37479-6
- 21 Селиверстова Е.В. Получение и исследование свойств диспергированного оксида графена / Е.В. Селиверстова, Н.Х. Ибраев, Р.Х. Джанабекова, Г. Каримова // *Вестн. Казах. нац. ун-та. Сер. хим.* — 2015. — Т. 79, № 3. — С. 67–70.
- 22 Seliverstova E. Effect of the conditions of transfer on the Structure and Optical Properties of Langmuir Graphene Oxide Films during Deposition on a Substrate / E. Seliverstova, N.Kh. Ibrayev, R.Kh. Dzhnanabekova // *Russian Journal of Physical Chemistry*. — 2017. — Vol. 91, No. 9. — P. 1761–1765. DOI: 10.1134/S003602441709028X
- 23 Sutar D.S. Spectroscopic studies of large sheets of graphene oxide and reduced graphene oxide monolayers prepared by Langmuir-Blodgett technique / D.S. Sutar, P.K. Narayanam, G. Singh, D.V. Botcha, S.S. Talwar, R.S. Srinivasa // *Thin Solid Films*. — 2012. — Vol. 520. — P. 5991–5996. DOI: 10.1016/j.tsf.2012.05.018
- 24 Raman spectroscopy in graphene related systems / A. Jorio, M. Dresselhaus, R. Saito, G.F. Dresselhaus — Verlag: Wiley-VCH, 2011. — 356 p. DOI: 10.1002/9783527632695
- 25 Paredes J.I. Atomic force and scanning tunneling microscopy imaging of graphene nanosheets derived from graphite oxid / J.I. Paredes, R.S. Villar, F.P. Solis, A.A. Martinez, J.M. Tascon // *Langmuir*. — 2009. — Vol. 25. — P. 5957–5968. DOI: 10.1021/la804216z

Е.В. Селиверстова, Н.Х. Ибраев, Д.А. Темирбаева, Г.С. Омарова

Су дисперсиясындағы аблирленген графен оксидінің оптикалық қасиеттері

Суда дисперсияланған графен оксидінің құрылымдық және оптикалық қасиеттеріне лазерлік сәулеленудің әсері зерттелген. Графен оксидін суда лазерлік абляциялау арқылы графен оксиді парағының мөлшерін едәуір азайтуға болатындығы көрсетілді. Бұл жағдайда алынған бөлшектердің мөлшері шамамен 110–120 нм болады және ол графен кванттық нүктелеріне ұқсас. Раман спектрін өлшеу лазерлік сәулелендіру кезінде графен оксидінің қалпына келетіндігін көрсетті. Бұл жағдайда қалыптасқан бөлшектердің қалыңдығы іс жүзінде өзгермейді, өйткені I_D/I_G қатынасы жақын мәндерге ие. Графен оксидінің дайындалған дисперсиялары 400–600 нм аймақта максимум 450 нм және өмір сүру ұзақтығы 1,6 нс болатын кең люминесценциялық жолақтарды көрсетті. Лазерлік абляция арқылы су ерітіндісінде графен оксидінің люминесценттік қабілетінің едәуір артуына қол жеткізуге болатындығы көрсетілген. Бұл жағдайда люминесценцияның қарқындылығы 2 есе өсті, ал ерітіндінің оптикалық тығыздығы бастапқы ерітіндімен салыстырғанда 5 %-ға өсті. Алынған нәтижелерді органикалық люминесцентті материалдарды, оптикалық нанотехнологияларды жасау үшін, сонымен қатар фотоэлектриктерде, биофизика мен биобейнелеуде қолдануға болады.

Кілт сөздер: графен оксиді, лазерлік абляция, дисперсия, өлшемдердің таралуы, құрылымы, жұтылу, люминесценция, өмір сүру кинетикасы.

Е.В. Селиверстова, Н.Х. Ибраев, Д.А. Темирбаева, Г.С. Омарова

Оптические свойства аблированного оксида графена в водных дисперсиях

Изучено влияние лазерного облучения на структурные и оптические свойства оксида графена, диспергированного в воде. Показано, что путем лазерной абляции оксида графена в воде можно добиться значительного уменьшения размеров листов оксида графена. При этом образующиеся частицы имеют размер преимущественно около 110–120 нм и схожи с графеновыми квантовыми точками. Измеренные раман-спектры указывают на восстановление оксида графена в процессе лазерного облучения. При этом толщина образуемых частиц практически не изменяется, так как отношение I_D/I_G имеет близкие значения. Приготовленные дисперсии оксида графена проявляют широкие полосы свечения в области 400–600 нм с максимумом около 450 нм и временем жизни 1,6 нс. Показано, что путем лазерной абляции можно добиться значительного увеличения люминесцентной способности оксида графена в водном растворе. При этом интенсивность свечения возросла почти в 2 раза, тогда как оптическая плотность раствора увеличилась лишь на 5 % относительно исходного раствора. Полученные результаты могут быть использованы для создания органических люминесцентных материалов в оптических нанотехнологиях, а также в фотовольтаике, биофизике и для бионимиджинга.

Ключевые слова: оксид графена, лазерная абляция, дисперсия, распределение по размерам, структура, поглощение, люминесценция, кинетика времени жизни.

References

- 1 Kamat, P.V. (2011). Graphene-based nanoassemblies for energy conversion. *The Journal of Physical Chemistry Letters*, 2, 242–251.

- 2 Wang, D., Choi, D., Li, J., Yang, Z., Nie, Z., & Kou, R., et al. (2009). Self-assembled TiO₂–graphene hybrid nanostructures for enhanced Li-Ion insertion. *ACS Nano*, 3, 907–914.
- 3 Wang, X., Zhi, L., & Müllen, K. (2008). Transparent, conductive graphene electrodes for dye-sensitized solar cells. *Nano Letters*, 8, 323–327. doi: 10.1021/nl072838r
- 4 Ng, Y.H., Lightcap, I.V., Goodwin, K., Matsumura, M., & Kamat, P.V. (2010). To what extent do graphene scaffolds improve the photovoltaic and photocatalytic response of TiO₂ nanostructured films. *The Journal of Physical Chemistry Letters*, 15, 2222–2227.
- 5 Li, Q., Guo, B., Yu, J., Ran, J., Zhang, B., & Yan, H., et al. (2011). Highly efficient visible-light-driven photocatalytic hydrogen production of CdS-cluster-decorated graphene nanosheets. *Journal of the American Chemical Society*, 133, 28, 10878–10884. DOI: 10.1021/ja2025454
- 6 Ozer, L.Y., Garlisi, C., Oladipo, H., Pagliaro, M., Sharief, S.A., & Yusuf, A., et al. (2017). Inorganic semiconductors-graphene composites in photo(electro)catalysis: Synthetic strategies, interaction mechanisms and applications. *Journal of Photochemistry and Photobiology C: Photochemistry Reviews*, 33, 132–164. DOI: 10.1016/j.jphotochemrev.2017.06.003
- 7 Zhang, Z., Wang, C.-C., Zakaria, R., & Ying, J.Y. (1998). Role of Particle Size in Nanocrystalline TiO₂-Based Photocatalysts. *J. Phys. Chem.: B*, 102, 10871–10878.
- 8 Kim, S., Hwang, S.W., Kim, M.-K., Shin, D.Y., Shin, D.H., Kim, C.O., & Hong, B.H. (2012). Anomalous behaviors of visible luminescence from graphene quantum dots: interplay between size and shape. *ACS Nano*, 6, 8203–8208.
- 9 Tang, Q., Zhu, W., He, B., & Yang, P. (2017). Rapid conversion from carbohydrates to large-scale carbon quantum dots for all-weather solar cells. *ACS Nano*, 11, 1540–1547.
- 10 Ryu, J., Lee, J.W., Yu, H., Yun, J., Lee, K., & Lee, J., et al. (2017). Correction: Size effects of a graphene quantum dot modified-blocking TiO₂ layer for efficient planar perovskite solar cells. *Journal of Materials Chemistry A*, 34, 18276–18276. DOI: 10.1039/C7TA90183F
- 11 Tsai, M.-L., Wei, W.-R., Tang, L., Chang, H.-C., Tai, S.-H., & Yang, P.-K., et al. (2016). Si hybrid solar cells with 13 % efficiency via concurrent improvement in optical and electrical properties by employing graphene quantum dots. *ACS Nano*, 10, 815–821.
- 12 Song, S.H., Jang, M.-H., Chung, J., Jin, S.H., Kim, B.H., & Hur, S.-H., et al. (2014). Highly efficient light-emitting diode of graphene quantum dots fabricated from graphite intercalation compounds. *Advanced Optical Materials*, 11, 1016–1023.
- 13 Arvand, M., & Hemmati, S. (2017). Analytical methodology for the electro-catalytic determination of estradiol and progesterone based on graphene quantum dots and poly(sulfosalicylic acid) co-modified electrode. *Talanta*, 174, 243–255. DOI: 10.1016/j.talanta.2017.05.083
- 14 Niu, Y., Wang, J., Zhang, J., & Shi, Z. (2018). Graphene quantum dots as a novel conductive additive to improve the capacitive performance for supercapacitors. *Journal of Electroanalytical Chemistry*, 828, 1–10.
- 15 Li, K., Liu, W., Ni, Y., Li, D., Lin, D., Su, Z., & Wei, G. (2017). Technical synthesis and biomedical applications of graphene quantum dots. *Journal of Materials Chemistry B*, 5, 4811–4826.
- 16 Xu, Q., Zhou, Q., Hua, Z., Xue, Q., Zhang, C., & Wang, X., et al. (2013). Single-particle spectroscopic measurements of fluorescent graphene quantum dots. *ACS Nano*, 12, 10654–10661.
- 17 Nuengmatcha, P., Sricharoen, P., Limchoowong, N., Mahachai, R., & Chanthai, S. (2018). The use of S₂O₈²⁻ and H₂O₂ as novel specific masking agents for highly selective «turn-on» fluorescent switching recognition of CN⁻ and I⁻ based on Hg²⁺–graphene quantum dots. *RSC Advances*, 8, 1407–1417.
- 18 Wang, D., Chen, J.-F., & Dai, L. (2015). Recent advances in graphene quantum dots for fluorescence bioimaging from cells through tissues to animals. *Particle&Particle Systems Characterization*, 32, 515–523.
- 19 Lin, T.N., Chih, K.H., Yuan, C.T., Shen, J.L., & Lin, C.A.J., et al. (2015). Laser-ablation production of graphene oxide nanostructures: From ribbons to quantum dots. *Nanoscale*, 7, 2708–2715.
- 20 Kang, S., Kim, K.M., Jung, K., Son, Y., Mhin, S., & Ryu, J. H., et al. (2019). Graphene oxide quantum dots derived from coal for bioimaging: facile and green approach. *Scientific Reports*, 9, 4101.
- 21 Seliverstova, E.V., Ibrayev, N.Kh., Dzhanabekova, R.Kh., & Karimova, G. (2015). Poluchenie i issledovanie svoystv disperhivannogo oksida hrafena [Obtaining a study of the properties of dispersed graphene oxide]. *Vestnik Kazakhskoho natsionalnoho universitieta. Seriya khimicheskaya — Bulletin of the Kazakh National University. Chemical Series*, 79, 3, 67–70 [in Russian].
- 22 Seliverstova, E.V., Ibrayev, N. Kh., & Dzhanabekova, R. Kh. (2017). Effect of the conditions of transfer on the structure and optical properties of Langmuir graphene oxide films during deposition on a substrate. *Russian Journal of Physical Chemistry A*, 91, 9, 1761–1765.
- 23 Sutar, D.S., Narayanam, P.K., Singh, G., Botcha, V.D., Talwar, S.S., & Srinivasa, R.S., et al. (2012). Spectroscopic studies of large sheets of graphene oxide and reduced graphene oxide monolayers prepared by Langmuir–Blodgett technique. *Thin Solid Films*, 520, 5991–5996.
- 24 Jorio, A., Saito, R., Dresselhaus, G., & Dresselhaus, M.S. (2011). Raman Spectroscopy in Graphene Related Systems: *Jorio: Raman O-BK*.
- 25 Paredes, J.I., Villar-Rodil, S., Solís-Fernández, P., Martínez-Alonso, A., & Tascón, J.M.D. (2009). Atomic force and scanning tunneling microscopy imaging of graphene nanosheets derived from graphite oxide. *Langmuir*, 25, 5957–5968.

T.M. Serikov*

*Karagandy University of the name of academician E.A. Buketov, Kazakhstan
(*E-mail: serikov-timur@mail.ru)*

The effect of electric transport properties of titanium dioxide nanostructures on their photocatalytic activity

Annotation. Films formed by nanoparticles, nanorods and nanotubes of titanium dioxide with a thickness of 3.9, 4.0 and 4.1 μm , respectively, with an area of 2 cm^2 were obtained by various methods. Nanostructures were characterized by X-ray phase analysis, scanning electron microscopy (SEM), BET (Brunauer–Emmett–Teller), BJH (Barrett–Joyner–Halenda). The electric transport properties of the films were studied by impedance spectroscopy. The photocatalytic activity of the samples was evaluated by the photocurrent and degradation of the methylene blue dye under xenon lamp illumination. The concentration of hydrogen released per unit time was determined by gas chromatography in a standard quartz cuvette using a platinum electrode. The study of texture characteristics showed that the obtained isotherms belong to type IV isotherms with a hysteresis loop, reflecting the process of capillary condensation in mesopores. The diffraction peaks for the films of nanoparticles and nanotubes of titanium dioxide are identical and correspond to the tetragonal phase of anatase, for films of nanorods to the tetragonal phase of rutile. When studying the electric transport properties of films, it was found that films of titanium dioxide nanoparticles have a higher resistance associated with unformed bonds between nanoparticles. Despite the low specific surface area, titanium dioxide nanorods showed higher photocatalytic activity than nanotubes and nanoparticles. The results are confirmed by measurements of photocurrent, dye decomposition and the splitting of water molecules into hydrogen gas and oxygen.

Keywords: nanoparticles, nanotubes, nanorods, titanium dioxide, BET, electric transport properties, photocatalytic activity, hydrogen

Introduction

Development and research to create effective photocatalysts for the degradation of organic compounds and toxic substances in drinking water, the splitting of water molecules into hydrogen and oxygen are the promising direction in «green energy». Semiconductors, often used as photocatalysts, have the ability to generate reactive oxygen species (ROS) O_2^- , $^1\text{O}_2$, H_2O_2 и OH . Over the past decade, nanostructures based on titanium dioxide (TiO_2) have been the most effective photocatalysts, due to their chemical stability, low cost, fairly high oxidizing capacity, optical properties and features of electronic transport [1].

It is known that the photocatalytic activity of nanomaterials is influenced by many factors, the most significant of which are the specific surface area, particle size, crystal phase, morphology, and electronic transport. Heterogeneous catalysis between catalysts and reagents occurs mainly on the surface or at the interface, so the efficiency depends partly on the specific surface area of the materials. A large specific surface area will provide a large active contact area, allowing the adsorbed water molecules and hydroxyl to react faster, and are also a place for fixing organic molecules for photodegradation [2–4]. The specific surface area increases dramatically with decreasing crystal size, so small spherical nanoparticles (NP) have a large surface area, making them the most common type of TiO_2 -based photocatalyst. On the other hand, one-dimensional (1D) TiO_2 nanostructures, such as nanotubes (NT), nanorods (NR), have unique properties and advantages for photocatalytic reactions due to their 1D geometry [5,6]. Structures with direct electron paths significantly increase the electric transport properties of films by excluding grain boundaries that occur when using films made of TiO_2 nanoparticles. NP, NR, NT TiO_2 can be in 3 main crystal phases: brookite, anatase and rutile. It is believed that the best photocatalytic activity is observed for anatase due to the lower recombination rate and high adsorption capacity [7, 8]. Although there are other opinions, for example, it has been experimentally proved that a mixture of the crystal phases of anatase and rutile shows better photocatalytic activity than separately [9, 10]. Therefore, what kind of photocatalyst will work better is still not known: a high specific surface area of NP TiO_2 or improved electron transport of NR and NT TiO_2 .

In this work, three types of nanostructures were used: NP, NR and NT TiO_2 , which differ in geometric characteristics, but have relatively the same thickness and area of the films. The most common, cheap and

simple methods of nanostructure synthesis were used, such as hydrothermal synthesis for NR [11] and electrochemical anodizing for NT [12, 13]. The characteristic difference between NT and TiO₂ nanorods is that the former have an open internal channel, which should significantly increase their specific surface area.

Experimental

The synthesis of films formed by the NP TiO₂

The film of NP TiO₂ was prepared as follows: 50 mg of TiO₂ colloidal titanium dioxide (Sigma Aldrich company Degussa P25) was ground in a porcelain mortar with the addition of 2 ml of deionized water and 0.2 ml of acetone and mixed for 24 hours using a magnetic stirrer to form a homogeneous paste. The finished paste was applied to the surface of pre-cleaned photo substrates (Sigma Aldrich, 8 Ohms/cm²) by the «doctor-blading» method and dried at a temperature of 100 °C for 30 minutes. The film thickness was controlled using tape applied to the edges of the substrate. Then the samples were calcined at a temperature of 500 °C for 2 hours.

The synthesis of films formed by the NR TiO₂

Nanostructured films based on HR TiO₂ were obtained by hydrothermal synthesis as follows: a solution containing 15 ml of deionized water (H₂O), 15 ml of hydrochloric acid (HCl) (36.5–38.0 %, Sigma–Aldrich) and 0.25 ml of titanium butoxide C₁₆H₃₆O₄Ti (titanium butoxide, 97 %, Sigma–Aldrich) was prepared in a 50 ml stainless steel vessel. Then, pre-cleaned glasses with a conducting layer of ITO (Sigma-Aldrich, 8 Ohms/cm²) were placed in the same vessel with the conducting side down. The stainless steel vessel is closed and placed in a convective oven at a temperature of 180 °C for 24 hours. The resulting samples were washed with deionized water and dried at room temperature. Then the samples were calcined at a temperature of 500 °C for 2 hours.

The synthesis of films formed by the NT TiO₂

The films were obtained by 2-stage electrochemical anodizing of pre-chemically polished, purified titanium foil (VT1–0, 99.7 %, Russia) at a temperature of 5–7 °C. The thickness of the foil was 60 microns. As the base of the electrolyte, C₂H₆O₂ was used, with a content of 0.3 wt.% NH₄F and 2 wt% H₂O. The cathode was platinum foil. The distance between the cathode and the anode was 3 cm. The anodizing voltage is 40 V. During the anodizing process, the solution was intensively mixed using a magnetic stirrer. During the first stage of anodizing, a film of NT TiO₂ and hydrolysis byproducts is formed on the surface of the titanium foil within 2 hours, which were removed from the surface of the foil in an ultrasonic bath, in a solution of hydrochloric acid. The duration of the second stage of anodizing was 4 hours. The amorphous phase of TiO₂ was crystallized by heat treatment of samples in a muffle furnace at a temperature of 500 °C within 2 hours.

X-ray phase analysis of films was studied using a rint 2000 diffractometer (model D5005). Images of the sample surface were obtained using a scanning electron microscope (SEM) MIRA 3 LMU (Tescan, Czech Republic). The textural characteristics of synthesized samples were calculated on the basis of nitrogen adsorption and desorption isotherms at a temperature of 77 K obtained at the quantachrome volumetric unit («Quantachrome Instruments», USA). The specific surface area of the samples was estimated by the Brunauer–Emmett–Taylor method (BET). To study the photocatalytic activity of films, the values of the photoinduced current and photodegradation of the methylene blue dye were measured. The photocurrent of nanostructures with an illuminated area of 1 cm² was measured at a constant potential of 0 V using a potentiostat (ELINS R-20XV, Russia) in a standard three-electrode cell. TiO₂ nanostructures were used as the working electrode. The opposite electrode was a platinum foil, and an AgCl electrode was used as the reference electrode. Measurements were made in an electrolyte of 0.1 M NaOH in a specially made photoelectrochemical cell with a quartz window. When registering the photocurrent, titanium dioxide films were irradiated with a 45 mW/cm² xenon lamp. The photoactivity of the films was evaluated in the reaction of photodegradation of an aqueous MB solution. Plates with a size of 1×2 cm were vertically lowered into a quartz reactor containing 50 ml of a MB solution with an initial concentration of 10⁻⁵ mol/l and kept for 20 hours to exclude errors in measuring the optical density of the dye associated with the adsorption of molecules into its pores. The solution is continuously mixed using a magnetic stirrer. The system was irradiated with a 45 mW/cm² xenon lamp.

The electrotransport properties of films were studied using the method of impedance spectroscopy. Measurements of the impedance spectra were performed on the biologic (Science Instruments) impedance meter. The amplitude of the applied signal was up to 25 mV, and the frequency range from 1 MHz to 100 MHz.

Results and discussion

Diffraction peaks shown in figure 1 (101), (004), (200), (105), (211), (204), (116), (220) and (215) for NP and NT TiO₂ films are identical and correspond to the tetragonal phase of anatase (JCPDS, no. 84–1286, $a = b = 0.1949$ nm and $c = 0.1980$ nm).

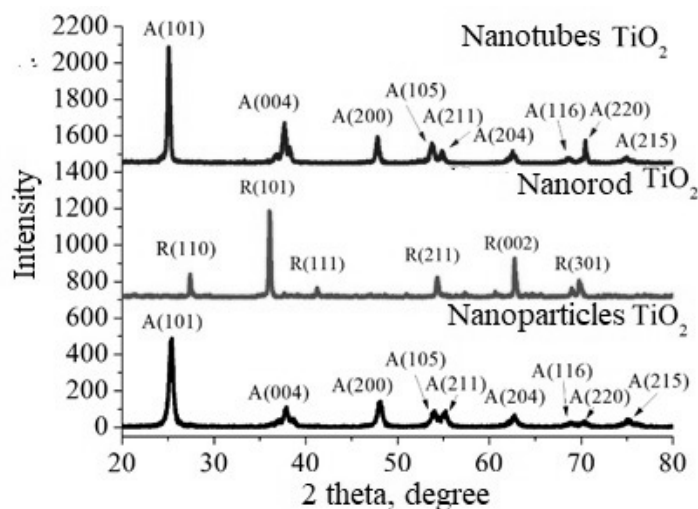


Figure 1. Radiographs of nanostructured films TiO₂

All diffraction peaks presented for NR films are in good agreement with the tetragonal phase of rutile TiO₂ (JCPDS, no. 21–1276, $a = b = 0.4517$ nm and $c = 0.2940$ nm). The presence of sharp peaks for NR indicates that the films have good crystallinity. The diffraction peaks (002) and (101) were significantly amplified, indicating that the deposited film is highly oriented relative to the substrate surface.

Figure 2 shows the results of a study of the surface morphology of TiO₂ nanostructured films.

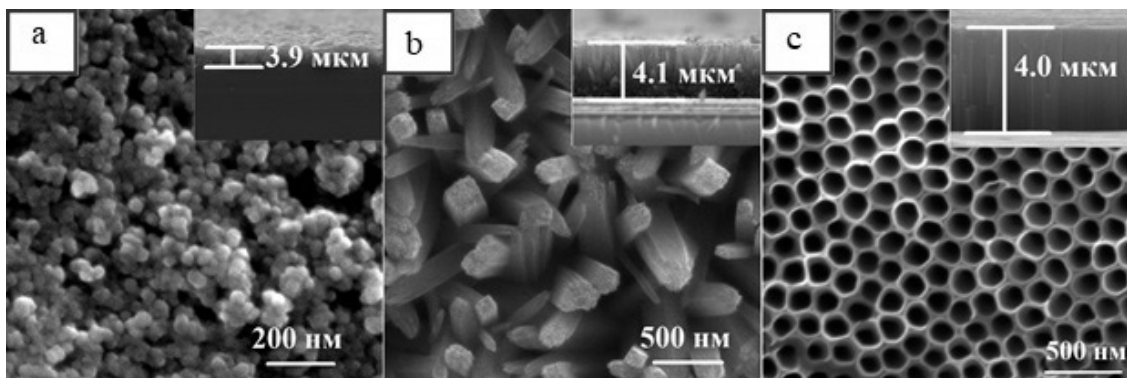


Figure 2. SEM images of TiO₂ nanostructured films

Figure 2a shows that the presented NP TiO₂ film has a clearly defined granular structure. The average particle diameter is 25 nm. Figure 2b shows that as a result of hydrothermal synthesis, nanorods made of titanium dioxide are formed on the surface of the FTO glass, located perpendicular to the substrate plane. The average diameter of the nanorods is 100–120 nm, and the length is 4.1 microns. Figure 2c shows that as a result of careful control of external conditions, films were obtained from tightly packed cylindrical geometrically anisotropic titanium dioxide fragments located perpendicular to the foil plane. The porous structure of the film and the size of individual channels, which are about 90 nm, are clearly visible. It is shown that the surface of TiO₂ films is low-defect, and they themselves have a clearly marked channel along their entire length. The thickness of all titanium dioxide nanostructures was selected so that their thickness was about ~4 microns. The thickness of the film from NP was controlled using tape (thickness of 1 layer ~2 microns), if necessary, the number of layers applied was repeated. The film thickness of NR TiO₂ was controlled by the

temperature and duration of hydrothermal synthesis, and NT TiO₂ by the time (4 hours) and the voltage (40 V) of anodizing. The active area of all samples was 1 cm².

The textural characteristics of TiO₂ nanostructures were calculated based on nitrogen adsorption and desorption isotherms at a temperature of 77 K. To obtain the adsorption-desorption curve, a powder from NP TiO₂ was used, and for NT and NR, the films were mechanically separated from the base. The isotherms are shown in Figure 3a.

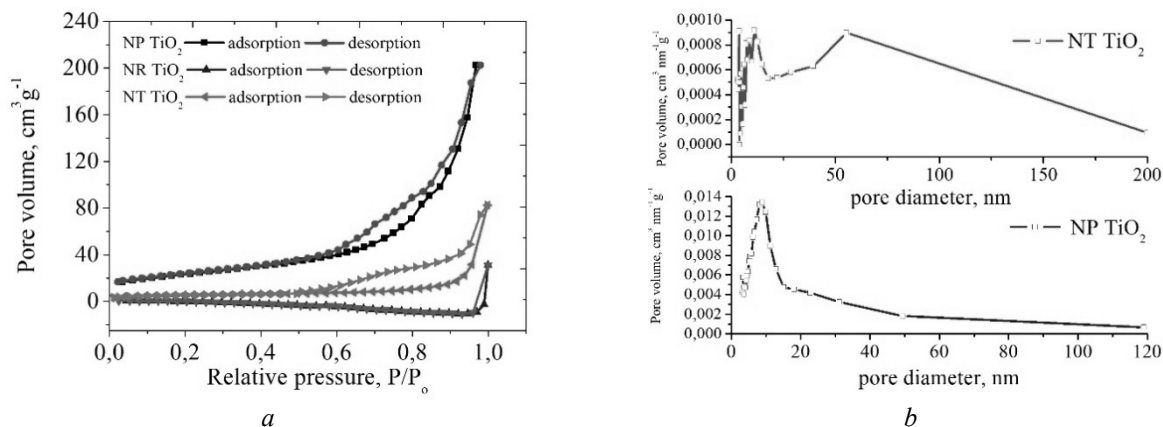


Figure 3. Adsorption-desorption isotherms and pore size distribution of TiO₂ nanostructures

From the presented data, it can be seen that the nitrogen adsorption-desorption isotherms for all samples have the same appearance, except for the volume of adsorbed nitrogen. At low relative pressures (P/P_0 less than 0.1), an increase in nitrogen adsorption is observed on the isotherms, which indicates the presence of micropores. With an increase in the relative partial pressure for samples of NP and NT TiO₂, the volume of adsorbed nitrogen increases, and an increase in the relative pressure range from 0.45 to 0.99 indicates the presence of a mesoporous (2–50 nm) structure. For NR TiO₂, the isotherm is characterized by a decrease in the amount of adsorbate with an increase in P/P_0 , as well as negative values of this value. With repeated measurements and an increase in the weight of the hitch does not lead to changes in the isotherm. Experiments were carried out when the weight of the hitch was comparable to the weight of the hitch NT. Further increase in the weight of the hitch for samples from the NR was not possible, since its separation from the surface of the substrate was difficult, the output was minimal. This may indicate a low surface of the test sample ($<1 \text{ m}^2/\text{g}$). In accordance with the IUPAC nomenclature, the obtained isotherms belong to type IV isotherms with a hysteresis loop, reflecting the process of capillary condensation in mesopores. The volume of mesopores was calculated using the Barrett–Joyner–Halenda method and the pore size distribution was obtained (Fig. 3b) for NP and NT. For NR films, calculations were not performed using this method. From the pore distribution curve for the NP film, one peak can be distinguished in the region of the pore diameter of 10 nm. For films made of NT TiO₂, two peaks can be identified in the region of the pore diameter of 10 and 55 nm. Pores with a diameter of less than 10 nm are probably located on the inner or outer surface of the walls of TiO₂ nanotubes. It should be noted that the samples also show the presence of macropores. The value of the surface area for films made of NR TiO₂ was estimated by the number of adsorbed molecules of the methylene blue dye ($S_{\text{molecule}}=130 \text{ \AA}^2$) on its surface. The results of the research are presented in Table 1.

Table 1

Textural characteristics of TiO₂ nanostructures

Sample	Surface area	Pore volume, cm ³ /g
NP TiO ₂	73.218 m ² /g	0.306 cm ³ /g
NR TiO ₂	62 cm ² /cm ²	-
NT TiO ₂	19.437 m ² /g	0.122 cm ³ /g

From the presented data, it can be seen that the specific surface area of NP TiO₂ is 4 times higher than NT TiO₂.

Electric transport properties of nanostructured films were studied by measuring the electrical impedance. Figure 4 shows the impedance hodographs in Nyquist coordinates for NP, NR, and NT TiO₂.

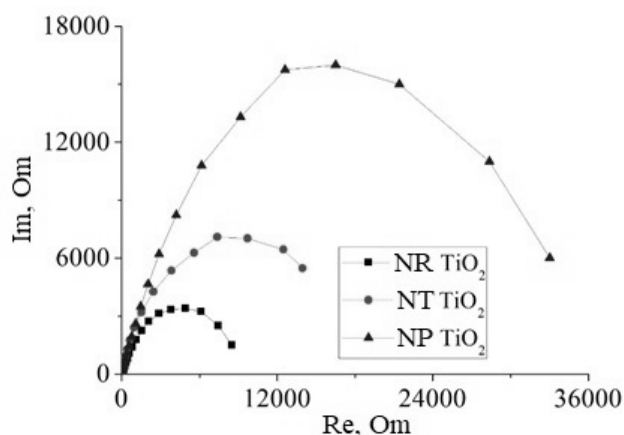


Figure 4. Impedance spectrum of titanium dioxide nanostructures

The values of the chain elements obtained in the framework of the model used are shown in Table 2. One of the important parameters that can be determined from the measurement of the solar cell impedance is the lifetime of charge carriers in a semiconductor film (τ). Since the impedance measurements were made when the film was illuminated, it can be concluded that τ characterizes the lifetime of photoelectrons. The calculations were performed using the methods described in [14, 15].

The effective electron diffusion coefficient D_{eff} , the effective recombination rate k_{eff} , the effective electron lifetime T_{eff} , the resistance to electron transport in R_w titanium dioxide films, and the charge transfer resistance R_k associated with electron recombination were calculated from the central arc of the impedance spectra. The results are presented in Table 2.

Table 2

Electric transport parameters of solar cells based on TiO₂ nanostructures

Sample	$D_{\text{eff}}, \text{cm}^2/\text{s}^{-1}$	$k_{\text{eff}}, \text{s}^{-1}$	$\tau_{\text{eff}}, \text{s}$	R_k, Ohm	R_w, Ohm	$\text{Con}, \text{Ohm} \cdot \text{cm} \cdot \text{s}^{-1}$	L, mkm
NP TiO ₂	$6.7 \cdot 10^{-3}$	16	0.062	33015	11.9	206	3.9
NT TiO ₂	$2.3 \cdot 10^{-3}$	12	0.083	13952	12.0	68	4.1
NR TiO ₂	$3.6 \cdot 10^{-4}$	9.6	0.104	8480	36.0	32.5	4.0

The recombination rate (k_{eff}) is directly proportional to the electron density in the trap state and the recombination rate constant c of the traps. In NP films, its value is 16, and for NR it is 9.6, which may indicate that the density of electrons in the trap states is less in NR. The lifetime of the T_{eff} electrons in the NP is lower than in films made of NT and NR. This may be due to the rapid recombination of electrons and holes. The resistance to electronic transport in TiO₂ (R_w) for NP films is higher than in NR and NT.

Based on this we can draw the following conclusion: High resistance in the films of NP is connected with the unformed relations between the nanoparticles. Unformed bonds lead to an increase in surface defects through which recombination occurs. The use of nanostructures with one-dimensional electron transport reduces the resistance and speed of recombination processes. Despite the low specific surface area of NR and NT than NP, they can be promising materials for photocatalysis. The photocatalytic properties of films are shown in the Figure 5 below.

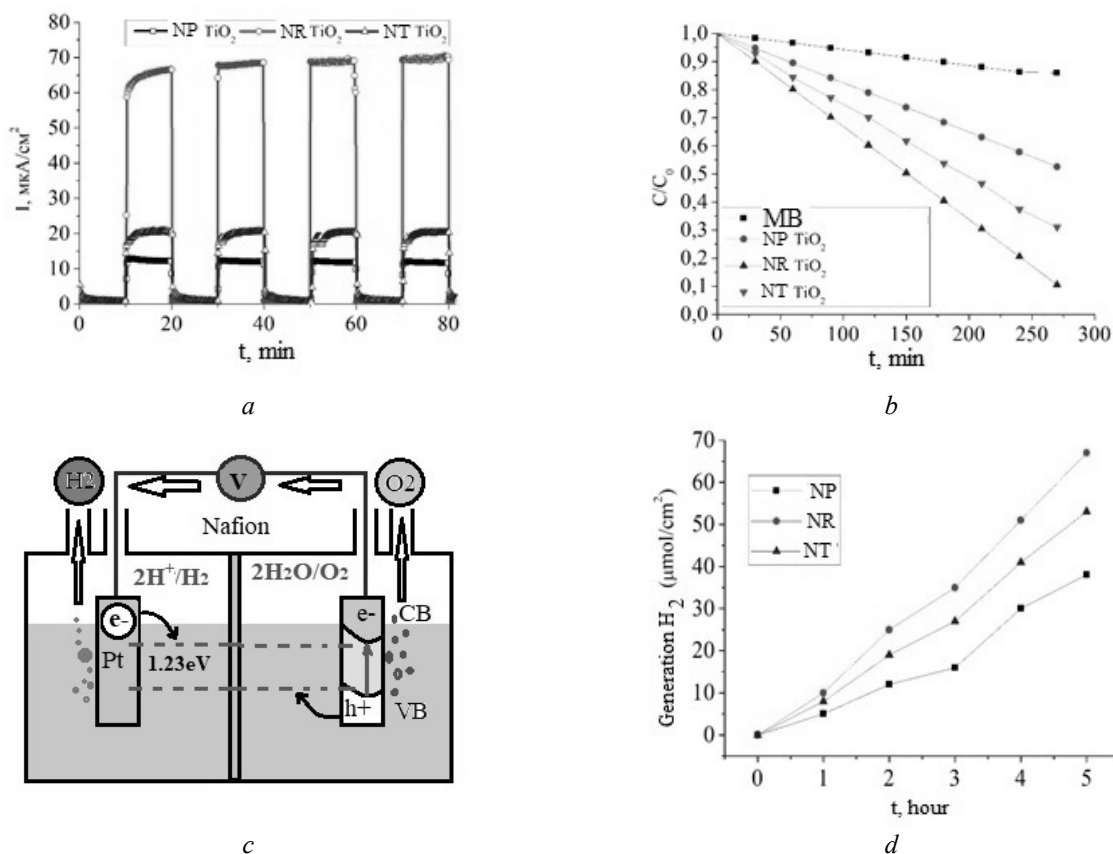


Figure 5. Photocatalytic properties of titanium dioxide nanostructures

Figure 5a shows the photo-feedback of titanium dioxide nanostructures when irradiated by an electromagnetic wave and its absence. All samples show fairly good stability. It should be noted that with an identical area and comparably the same thickness of films, the photocurrent for NR is 3 times higher than for NT, and 5 times higher than for NP titanium dioxide. At the same time, the value of the active surface area (Table 1) is much lower for NR than for NP and NT. Given the above, we can conclude that the formation of photocurrent is associated with one-dimensional electron transport along the surface of the nanorods. NT titanium dioxide has a one-dimensional electron transport and a high specific surface area. The low value of the photocurrent can be associated with a number of circumstances: when forming NT, titanium foil is used, which has foreign impurities, such as Al, Zn, F, etc., which is simply impossible to exclude; during electrochemical anodizing, hydrolysis products, TiF₆, can be formed on the surface of nanotubes; during heat treatment of NT samples, an additional oxide layer or barrier may occur due to partial peeling of the oxide layer between the NT and the titanium foil. The low value of the photocurrent for NP can be associated with unformed bonds between nanoparticles, which leads to rapid recombination of electrons and holes, as evidenced by the results of the study by impedance spectroscopy. The photocatalytic activity of nanostructures in the MB dye degradation reaction was studied (see Fig. 5b). When irradiated with a xenon lamp MB dye, its concentration changed slightly. When irradiated for 4.5 hours in the presence of titanium dioxide films, its concentration decreased linearly, which indicates its degradation. The results obtained show that the best photocatalytic activity is the film from NR. Degradation to 95 % is achieved in 270 min., and for NT and NP this time is much higher. It should be noted that this work was done solely to compare the photocatalytic activity of titanium dioxide nanostructures with each other. Since the obtained results on the degradation of the dye do not correspond to the values given in similar scientific papers published in journals. First of all, this is due to the radiation source used. Usually, xenon lamps with a power of 100mW/cm² or 300 W are used in the works. In this work, 45 mw/cm².

Figure 5c shows a cell in which photocatalytic water splitting occurs. The cell material is quartz (Minihua Store). The opposite electrode is platinum. Separation of solutions was performed using a Nafion filter. Titanium dioxide nanostructures were used as the working electrode. Both sides of the cell were pre-purged with a stream of argon gas. Then, when irradiated, the sample was sampled and identified using an

Agilent gas chromatograph. Figure 5d shows that when using films from NR, hydrogen generation is higher than for films from NT and NP.

Conclusions

Films were synthesized from NP, NR and NT of titanium dioxide with a thickness of 3.9, 4.0 and 4.1 microns, with an area of 2 cm². The textural characteristics of films are studied. The obtained isotherms belong to type IV isotherms with a hysteresis loop, reflecting the process of capillary condensation in mesopores. The volume of mesopores was calculated using the Barrett–Joyner–Halenda method and the pore size distribution was obtained. For NP films, the specific surface area was 73.218 m²/g, and for NR and NT, 62 cm²/cm² and 19.437 m²/g, respectively. The diffraction peaks for NP and NT TiO₂ films are identical and correspond to the tetragonal phase of anatase, for NR films, with the tetragonal phase of rutile. Electric transport properties of nanostructured films were studied by measuring the electrical impedance. From the central arc of the impedance spectra were computed effective diffusion coefficient D_{eff} of electrons, the effective recombination rate k_{eff} , the effective lifetime τ_{eff} of the electron, the resistance of electron transport in films of titanium dioxide R_w , resistance of charge transfer R_k associated with the recombination of an electron. High resistance in the films of NP is connected with the unformed bonds between nanoparticles. Unformed relations lead to the increase of surface defects, which occur through recombination. The use of nanostructures with one-dimensional electron transport reduces the resistance and speed of recombination processes. Despite the low specific surface area of NR and NT than NP, they can be promising materials for photocatalysis. The photocurrent for RS is 3 times higher than for NT, and 5 times higher than for NP of titanium dioxide. The photocatalytic activity of nanostructures in the MB dye degradation reaction was investigated. When the dye was irradiated for 4.5 hours in the presence of titanium dioxide films, its concentration decreased linearly, which indicated its degradation. The results obtained show that the best photocatalytic activity is the film from NR. Degradation to 95 % is achieved in 270 min., and for NT and NP this time is much higher. When splitting water molecules into hydrogen gas and oxygen, it was found that when using films from NR, its release occurs significantly more than in NP and NT.

References

- 1 Rosales M. The influence of the morphology of 1D TiO₂ nanostructures on photogeneration of reactive oxygen species and enhanced photocatalytic activity / M. Rosales, T. Zoltan, C. Yadarola // *Journal of Molecular Liquids*. — 2019. — Vol. 281. — P. 59–69. DOI:10.1016/j.molliq.2019.02.070
- 2 Tian G. Preparation and characterization of stable biphasic TiO₂ photocatalyst with high crystallinity, large surface area, and enhanced photoactivity / G. Tian, L. Fu, B. Jing, K. Pan // *J. Phys. Chem. C*. — 2008. — Vol. 112. — P. 3083. DOI: 10.1021/jp710283p
- 3 Chen C.H. Effect of phase composition, morphology, and specific surface area on the photocatalytic activity of TiO₂ nanomaterials / C.H. Chen, Q.W. Liu, S.M. Gao, K. Li, H. Xu, Z.Z. Lou, B.B. Huang, Y. Dai // *RSC Adv*. — 2014. — Vol. 105. — P. 12098. DOI:10.1039/C4RA05509H
- 4 Joo B. Control of the nanoscale crystallinity in mesoporous TiO₂ shells for enhanced photocatalytic activity / B. Joo, Q. Zhang, M. Dahl, I. Lee, J. Goebel, F. Zaera, Y. Yin // *Energy & Environmental Science*. — 2012. — Vol. 5. — P. 6321–6327. DOI: 10.1039/c1ee02533c
- 5 Yuan Z.-Y. Titanium oxide nanotubes, nanofibers and nanowires / Z.-Y. Yuan, B.-L. Su // *Colloids Surf. A Physicochem. Eng. Asp.* — 2004. — Vol. 241. — P. 173–183. DOI: 10.1016/j.colsurfa.2004.04.030
- 6 Benjwal P. 1-D and 2-D morphology of metal cation co-doped (Zn, Mn) TiO₂ and investigation of their photocatalytic activity / P. Benjwal, B. De, K.K. Kar // *Appl. Surf. Sci.* — 2018. — Vol. 427. — P. 262–272. DOI: 10.1016/j.apsusc.2017.08.226
- 7 Liu H. Preparation and properties of nanocrystalline alpha-Fe₂O₃-sensitized TiO₂ nanosheets as a visible light photocatalyst / H. Liu, L. Gao // *J. Am. Ceram. Soc.* — 2006. — Vol. 89. — P. 370–373. DOI: 10.1111/j.1551-2916.2005.00686.x
- 8 Kongsong P. Effect of nitrogen doping on the photocatalytic activity and hydrophobic property of rutile TiO₂ nanorods array / P. Kongsong, A. Taleb, M. Masae, A. Jeenarong, P. Hansud, S. Khumruean // *Surf Interface Anal.* — 2018. — Vol. 44. — P. 1–7. DOI: 10.1002/sia.6518
- 9 Su R. Density functional theory study of mixed-phase TiO₂: heterostructures and electronic properties / R. Su, R. Bechstein, L. So, R.T. Vang, M. Sillassen, B. Esbjornsson, A. Palmqvist, F. Besenbacher // *J. Phys. Chem. C*. — 2011. — Vol. 115. — P. 24287. DOI: 10.1007/s00894-014-2215-7
- 10 Ravidhas C. Tunable morphology with selective faceted growth of visible light active TiO₂ thin films by facile hydrothermal method: structural, optical and photocatalytic properties / C. Ravidhas, B. Anitha, D. Arivukarasan // *Journal of Materials Science: Materials in Electronics*. — 2016. — Vol. 27. — P. 5020–5032. DOI: 10.1007/s10854-016-4389-5
- 11 Ibrayev N.Kh. Investigation of the structural, optical and photocatalytic properties of TiO₂ nanotubes / N.Kh. Ibrayev, T.M. Serikov, A.K. Zeinidenov // *Eurasian physical technical journal*. — 2017. — Vol. 14, No. 2(28). — P. 72–78.

12 Serikov T.M. Surface and sorption properties of TiO₂ nanotubes, synthesized by electrochemical anodization / T.M. Serikov, N.K. Ibrayev, Z. Smagulov // IOP Conference Series — Materials Science and Engineering. — 2016. — Vol. 110. — P. 012066. DOI: 10.1088/1757-899X/110/1/012066

13 Serikov T.M. Influence of surface properties of the titanium dioxide porous films on the characteristics of solar cells / T.M. Serikov, N.K. Ibrayev, N.N. Nuraje, S.V. Savilov, V.V. Lunin // Russian Chemical Bulletin. — 2017. — Vol. 66, No. 4. — P. 614–621. DOI: 10.1007/s11172-017-1781-0

14 Fabregat-Santiago F. Electrochemical impedance spectra of dye-sensitized solar cells: fundamentals and spreadsheet calculation / F. Fabregat-Santiago, J. Bisquert, G. Garcia-Belmonte // Solar Energy Materials & Solar Cells. — 2005. — Vol. 87. — P. 117. DOI: 10.1155/2014/851705

15 Adachi M. Determination of parameters of electron transport in dye-sensitized solar cells using electrochemical impedance spectroscopy / M. Adachi, M. Sakamoto, J. Jiu // Journal Physics Chemistry B. — 2006. — Vol. 110. — P. 13872. DOI: 10.1021/jp061693u

T.M. Сериков

Титан диоксиді нанокұрылымдарының электрлік тасымалдау қасиеттерінің олардың фотокаталитикалық белсенділігіне әсері

Әртүрлі әдістерді қолдана отырып, ауданы 2 см², ал қалыңдықтары 3,9, 4,0 және 4,1 мкм болатын нанобөлшектерден, нанотүтікшелерден және наноөзекшелерден тұратын қабыршақтар синтезделді. Нанокұрылымдар рентгенді-фазалық анализ, сканерлеуші электронды микроскопия, БЭТ (Брунауэр, Эмметт және Тейлор), БДХ (Баретт–Джойнер–Халенд) әдістерінің көмегімен сипатталды. Қабыршақтардың электр тасымалдау қасиеттері импедансты спектроскопия әдісімен зерттелген. Үлгілердің фотокаталитикалық белсенділігі ксенон лампының жарықтандыруы кезінде метилен көгілдір бояғышының деградациясы және фототокты тіркеу арқылы бағаланды. Бірлік уақытта шығарылған сутегінің концентрациясы платина электродының, арнайы кварцтық кюветасының және газ хроматографиясының көмегімен анықталған. Беттік қасиеттерін зерттеу барысында алынған изотермалар IV типіне жатады және мезопорларда капиллярлық конденсация процесінің өтетінін көрсетеді. Титан диоксидінің нанобөлшектері мен нанотүтікшелерінің дифракциялық шыңдары бірдей және анатаздың тетрагональды фазасына, наноөзекшелердің қабыршақтары рутилдің тетрагональды фазасына сәйкес келеді. Қабыршақтардың электрлік қасиеттерін зерттеу кезінде титан диоксидінің нанобөлшектері қабыршақтарының нанобөлшектер арасында өзара түзілмеген байланыстарға байланысты жоғары электр кедергіге ие екендігі анықталды. Беттік ауданы төмен болғанына қарамастан, титан диоксиді наноөзекшелері нанотүтікшелер мен нанобөлшектерге қарағанда жоғары фотокаталитикалық белсенділік көрсетті. Алынған нәтижелер фототокты өлшеу, бояғыштың ыдырауы және су молекулаларының сутегі газы мен оттегіне бөлінуі арқылы расталған.

Кілт сөздер: нанобөлшектер, нанотүтікшелер, наноөзекшелер, титан диоксиді, БЭТ, электр тасымалдау қасиеттері, фотокаталитикалық белсенділік, сутегі.

T.M. Сериков

Влияние электротранспортных свойств наноструктур диоксида титана на их фотокаталитическую активность

Различными методами были получены пленки, образованные наночастицами, наностержнями и нанотрубками диоксида титана, толщиной 3,9; 4,0 и 4,1 мкм, соответственно, с площадью 2 см². Наноструктуры были охарактеризованы методом рентгенофазового анализа, сканирующим электронным микроскопом, методами БЭТ (Брунауэр, Эмметт и Тейлор) и БЖХ (Баретт–Джойнер–Халенд). Электротранспортные свойства пленок исследованы методом импедансной спектроскопии. Фотокаталитическую активность образцов оценивали по фототоку и деградации красителя метиленового голубого при освещении светом ксеноновой лампы. Концентрацию выделяемого водорода в единицу времени определяли методом газовой хроматографии в стандартной кварцевой кювете с использованием платинового электрода. Исследования текстурных характеристик показали, что полученные изотермы относятся к изотермам типа IV с петлей гистерезиса, отражая процесс капиллярной конденсации в мезопорах. Дифракционные пики для пленок наночастиц и нанотрубок диоксида титана идентичны и соответствуют тетрагональной фазе анатаза, для пленок из наностержней — тетрагональной фазе рутила. При исследовании электротранспортных свойств пленок было установлено, что пленки из наночастиц диоксида титана обладают более высоким сопротивлением, связанным с неформованными связями между наночастицами. Несмотря на низкую удельную поверхность, наностержни диоксида титана демонстрировали более высокую фотокаталитическую активность, чем нанотрубки и наночастицы. Полученные результаты подтверждаются измерениями фототока, разложением красителя и расщеплением молекул воды на газообразный водород и кислород.

Ключевые слова: наночастицы, нанотрубки, наностержни, диоксид титана, БЭТ, электротранспортные свойства, фотокаталитическая активность, водород.

References

- 1 Rosales, M., Zoltan, T., & Yadarola, C. (2019). The influence of the morphology of 1D TiO₂ nanostructures on photogeneration of reactive oxygen species and enhanced photocatalytic activity. *Journal of Molecular Liquids*, 281, 59–69.
- 2 Tian, G., Fu, L., Jing, B., & Pan, K. (2008). Preparation and characterization of stable biphasic TiO₂ photocatalyst with high crystallinity, large surface area, and enhanced photoactivity. *J. Phys. Chem. C*, 112, 3083.
- 3 Chen, C.H., Liu, W., Gao, S.M., Li, K., Xu, H., Lou, Z.Z., Huang, B.B., & Dai, Y. (2014). Effect of phase composition, morphology, and specific surface area on the photocatalytic activity of TiO₂ nanomaterials. *RSC Adv*, 105, 12098.
- 4 Joo, B., Zhang, Q., Dahl, M., Lee I., Goebel, J., Zaera, F., & Yin, Y. (2012). Control of the nanoscale crystallinity in mesoporous TiO₂ shells for enhanced photocatalytic activity. *Energy & Environmental Science*, 5, 6321–6327.
- 5 Yuan, Z.-Y., & Su, B.-L. (2004). Titanium oxide nanotubes, nanofibers and nanowires. *Colloids Surf. A Physicochem. Eng. Asp*, 241, 173–183.
- 6 Benjwal, P., De, B., & Kar, K.K. (2018). 1-D and 2-D morphology of metal cation co-doped (Zn, Mn) TiO₂ and investigation of their photocatalytic activity. *Appl. Surf. Sci.*, 427, 262–272.
- 7 Liu, H., & Gao, L. (2006). Preparation and properties of nanocrystalline alpha-Fe₂O₃-sensitized TiO₂ nanosheets as a visible light photocatalyst. *J. Am. Ceram. Soc.*, 89, 370–373.
- 8 Kongsong, P., Taleb, A., Masae, M., Jeenarong, A., Hansud, P., Khumruean, S. (2018). Effect of nitrogen doping on the photocatalytic activity and hydrophobic property of rutile TiO₂ nanorods array. *Surf Interface Anal.*, 44, 1–7.
- 9 Su, R., Bechstein, R., So, L., Vang, R.T., Sillassen, M., Esbjornsson, B., Palmqvist, A., & Besenbacher, F. (2011). Density functional theory study of mixed-phase TiO₂: heterostructures and electronic properties. *J. Phys. Chem. C.*, 115, 24287.
- 10 Ravidhas, C., Anitha, B., & Arivukarasan, D. (2016). Tunable morphology with selective faceted growth of visible light active TiO₂ thin films by facile hydrothermal method: structural, optical and photocatalytic properties. *Journal of Materials Science: Materials in Electronics*, 27, 5020–5032.
- 11 Ibrayev, N.Kh., Serikov, T.M., & Zeinidenov, A.K. (2017). Investigation of the structural, optical and photocatalytic properties of TiO₂ nanotubes. *Eurasian physical technical journal*, 14, 2(28), 72–78.
- 12 Serikov, T.M., Ibrayev, N.K., & Smagulov, Z. (2016). Surface and sorption properties of TiO₂ nanotubes, synthesized by electrochemical anodization. *IOP Conference Series — Materials Science and Engineering*, 110, 012066.
- 13 Serikov, T.M., Ibrayev, N.K., Nuraje, N.N., Savilov, S.V., & Lunin V.V. (2017). Influence of surface properties of the titanium dioxide porous films on the characteristics of solar cells. *Russian Chemical Bulletin*, 66(4), 614–621.
- 14 Fabregat-Santiago, F., Bisquert, J., & Garcia-Belmonte, G. (2005). Electrochemical Impedance Spectra of Dye-Sensitized Solar Cells: Fundamentals and Spreadsheet Calculation. *Solar Energy Materials & Solar Cells*, 87, 117.
- 15 Adachi, M., Sakamoto, M., & Jiu, J. (2006). Determination of parameters of electron transport in dye-sensitized solar cells using electrochemical impedance spectroscopy. *Journal Physics Chemistry B.*, 110, 13872.

A.S. Rudenkov¹, M.A. Yarmolenko¹, A.A. Rogachev²,
A.P. Surzhikov³, A.P. Luchnikov^{4*}, O.A. Frolova⁴

¹Francisk Skorina Gomel State University, Gomel, Belarus;

²Belarusian State University of transport, Gomel, Belarus;

³Tomsk Polytechnic University, School of Non-Destructive Testing, Tomsk, Russia;

⁴MIREA – Russian Technological University, Russia

(*E-mail: fisika@mail.ru)

Phase composition and morphology of nanostructured coatings deposited by laser dispersion of a mixture of polyethylene with iron oxalate

Peculiarities of forming of iron oxide coatings with reinforced carbon nanostructures from gas phase generated by laser dispersion of composite target were explored. Influence of technological modes of heat treatment on morphology and phase composition of nanostructured film layers was determined. It was found that on a substrate highly dispersed layers containing carbon nanostructures are formed. Using Raman spectroscopy it was shown that in oxide matrix carbon structures, which are mainly in the form of planar located nanotubes, appear. It was found that with a mass ratio of polyethylene and iron oxalate equal to 1:1, the distribution of the formed nanostructures in size is unimodal with a maximum near 20 nm. At dispersing of polyethylene and iron oxalate mixture with mass ratio 1:2 in deposited layers nanotubes have the least defectiveness. Patterns of influence on morphology and coatings phase composition of relative component abundance in being dispersed by laser radiation composite target were determined. It was shown that with the growing of iron oxalate concentration in the target coating structural heterogeneity increases, subroughness and average size of separate nanostructures in the deposited condensate grow. The obtained polymer matrix nanocomposite films can be used in sensors.

Keywords: polyethylene, oxalate mixture, coating, nanostructures, morphology, phase composition, Raman spectroscopy.

Introduction

One of the promising ways to increase mechanical, thermophysical properties of thin coatings is to reinforce them with nanosized structures, in particular, carbon nanotubes, fullerenes [1–3]. Reinforcement of coatings with carbon nanostructures (nanocrystalline graphite, carbon nanotubes etc) due to their high mechanical properties will allow increasing strength and plasticity of such coatings with simultaneous preservation of high hardness. At the same time, the implementation of such technological technique, as a rule, involves complex, sequentially conducted operations and hence the development of methods for vacuum synthesis of such heterogeneous structures carried out in a single technological cycle with the possibility of controlling the degree of reinforcement, morphology, and phase composition becomes relevant.

It is known that one of the effective methods of nanotubes synthesis is their formation from carbon gases at high enough temperature in the presence of catalysts, for which compounds, as a rule, oxides of transition metals are used [4]. It should be noted that layer deposition of metal oxide is of special interest and implementation of conditions, under which oxides being deposited on the surface as coatings catalyze processes of carbon nanotubes increase being formed in the volume of oxide have scientific and practical interest.

The study considers formation peculiarities of iron oxide coatings with reinforced carbon nanostructures from gas phase generated by laser dispersion of composite target and determines influence of technological modes of heat treatment on morphology and phase composition of nanostructured film layers.

Samples and research methods

Nanostructured coatings using iron oxide were obtained by laser dispersion of composite target based on polyethylene and iron oxalate, preheated to the temperature 330 °C. The target was prepared by polyethylene powder (PP) and iron oxalate ($\text{FeC}_2\text{O}_4 \cdot 2\text{H}_2\text{O}$) mixing with various mass ratio 1:1, 1:2, 1:3. The received powders mixture was placed into crucible on the heating panel. When the pressure in the vacuum chamber was $\sim 4 \cdot 10^{-3}$ Pa the power of the heating panel turned on providing the target heating up to 330 °C. Laser L-2137U+HG-5 was used as a source of laser radiation, which enables to carry out wavelength agility of laser radiation within the interval from infra-red (1064 nm) to ultraviolet range (355, 266 nm). Frequency of

impulse rate was 10 Hz, the duration of pumping impulse in Q-switched mode was 6 ns. The laser spot diameter made 7 mm. Radiation with wavelength of $\lambda = 532$ nm was used in the study. Pulse energy corresponded to 380 mJ.

The source of laser radiation switched on only after the formation of homogenous melt in the crucible. The impact of laser radiation with melt was accompanied by intensive gas phase generation. The crucible heating wasn't turned off within the whole period of laser dispersion. The substrate temperature was 350 °C that was considerably lower than the temperature of the synthesis of carbon nanostructures from the carbons on the surface of the catalyst which makes 500–700 °C [1–4].

Experimental results and their discussion

Patterns of influence on morphology and coatings phase composition of relative component abundance in being dispersed by laser radiation composite target were determined. It was shown that with the growing of iron oxalate concentration in the target coating structural heterogeneity increases, subroughness and average size of separate nanostructures in the deposited condensate grow (Fig. 1, Table 1).

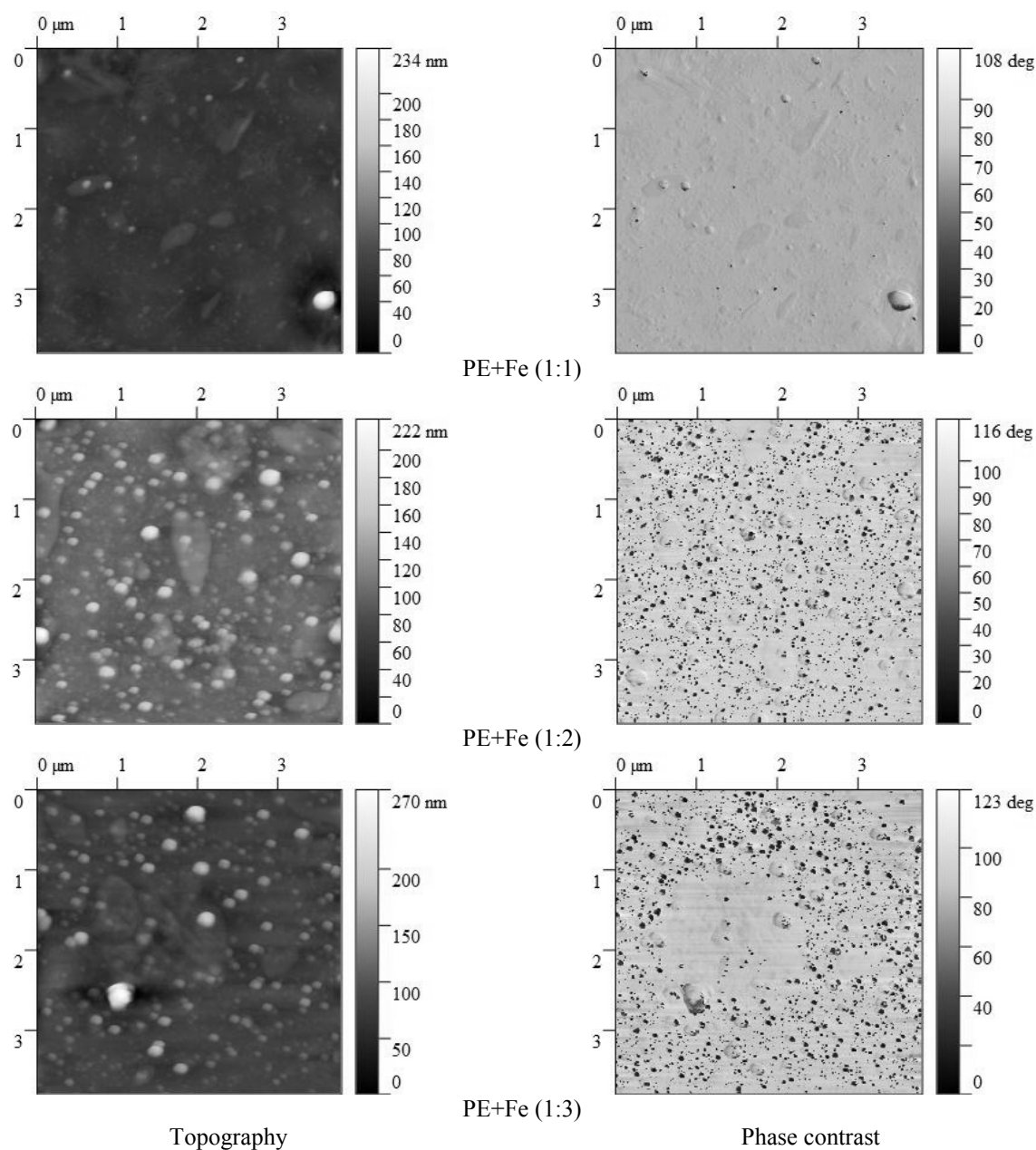


Figure 1. AFM images of deposited metal carbon films of the condensate with mass ratio (1:1, 1:2 and 1:3) of the target components (PE+Fe)

Influence of mass ratio of the target (PE+Fe) on morphological peculiarities of deposited metal-carbon condensate

Coating	Mass ratio	Medium height, nm	R_{ms} , nm	Grain density, pc.	Average diameter of grains, nm
PE+Fe	1:1	59.3/139.4	11.0/22.6	246/94	50/91
	1:2	84.0/64.6	14.9/15.3	255/138	70/112
	1:3	98.5/39.2	18.6/6.5	244/85	77/52

Note. Without thermal annealing/thermal annealing.

Particles on the surface contain intermediate compounds of molecule decomposition of iron oxalate and their size increase can be explained by their more intensive dissociation with phase formation of various compositions. Besides, it must be taken into consideration that laser dispersion is conducted in the preheated to 330 °C mixture of polyethylene and iron oxalate. According to [5] iron oxalate hydrant loses crystallization water in the vacuum at 142 °C. At further heating to 400–500 °C due to laser treatment, decomposition products consist of iron oxide Fe_3O_4 or FeO , containing pure iron. As on the figures of phase contrast (Fig. 1) structural heterogeneity is darker, they can be interpreted as objects with lower hardness consisting of iron mainly.

It was found that with a mass ratio of polyethylene and iron oxalate equal to 1:1 the distribution of the formed nanostructures N in size (radius R_N) is unimodal with a maximum near 20 nm (Fig. 2). With the further increase in the content of iron oxalate (1:2, 1:3) the radius distribution of the formed nanostructures shifts towards large particles and with high iron oxalate content in the target becomes unimodal, local maxima appear in the range from 30 to 50 nm, indicating more intensive emission of nanophase iron.

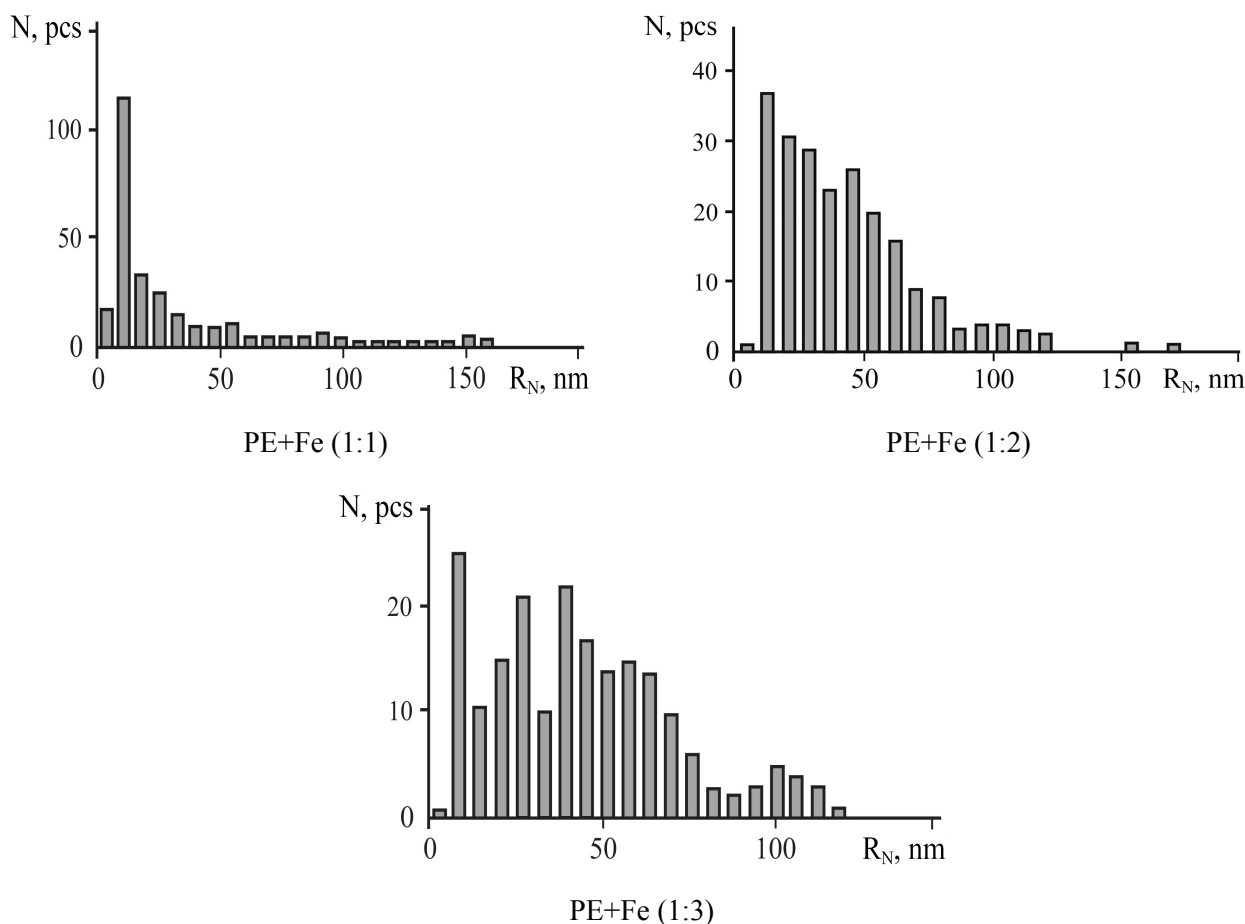


Figure 2. Distribution histogram of the forming nanostructures N in their radius size R_N with mass ratio (1:1, 1:2 and 1:3) of the target components (PE+Fe)

Heat treatment of coatings during an hour in air at a temperature of 500 °C, in case of mass ratio polyethylene-iron oxalate 1:1 and 1:2, leads to the density reduction of structural formations and their size R_N increase (Fig. 3, 4 and Table 1). The process is considerably stemmed from the occurrence of coalescence and partial oxidation of pure iron particles. At the same time in case of dispersion of the target with high content of iron oxalate (1:3) the distribution of the particles in size transforms from unimodal into exponential. Their size decrease is observed which is probably related with the intensive occurrence of iron oxidation. The conclusion is supported by significant (more than 3 times) decrease of particles density (Table 1).

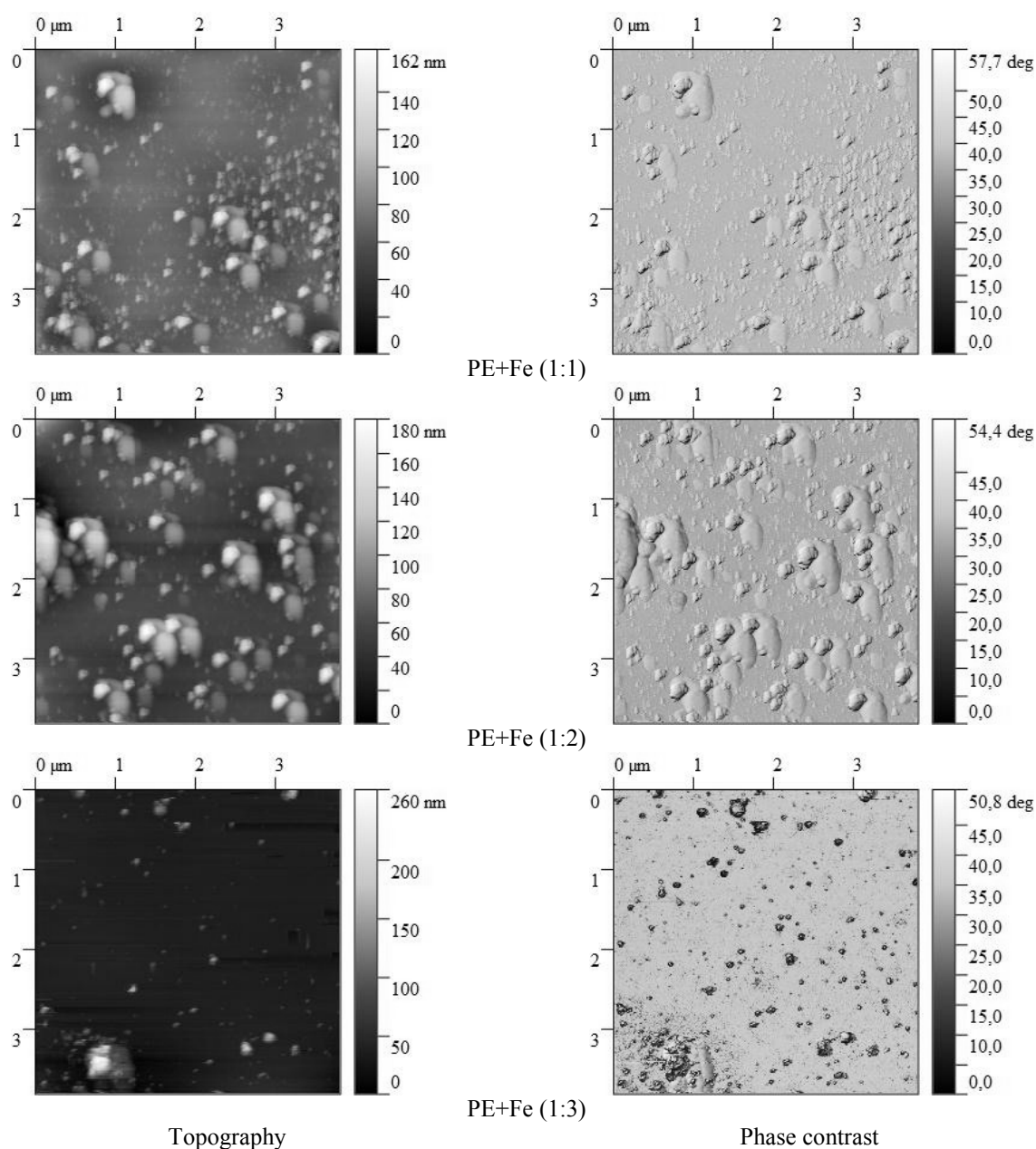


Figure 3. AFM images of deposited metal carbon films of the condensate after the thermal annealing at a temperature of 500 °C with mass ratio (1:1, 1:2 and 1:3) of the target components (PE+Fe)

On Figure 5 Raman spectra of nanostructured layers deposited by laser dispersion of the target with various content are shown. According to [6–10] spectra of such form are typical for carbon nanomaterials. It is known that vibration band (G-peak) at 1575 cm^{-1} is determined by stretching vibration mode E_{2g} of graphite lattice of infinite crystal [11]. The mode at 1355 cm^{-1} (D-peak) Raman spectrum corresponds to A_{1g} mode, radial modes of hexagonal rings (often called «breathing» mode) [12]. D-peak occurs as a result of a binary resonant process [13] and appears if there are defects of structured carbon [14] and evidently marked bound-

aries of nanocrystalline areas, it is typical for various carbon nanostructures (single-walled and multi-walled nanotubes, fullerenes, graphenes etc.) [15].

It should be mentioned that the band, determined by symmetric modes of C–H bonds in CH₂ and asymmetric ones in CH₃ [7], is also registered in the interval between 2800–3000 cm⁻¹. C–H bonds in the coating result from the dispersion of polyethylene and adsorption of volatile products on the substrate surface.

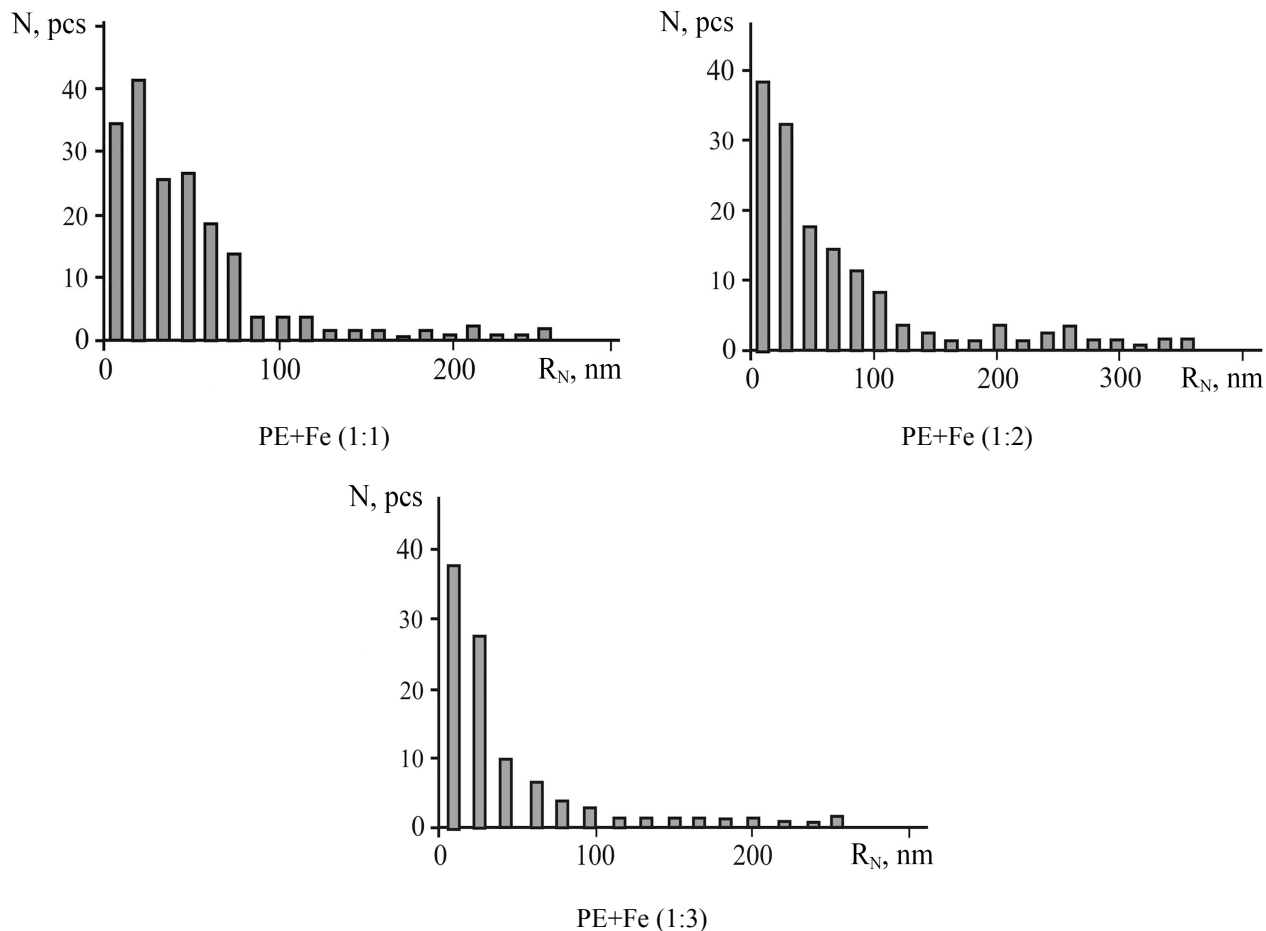


Figure 4. Distribution histogram of the forming nanostructures N in their radius size R_N after the thermal annealing at a temperature of 500 °C with mass ratio (1:1, 1:2 and 1:3) of the target components (PE+Fe)

The presented Raman spectra clearly indicate that resulting from laser dispersion of a mixture of polyethylene with iron oxalate in the volume of the layer, carbon nanostructures such as fullerenes, nanotubes and probably multi-walled nanotubes (MWNT) are formed. Except E_{2g} and A_{1g} the occurrence of radial modes near 200 cm⁻¹ [16] and G'-peak in the range of 2450–2650 cm⁻¹ [17] is characteristic of single-walled nanotubes. Spectra do not allow identifying them clearly as they have only E_{2g} and A_{1g} modes which are typical for carbon coatings and materials. Aiming at analysis of dispersion influence on the content of carbon formations, the obtained Raman spectra were arranged according to Gaussian elimination on D- (~ 1350 cm⁻¹) and G-peaks (~ 1580 cm⁻¹). Besides, base on requirements of error minimization, at decomposition extra D1-peak near 1500 cm⁻¹ (Fig. 5), associated with defective packaging and fullerenes and graphene clusters [8] was added.

The intensity ratio of I_G and I_D , is usually used to determine defect rates of structures [7, 10]. For example, if I_D is higher than I_G , this points to the failure of long-range crystalline and disordered areas. Such effect can be observed not only in nanotubes with a large number of defects, but also can appear due to metal impurities in amorphous carbon particles, short carbon fiber and simply due to layers of amorphous carbon on external surfaces of nanotubes [7].

Among examined testing samples layers deposited by dispersion of polyethylene with iron oxalate mixture with mass ratio 1:2, are characterized by the minimum value of I_D/I_G ratio (Table 2) which combined

with the smallest width of D1-peak indicates minimum content of nanostructures defects. G-peak discomposition to 1600 cm^{-1} also demonstrates disorderliness of crystalline lattice of graphite [9]. Besides, indicated samples are characterized by great D-peak width value showing high content of nanoclusters of sp^3 -hybridized carbon [18].

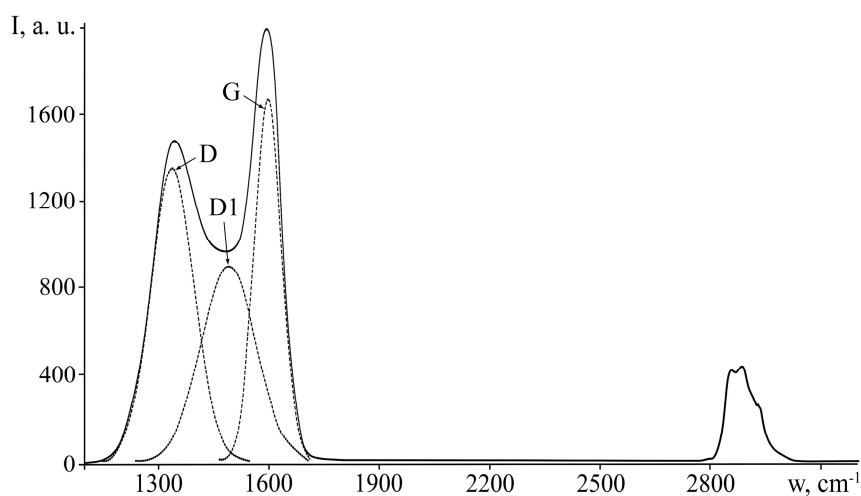


Figure 5. Typical Raman spectrum for nanostructured coatings deposited by laser dispersion of a mixture of polyethylene with iron oxalate

At the same time D1-peak shifting to 1520 cm^{-1} is typical for samples deposited by dispersion of polyethylene with iron oxalate mixture with mass ratio 1:3, which combined with I_D/I_G increase, the decrease of the size of graphene clusters can be explained [8], since under [11] I_D/I_G is in inverse proportion to the size of carbon clusters. Nanostructures (nanotubes, fullerenes or graphene fragment) in condensate deposited by laser dispersion of polyethylene with iron oxalate are indirectly confirmed by Raman spectrum of carbon coatings (Table 2) deposited by laser dispersion of graphite.

Table 2

Phase composition of nanostructured coatings

Mass ratio PE+Fe	D-peak		D1-peak		G-peak		I_D/I_G
	Position, cm^{-1}	Width, cm^{-1}	Position, cm^{-1}	Width, cm^{-1}	Position, cm^{-1}	Width, cm^{-1}	
УП	1430	245	—	—	1562	200	0,46
1:1	1330	138	1479	222	1599	90	0,54
1:2	1348	180	1480	105	1590	97	0,60
1:3	1348	148	1520	149	1602	88	1,01

Firstly, D-peak of carbon coatings is near 1430 cm^{-1} , and D-peak of nanostructured carbon layers is near 1350 cm^{-1} . Such displacement is caused by structure disorder to a greater degree that is evident as carbon coatings are an amorphous carbon matrix [19]. Secondly, Raman spectra decomposition of carbon coatings excludes variants of peak arrangement near 1500 cm^{-1} , related to defective packaging and graphene clusters.

After condensate heat treatment deposited by laser dispersion of polyethylene with iron oxalate due to the occurrence of processes of coalescence on Raman spectrum peaks appear near 220 cm^{-1} , 280 cm^{-1} , 392 cm^{-1} , 601 cm^{-1} , corresponding to $\alpha\text{-Fe}$ and iron carbide [20], and also the peak near 650 cm^{-1} , caused by Fe_3O_4 can be seen [21]. Peaks occurrence near 520 cm^{-1} and 960 cm^{-1} , relating with polycrystalline silicon [22], is explained by lack of coating density. After heat treatment the peak near $2800\text{--}3000\text{ cm}^{-1}$, as well as D- and G- peaks disappear caused by destruction of C–N bonds and carbon oxidation in the air.

Conclusion

It was shown that upon laser dispersion of a composite target based on polyethylene and iron oxalate, preheated to a temperature of $330\text{ }^\circ\text{C}$, coatings consisting of iron and its oxides and reinforced with carbon nanostructures are deposited. It was found that with a mass ratio of polyethylene and iron oxalate equal to 1:1, the distribution of the formed nanostructures in size (radius) is unimodal with a maximum near 20 nm.

With a further increase in the content of iron oxalate (1: 2, 1:3), the radius distribution of the formed nanostructures becomes multimodal, local maxima appear in the range from 30 to 50 nm. During heat treatment of coatings in air at a temperature of 500 °C, the density of structural formations decreases and their size increases which is explained by the occurrence of processes of coalescence and partial oxidation of pure iron particles. Using Raman spectroscopy it was found that carbon nanostructures formed in the coating volume are highly defective and the phase composition depends on the content of polyethylene in the target. The obtained polymer matrix nanocomposite films can be used in sensors [23, 24].

The study was supported by the Ministry of Education of the Republic of Belarus (task 2.64), as well as by the Ministry of Science and Higher Education of Russian Federation (project No. 0706–2020–0022).

References

- 1 Booker R. Nanotechnology for dummies / R. Booker. — Wiley Publishing Inc, 2005. — 366 с. ISBN 978–0–7645–8368–1
- 2 Boul P.J. Reversible sidewall functionalization of buckytubes / P.J. Boul // *Chemical Physics Letters*. — 1999. — Vol. 310. — P. 367–372. DOI: 10.1016/S0009–2614(99)00713–7
- 3 Белянин А.Ф. Наноструктурированные углеродные материалы в эмиссионной электронике / А.Ф. Белянин, В.В. Борисов, А.С. Багдасарян // *Рос. технол. журн.* — 2017. — Т. 5, № 5. — С. 22–40. <https://doi.org/10.32362/2500-316X-2017-5-3-22-40>
- 4 Колокольцев С.Н. Углеродные материалы. Свойства, технологии, применения / С.Н. Колокольцев. — Долгопрудный: ИД «Интеллект», 2012. — 296 с.
- 5 Чуриков А.В. Об использовании оксалата железа $\text{FeC}_2\text{O}_4 \cdot 2\text{H}_2\text{O}$ для синтеза электродного материала LiFePO_4 / А.В. Чуриков, И.А. Леенсон // *Электрохимическая энергетика*. — 2012. — Т. 11. — С. 14–20.
- 6 Zhang H.B. Raman spectra of MWCNTs and MWCNT-based H_2 -adsorbing system / H.B. Zhang // *Carbon*. — 2002. — Vol. 40. — P. 2429–2436. DOI:10.1016/S0008–6223(02)00148–3
- 7 Song J.I. Formation of carbon nanotubes catalyzed by rare earth oxides / J.I. Song // *New Carbon Materials*. — 2013. — Vol. 28. — P. 191–198. DOI:10.1016/S1872–5805(13)60076–1
- 8 Chernyak S.A. N-doping and oxidation of carbon nanotubes and jellyfish-like grapheme nanoflakes through the prism of Raman spectroscopy / S.A. Chernyak // *Applied Surface Science*. — 2019. — Vol. 488. — P. 51–60. DOI: 10.1016/j.apsusc.2019.05.243
- 9 Haque A. Synthesis of diamond nanostructures from carbon nanotube and formation of diamond-CNT hybrid structures / A. Haque // *Carbon*. — 2019. — Vol. 150. — P. 388–395. DOI: 10.1016/j.carbon.2019.05.027
- 10 Hur J. Raman intensity and vibrational modes of armchair CNTs / J. Hur // *Chemical Physics Letters*. — 2017. — Vol. 679. — P. 45–51. DOI:10.1016/j.cplett.2017.04.078
- 11 Tuinstra F. Raman spectrum of graphite / F. Tuinstra, J.L. Koenig // *Journal of Chemical Physics*. — 1970. — Vol. 53. — P. 1126–1130. DOI: 10.1063/1.1674108
- 12 Kusiak-Nejman E. Hybrid carbon-TiO₂ spheres: investigation of structure, morphology and spectroscopic studies / E. Kusiak-Nejman // *Applied Surface Science*. — 2018. — Vol. 469. — P. 684–690. DOI: 10.1016/j.apsusc.2018.11.093
- 13 Thomsen C. Double resonant Raman scattering in graphite / C. Thomsen, S. Reich // *Physical Review Letters*. — 2000. — Vol. 85. — P. 5214–5217. DOI: 10.1103/PhysRevLett.85.5214
- 14 Wang Y. Raman spectroscopy of carbon materials: structural basis of observed spectra / Y. Wang, D.C. Alsmeyer, R.L. McCreery // *Chemistry of Materials*. — 1990. — Vol. 2. — P. 557–563. DOI: 10.1021/cm00011a018
- 15 Данишевский А.М. Комбинационное рассеяние света в нанопористом углероде, получаемом из карбидов кремния и титана / А.М. Данишевский, Э.А. Сморгонская, С.К. Гордеев, А.В. Гречинская // *Физика твердого тела*. — 2001. — Т. 43. — С. 132–149.
- 16 Dresselhaus M.S. Raman spectroscopy of carbon nanotubes / M.S. Dresselhaus // *Physics Reports*. — 2005. — Vol. 409. — P. 47–99. DOI: 10.1016/j.physrep.2004.10.006
- 17 Aqel A. Carbon nanotubes, science and technology part (I) structure, synthesis and characterization / A. Aqel // *Arabian Journal of Chemistry*. — 2012. — Vol. 5. — P. 1–23. DOI: 10.1016/j.arabjc.2010.08.022
- 18 Praver S. Raman spectroscopy of diamond and doped diamond / S. Praver, R.J. Nemanich // *Philosophical Transactions of the Royal Society A: Mathematical, Physical and Engineering Sciences*. — 2004. — Vol. 362. — P. 2537–2565. DOI: 10.1098/rsta.2004.1451
- 19 Piliptsov D.G. XPS study of the structure of nitrogen doped a-C film / D.G. Piliptsov, A.S. Rudenkov, A.V. Rogachev, Xiaohong Jiang, P.A. Lychnikov, V.A. Emel'yanov // *IOP Conference Series: Materials Science and Engineering*. — 2017. — Vol. 168. — P. 012103 (P.1). DOI: 10.1088/1757–899X/168/1/012103.
- 20 Подгорный В.И. Получение образцов карбидов в плазме дугового разряда / В.И. Подгорный, Б.З. Белашев, Р.Н. Осауленко, А.Н. Терновой // *Журн. техн. физ.* — 2013. — Т. 83. — С. 77–81.
- 21 Iconaru S.L. Magnetite (Fe_3O_4) nanoparticles as adsorbents for As and Cu removal / S.L. Iconaru, R. Guégan, C.L. Popa, M. Motelica-Heino, C.S. Ciobanu, D. Predoi // *Applied Clay Science*. — 2016. — Vol. 134. — P. 128–135. DOI: 10.1016/j.clay.2016.08.019
- 22 Mercaldo L.V. First and second-order Raman scattering in Si nanostructures within silicon nitride / L.V. Mercaldo // *Applied Physics Letters*. — 2010. — Vol. 97. — P. 153112–1–153112–3. DOI: 10.1063/1.3501133

23 Wang S. Structure and properties of polyaniline nanocomposite coatings containing gold nanoparticles formed by low-energy electron beam deposition / S. Wang, A.A. Rogachev, M.A. Yarmolenko, A.V. Rogachev, Xiaohong Jiang, M.S. Gaur, P.A. Luchnikov, O.V. Galtseva, S.A. Chizhik // Applied Surface Science. — 2018. — Vol. 428. — P. 1070–1078. DOI: 10.1016/j.apsusc.2017.09.225

24 Sakenova R.E. The study of multilayer coatings based on MoN(MoZr)ZrN and (TiMo)N/(TiMo)₂(CrZr)N/(CrZr) obtained by the method of vacuum-arc deposition / R.E. Sakenova, N.K. Erdybaeva, A.D. Pogrebnyak, M.K. Kylyshkanov // Bulletin of the Karaganda University. Physics series. — 2019. — No. 2(94). — P. 14–21. DOI: 10.31489/2019Ph2/14–21

А.С. Руденков, М.А. Ярмоленко, А.А. Рогачев,
А.П. Суржиков, А.П. Лучников, О.А. Фролова

Полиэтиленнің темір оксалатымен қоспасын лазерлік диспергирлеу арқылы тұндырылатын наноқұрылымды жабындардың фазалық құрамы мен морфологиясы

Композиттік нысанның лазерлік дисперсиясы нәтижесінде пайда болатын газ фазасынан күшейтілген көміртекті наноқұрылымдары бар темір оксиді жабындарының қалыптасу ерекшеліктері зерттелген. Термиялық өндеудің технологиялық режимдерінің наноқұрылымды пленка қабаттарының морфологиясы мен фазалық құрамына әсері нақтыланған. Төсеніште көміртегі наноқұрылымдары бар жоғары дисперсті қабаттар пайда болатындығы дәлелденген. Раман спектроскопиясы әдісімен оксид матрицасында көміртекті құрылымдар пайда болатындығы көрсетілді, олар негізінен жалпақ орналасқан нанотүтікшелер түрінде ұсынылған. Полиэтилен мен темір оксалатының 1: 1 массалық қатынасында қалыптасқан наноқұрылымдардың мөлшері бойынша таралуы шамамен 20 нм болатын унимодальды екендігі анықталды. 1: 2 массалық қатынасы бар полиэтилен мен темір оксалатының қоспасын дисперсиялаған кезде, нанотүтікшелер балқытылған қабаттарда ең аз ақауларға ие болады. Лазерлік сәулеленудің композициялық нысанын дисперсиялау кезінде компоненттердің салыстырмалы құрамы жабындардың морфологиясы мен фазалық құрамына әсер ету заңдылықтары анықталған. Мақсатты жабындағы темір оксалатының концентрациясының жоғарылауымен құрылымдық гетерогенділік жоғарылайды, ішкі кедір-бұдыр және босатылған конденсаттағы жеке наноқұрылымдардың орташа мөлшері артады. Алынған полимерлі матрицасы бар нанокомпозитті пленкаларды сенсорларда қолдануға болады.

Кілт сөздер: полиэтилен, темір оксалат, жабын, наноқұрылымдар, морфология, фазалық құрам, раман спектроскопиясы.

А.С. Руденков, М.А. Ярмоленко, А.А. Рогачев,
А.П. Суржиков, А.П. Лучников, О.А. Фролова

Фазовый состав и морфология наноструктурированных покрытий, осаждаемых лазерным диспергированием смеси полиэтилена с оксалатом железа

Исследованы особенности формирования покрытий оксида железа с армированными углеродными наноструктурами из газовой фазы, генерируемой лазерным диспергированием композитной мишени. Определено влияние технологических режимов термообработки на морфологию и фазовый состав наноструктурированных пленочных слоев. Обнаружено, что на подложке формируются высокодисперсные слои, содержащие углеродные наноструктуры. Методом рамановской спектроскопии было показано, что в оксидной матрице возникают углеродные структуры, которые в основном представлены в виде плоскорасположенных нанотрубок. Установлено, что при массовом соотношении полиэтилена и оксалата железа 1: 1 распределение сформированных наноструктур по размерам является унимодальным с максимумом около 20 нм. При диспергировании смеси полиэтилена и оксалата железа с массовым соотношением 1: 2 в наплавленных слоях нанотрубки имеют наименьшую дефектность. Определены закономерности влияния на морфологию и фазовый состав покрытий относительного содержания компонентов при диспергировании композитной мишени лазерного излучения. Показано, что с увеличением концентрации оксалата железа в целевом покрытии повышаются структурная неоднородность, внутренняя шероховатость и средний размер отдельных наноструктур в выпавшем конденсате. Полученные нанокомпозитные пленки с полимерной матрицей могут быть использованы в сенсорах.

Ключевые слова: полиэтилен, оксалат железа, покрытие, наноструктуры, морфология, фазовый состав, КР-спектроскопия.

References

- 1 Booker, R. (2005). *Nanotechnology for dummies*. New York: Wiley Publishing Inc.
- 2 Boul, P.J. (1999). Reversible sidewall functionalization of buckytubes. *Chemical Physics Letters*, 310, 367–372, DOI: 10.1016/S0009-2614(99)00713-7.
- 3 Belyanin, A.F., Borisov, V.V., & Bagdasaryan, A.S. (2017). Nanostrukturirovannye uhlerodnye materialy v emissionnoi elektronike [Nanostructured carbon materials in emission electronics]. *Rossiiskii tekhnologicheskii zhurnal — Russian Technological Journal*, 5(3), 22–40 [in Russian].
- 4 Kolokol'cev, S.N. (2012). *Uhlerodnye materialy. Svoistva, tekhnologii, primeneniia [Carbon materials. Properties, technologies, applications]*. Dolgoprudnyi: ID «Intellekt» [in Russian].
- 5 Churikov, A.V., & Leenson, A.V. (2012). Ob ispolzovanii oksalata zheleza $\text{FeC}_2\text{O}_4 \cdot 2\text{H}_2\text{O}$ dlia sinteza elektrodnoho materiala LiFePO_4 [On the use of iron oxalate $\text{FeC}_2\text{O}_4 \cdot 2\text{H}_2\text{O}$ for synthesis of electrode material LiFePO_4]. *Elektrokhimicheskaiia enerhetika — Electrochemical engineering*, 11, 14–20 [in Russian].
- 6 Zhang, H.B. (2002). Raman spectra of MWCNTs and MWCNT-based H_2 -adsorbing system. *Carbon*, 40, 2429–2436, DOI: 10.1016/S0008-6223(02)00148-3.
- 7 Song, J.I. (2013). Formation of carbon nanotubes catalyzed by rare earth oxides. *New Carbon Materials*, 28, 191–198, DOI: 10.1016/S1872-5805(13)60076-1.
- 8 Chernyak, S.A. (2019). N-doping and oxidation of carbon nanotubes and jellyfish-like grapheme nanoflakes through the prism of Raman spectroscopy. *Applied Surface Science*, 488, 51–60, DOI: 10.1016/j.apsusc.2019.05.243.
- 9 Haque, A. (2019). Synthesis of diamond nanostructures from carbon nanotube and formation of diamond-CNT hybrid structure. *Carbon*, 150, 388–395, DOI: 10.1016/j.carbon.2019.05.027
- 10 Hur, J. (2017). Raman intensity and vibrational modes of armchair CNTs. *Chemical Physics Letters*, 679, 45–51. DOI: 10.1016/j.cplett.2017.04.078.
- 11 Tuinstra, F. (1970). Raman spectrum of graphite. *Journal of Chemical Physics*, 53, 1126–1130, DOI: 10.1063/1.1674108.
- 12 Kusiak-Nejman, E. (2018). Hybrid carbon-TiO₂ spheres: investigation of structure, morphology and spectroscopic studies. *Applied Surface Science*, 469, 684–690, DOI: 10.1016/j.apsusc.2018.11.093.
- 13 Thomsen, C. (2000). Double resonant Raman scattering in graphite. *Physical Review Letters*, 85, 5214–5217, DOI: 10.1103/PhysRevLett.85.5214.
- 14 Wang, Y. (1990). Raman spectroscopy of carbon materials: structural basis of observed spectra. *Chemistry of Materials*, 2, 557–563. DOI: 10.1021/cm00011a018.
- 15 Danishevskii, A.M., Smorgonskaya, E.A., Gordeev, S.K., & Grechinskaya, A.V. (2001). Kombinatsionnoe rasseianie sveta v nanoporistom uhlerode, poluchaemom iz karbidov kremniia i titana [Raman scattering in nanoporous carbon, obtaining from silicon and titanium carbide]. *Fizika tverdogo tela — Solid state physics*, 43, 132–149 [in Russian].
- 16 Dresselhaus, M.S. (2005). Raman spectroscopy of carbon nanotubes. *Physics Reports*, 409, 47–99. DOI:10.1016/j.physrep.2004.10.006.
- 17 Aqel, A. (2012). Carbon nanotubes, science and technology part (I) structure, synthesis and characterization. *Arabian Journal of Chemistry*, 5, 1–23, DOI: 10.1016/j.arabjc.2010.08.022.
- 18 Praver, S. (2004). Raman spectroscopy of diamond and doped diamond. *Philosophical Transactions of the Royal Society A: Mathematical, Physical and Engineering Sciences*, 362, 2537–2565, DOI: 10.1098/rsta.2004.1451.
- 19 Piliptsov, D.G. (2017). XPS study of the structure of nitrogen doped a-C film. *IOP Conference Series: Materials Science and Engineering*, 168, 012103, DOI: 10.1088/1757-899X/168/1/012103.
- 20 Podgorny, V.I. (2013). Poluchenie obraztsov karbidov v plazme duhovoho razriada [Obtaining of carbide samples in arc discharge plasma]. *Zhurnal tekhnicheskoi fiziki — The Journal of Technical Physics*, 83, 77–81 [in Russian].
- 21 Iconaru, S.L. (2016). Magnetite (Fe_3O_4) nanoparticles as adsorbents for As and Cu removal. *Applied Clay Science*, 134, 128–135. DOI: 10.1016/j.clay.2016.08.019.
- 22 Mercaldo, L.V. (2010). First and second-order Raman scattering in Si nanostructures within silicon nitride. *Applied Physics Letters*, 97, 153112–1–153112–3, DOI: 10.1063/1.3501133.
- 23 Wang, S. (2018). Structure and properties of polyaniline nanocomposite coatings containing gold nanoparticles formed by low-energy electron beam deposition. *Applied Surface Science*, 428, 1070–1078. DOI: 10.1016/j.apsusc.2017.09.225.
- 24 Sakenova, R.E., Erdybaeva, N.K., Pogrebnjak, A.D., & Kylyshkanov, M.K. (2019). The study of multilayer coatings based on $\text{MoN}(\text{MoZr})\text{ZrN}$ and $(\text{TiMo})\text{N}/(\text{TiMo})_x(\text{CrZr})\text{N}/(\text{CrZr})$ obtained by the method of vacuum-arc deposition. *Bulletin of the Karaganda University. Physics series*, 2(94), 14–21, DOI: 10.31489/2019Ph2/14–21.

D.G. Piliptsou¹, A.S. Rudenkov¹, A.V. Rogachev¹, Jiang Xiao Hong²,
E.A. Kulesh¹, A.P. Surzhikov³, A.P. Luchnikov^{4*}, O.A. Frolova⁴

¹Francisk Skorina Gomel State University, Gomel, Belarus;

²Nanjing University of science and technology, Nanjing, Republic of China;

³Tomsk Polytechnic University, School of Non-Destructive Testing, Tomsk, Russia;

⁴MIREA – Russian Technological University, Russia

(*E-mail: fisika@mail.ru)

Structural properties of carbon composites doped with boron

The article considers morphology, chemical and phase composition of composite boro-carbon coatings, received by ion-plasma synthesis, depending on the boron content. Specimens of carbon coating doped with boron were obtained in vacuum unit by combined method coupled with co-deposition of carbon layer from pulse carbon plasma and its doping with boron atom flow. The obtained specimens of composite CC had embedded boron atoms with various concentration (N_B), namely, 2.3 at.% were contained in $\alpha\text{-C}_{91.2}\text{B}_{2.3}$, in $\alpha\text{-C}_{79.3}\text{B}_{17.4}$ — 17.4 at.%, in $\alpha\text{-C}_{53.3}\text{B}_{43.2}$ — 43.2 at.%. Carbon structures and carbon clusters graphitization were examined by X-ray photoelectron spectroscopy and Raman spectroscopy. Aiming at chemical interaction between carbon and boron in CC establishment we conducted mathematical processing of XPS for energy states C1s, B1s, O1s of carbon, boron and oxygen atoms. XPS C1s was presented as peaks superposition with centers located at 284.5; 285.5; 283.5 and 288 eV and consequently responsible for Csp^2 , Csp^3 , C–B and C–O carbon atom interaction. With the growth of N_B in boron-doped carbon coating a grain structure is formed, its size and grain orientation regarding the surface of the substrate increase, resulting in a decrease in the coating layer surface roughness.

Keywords: composite carbon coatings, boron doping, atomic force microscopy, X-ray photoelectron spectroscopy, Raman spectroscopy, clusters, boron carbide.

Introduction

Boron doping is considered to be an effective technological method of improving operational metal resources and their alloys [1]. Boron being the second solid element and having metal matrix in the volume as a separate phase, solid solution or chemical compound, deforms crystalline lattice and causes solid phase formation in materials that significantly increase their mechanical properties, thermal and wear resistance [2]. Boron on contact with carbon can form chemically stable boron carbide B_4C , which is resistant at temperature up to 2450 °C. These characteristics of boron determine high prospectivity of its use as a doping element in forming compositional carbon-contained coatings [3]. On [4] it is indicated, that phase and structural characteristics of such coatings are significantly defined by conditions and regimes of their formation by means of ion-plasma synthesis. In implementing of carbon layers' deposition methods from pulse cathode plasma, intensive thermal excitation processes are carried out, ionized particles streams having sufficiently high reaction activity are formed. At the same time carbon layers are condensed in the form of heterophase coatings containing carbon atoms in the state of sp^3 , sp^2 and even sp^1 -hybridized bonds. Such features of carbon coating (CC) deposition suggest that when they are doped with boron in the process of ion plasma synthesis it is possible to form a wide range of different phases in the layer structure, including based on chemical compounds. Composite materials with clusters from compounds on the basis of doping substance can have the same structure as nanocomposites based on polymer matrix [5].

The article considers structural properties of composite boron-carbon coatings obtained by ion-plasma synthesis based on their boron content.

Samples and research methods

Specimens of CC doped with boron were obtained in vacuum unit by combined method coupled with co-deposition of carbon layer from pulse carbon plasma and its doping with boron atom flow. Target evaporation from boron was conducted by pulsed radiation from solid-state YAG: Nd^{3+} laser at wavelength 1,064 nm in the frequency range of (f_L) 5 to 50 Hz. Boron atoms flow with pulse length 150 μs and frequency $f_L = 5, 30$ and 50 Hz was deposited on CC surface together with carbon plasma flow from vacuum-arc evaporator with pulse length 150 μs and frequency $f_C = 10$ Hz.

The elemental composition of the obtained α -C:B CC was regulated through changing of laser radiation pulse frequency f_L and was determined by X-ray photoelectron spectroscopy (XPS). X-ray photoelectron spectra of obtained carbon coatings were shot using PHI Quanta type, Japan.

The obtained specimens of composite CC had embedded boron atoms with various concentration (N_B), namely, 2.3 at.% were contained in α -C_{91.2}:B_{2.3}, in α -C_{79.3}:B_{17.4} — 17.4 at.%, in α -C_{53.3}:B_{43.2} — 43.2 at.%.

Carbon coating thickness was defined by means of transversal specimen chip with the help of scanning electron microscope (SEM) of Hitachi S-4800 type. A comparative analysis was carried out on CC specimens with the same effective thickness 363 ± 16 nm. Surface morphology of composite carbon coatings α -C:B was investigated with the help of atomic-force microscope (AFM) of Solver Pro and NT-MDT (Russia) types in topography and phase contrast measuring mode. The scanning field was $10 \times 10 \mu\text{m}^2$ at probe speed of $1.0 \mu\text{m/s}$. High heterogeneous projections on the surface were monitored using the methods [6].

The microstructure of composite CC was studied by Raman spectroscopy at radiation excitation at wavelength 532 nm with power flow 20 mW using Senterra, Bruker.

The chemical composition and types of molecular bonds between carbon and boron atoms in the composite CC were determined by X-ray photoelectron spectroscopy using a PHI quanta 2 XPS device. XPS spectra were excited by Al (K α) cathode emission with the energy of 1486.6 eV at a voltage of 15 kW. The capacity of exciting radiation power was 25 W. The spectrum was collected in the area of interaction of the probing radiation with the surface of a spot CC specimen with a diameter of 100 μm . Bonds energy in XPS spectra was calibrated through C1s (284.6 eV). It should be noted that since the atomic sensitivity coefficient for boron (0.088) is significantly lower than for carbon C (0.205), the intensity of the B1s peak in XPS spectrum is significantly lower than that of the C1s peak.

Experimental results and their discussion

On Figure 1 SEM-images of CC specimen chip doped with boron are represented. It is seen that the structure of CC doped with boron differs from the structure of one-component α -C coating (Fig. 1, *a*). In the volume α -C:B of CC the formation of grain structure occurs, what is more, grain size depends on boron concentration N_B and increases with its growth: at a concentration ~ 2.3 at. % the structure becomes fine-grained, with its further growth N_B achieves ~ 43.2 at. % with grain formation in 3–3.5 times larger with marked orientation towards substrate surface [7]. There are no defects like pores or cracks on the surface and in the volume of deposited composite CC, as well as there are no substrate layers. The latter shows high adhesion of CC to silicon substrate.

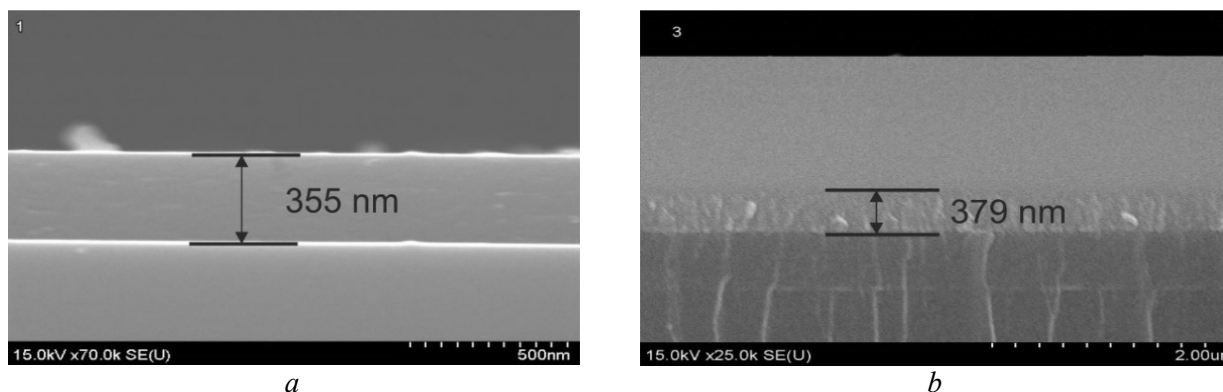


Figure 1. SEM-images of chip α -C (*a*) and α -C_{53.3}:B_{43.2} (*b*) of CC

On Figure 2 dependency diagram of N_C content of carbon component (curve 1) and average size of grain (R_g) in CC doped with boron is shown. The composition of elements of CC specimens, deposited together from pulse carbon plasma and boron atom flow doped with boron concentration 2.3 at.%, 17.4 at.% and 43.2 at.% with dopant boron atom flow frequency f_L increase changes essentially. Oxygen in CC structure is within the limits 2.4...6.5 at. % and in bound state with carbon mainly.

It can be seen that N_B increase in the coating leads to higher defectiveness of the composite CC and the formation of larger surface heterogeneities. Grain structure increase of boron-doped CC is caused by high activity of agglomeration processes with formation of boron in initial one-component carbon material. Grain

size increase R_g in boron-carbon coating with higher boron content N_B is consistent with diamond-like films morphology data [8].

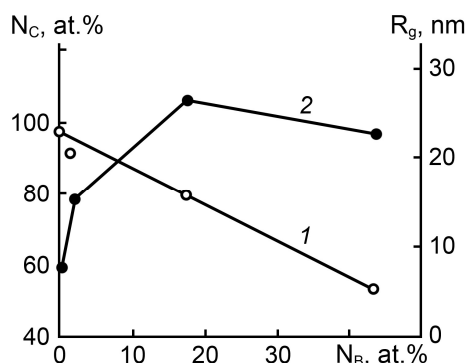


Figure 2. Dependency diagram of carbon component N_C content (1) and grain R_g average size (2) in CC structure on N_B concentration of dopant boron atoms.

It should be noted that geometric parameters of CC structural state, surface roughness (R_{ms}) and grain R_g average size of the layer structure depend on conditions and modes of the coating process. Thus, one-component α -C of CC, deposited from pulse flows, are characterized by low values R_{ms} , that can be explained by small sizes and clusters close packing Csp^3 [9].

On Figure 3 typical Raman spectra α -C (a) and α -C_{53.3}:B₄₃ (b) of CC are presented. Raman spectra (RS) envelope shape of all CC is peculiar to amorphous CC, containing carbon atoms both in sp^2 and sp^3 bond hybridization state.

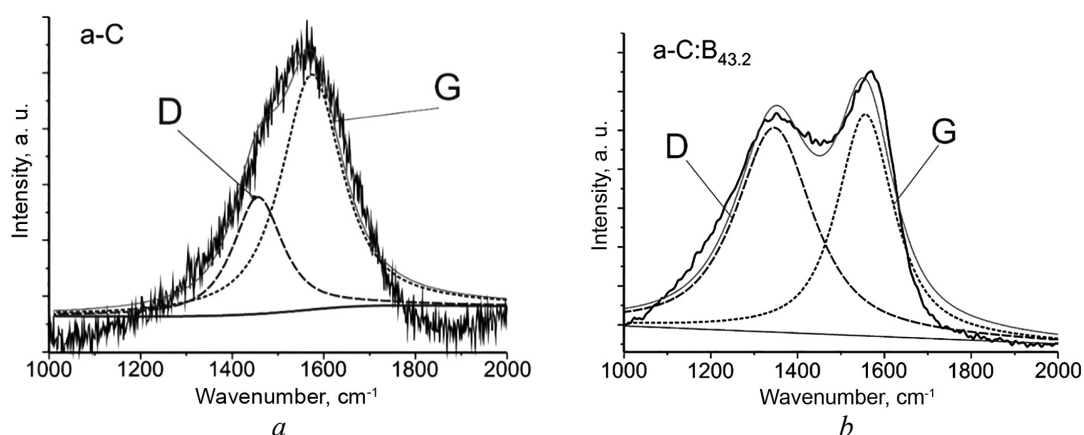


Figure 3. Raman-spectra α -C (a) and α -C_{53.3}:B₄₃ (b) of CC

Figure 3 shows that RS of boron-carbon CC have broad asymmetric peak in the range 1000 to 2000 cm^{-1} , that according to [10] contains information about sp^2 hybridized carbon bonds, order degree and relative size of carbon clusters Csp^2 and Csp^3 . Raman spectrum can be represented in superposition of peaks (G-peak and D-peak) by Gaussian function. Herewith theoretical curve, being the result of spectrum simulation, is well consistent to basic experimental data that testifies the certainty of RS mathematical processing.

With N_B growth in CC changes of RS relative to intensity ratio of D- and G-peaks occur (Fig. 3, Table 1), that are determined not only by changes of Csp^2 and Csp^3 clusters quantity and size in accordance with [11], but also by metal content in the layer, its chemical activity. There is molecular bonds process between carbon and boron that leads to changes of carbon clusters degree of order.

It was found that at $N_B = 2.3$ at. % in carbon coating D- and G-peaks intensity ratio insignificantly changes in comparison with RS parameters of one-component carbon coating. It indicates little impact of small N_B on the ordering degree and relative distribution of Csp^2/Csp^3 carbon phases in the coating.

With N_B growth in CC D-peak intensity increase occurs, as well as G-peak centreshift towards lower values of wave numbers. Essential changes of RS shape and I_D/I_G ratio increase (Table 1) for carbon coatings α -C highly doped with boron (Fig. 3, b) ($N_B = 43.2$ at. %) happen.

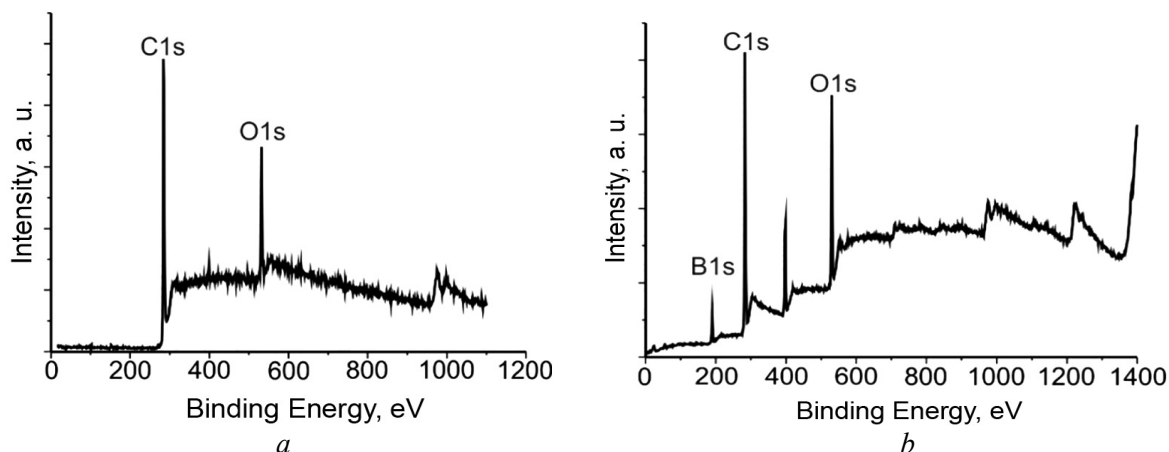
Parameters of the Raman spectra of carbon coatings doped with boron

Type of CC	f_L , Hz	N_C , at. %	N_B , at. %	N_O , at. %	I_D/I_G	Position of G-peak, cm^{-1}	Width of G-peak, cm^{-1}
α -C	–	97.6	–	2.4	0.58	1573.5	157.2
α -C _{91.2} :B _{2.3}	5	91.2	2.3	6.5	0.62	1571.3	168.7
α -C _{79.3} :B _{17.4}	33	79.3	17.4	3.3	0.73	1552.3	189.9
α -C _{53.3} :B _{43.2}	50	53.3	43.2	3.5	1.25	1556.2	155.7

In accordance with [12] CC received from pulse flows of carbon plasma are characterized by high mechanical properties under the condition ($I_D/I_G \leq 1$) and for CC α -C carbon atom concentration with sp^3 hybridized bonds increases with I_D/I_G ratio reduction. According to Table 1 with N_B growth up to 17.4 at. % some I_D/I_G ratio increase is observed in the coating, that indicates the reduction of carbon atom concentration with sp^3 hybridized bonds.

Together with the increase of I_D/I_G ratio G-peak shifting toward lower wave numbers in comparison with peak's position for CC α -C takes place. According to [13] such change corresponds to the decrease of carbon matrix ordering degree and is defined by carbon atom concentration degree with sp^3 hybridized bonds. Based on data from Table 1 we can conclude that the shifting of G-peak position and insignificant value increase of I_D/I_G ratio, typical of CC α -C with $N_B = 2.3$ at. % and 17.4 at. %, are caused by the concentration growth of CC Csp^3 . In [12] it is shown that the increase in carbon atoms number in sp^3 hybridized bonds is probably connected with C–B bonds formation in CC, while boron interacts mainly with carbon atoms with sp^3 hybridization. It leads to the growth of structural heterogeneity that causes the ordering degree decrease of carbon clusters Csp^2 and shows in RS of CC as G-peak broadening. At high N_B value the density reduction of sp^3 bonds occurs in CC.

X-ray photoelectron spectroscopy (XPS) analysis for CC α -C and α -C:B presented on Figure 4 shows that except boron there is also oxygen in the surface layer in the bond state with carbon (C–O) and boron (B–O). These bonds are formed at the stage of CC deposition as a result of interaction of carbon and boron components with oxygen in the operating environment of the vacuum chamber, as well as at its depressurization. Since the contribution of oxygen C–O and B–O — bonds to the integrated intensity was insignificant in relation to the total basic peaks area, their impact on CC structure and properties was not studied.

Figure 4. XPS α -C (a) and α -C:B_{43.2} (b) CC

Aiming at chemical interaction between carbon and boron in CC establishment we conducted mathematical processing of XPS for energy states C1s, B1s, O1s of carbon, boron and oxygen atoms. XPS C1s was presented as peaks superposition with centers located at 284.5; 285.5; 283.5 and 288 eV and consequently responsible for Csp^2 , Csp^3 , C–B and C–O carbon atom interaction [14].

X-ray photoelectronic spectrum B1s can be considered as the peaks superposition characteristic of B–O, B–C and B–B interactions and located at energies 190.7, 189.4 and 190 eV correspondently.

There are peaks typical of O–C, O–O and O–B bonds in X-ray photoelectronic spectrum of oxygen O1s. As a result of statistical data processing of C1s XPE-spectrum it was found that integrated area share for C–O bonds does not exceed 5 %.

XPS for boron doped CC ambiguously depend on N_B value in CC. At low boron N_B (2.3 at. %) B–C carbene bonds are mainly formed. With further N_B growth B–B bonds increase in the structure of composite CC occurs. However, at high N_B value (43.2 at. %) we observe carbon matrix restructuring with dominant Csp^2 and carbide phases content in CC volume. There is some C- sp^3 -peak shiftcenter (up to ~ 0.3 eV) towards higher energies as well as the reduction of this peak half-width at N_B increase in CC. It can be connected with the presence of more than one heterophase forming the structure in CC [15], as well as the development of competing forming processes in the coating layer of carbide compounds and boron oxide.

With N_B growth we observe the reduction of Csp^3 carbon atom bonds and considerable increase of B–C-bonds, characteristic of boron carbide in the coating. It can be assumed that Csp^3 reduction of carbon clusters is caused by their replacement for boron carbide. It corresponds to the results of CC RS analysis where graphitization of carbon structure and orientation increase of carbon Csp^2 -clusters due to boron bonds with carbon atoms in sp^3 hybridization state are observed. Such phase changes in CC with different N_B values allow for their high mechanical properties preservation.

Conclusion

The structural properties of composite boron-carbon coatings obtained by ion-plasma synthesis are largely determined by the boron content in them. At a low concentration of NB (2.3 at.%) Boron, bonds with carbon of the B–C type are predominantly formed. With the growth of N_B in boron-doped carbon coating a grain structure is formed, its size and grain orientation regarding the surface of the substrate increase, resulting in a decrease in the coating layer surface roughness. An increase in the grain size of the structure of boron-doped UPs is caused by the high activity of agglomeration processes with the formation of boron-containing microvolumes in the original one-component carbon material. With the subsequent growth of NB, there is an increase in the B–B bonds in the structure of the composite UP. Also, the increase of N_B in carbon coating structure leads to the reduction of carbon phase content with sp^3 hybridized bonds and is replaced by boron carbide clusters. It is confirmed by graphitization of carbon structure and increase of carbon Csp^2 clusters due to chemical boron and carbon atoms interaction in the state with sp^3 hybridized bonds. At a high NB value (43.2 at.%), The structure of the carbon matrix is restructured with a predominant content of Csp^2 and carbide phases in the volume.

The study was supported by the Chinese Ministry of Science and Technology (projects No.2016YFE0111800, for 2016–2019), as well as in the framework of the execution of the task 3.4.23 SPSP «Physical materials science, new materials and technologies» (Republic of Belarus) and by the Ministry of Science and Higher Education of Russian Federation (project No. 0706–2020–0022).

References

- 1 He D. Tailoring the mechanical and tribological properties of B4C/a-C coatings by controlling the boron carbide content / D. He, L. Shang, Z. Lu, G. Zhang, L. Wang, Q. Xue // Surface and Coatings Technology. — 2017. — Vol. 329. — P. 11–18. DOI: 10.1016/j.surfcoat.2017.09.017.
- 2 Cuong P.D. Effects of relative humidity on tribological properties of boron carbide coating against steel / P.D. Cuong, Hyo-Sok Ahn, Eui-Sung Yoon, Kyung-Ho Shin // Surface and Coatings Technology. — 2006. — Vol. 201. — P. 4230–4235. DOI: 10.1016/j.surfcoat.2006.08.093.
- 3 Solozhenko V.L. Synthesis of superhard cubic BC_2N / V.L. Solozhenko, D. Andrault, G. Fiquet, M. Mezouar, D.C. Rubie // Applied Physics Letters. — 2001. — Vol. 78. — P. 1385–1387. DOI: 10.1063/1.1337623.
- 4 Chepkasov S. Properties of ta-C coatings prepared by pulsed cathodic arc source at various distances / S. Chepkasov, A. Zolkin, D. Piliptsov, E. Gladkikh, K. Kravchuk // IOP Conf. Series: Journal of Physics: Conf. Series. — 2018. — Vol. 1115. — P. 032066. DOI: 10.1088/1742-6596/1115/3/032066.
- 5 Wang S. Structure and properties of polyaniline nanocomposite coatings containing gold nanoparticles formed by low-energy electron beam deposition / S. Wang, A.A. Rogachev, V.A. Yarmolenko, A.V. Rogachev, Jiang Xiaohong, M.S. Gaur, A.P. Luchnikov, O.V. Galtseva, S.A. Chizhik // Applied Surface Science. — 2018. — Vol. 428. — P. 1070–1078. DOI: 10.1016/j.apsusc.2017.09.225.
- 6 Luchnikov P.A. Deformable Polymer Dielectric Films in Phase Light Modulators / P.A. Luchnikov, V.V. Vetrova, N.P. Zubkov, O.A. Surzhikova, N.I. Chernova // IOP Conference Series: Materials Science and Engineering. — 2017. — Vol. 189. — P. 012027. DOI: 10.1088/1757-899X/189/1/012027.

- 7 You M.S. Low temperature growth of highly transparent nanocrystalline diamond films on quartz glass by hot filament chemical vapor deposition / M.S. You, F.C.N. Hong, Y.R. Jeng, S.M. Huang // *Diamond and Related Materials*. — 2009. — Vol. 18. — P. 155–159.
- 8 Dvorkin V.V. Use of ultrafine-dispersed nanodiamond for selective deposition of boron-doped diamond films / V.V. Dvorkin, N.N. Dzbanovskii, N.V. Suetin, A.Yu. Yur'ev, A.F. Pal', P.Ya. Detkov // *Physics of the Solid State*. — 2004. — Vol. 46. — P. 729–732. DOI: 10.1134/1.1711460.
- 9 Mori H. Low Friction Property of Boron Doped DLC under Engine Oil / H. Mori, M. Tohyama, M. Okuyama, T. Ohmori, N. Ikeda, K. Hayashi // *Tribology Online*. — 2017. — Vol. 12, № 3. — P. 135–140. DOI: 10.2474/trol.12.135.
- 10 Sikora A. Structural and electrical characterization of boron containing diamond-like carbon films deposited by femtosecond pulsed laser ablation / A. Sikora, A. Berkesse, O. Bourgeois, J.-L. Garden, C. Guerret-Piécourt, J.-N. Rouzaud, A.-S. Loir, F. Garrelie, C. Donnet // *Solid State Sci.* — 2009. — Vol. 11. — P. 1738–1741. DOI: 10.1016/j.solidstatesciences.2008.07.013.
- 11 Liza S. Deposition of boron doped DLC films on TiNb and characterization of their mechanical properties and blood compatibility / S. Liza, J. Hieda, H. Akasaka, N. Ohtake, Yu. Tsutsumi, A. Nagai, T. Hanawa // *Science and Technology of Advanced Materials*. — 2017. — Vol. 18, No. 1. — P. 76–87. DOI: 10.1080/14686996.2016.1262196.
- 12 Zhang L.L. Synthesis and characterization of boron incorporated diamond-like carbon thin films / L.L. Zhang, Q. Yang, Y. Tang, L. Yang, C. Zhang, Y. Hu, X. Cui / *Thin Solid Films*. — 2015. — Vol. 589. — P. 457–464. DOI: 10.1016/j.tsf.2015.05.067.
- 13 Buzhinskij O.I. Plasma deposition of boron films with high growth rate and efficiency using carborane / O.I. Buzhinskij, V.G. Otroshchenko, D.G. Whyte, M. Baldwin, R.W. Conn, R.P. Doerner, R. Seraydarian, S. Luckhardt, H. Kugel, W.P. West // *Journal of Nuclear Materials*. — 2003. — Vol. 313–316. — P. 214–218. DOI: 10.1016/S0022-3115(02)01482-4.
- 14 Panwar O.S. Characterization of Boron- and Phosphorous Incorporated Tetrahedral Amorphous Carbon Films Deposited by the Filtered Cathodic Vacuum Arc Process / O.S. Panwar, M.A. Khan, M. Kumar, S.M. Shivaprasad, B.S. Satyanarayana, P.N. Dixit, R. Bhattacharyya // *Jpn. J. Appl. Phys.* — 2009. — Vol. 48. — P. 065501. DOI: 10.1143/jjap.48.065501.
- 15 Белянин А.Ф. Наноструктурированные углеродные материалы в эмиссионной электронике / А.Ф. Белянин, В.В. Борисов, А.С. Багдасарян // *Рос. технол. журн.* — 2017. — Т. 5, № 3. — С. 22–40. DOI: 10.32362/2500-316X-2017-5-3-22-40.

Д.Г. Пилипцов, А.С. Руденков, А.В. Рогачев, Цзян Сяо Хун,
Е.А. Кулеш, А.П. Суржигов, А.П. Лучников, О.А. Фролова

Бормен легирленген көміртекті композициялық материалдардың құрылымдық қасиеттері

Мақалада бордың құрамына байланысты ион-плазмалық синтез нәтижесінде алынған бор-көміртегі композицияларының морфологиясы, химиялық және фазалық құрамы қарастырылған. Бормен байланған көміртегі жабының (КЖ) үлгілері вакуумдық қондырғыда импульсті көміртегі плазмасынан көміртегі қабатының түсуімен және бор атомдары ағымының тұтасуымен алынған. Алынған композициялық КЖ үлгілерінде әртүрлі концентрациясы бар бор атомдары, атап айтқанда 2,3 % болды, олар $\alpha\text{-C}_{91,2}\text{:B}_{2,3}$, $\alpha\text{-C}_{79,3}\text{:B}_{17,4}$ — 17,4 ат.%, $\alpha\text{-C}_{53,3}\text{:B}_{43,2}$ — 43,2 ат.%. Көміртекті құрылымдар және көміртегі кластерлерінің графитизациясы рентгендік фотоэлектронды спектроскопия (XPS) және раман спектроскопиясымен зерттелді. КЖ құру кезінде көміртегі пен бордың химиялық өзара әрекеттесуі мақсатында C1s, B1s, O1s атомдарының көміртегі, бор және оттегі энергетикалық күйлері үшін XPS математикалық өңдеу жүргізілді. XPS C1s 284,5-де орналасқан орталықтары бар шыңдардың суперпозициясы ретінде ұсынылды; 285,5; 283,5 және 288 эВ, демек, Csp^2 , Csp^3 , C–B және C–O көміртегі атомдарының өзара әрекеттесуіне жауап береді. N_B өсуімен бормен қапталған көміртегі жабында түйіршікті құрылым пайда болады, оның мөлшері мен астықтың субстрат беткейінің ұлғаюына қарай бағдарлануы қабатының беттік кедір-бұдырының төмендеуіне әкеледі.

Кілт сөздер: композициялық көміртегі жабыны, бор тамшысының пайда болуы, атомдық күш микроскопиясы, рентгендік фотоэлектронды спектроскопия, раман спектроскопиясы, кластерлер, бор карбиді.

Д.Г. Пилипцов, А.С. Руденков, А.В. Рогачев, Цзян Сяо Хун,
Е.А. Кулеш, А.П. Суржигов, А.П. Лучников, О.А. Фролова

Структурные свойства углеродных композиционных материалов, легированных бором

В статье рассмотрены морфология, химический и фазовый состав композиционных боруглеродных покрытий, полученных ионно-плазменным синтезом, в зависимости от содержания бора. Образцы углеродного покрытия (УП), легированного бором, были получены в вакуумной установке комбиниро-

ванным способом в сочетании с осаждением углеродного слоя из импульсной углеродной плазмы и его легированием потоком атомов бора. Полученные образцы композиционных УП содержали внедренные атомы бора с различной концентрацией (N_B), а именно 2,3 ат.% содержались в α - $C_{91,2}:B_{2,3}$, в α - $C_{79,3}:B_{17,4}$ — 17,4 ат.%, в α - $C_{53,3}:B_{43,2}$ — 43,2 ат.%. Структуры углерода и графитизация углеродных кластеров были исследованы методами рентгеновской фотоэлектронной спектроскопии (XPS) и рамановской спектроскопии. С целью химического взаимодействия между углеродом и бором при создании УП была проведена математическая обработка XPS для энергетических состояний C1s, B1s, O1s атомов углерода, бора и кислорода. XPS C1s была представлена как суперпозиция пиков с центрами, расположенными в 284,5; 285,5; 283,5 и 288 эВ, и, следовательно, они являлись ответственными за взаимодействие атомов углерода Csp^2 , Csp^3 , C–B и C–O. С ростом N_B в углеродном покрытии, легированном бором, образуется зернистая структура, увеличиваются ее размер и ориентация зерен относительно поверхности подложки, что приводит к уменьшению шероховатости поверхности слоя покрытия.

Ключевые слова: композитные углеродные покрытия, каплеобразование бора, атомно-силовая микроскопия, рентгеновская фотоэлектронная спектроскопия, комбинационная спектроскопия, кластеры, карбид бора.

References

- 1 He, D., Shang, L., Lu, Z., Zhang, G., Wang, L., & Xue, Q. (2017). Tailoring the mechanical and tribological properties of B4C/a-C coatings by controlling the boron carbide content. *Surface and Coatings Technology*, 329, 11–18, DOI: 10.1016/j.surfcoat.2017.09.017.
- 2 Cuong, P.D., Hyo-Sok, A., Eui-Sung, Y., & Kyung-Ho, Sh. (2006). Effects of relative humidity on tribological properties of boron carbide coating against steel. *Surface and Coatings Technology*, 201, 4230–4235, DOI: 10.1016/j.surfcoat.2006.08.093.
- 3 Solozhenko, V.L., Andrault, D., Fiquet, G., Mezouar, M., & Rubie, D.C. (2001). Synthesis of superhard cubic BC2N. *Applied Physics Letters*, 78, 1385–1387, DOI: 10.1063/1.1337623.
- 4 Chepkasov, S., Zolkin, A., Piliptsov, D., Gladkikh, E., & Kravchuk, K. (2018). Properties of ta-C coatings prepared by pulsed cathodic arc source at various distances. *IOP Conf. Series: Journal of Physics: Conf. Series*, 1115, 032066, DOI: 10.1088/1742-6596/1115/3/032066.
- 5 Wang, S., Rogachev, A.A., Yarmolenko, V.A., Rogachev, A.V., Jiang Xiaohong, & Gaur, M.S. et al. (2018). Structure and properties of polyaniline nanocomposite coatings containing gold nanoparticles formed by low-energy electron beam deposition. *Applied Surface Science*, 428, 1070–1078, DOI: 10.1016/j.apsusc.2017.09.225.
- 6 Luchnikov, P.A., Vetrova, V.V., Zubkov, N.P., Surzhikova, O.A., & Chernova, N.I. (2017). Deformable Polymer Dielectric Films in Phase Light Modulators. *IOP Conference Series: Materials Science and Engineering*, 189, 012027, DOI: 10.1088/1757-899X/189/1/012027.
- 7 You, M.S., Hong, F.C.N., Jeng, Y.R., & Huang, S.M. (2009). Low temperature growth of highly transparent nanocrystalline diamond films on quartz glass by hot filament chemical vapor deposition. *Diamond and Related Materials*, 18, 155–159, DOI: 10.1016/j.diamond.2008.07.015.
- 8 Dvorkin, V.V., Dzbanovskii, N.N., Suetin, N.V., Yur'ev, A.Yu., Pal', A.F., & Detkov, P.Ya. (2004). Use of ultrafine-dispersed nanodiamond for selective deposition of boron-doped diamond films. *Physics of the Solid State*, 46, 729–732, DOI: 10.1134/1.1711460.
- 9 Mori, H., Tohyama, M., Okuyama, M., Ohmori, T., Ikeda, N., & Hayashi, K. (2017). Low Friction Property of Boron Doped DLC under Engine Oil. *Tribology Online*, 12(3), 135–140, DOI: 10.2474/trol.12.135.
- 10 Sikora, A., Berkesse, A., Bourgeois, O., Garden, J.-L., Guerret-Piécourt, C., & Rouzaud, J.-N. et al. (2009). Structural and electrical characterization of boron containing diamond-like carbon films deposited by femtosecond pulsed laser ablation. *Solid State Sci.*, 11, 1738–1741, DOI: 10.1016/j.solidstatesciences.2008.07.013.
- 11 Liza, S., Hieda, J., Akasaka, H., Ohtake, N., Tsutsumi, Yu., & Nagai, A. et al. (2017). Deposition of boron doped DLC films on TiNb and characterization of their mechanical properties and blood compatibility. *Science and Technology of Advanced Materials*, 18(1), 76–87. DOI: 10.1080/14686996.2016.1262196.
- 12 Zhang, L.L., Yang, Q., Tang, Y., Yang, L., Zhang, C., & Hu, Y. et al. (2015). Synthesis and characterization of boron incorporated diamond-like carbon thin films. *Thin Solid Films*, 589, 457–464, DOI: 10.1016/j.tsf.2015.05.067.
- 13 Buzhinskij, O.I., Otroshchenko, V.G., Whyte, D.G., Baldwin, M., Conn, R.W., & Doerner, R.P. et al. (2003). Plasma deposition of boron films with high growth rate and efficiency using carborane. *Journal of Nuclear Materials*, 313–316, 214–218, DOI: 10.1016/S0022-3115(02)01482-4.
- 14 Panwar, O.S., Khan, M.A., Kumar, M., Shivaprasad, S.M., Satyanarayana, B.S., & Dixit, P.N. et al. (2009). Characterization of Boron- and Phosphorus Incorporated Tetrahedral Amorphous Carbon Films Deposited by the Filtered Cathodic Vacuum Arc Process. *Jpn. J. Appl. Phys.*, 48, 065501, DOI: 10.1143/jjap.48.065501.
- 15 Belyanin, A.F., Borisov, V.V., & Bagdasarvan, A.S. (2017). Nanostrukturirovannye uhlernodnye materialy v emissionnoi elektronike [Nanostructured carbon materials in emission electronics]. *Rossiiskii tekhnologicheskii zhurnal — Russian Technological Journal*, 5(3), 22–40, DOI: 10.32362/2500-316X-2017-5-3-22-40 [in Russian].

E.A. Dmitriyeva¹, I.A. Lebedev¹, E.A. Grushevskaya^{1*}, D.O. Murzalinov^{1,2},
A.S. Serikkanov¹, N.M. Tompakova¹, A.I. Fedosimova¹, A.T. Temiraliyev¹

¹Satbayev University, Institute of Physics and Technology, Almaty, Kazakhstan;

²Kazakh Agrotechnical University named after S. Seifullin, Nursultan, Kazakhstan

(*E-mail: grushevskaiya@bk.ru)

The effect of three-minute exposure of oxygen plasma on the properties of tin oxide films

Research devoted to the effect of three-minute exposure of oxygen plasma on the properties of tin oxide films investigation. The films were obtained by sol-gel method from five-water tin tetrachloride solution. The concentration of tin ions in the SnCl₄/EtOH film-forming system was 0.14 mol/l. The solution system was deposited on the glass substrate by carrying out a modified dipping method. Plasma treatment was performed at a pressure of 6.5 Pa and a power of about 20 Watts. The frequency of the oscillations produced by the generator was 27.12 ± 0.6 % MHz as well. The temperature of the samples during processing did not exceed 100 °C. As a result of the formation of tin oxide (II), the film transmittance decreased after treatment with oxygen plasma. The width of the electric forbidden zone of the obtained samples was calculated, which was 3.95 eV for glass and 3.79 eV for film. The resistance of the films was determined by 10 measurements on different parts of the samples. The film without processing has a resistance of about 4255 ± 1158 kΩ, after processing, the resistance decreased by 25 times and amounted to 167 ± 26 kΩ. A decrease in resistance indicates an increase in the concentration of charge carriers in the sample. The resulting SnO is a semiconductor that lowers the transmittance of the studied films and contributes to reducing their resistance. X-ray structural analysis of the samples was also performed. After processing in oxygen plasma, the intensity of reflection from the (110) plane have increased. It should be noted that the number of planes with (101) indexes has decreased. The study of the sample surface showed the destructive nature of three-minute exposure by oxygen plasma.

Keywords: thin films, SnO₂, sol-gel method, oxygen plasma treatment, transparency, structure, resistance, tin oxide (II).

Introduction

The study of tin oxide is associated with its multifunctional application. Tin dioxide belongs to a class of materials that combines high electrical conductivity with optical transparency and is therefore an important component for optoelectronic applications [1–3]. The lattice oxygen from the surface of the tin oxide is able to react chemically with the reagent and after the reaction to be renewed by the oxygen of the gas phase (mechanism of Mars – van Krevelen) [4]. This ability makes it possible to use SnO₂ as a catalyst for oxidative processes [5–7]. The change in the resistance of tin oxide in the presence of various gases formed the basis for use as a sensitive element in gas sensors [8–10].

Among the various methods used to improve the functional properties of metal oxide layers, plasma treatment is of particular interest [11–13]. Analysis of changes in the optical parameters and structural characteristics of tin dioxide after plasma treatment allows us to better understand the dynamics of changes in the physical properties of thin films of tin dioxide.

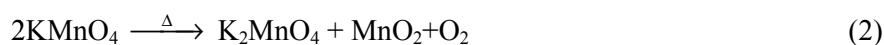
Experimental

To produce SnO₂ films, five-water tin tetrachloride was used as the initial reagent, and 97 % ethanol was used as the solvent. In tin tetrachloride systems, ethanol does not precipitate longer than in water-based systems. SnCl₄/EtOH film-forming systems with a tin ion concentration of 0.14 mol/l were prepared. Film-forming systems were applied to substrates (glass slides) by a modified dipping method. They were air-dried for 1–2 minutes and annealed on IKA C-MAG HP7 electric stoves at a temperature of 400°C in the air. In this case, tin tetrachloride interacts with water from the air to form tin hydroxide and hydrochloric acid. Hydrochloric acid and solvent are removed from the film-forming system when heated, and unstable Sn(OH)₄ decomposes to form water and the desired tin oxide by reaction [14, 15]:



12 layers were applied. The film thickness was determined by a microbalance [16] and amounted to $413 = 7$ nm.

Treatment of SnO₂ thin films in oxygen plasma was performed in a quartz tube. Oxygen was obtained by pyrolytic decomposition of potassium permanganate:



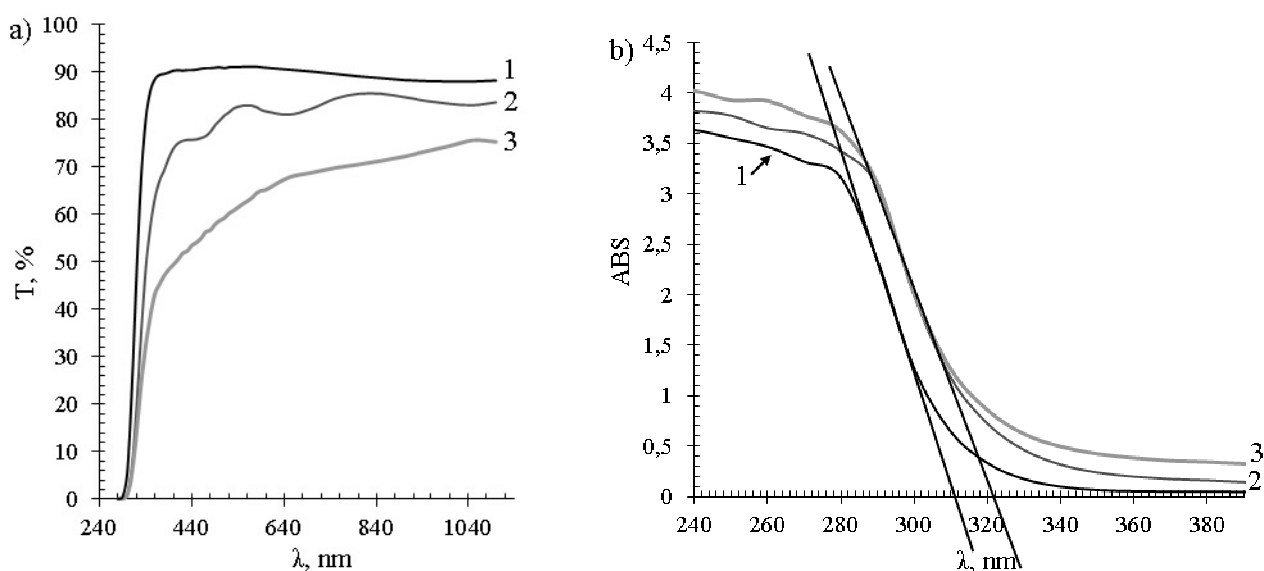
Plasma treatment was performed at a pressure of 6.5 Pa and a power of about 20 Watts. The frequency of the oscillations produced by the generator was 27.12 ± 0.6 % MHz as well. The temperature of the samples during processing did not exceed 100 °C. The processing time was 3 minutes.

Transmission and absorption spectra were measured using a UNICO SpectroQuest 2800 spectrophotometer. The structure of the films was studied using a scanning electron microscope JSM-6490LA, JEOL and an optical microscope MPE-11. To output data to a personal computer, a television camera for a vec-535 microscope was used. The composition of the films was determined using x-ray diffraction analysis on a DRON-6 diffractometer. The resistance of the films was determined using a UT70B multimeter. The distance between the contacts was 1 mm.

Results and Discussion

Optical property

Figure 1 shows the transmission and absorption spectra of tin oxide thin films before and after oxygen plasma treatment.



1 — glass substrate; 2 — film after application; 3 — film after plasma treatment

Figure 1. *a* — transmission spectra of films; *b* — absorption spectra of films

Figure 1*a* shows that after treatment with oxygen plasma (Fig. 1*a* curve 3) the film transmittance has decreased compared to the film transmittance without processing (Fig. 1*a* nodding 2). The decrease in the transmission coefficient may be caused by the formation of compounds that are opaque in the visible region of the spectrum [17, 18]. The formation of tin oxide (II) is most likely. The mechanism of formation of SnO in SnO₂ films under the influence of oxygen-rich plasma in a chemically active (ionized) form requires further development. One of the assumptions, according to the «activated complex theory», is the formation of a complex of ionized oxygen with film defects. The resulting complex can decay to form SnO + O₂ or supplement the crystal structure to stoichiometric SnO₂.

At the edge of the fundamental absorption (Fig. 1*b*) λ_{cr} were determined for the glass substrate and film before and after treatment with oxygen plasma. For the glass substrate $\lambda_{\text{cr}} = 311$ nm, for the film without processing and after processing, the edge of the fundamental absorption coincided and λ_{cr} was 322 nm. Using a well-known formula:

$$Eg = (hc)/\lambda_{cr},$$

where h is the Planck constant in eV; c is the speed of light, and λ_{cr} is the long-wave boundary of its own absorption.

The width of the electric forbidden zone of the glass — 3.95 eV and the film — 3.79 eV were calculated.

The resistance of the films

The resistance of the films was determined by 10 measurements on different parts of the samples. Student's coefficient for 10 measurements is equal to 2.262 with a reliability of 0.95. The error was calculated using the formula:

$$\Delta\bar{A} = t_{\gamma, n-1} \frac{\sqrt{\frac{\sum_{i=1}^n (A_i - \bar{A})^2}{n-1}}}{\sqrt{n}},$$

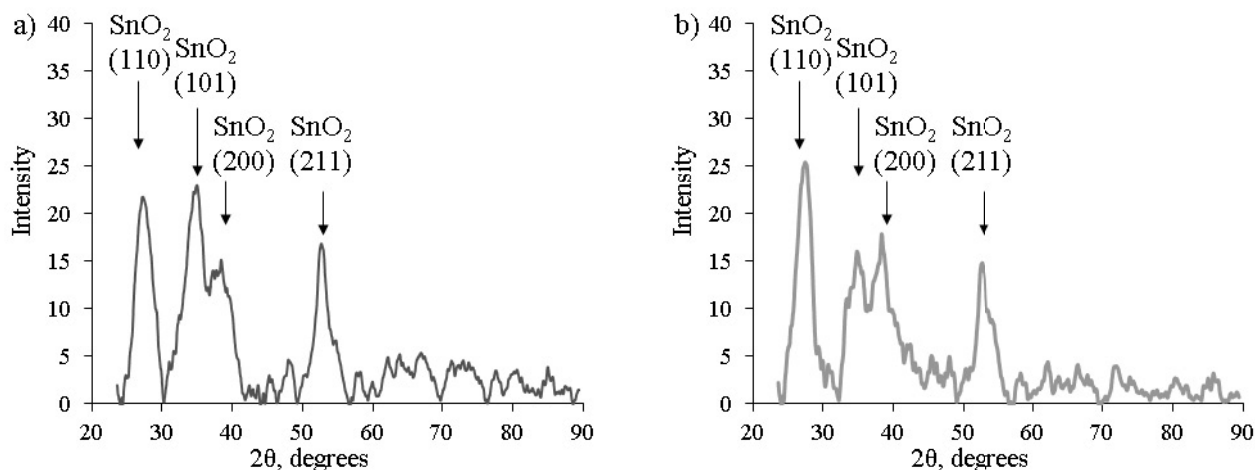
where $\Delta\bar{A}$ — is the absolute measurement error; $t_{\gamma, n-1}$ — is the Student's coefficient; A_i — is the value of the i -th measurement; \bar{A} — is the arithmetic mean; n — is the number of measurements.

Despite the fact that the width of the band gap of the film, calculated from the absorption spectra, did not change after processing, the resistance of the film significantly decreased. The film without processing has a resistance of 4255 ± 1158 k Ω , after processing, the resistance decreased by 25 times and amounted to 167 ± 26 k Ω .

The conductivity of tin dioxide is associated with the presence of intrinsic defects — oxygen vacancies that form small donor levels [19]. These levels can also be formed by impurities. A decrease in resistance indicates an increase in the concentration of charge carriers. The resulting SnO, which reduces the transmittance, is a semiconductor and can also contribute to reducing the resistance.

Diffraction analysis

The source signal from thin films on a glass substrate has a high noise level. Using the method of increasing the signal-to-noise ratio [20, 21], the following data were obtained and analyzed. Figure 2 shows the results of signal selection.



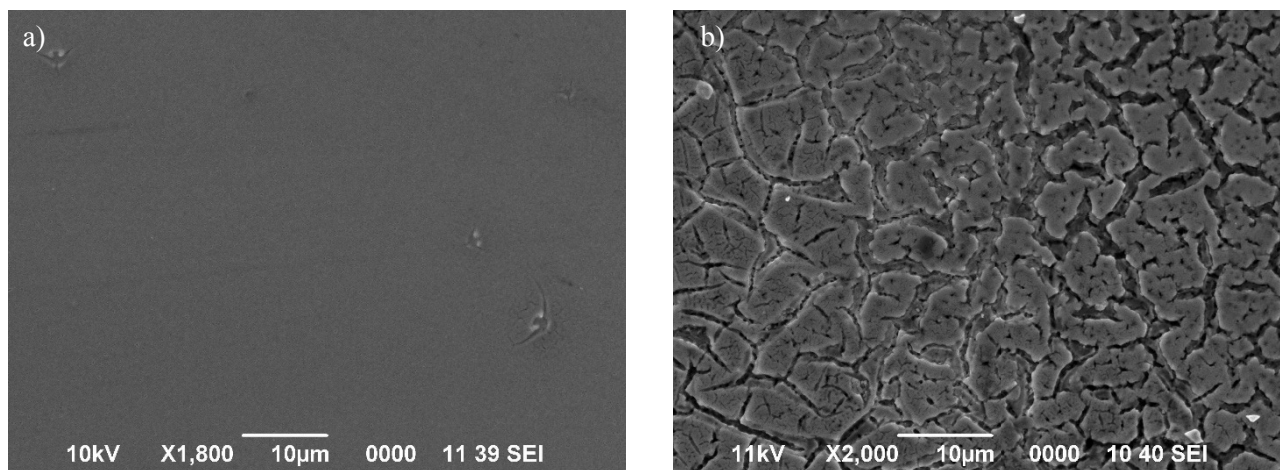
a — after application; *b* — after plasma treatment

Figure 2. X-ray diagram of tin oxide films

On X-ray diagrams (Fig. 2 *a, b*) peaks of reflections from the SnO₂ planes are observed. Peaks from other tin oxides are not observed. This indicates the absence of SnO in the crystalline form, and does not cancel the possibility of its existence in an amorphous state. It can be also noticed that the intensity of reflection from the (110) plane, after processing in oxygen plasma, increased. This indicates an increase in the number of planes with these Miller indexes. And the number of planes with indexes (101) has decreased. The destruction of crystallites along the planes (101) and (200) is associated with the transformation of the polycrystalline structure into a sub-nanometric cluster structure after plasma exposure [22, 23].

Surface structure

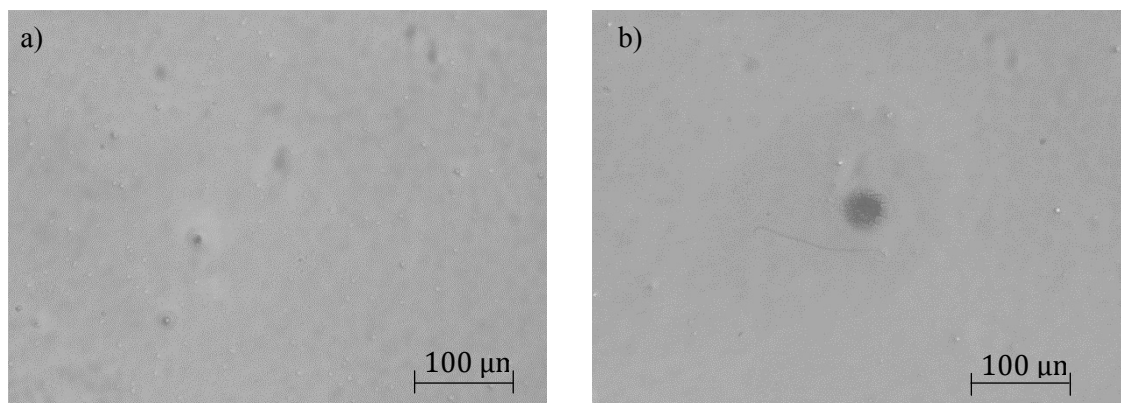
The surface structure depends on many parameters: the method of application, the concentration of the initial reagents, alloying impurities, etc. The dominant mechanism for the formation of spatial structures may be the phenomenon of self-organization [24]. Figure 3 shows images of the film surface after application and after plasma treatment.



a — after application; *b* — after plasma treatment

Figure 3. SEM images of the surface of tin oxide films

Figure 3*a* and *b* show that three-minute oxygen plasma treatment is destructive. The surface of the film was cracked. Figure 4 shows photos of the surface taken with an optical microscope with a smaller magnification.



a — after application; *b* — after plasma treatment

Figure 4. Surface of tin oxide films obtained using an optical microscope

Figure 4*a* shows that on the surface of the film after its application, there are rare, chaotically located hills — blisters [25]. They are formed by heating a wet gel. The reaction by-products and the solvent evaporate here. In places where the process of gelation has already begun, but evaporation has not yet occurred, the formation of blisters occurs. Figure 4*b* shows that the highest and most exposed blisters have darkened. Probably, in these places that SnO is formed, and it reduces the transparency of the films.

Conclusions

It was found that treatment of a glow discharge with a low-temperature plasma in an oxygen-rich atmosphere for three minutes leads to a decrease in the transparency of the films. Also, as a result of this ef-

fect, the resistance of the films is sharply reduced (by 25 times). There is a destructive effect of plasma in the destruction of SnO₂ crystallites and the appearance of cracks at the micron level on the surface of the film. An increase in the conductivity of the films indicates the formation of additional charge sources. The formation of tin oxide (II) clusters in the places of large and opened blisters was revealed.

The work was carried out with the financial support of the Ministry of Education and Science on the topic BR05236404.

References

- 1 Cui H.T. Electrically conductive TiO₂/indium tin oxide coated glass substrates with high visible light transparency prepared by an electrodeposition method / H.T. Cui, Z.Q. Zheng // *Thin solid films*. — 2019. — Vol. 691. — P. 137612–137618. DOI: 10.1016/j.tsf.2019.137612.
- 2 Mohammad T. Spray deposited indium doped tin oxide thin films for organic solar cell application / T. Mohammad, V. Kumar, V. Dutta // *Physica e-low-dimensional systems & nanostructures*. — 2020. — Vol. 117. — P. 113793–113799. DOI: 10.1016/j.physe.2019.113793.
- 3 Ozen Y. SnO₂ interlayer effects on the inverted polymer solar cells / Y. Ozen, I. Candan // *Chemical physics letters*. — 2020. — Vol. 740, Id. 137078. — P. 1–5. DOI: 10.1016/j.cplett.2019.137078.
- 4 Batzill M. The surface and materials science of tin oxide / M. Batzill, U. Diebold // *Progress in Surface Science*. — 2005. — Vol. 79. — P. 47–154. DOI: 10.1016/j.progsurf.2005.09.002.
- 5 Zhang R.Y. Function promotion of SO₄²⁻/Al₂O₃-SnO₂ catalyst for biodiesel production from sewage sludge / R.Y. Zhang, F.F. Zhu, Y. Dong, X.M. Wu, Y.H. Sun, D.R. Zhang, T. Zhang, M.L. Han // *Renewable energy*. — 2020. — Vol. 147. — P. 275–283. DOI: 10.1016/j.renene.2019.08.141.
- 6 Chen Z. Wavy SnO₂ catalyzed simultaneous reinforcement of carbon dioxide adsorption and activation towards electrochemical conversion of CO₂ to HCOOH / Z. Chen, T.T. Fan, Y.Q. Zhang, J. Xiao, M.R. Gao, N.Q. Duan et al. // *Applied catalysis b-environmental*. — 2020. — Vol. 261. — P. 118243–118249. DOI: 10.1016/j.apcatb.2019.118243.
- 7 Zhang B.H. Well-dispersed SnO₂ nanocrystals on N-doped carbon nanowires as efficient electrocatalysts for carbon dioxide reduction / B.H. Zhang, L.Z. Sun, Y.Q. Wang, S. Chen, J.T. Zhang // *Journal of energy chemistry*. — 2020. — Vol. 41. — P. 7–14. DOI: 10.1016/j.jechem.2019.04.022.
- 8 Grushevskaya E.A. Sensitivity to ethanol vapour of thin films SnO₂ doped with fluorine / E.A. Grushevskaya, S.A. Ibraimova, E.A. Dmitriyeva, I.A. Lebedev, K.A. Mit', D.M. Mukhamedshina, A.I. Fedosimova, A.S. Serikkanov, A.T. Temiraliyev // *Eurasian Chemico-Technological Journal*. — 2019. — Vol. 21. — P. 13–17. DOI: 10.18321/ectj781.
- 9 Dmitriyeva E.A. Doping of fluorine of tin dioxide films synthesized by sol-gel method / E.A. Dmitriyeva, D.M. Mukhamedshina, K.A. Mit', I.A. Lebedev, I.I. Girina, A.I. Fedosimova, E.A. Grushevskaya // *News of the National Academy of Sciences of the Republic of Kazakhstan (series of geology and technical sciences)*. — 2019. — Vol. 433. — P. 73–79. DOI: 10.32014/2019.2518–170X.9.
- 10 Manikandan V. A reliable chemiresistive sensor of nickel-doped tin oxide (Ni-SnO₂) for sensing carbon dioxide gas and humidity / V. Manikandan, I. Petrila, S. Vigneselvan, R.S. Mane, B. Vasile, R. Dharmavarapu, S. Lundgaard, S. Juodkazis, J. Chandrasekaran // *RSC advances*. — 2020. — Vol. 10, Iss. 7. — P. 3796–3804. DOI: 10.1039/c9ra09579a.
- 11 Somjaijaroen N. Simultaneous O-2 plasma and thermal treatment for improved surface conductivity of Cu-Doped SnO₂ films / N. Somjaijaroen, R. Sakdanuphab, N. Chanlek, P. Chirawatkul, A. Sakulkalavek // *Vacuum*. — 2019. — Vol. 166. — P. 212–217. DOI: 10.1016/j.vacuum.2019.05.017.
- 12 Stuckert E.P. Ar/O-2 and H₂O plasma surface modification of SnO₂ nanomaterials to increase surface oxidation / E.P. Stuckert, E.R. Fisher // *Sensors and actuators b-chemical*. — 2015. — Vol. 208. — P. 379–388. DOI: 10.1016/j.snb.2014.11.049.
- 13 Seo H.B. Effects of plasma treatment on the composition and phase changes of sputter-deposited SnO_x thin films / H.B. Seo, B.S. Bae, H.I. Bang, E.J. Yun // *Journal of nanoscience and nanotechnology*. — 2020. — Vol. 20, Iss. 1. — P. 197–205. DOI: 10.1166/jnn.2020.17225.
- 14 Neeraj K. Mishra. Structural and optical properties of SnO₂-Al₂O₃ nanocomposite synthesized via sol-gel route / Neeraj K. Mishra, Chaitanya Kumar, Amit Kumar, Manish Kumar, Pratibha Chaudhary, Rajeev Singh // *Materials Science-Poland*. — 2015. — Vol. 33, No. 4. — P. 714–718. DOI: 10.1515/msp-2015–0101.
- 15 Ярмонов А.Н. Получение оптически прозрачных токопроводящих покрытий термическим испарением / А.Н. Ярмонов, Д.Д. Ларионов, Р.Р. Яхиханов // *Изв. Самар. науч. центра РАН*. — 2015. — Т. 17, № 2(4). — С. 936–939.
- 16 Dmitriyeva E.A. The effect of NH₄F and NH₄OH on the structure and physical properties of thin SnO₂ films synthesized by the sol-gel method / E.A. Dmitriyeva, D.M. Mukhamedshina, N.B. Beisenkhanov, K.A. Mit' // *Glass Physics and Chemistry*. — 2014. — Vol. 40, No. 1. — P. 31–36. DOI: 10.1134/S1087659614010076.
- 17 Mukhamedshina D.M. Influence of plasma treatment on physical properties of thin SnO₂ films obtained from SnCl₄ solutions with additions of NH₄F and NH₄OH / D.M. Mukhamedshina, A.I. Fedosimova, E.A. Dmitriyeva, I.A. Lebedev, E.A. Grushevskaya, S.A. Ibraimova, K.A. Mit', A.S. Serikkanov // *Eurasian Chemico-Technological Journal*. — 2019. — Vol. 21. — P. 57–61.
- 18 Томпакова Н.М. Влияние трехминутной обработки водородной плазмой на структуру и свойства тонких пленок SnO₂ / Н.М. Томпакова, Е.А. Дмитриева, Е.А. Грушевская, И.А. Лебедев, А.С. Серикканов, Д.М. Мухамедшина, К.А. Мить // *Recent Contributions to Physics*. — 2019. — № 4(71). — С. 67–74. <https://doi.org/10.26577/RCPH-2019-i4-9>.
- 19 Kiliç C. Origins of coexistence of conductivity and transparency in SnO₂ / C. Kiliç, A. Zunger // *Physical Review Letters*. — 2002. — Vol. 88. — P. 1–4.

20 Грушевская Е.А. Способ увеличения отношения сигнал/шум в ЭПР спектроскопии / Е.А. Грушевская, Е.А. Дмитриева, И.А. Лебедев, Ю.А. Рябикин, А.Т. Темиралиев, А.И. Федосимова // Вестн. Казах. нац. ун-та. Сер. Физика. — 2018. — № 2(65). — С. 76–82.

21 Предварительный патент 12779. Казахстан. Способ увеличения отношения сигнал/шум в спектроскопии / Ю.А. Рябикин, И.А. Лебедев. — МПК G01N 24/00. 2001.

22 Mukhamedshina D.M. Influence of plasma treatments on the properties of SnO_x thin films / D.M. Mukhamedshina, N.B. Beisenkhanov, K.A. Mit', V.A. Botvin, I.V. Valitova, E.A. Dmitrieva // High Temperature Material Processes. — 2006. — Vol. 10. — P. 603–615. DOI: 10.1615/HighTempMatProc.v10.i4.110.

23 Mukhamedshina D.M. Influence of plasma treatments on the microstructure and electrophysical properties of SnO_x thin films synthesized by magnetron sputtering and sol-gel technique / D.M. Mukhamedshina, K.A. Mit', N.B. Beisenkhanov, E.A. Dmitrieva, I.V. Valitova // Journal of Materials Science-Materials in Electronics. — 2008. — Vol. 19. — P. 382–387. DOI: 10.1007/s10854-008-9695-0.

24 Fedosimova A.I. Modeling the process of formation of fractal structures in thin films / A.I. Fedosimova, E.A. Dmitrieva, I.A. Lebedev, A.T. Temiraliyev, M.E. Abishev, B.A. Baitimbetova, Yu.A. Ryabikin, A.S. Serikkanov // IOP Conf. Series: Journal of Physics: Conf. Series. — 2018. — Vol. 1141, Id. 012004. — P. 1–7. DOI: 10.1088/1742-6596/1141/1/012004.

25 Guo T. High temperature brittle film adhesion measured from annealing-induced circular blisters / T. Guo, J.Y. He, X.L. Pang, A.A. Volinsky, Y.J. Su, L.J. Qiao // Acta materialia. — 2017. — Vol. 138. — P.1–9. DOI: 10.1016/j.actamat.2017.07.026.

Е.А. Дмитриева, И.А. Лебедев, Е.А. Грушевская, Д.О. Мурзалинов,
А.С. Серикканов, Н.М. Томпакова, А.И. Федосимова, А.Т. Темиралиев

Оттегі плазмасының үш минуттық қалайы оксиді қабықшаларының қасиеттеріне әсері

Оттегі плазмасының үш минуттық қалайы оксиді қабықшаларының қасиеттеріне әсері зерттелген. Қабықшалар бес текті тетрахлорид қалайының ерітіндісінен золь-гель әдісімен алынған. $\text{SnCl}_4/\text{EtOH}$ қабықша түзуші жүйесіндегі қалайы иондарының концентрациясы 0,14 моль/л құрайды. Шыныдан жасалған төсенішке ерітінді батыру әдісімен жағылды. Плазма өңдеуі қысымы 6,5 Па және қуаттылығы 20 Ватт шамасында жүргізілген. Генератор жасайтын тербеліс жиілігі $27,12 \pm 0,6$ %-МГц-ді құрады. Өңдеу кезіндегі үлгілердің температурасы 100°C-тан артылмады. Оттегі плазмасымен өңдеуден кейін (II) валентті қалайы оксидінің пайда болуы салдарынан қабықшаның өткізу коэффициенті төмендеді. Алынған үлгілердің электрондық шекті зонасының аймағы есептелген, ол шыны төсеніш үшін — 3,95 эВ, қабықша үшін — 3,79 эВ. Қабықшалардың кедергісі үлгілердің 10 әртүрлі нүктелік аймағында өлшеніп, анықталған. Өңдеусіз қабықшаның кедергісі 4255 ± 1158 кОм-ға тең болады, өңдеуден кейін олардың кедергісі 25 есе азайды және шамасы 167 ± 26 кОм құрады. Кедергінің кемуі заряд тасымалдаушылардың концентрациясының ұлғаюын көрсеткен. Зерттеу барысында пайда болған SnO қабықшалардың өткізу коэффициентін төмендететін және олардың кедергісін азайтуға үлес қосатын жартылай өткізгіш болып табылады. Үлгілерге рентген талдауы да жүргізілген. Оттегі плазмасында өңдеуден кейін (110) жазықтықтан шағылысу интенсивтілігі артты. Бұл жерде (101) индексі бар жазықтар саны азайғанын да атап өту керек. Үлгілердің беттік зерттеуі оттегі плазмасының үш минуттық әсерінің деструктивті сипатын көрсеткен.

Кілт сөздер: жұқа қабықшалар, SnO_2 , золь-гель әдісі, оттегі плазмасымен өңдеу, мөлдірлік, қабықша құрылымы, кедергі, (II) валентті қалайы оксиді.

Е.А. Дмитриева, И.А. Лебедев, Е.А. Грушевская, Д.О. Мурзалинов,
А.С. Серикканов, Н.М. Томпакова, А.И. Федосимова, А.Т. Темиралиев

Влияние трехминутного воздействия кислородной плазмой на свойства пленок оксида олова

Исследовано влияние трехминутного воздействия кислородной плазмой на свойства пленок оксида олова. Пленки были получены золь-гель методом из пятиводного тетрахлорида олова. Концентрация ионов олова в пленкообразующей системе $\text{SnCl}_4/\text{EtOH}$ составляла 0,14 моль/л. Нанесение на стеклянную подложку проводилось модифицированным методом окунания. Обработка плазмой осуществлялась при давлении 6,5 Па и мощности около 20 Вт. Частота колебаний, создаваемых генератором, составляла $27,12 \text{ МГц} \pm 0,6$ %. Температура образцов при обработке не превышала 100 °С. Вследствие образования оксида олова (II) понизился коэффициент пропускания пленки после обработки кислородной плазмой. Рассчитана ширина запрещенной зоны полученных образцов, которая для стекла составила 3,95 эВ, для пленки — 3,79 эВ. Сопротивление пленок определялось по 10 измерениям на разных участках образцов. Пленка без обработки обладает сопротивлением 4255 ± 1158 кОм, после

обработки сопротивление уменьшилось в 25 раз и составило 167 ± 26 кОм. Уменьшение сопротивления указывает на увеличение концентрации носителей заряда. Образовавшийся SnO является полупроводником, который понижает коэффициент пропускания исследуемых пленок и вносит вклад в уменьшение их сопротивления. Проведен рентгеноструктурный анализ образцов. После обработки в кислородной плазме повысилась интенсивность отражения от плоскости (110). Следует отметить, что количество плоскостей с индексами (101) уменьшилось. Исследование поверхности образцов показало деструктивный характер трехминутного воздействия кислородной плазмой.

Ключевые слова: тонкие пленки, SnO₂, золь-гель метод, обработка кислородной плазмой, прозрачность, структура, сопротивление, оксид олова (II).

References

- 1 Cui, H.T., & Zheng, Z.Q. (2019). Electrically conductive TiO₂/indium tin oxide coated glass substrates with high visible light transparency prepared by an electrodeposition method. *Thin solid films*, 691, 137612–137618. DOI: 10.1016/j.tsf.2019.137612.
- 2 Mohammad, T., Kumar, V., & Dutta, V. (2020). Spray deposited indium doped tin oxide thin films for organic solar cell application. *Physica e-low-dimensional systems & nanostructures*, 117, 113793–113799. DOI: 10.1016/j.physe.2019.113793.
- 3 Ozen, Y., & Candan, I. (2020). SnO₂ interlayer effects on the inverted polymer solar cells. *Chemical physics letters*, 740, 137078, 1–5. DOI: 10.1016/j.cplett.2019.137078.
- 4 Batzill, M., & Diebold, U. (2005). The surface and materials science of tin oxide. *Progress in Surface Science*, 79, 47–154. DOI: 10.1016/j.progsurf.2005.09.002.
- 5 Zhang, R.Y., Zhu, F.F., Dong, Y., Wu, X.M., Sun, Y.H., Zhang, D.R., Zhang, T., & Han, M.L. (2020). Function promotion of SO₄²⁻/Al₂O₃-SnO₂ catalyst for biodiesel production from sewage sludge. *Renewable energy*, 147, 275–283. DOI: 10.1016/j.renene.2019.08.141.
- 6 Chen, Z., Fan, T.T., Zhang, Y.Q., Xiao, J., Gao, M.R., & Duan, N.Q., et al. (2020). Wavy SnO₂ catalyzed simultaneous reinforcement of carbon dioxide adsorption and activation towards electrochemical conversion of CO₂ to HCOOH. *Applied catalysis b-environmental*, 261, UNSP 118243–118249. DOI: 10.1016/j.apcatb.2019.118243.
- 7 Zhang, B.H., Sun, L.Z., Wang, Y.Q., Chen, S., & Zhang, J.T. (2020). Well-dispersed SnO₂ nanocrystals on N-doped carbon nanowires as efficient electrocatalysts for carbon dioxide reduction. *Journal of energy chemistry*, 41, 7–14. DOI: 10.1016/j.jechem.2019.04.022.
- 8 Grushevskaya, E.A., Ibraimova, S.A., Dmitriyeva, E.A., Lebedev, I.A., Mit', K.A., Mukhamedshina, D.M., & Fedosimova, A.I., et al. (2019). Sensitivity to ethanol vapour of thin films SnO₂ doped with fluorine. *Eurasian Chemical-Technological Journal*, 21, 13–17. DOI: 10.18321/ectj781.
- 9 Dmitriyeva, E.A., Mukhamedshina, D.M., Mit', K.A., Lebedev, I.A., Girina, I.I., Fedosimova, A.I., & Grushevskaya, E.A. (2019). Doping of fluorine of tin dioxide films synthesized by sol-gel method. *News of the National Academy of Sciences of the Republic of Kazakhstan (series of geology and technical sciences)*, 433, 73–79. DOI: 10.32014/2019.2518–170X.9.
- 10 Manikandan, V., Petriola, I., Vignesvelan, S., Mane, R.S., Vasile, B., Dharmavarapu, R., & Lundgaard, S., et al. (2020). A reliable chemiresistive sensor of nickel-doped tin oxide (Ni-SnO₂) for sensing carbon dioxide gas and humidity. *RSC advances*, 10(7), 3796–3804. DOI: 10.1039/c9ra09579a.
- 11 Somjaijaroen, N., Sakdanuphab, R., Chanlek, N., Chirawatkul, P., & Sakulkalavek, A. (2019). Simultaneous O-2 plasma and thermal treatment for improved surface conductivity of Cu-Doped SnO₂ films. *Vacuum*, 166, 212–217. DOI: 10.1016/j.vacuum.2019.05.017.
- 12 Stuckert, E.P., & Fisher, E.R. (2015). Ar/O-2 and H₂O plasma surface modification of SnO₂ nanomaterials to increase surface oxidation. *Sensors and actuators b-chemical*, 208, 379–388. DOI: 10.1016/j.snb.2014.11.049.
- 13 Seo, H.B., Bae, B.S., Bang, H.I., & Yun, E.J. (2020). Effects of plasma treatment on the composition and phase changes of sputter-deposited SnO_x thin films. *Journal of nanoscience and nanotechnology*, 20(1), 197–205. DOI: 10.1166/jnn.2020.17225.
- 14 Neeraj K. Mishra, Chaitanya Kumar, Amit Kumar, Manish Kumar, Pratibha Chaudhary & Rajeev Singh. (2015). Structural and optical properties of SnO₂-Al₂O₃ nanocomposite synthesized via sol-gel route. *Materials Science-Poland*, 33(4), 714–718. DOI: 10.1515/msp-2015-0101.
- 15 Yarmonov, A.N., Larionov, D.D., & Yakhikhanov, R.R. (2015). Poluchenie opticheski prozrachnykh tokoprovodiashchikh pokrytii termicheskim isparenem [Obtaining optically transparent conductive coatings by thermal evaporation]. *Izvestiia Samarskoho nauchnogo tsentra Rossiiskoi akademii nauk — Proceedings of the Samara scientific center of the Russian Academy of Sciences*, 17, 2(4), 936–939 [in Russian].
- 16 Dmitriyeva, E.A., Mukhamedshina, D.M., Beisenkhanov, N.B., & Mit', K.A. (2014). The effect of NH₄F and NH₄OH on the structure and physical properties of thin SnO₂ films synthesized by the sol-gel method. *Glass Physics and Chemistry*, 40(1), 31–36. DOI: 10.1134/S1087659614010076.
- 17 Mukhamedshina, D.M., Fedosimova, A.I., Dmitriyeva, E.A., Lebedev, I.A., Grushevskaya, E.A., Ibraimova, S.A., & Mit', K.A., et al. (2019). Influence of plasma treatment on physical properties of thin SnO₂ films obtained from SnCl₄ solutions with additions of NH₄F and NH₄OH. *Eurasian Chemical-Technological Journal*, 21, 57–61.
- 18 Tompakova, N.M., Dmitriyeva, E.A., Grushevskaya, E.A., Lebedev, I.A., Serikkanov, A.S., Mukhamedshina, D.M., & Mit', K.A. (2019). Vliianie trekhminutnoi obrabotki vodorodnoi plazmoi na strukturu i svoistva tonkikh plenok SnO₂ [The effect of a three-minute treatment with hydrogen plasma on the structure and properties of thin SnO₂ films]. *Recent Contributions to Physics*, 4(71), 67–74. <https://doi.org/10.26577/RCPH-2019-i4-9> [in Russian].
- 19 Kiliç, C., & Zunger, A. (2002). Origins of coexistence of conductivity and transparency in SnO₂. *Physical Review Letters*, 88, 1–4.

- 20 Grushevskaya, E.A., Dmitriyeva, E.A., Lebedev, I.A., Ryabikin, Yu.A., Temiraliyev, A.T. & Fedosimova, A.I. (2018). Sposob uvelicheniia otnosheniia signal/shum v EPR spektroskopii [The way to increase the signal-to-noise ratio in EPR spectroscopy]. *Vestnik Kazakhskoho natsionalnoho universiteta. Seriya Fizika — Bulletin of Kazakh National University. Physics series*, 2(65), 76–82 [in Russian].
- 21 Riabikin, Yu.A., & Lebedev, I.A. (2001). Sposob uvelicheniia otnosheniia signal/shum v spektroskopii [Method for increasing signal-to-noise ratio in spectroscopy]. *Preliminary patent No. 12779. MPK G01N 24/00*. Kazakhstan [in Russian].
- 22 Mukhamedshina, D.M., Beisenkhanov, N.B., Mit', K.A., Botvin, V.A., Valitova, I.V., & Dmitrieva, E.A. (2006). Influence of plasma treatments on the properties of SnO_x thin films. *High Temperature Material Processes*, 10, 603–615. DOI: 10.1615/HighTempMatProc.v10.i4.110.
- 23 Mukhamedshina, D.M., Mit', K.A., Beisenkhanov, N.B., Dmitriyeva, E.A., & Valitova I.V. (2008). Influence of plasma treatments on the microstructure and electrophysical properties of SnO_x thin films synthesized by magnetron sputtering and sol-gel technique. *Journal of Materials Science-Materials in Electronics*, 19, 382–387. DOI: 10.1007/s10854-008-9695-0.
- 24 Fedosimova, A.I., Dmitrieva, E.A., Lebedev, I.A., Temiraliyev, A.T., Temiraliyev, A.T., Abishev, M.E., & Baitimbetova, B.A., et al. (2018). Modeling the process of formation of fractal structures in thin films. *IOP Conf. Series: Journal of Physics: Conf. Series*, 1141, 012004, 1–7. DOI: 10.1088/1742-6596/1141/1/012004.
- 25 Guo, T., He, J.Y., Pang, X.L., Volinsky, A.A., Su, Y.J., & Qiao, L.J. (2017). High temperature brittle film adhesion measured from annealing-induced circular blisters. *Acta materialia*, 138, 1–9. DOI: 10.1016/j.actamat.2017.07.026.

Y.V. Borodin^{1*}, K.V. Sysolov¹, V.R. Rande¹, G.V. Vavilova¹, O. Stary²¹Tomsk Polytechnic University, Russia;²Czech Technical University in Prague, Czech Republic

(*E-mail: uryborodin@tpu.ru)

Spectroscopy of nanoscale crystalline structural elements

The study of structural elements, nanoparticles, microblocks and other nanoscale objects was an important part of the study of crystals non-equilibrium properties. The behavior of nanoscale structures allows us to judge the dynamics of the crystal lattice during doping, deformation, and interactions with radiation. Along with x-ray and electron microscopic studies, optical methods for determining the size of nanoscale objects, the energy of their electrons, and the symmetry of electronic States are increasingly being used. Among nanoscale objects, proton-separated structural elements (PSE) attract special attention in connection with the development of crystal structure block-hierarchical (BH) model. In this paper, we consider the possibility of calculating the size of PSE crystals in a model of quantum-dimensional structures. According to this model except values of the crystal potential in PSE, you should consider the area of high electron density, the existence of which is beyond the scope of conventional theory. Experimental data allow us to determine the position of this zone as localized around the atomic core of the PSE. Note that the atomic backbone generally coincides with the unit cell, that is, it consists of the same number of atoms and has the same point symmetry group.

Keywords: nanoparticles, microblocks, nanoscale structural elements, proton-separated structural elements.

Introduction

The solution of the Schrodinger equation is quite difficult to obtain for arbitrary functions of the crystal potential and the potential of the zone of increased electron density $U(r)$ and $V(r)$. We can use the spherical approximation and assume that the function $V(r)$ is spherically symmetric inside the sphere of radius R surrounding the atoms. A similar approach takes place in the theory of a solid body as the method of attached plane waves (APW) [1]. Within a unit cell, the eigenfunction $\psi(k, r)$ corresponding to the energy $E(k)$ can be represented as a series

$$\psi(k, r) = \sum_{l=0}^{\infty} \sum_{m=-l}^l C_{lm}(k) \cdot Y_{lm}(\theta, \varphi) \cdot R_l(E, r) \cdot \eta(R-r) + \sum_j b_j(k) \cdot \exp[i \cdot k_j \cdot r] \cdot \eta(r-R),$$

where r, θ, φ are the polar coordinates of the radius vector r relative to the center of the PSE, $\eta(x)$ is a step function

$$\eta(x) = \begin{cases} 0, & x < 0; \\ 1, & x > 0. \end{cases}$$

The main difference between the approach considered in this paper and the PPV is that there is no translational symmetry of quantum-dimensional structures [2–9]. We have the standard problem of an atom located in a spherically symmetric quantum well [1]. The wave function will take the form: $\psi_{lm} = R_l(r) \cdot Y_{lm}(\theta, \varphi)$. The Schrodinger equation describing the stationary States of an electron with energy E has the form

$$\frac{\hbar^2}{2m} \cdot \Delta \psi + (E - V(r)) \cdot \psi = 0.$$

The equation for the radial component will look like this:

$$R_l'' + \frac{2}{r} \cdot R_l' + \left[k^2 - \frac{l(l+1)}{r^2} \right] \cdot R_l = 0, \quad (1)$$

where $k^2 = \frac{2mE}{\hbar^2}$.

The absorption spectra of the structural elements

The model under consideration, according to experimental data, assumes the value of the potential of the zone of increased electron density, which is sufficiently large in comparison with the crystal potential. Equation (1) is written in the infinite potential approximation. The function $R_l(E, r)$ can be defined by numerically integrating a differential equation in the domain under consideration for a series of values E and l . Using substitution, equation (1) can be reduced to the form

$$\chi_k'' + \frac{2(l+1)}{r} \chi_l' + k^2 \chi_l = 0. \quad (2)$$

Differentiating equation (2) by r , we get

$$\chi_l''' + \frac{2(l+1)}{r} \chi_l'' + \left[k^2 - \frac{2(l-1)}{r^2} \right] \chi_l' = 0. \quad (3)$$

By substituting $\chi_l' = r\chi_{l+1}$ (3), it is reduced to the form

$$\chi_{l+1}'' + \frac{2(l+2)}{r} \chi_{l+1}' + k^2 \chi_{l+1} = 0,$$

coincides with the one that the function must satisfy χ_{l+1} . Thus, successive functions are related by the relation

$$\chi_{l+1} = \frac{1}{r} \chi_l'; \quad \chi_l = \left(\frac{1}{r} \frac{d}{dr} \right)^l \chi_0.$$

Finally we find the following expression for radial functions

$$R_l = 2k \cdot j_l(r),$$

where $j(r)$ are spherical Bessel functions.

The electron energy $E_{n,l}$ is defined by the expression under the condition

$$J_{l+1/2}(kR) = 0. \quad (4)$$

Numerically solving equation (4), a set of k values is obtained and the band spectrum is determined. The final expression for the electron energy has the form

$$E_{n,l} = \frac{\hbar^2}{2mR^2} x_{n,l}^2,$$

where $x_{n,l}$ are the constants found from equation (4) that characterize the electron energy levels in a crystal with indices n, l [10].

Having a band spectrum, we find the allowed transitions between energy levels. Let's define the selection rules for absorption in the crystal. The symmetry of the crystal is important. When calculating the selection rules for a specific crystalline substance, it is necessary to determine the point symmetry group G of the unit cell (the same symmetry group will be inherent in the PSE). We find the decomposition of the representation of this group by irreducible representations:

$$T = \sum_v a_v T^{(v)}$$

The probability of a transition between energy States and is determined by the square of the matrix element $\psi_i H_{VZ} \psi_0$ of the H_{VZ} operator of the interaction of radiation with matter. If executed

$$\psi_i H_{VZ} \psi_0 = 0, \quad (5)$$

then the system cannot go from state ψ_i to ψ_j by emitting or absorbing a quantum of light. On the other hand, the functions ψ_i and ψ_j can be considered as elements of some linear spaces L_i and L_j , which are transformed by representations T_i and T_j of the group G of the point symmetry of the crystal. As a result, the left side of equation (5) is transformed by the action of the elements G in the representation $\tilde{T}_i \times V \times T_j$. Here the H_{VZ} operator is transformed by the vector representation V of group G . If the representation $\tilde{T}_i \times V \times T_j$ does not contain a single representation, then the matrix element in (5) is zero and the transition $\psi_i \rightarrow \psi_j$ in the considered approximation is forbidden. The representation $\tilde{T}_i \times V \times T_j$ must contain a single

representation, and this requires that the product $V \times T_j$ contains at least one representation included in T_i [11]. Then the selection rules in the crystal for light absorption PSE and PSE blocks are reduced to the following criterion

$$V \times T_j \cap T_i \neq 0. \quad (14)$$

Taking into account the selection rules, we get a finite number of absorption lines in the crystal on the PSE, and the number of electrons at the level with the index l is equal to $(2l+1)2$. You can also solve the inverse problem, that is, calculate the size of the PSE from a given absorption spectrum.

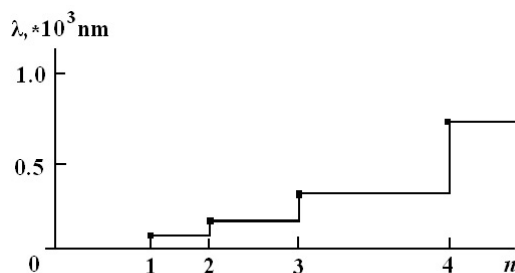


Figure 1. Dependence of the absorption wavelength of PSE blocks on the step of a series of numbers in the Fibonacci series

This approach can be applied in some approximation to PSE blocks. There will be a difference in the determination of the electronic density of the PSE block. It can be assumed that in this process, the determining value is the conduction electrons of the crystal. Changes in the structure of a block's potential are made by its point symmetry relative to lower-order blocks. As can be seen from the expression for determining the proper energy of an electron in a PSE, its energy spectrum depends on the size. Given the correspondence of the PSE size to a number of Fibonacci numbers, it is possible to predict the absorption spectrum of PSE blocks based on the specified PSE characteristics. Figure 1 shows the dependence of the absorption wavelength of a crystal on a structural element on the number of the Fibonacci series. The calculation method discussed above provides sufficient accuracy for qualitative consideration of the spectrum.

The decrease of the electron density in the zones surrounding the PSE blocks is experimentally established, and the block structure is modulated in the crystal space with an increase in their size. This is observed until the value of the potential barrier of the zone of increased electron density of the next block becomes equal to the crystal potential considered in the solid state theory. This imposes a condition of finiteness of the modulation order and its critical value is different for different materials due to the difference in the overall potential picture of the crystal lattice.

In the method of calculating the parameters of the PSE, significant approximations were made: the one-electron theory was used, which replaced the interaction of the crystal's electrons with a certain effective field, the zone of increased electron density had a spherical symmetry relative to the center of the PSE, and the value of the potential barrier rushed to infinity. Despite the above-mentioned approximations, there is a sufficient agreement between the calculated PSE sizes and experimental data from X -ray diffraction and absorption spectra at the f-centers of crystal color [12]. In this case, the F-center performed the function of the PSE, and the feature of localization of an electron from an anionic vacancy on a cationic environment satisfies the formalism of the considered quantum-dimensional model of the crystal. The sizes of F-centers for a number of alkali metal halides are estimated using known absorption lines. The considered model of the F-center likens it to a block of a crystal. Satisfactory results are obtained when the potential of the F-center is approximated by the rectangular well function. The choice of F-centers as the PSE model is quite justified, since the crystals of alkali metal halides have a high symmetry, and therefore, the distribution of the uncompensated positive charge of cations surrounding the anionic vacancy is close to spherical.

Oscillatory Raman spectra of structural elements

The method of studying the quantum-dimensional structure of a material based on light absorption is generally simple. Solving the absorption problem, it is possible to obtain its band spectrum and other characteristics obtained in the previous section. However, this method does not allow us to study the dynamics of the lattice, both translational and quantum-dimensional, modulated, considered by the model in this work.

The method associated with Raman scattering of light on the microblocks we are considering actually displays the properties of a modulated low-dimensional lattice and allows us to calculate its vibrational States. Here, the symmetry of the crystal plays a crucial role and determines the matrix elements that are different from zero.

We solve the vibrational problem and assume that the PSE vibrational movements occur in the crystal space, similar to the vibrations of atoms in the translational model of a crystal. The vibrational motion of the atomic core is considered as a collective vibrational process. Formally, this can be represented as a system of 3-dimensional oscillating oscillators with dimensions equal to the PSE and some effective masses. It is quite difficult to solve such a 3-dimensional case of the problem, since, according to the quantum-dimensional model, the distances between oscillating oscillators are not the same. It is necessary to simplify the problem to the one-dimensional case, provided that the process of linearization of the crystal lattice preserves some of its properties unchanged and does not significantly affect the values of those characteristics that need to be studied in this work. The problem is reduced to the study of the characteristics of a one-dimensional aperiodic chain of oscillating oscillators. The chain through some transformations can be described by the Fibonacci sequence, which is a special case of aperiodic sequences. Then the one-dimensional Fibonacci chain will preserve some properties of the crystal in 2- and 3-dimensional lattices [13]. This may be the property of self-similarity, which is a fairly important characteristic of any Fibonacci sequences [1].

Let all PSE in a linear chain oscillate near the equilibrium position with an offset $U\left(\begin{smallmatrix} l \\ \alpha \end{smallmatrix}\right)$. Here α is the PSE number in the chain, and l is the coordinate of the center of each PSE. Then the Hamilton and Lagrange functions of the system in the harmonic approximation have the form

$$H = T + \Phi = \frac{1}{2} \sum_{l, \alpha} m_{\alpha} \left[\dot{u}\left(\begin{smallmatrix} l \\ \alpha \end{smallmatrix}\right) \right]^2 + \frac{1}{2} \sum_{\substack{l, l' \\ \alpha, \alpha'}} \Phi\left(\begin{smallmatrix} ll' \\ \alpha\alpha' \end{smallmatrix}\right) \cdot u\left(\begin{smallmatrix} l \\ \alpha \end{smallmatrix}\right) \cdot u\left(\begin{smallmatrix} l' \\ \alpha' \end{smallmatrix}\right);$$

$$L = T - \Phi = \frac{1}{2} \sum_{l, \alpha} m_{\alpha} \left[\dot{u}\left(\begin{smallmatrix} l \\ \alpha \end{smallmatrix}\right) \right]^2 - \frac{1}{2} \sum_{\substack{l, l' \\ \alpha, \alpha'}} \Phi\left(\begin{smallmatrix} ll' \\ \alpha\alpha' \end{smallmatrix}\right) \cdot u\left(\begin{smallmatrix} l \\ \alpha \end{smallmatrix}\right) \cdot u\left(\begin{smallmatrix} l' \\ \alpha' \end{smallmatrix}\right).$$

Here m_{α} — the effective mass of the PSE with the number α , $\Phi\left(\begin{smallmatrix} ll' \\ \alpha\alpha' \end{smallmatrix}\right)$ — the coefficients of the second order in the decomposition of potential energy by deviations of the PSE.

The equations of motion respectively have the form

$$m_{\alpha} \ddot{u}\left(\begin{smallmatrix} l \\ \alpha \end{smallmatrix}\right) + \sum_{l'} \Phi\left(\begin{smallmatrix} ll' \\ \alpha\alpha' \end{smallmatrix}\right) \cdot u\left(\begin{smallmatrix} l' \\ \alpha' \end{smallmatrix}\right) = 0. \quad (6)$$

Solutions of equation (6) have the form

$$u\left(\begin{smallmatrix} l \\ \alpha \end{smallmatrix}\right) = u^0\left(\begin{smallmatrix} l \\ \alpha \end{smallmatrix}\right) \cdot e^{-i\omega t}. \quad (7)$$

After substituting (7) in (6), we get

$$\sum_{l'} \left[\Phi\left(\begin{smallmatrix} ll' \\ \alpha\alpha' \end{smallmatrix}\right) - w^2 m_{\alpha'} \delta_{\alpha\alpha'} \delta_{ll'} \right] \cdot u^0\left(\begin{smallmatrix} l' \\ \alpha' \end{smallmatrix}\right) = 0. \quad (8)$$

The solvability condition of the system (8) is that the determinant is equal to zero

$$\left(\Phi\left(\begin{smallmatrix} ll' \\ \alpha\alpha' \end{smallmatrix}\right) - w^2 m_{\alpha'} \delta_{\alpha\alpha'} \right) = 0. \quad (9)$$

Equation (9) is an algebraic equation of degree N with respect to w^2 . Denote the eigenvectors of the system (8) $l(\alpha(j))$ and the corresponding eigenvalues $w^2(j)$. Making the transition to normal coordinates

$$u_{\alpha}\left(\begin{smallmatrix} l \\ \alpha \end{smallmatrix}\right) = \sum_j l_{\alpha}(\alpha(j)) \cdot Q(j).$$

The Hamilton function takes the following form

$$H = \frac{1}{2} \sum_j (\dot{Q}^*(j) \cdot \dot{Q}(j) + w^2(j) \cdot Q^*(j) \cdot Q(j)).$$

From here we get the equation of motion for the PSE

$$\ddot{Q}(j) + w^2(j) \cdot Q(j) = 0.$$

Normal coordinates are complex. You can go to the coordinates $q(j)$, which results in the Hamilton function being reduced to the form

$$H = \frac{1}{2} \sum_j [p^2(j) + w^2 q^2(j)],$$

where $p(j) = \dot{q}(j)$ and the variables $p(j)$ $q(j)$ and are real.

We pass to the quantum case, in which these quantities are considered as operators

$$\hat{p}(j) = -i\hbar \frac{\partial}{\partial q(j)} \quad \hat{q}(j) = q(j).$$

In this case, the Schrodinger equation has the form

$$\frac{1}{2} \sum_j \left\{ -\hbar^2 \frac{\partial}{\partial q(j)} + w^2(j) \cdot q^2(j) \right\} \Psi = E \Psi. \quad (10)$$

The solution of equation (10) is well known and is written as

$$\Psi = \prod_j \Psi_m(j) \cdot [q(j)],$$

where is the vibrational quantum number of the oscillator with index j . Each of these functions satisfies the equation

$$\left\{ -\frac{\hbar^2}{2} \cdot \frac{\partial^2}{\partial q^2(j)} + \frac{1}{2} \cdot w^2 \cdot q^2(j) \right\} \Psi_m = E_m \cdot \Psi_m. \quad (11)$$

The total energy E of a crystal in the state described by the numbers is

$$E = \sum_j E_{m(j)}.$$

Solutions of such an equation as (11) are well known [14]

$$\Psi_m(q) = \left(\frac{\beta}{\pi^{\frac{1}{2}} \cdot 2^n \cdot m} \right)^{1/2} \cdot \exp\left(-\frac{1}{2} \cdot \beta^2 q^2\right) \cdot H_m(\beta q), \quad (12)$$

where $\beta^2 = \frac{1}{\hbar} \cdot w^2(j)$, $H_m(x)$ is a Hermite polynomial of order m .

The corresponding energy levels are determined by the formula

$$E_m = \left[m(j) + \frac{1}{2} \right] \cdot \hbar w(j).$$

Having determined a fairly General solution to this oscillatory problem, it is necessary to proceed to the consideration of Raman scattering of light on the discussed PSE. We introduce the intensity of light scattering in a single solid angle I , which is proportional to the transition probability:

$$I_{\lambda\lambda\lambda\lambda'} = \sum_n (n (P_{\lambda\lambda'} (\bar{n} (\bar{n} (P_{\lambda\lambda'} (n (\delta(\Delta w - w_{n\bar{n}})). \quad (13)$$

Here $(n = (\chi_{0n}$ are the initial and $(\bar{n} = (\chi_{0\bar{n}}$ final vibrational States. Expression (13) corresponds to the case of a temperature equal to zero. To generalize to the case $T \neq 0$, we should include in (13) the temperature averaging over the initial States. Assuming further that the energy change during scattering is equal to Δw is fixed, we write a generalized expression for the scattering tensor [15]:

$$I_{\lambda\lambda\lambda\lambda'}(\Delta w, T) = \frac{1}{Z} \sum_{n\bar{n}} (n (P_{\lambda\lambda'} (\bar{n} (\bar{n} (P_{\lambda\lambda'} (n (e^{-\beta E_n} \cdot \delta(\Delta w - w_{n\bar{n}}), \quad (14)$$

where $\beta = (k \cdot T)^{-1}$, $Z = \sum_n e^{-\beta E_n}$.

Expression (14) can be represented in terms of the spectral density of the green temperature function by rewriting the matrix elements of the polarizability operator in the framework of secondary quantization. After that, the expression for intensity can be written using the green function or its Fourier components [15]. We can limit ourselves to a simple calculation of matrix elements with a known expression (12) for the wave function of oscillating PSE. Thus, knowing the matrix elements of the polarizability operator, it is easy to calculate the matrix elements of the form $\langle n | P_{\lambda\lambda'} | \bar{n} \rangle$ and find values for the intensity of Raman scattering of light on the PSE for a specific vibrational transition.

In addition to this method of calculating the intensity of Raman scattering of light on structures, another method can be used, which is somewhat different from this [13]. By finding the equation of motion for the green function, one can obtain a system of linear non-uniform equations that is sufficiently easy to solve. This method allows you to calculate the elements of the series that the intensity is decomposed into.

Recently, it is common to refer aperiodic structures to structures that are in accordance with the Fibonacci series. We obtain solutions that allow us to judge the structure of any aperiodic lattice. In [13], we obtained a ratio for Raman scattering frequencies that corresponded to the numbers of the Fibonacci series. Intensity peaks were detected in the acoustic region with frequencies: $w_1=13.4$, $w_2=21.7$, $w_3=35.0$ and $w_4=56.7 \text{ cm}^{-1}$. It is not difficult to notice that $w_2/w_1=w_3/w_2=w_4/w_3= \frac{\sqrt{5}+1}{2}$ is the number of the Golden section, that is, with some accuracy, the frequencies obtained both from the calculation and from the experiment are multiples of the corresponding Fibonacci numbers. The superatomic lattice of the studied sample was dimensionally quantized by the numbers of this series. The obtained result of this work gives grounds to assert that the vibrational Raman spectra represent direct information about the structure of the superatomic lattice.

Conclusion

Two methods for calculating the parameters of a block modulated lattice are considered. Despite the approximations, the methods allow us to reveal a qualitative picture of the electronic crystal in some cases, the theory and experiment give a satisfactory match. In other cases, such approximations are crude and insufficient to obtain accurate values of the spectral characteristics of a quantum-dimensional lattice. To get a more accurate picture, several significant amendments should be included in the consideration of both tasks. In the method based on the light absorption spectra of the BH structure, it is necessary to take into account the presence of wave functions outside the PSE. The symmetry of the PSE makes a significant contribution to the solution, and in the future it is possible to abandon the spherical symmetry of its potential. Taking these amendments into account is the next step in this task. In the method based on the vibrational Raman spectra of light by the microblock structure of the crystal, it is possible to further consider the 3-dimensional case. Currently, issues related to quantization of the crystal structure are widely considered. A significant interest is the study of the properties of such crystal lattices based on pre-known models of the crystal at a level other than the atomic one.

References

- 1 Бассани Ф. Электронные состояния и оптические переходы в твердых телах / Ф. Бассани, Дж. Пастори Парравичини. — М.: Наука, 1982. — 391 с.
- 2 Borodin Y.V. Research of nanocomposite structure of boron nitride at proton radiation / Y.V. Borodin, D.S. Ermolaev, V. Pak, K. Zhang // IOP Conference Series: Materials Science and Engineering. — 2016. — Vol. 110. — 4 p. DOI: 10.1088/1757-899X/110/1/012072.
- 3 Tsu R. Passivation defects in polycrystalline superlattices and quantum well structures / R. Tsu, E.H. Nicollian, A. Reisman // Appl. Phys. Lett. — 1989. — Vol. 55, No. 18. — P. 1897–1899.
- 4 Borodin Y.V. The formation of nanocomposition structure in crystals / Y.V. Borodin and A.N. Sergeev // Proceedings of the 3rd International Forum on Strategic Technology, IFOST. — 2008. — P. 174–176.
- 5 Yurov V.M. Study of dimensional dependencies of thermodynamic characteristics of nanoparticles / V.M. Yurov, V.V. Arkhipov, G.A. Ranova, V.Ch. Laurinas // Bulletin of the University of Karaganda – Physics. — 2019. — No. 2(94). — P. 35–41. DOI: 10.31489/2019Ph2/35–41.
- 6 Yurov V.M. Structural phase transition in surface layer of metals / V.M. Yurov, S.A. Guchenko, V.Ch. Laurinas, O.N. Zavatskaya // Bulletin of the University of Karaganda – Physics. — 2019. — No. 1(93). — P. 50–60. DOI 10.31489/2019Ph1/50–60.

- 7 Vereshchagin, V.I. Boron nitride with packets of nanotubes for microcomposite ceramics / V.I. Vereshchagin, M.A. Sergeev, B.S. Semukhin, Yu.V. Borodin // *Refractories and Industrial Ceramics*. — 2000. — Vol. 41, No. 11–12. — P. 440–443.
- 8 Каули Дж. Физика дифракции / Дж. Каули. — М.: Мир, 1979. — 431 p.
- 9 Borodin Y.V. Low-temperature nanodoping of protonated LiNbO_3 crystals by univalent ions / Y.V. Borodin // *Technical Physics*. — 2015. — Vol. 60. — P. 107–111.
- 10 Флюгге З. Задачи по квантовой механике. — Т. 1 / З. Флюгге. — М.: Мир, 1974. — 286 с.
- 11 Любарский Г.Я. Теория групп и ее применение в физике / Г.Я. Любарский. — М.: Наука, 1958. — 354 с.
- 12 Локтюшин А.А. Оптические спектры электронных центров окраски / А.А. Локтюшин. — Томск, 1983. — 9 с. Рукоп. деп. в ВИНТИ 12 июля 1983 г., № 4328–83.
- 13 Wang Chumin. Theory of the Raman Response in Fibonacci Superlattices / Chumin Wang, R.A. Barrio // *Phys. Rev. B*. — 1988. — Vol. 61. — P. 191.
- 14 Сушинский М.М. Спектры комбинационного рассеяния молекул и кристаллов / М.М. Сушинский. — М.: Наука, 1969. — 576 с.
- 15 Бирман Дж. Пространственная симметрия и оптические свойства твердых тел / Дж. Бирман. — М.: Наука, 1978. — Т. 2. — 352 с.

Ю.В. Бородин, К.В. Сысолов, В.Р. Ранде, Г.В. Вавилова, О. Стары

Наноөлшемді кристалды құрылымдық элементтердің спектроскопиясы

Құрылымдық элементтерді, нанобөлшектерді, микроблоктарды және басқа да наноөлшемді объектілерді зерттеу кристалдардың тепе-тең емес қасиеттерін зерттеудің маңызды бөлігі. Наноөлшемді құрылымдардың тәртібі қоспалау, деформация және сәулемен өзара әрекеттесуде кристалды торлардың динамикасын бағалауға мүмкіндік береді. Рентгендік және электронды-микроскопиялық зерттеулермен қатар наноөлшемді объектілердің өлшемдерін, олардың электрондарының энергиясын және электрондық күйдің симметриясын анықтаудың оптикалық әдістері кеңінен қолданылады. Наноөлшемді объектілер арасында кристалды құрылымның блоктық-иерархиялық (БИ) моделін әзірлеуге байланысты протон-бөлінген құрылымдық элементтер (ПҚЭ) ерекше назар аударылады. Мақалада кванттық-өлшемді құрылымдар моделіндегі ПҚЭ кристалдарының мөлшерін есептеу мүмкіндігі қарастырылған. Бұл модельге сәйкес, ПҚЭ-де кристалдар әлеуетінің мәндерінен басқа, жалпы қабылданған теориядан тыс жоғары электрондық тығыздық аймағын қарастыру керек. Эксперименталды деректер осы аймақтың жағдайын ПҚЭ атом ядросының айналасында оқшауландырылған деп анықтауға мүмкіндік береді. Атомдық қаңқа жалпы жағдайда элементарлық ұяшыққа сәйкес келеді, яғни атомдардың бір санынан тұрады және симметрияның бір нүктелі тобы бар.

Кілт сөздер: нанобөлшектер, микроблоктар, наноөлшемді құрылымдық элементтер, протонды-бөлінген құрылымдық элементтер.

Ю.В. Бородин, К.В. Сысолов, В.Р. Ранде, Г.В. Вавилова, О. Стары

Спектроскопия наноразмерных кристаллических структурных элементов

Изучение структурных элементов, наночастиц, микроблоков и других наноразмерных объектов было важной частью изучения неравновесных свойств кристаллов. Поведение наноразмерных структур позволяет судить о динамике кристаллической решетки при легировании, деформации и взаимодействии с излучением. Наряду с рентгеновскими и электронно-микроскопическими исследованиями все шире используются оптические методы определения размеров наноразмерных объектов, энергии их электронов и симметрии электронных состояний. Среди наноразмерных объектов особое внимание привлекают протонно-разделенные структурные элементы (ПСЭ) в связи с разработкой блочно-иерархической (ВИ) модели кристаллической структуры. В статье рассмотрена возможность расчета размеров кристаллов ПСЭ в модели квантово-размерных структур. Согласно этой модели, кроме значений потенциала кристалла в ПСЭ, следует изучить область высокой электронной плотности, существование которой выходит за рамки общепринятой теории. Экспериментальные данные позволяют определить положение этой зоны как локализованной вокруг атомного ядра ПСЭ. Заметим, что атомный остов в общем случае совпадает с элементарной ячейкой, то есть состоит из одного и того же числа атомов и имеет одну и ту же точечную группу симметрии.

Ключевые слова: наночастицы, микроблоки, наноразмерные структурные элементы, протонно-разделенные структурные элементы.

References

- 1 Bassani, F., & Pastori Parravicchini, Dzh. (1982). *Elektronnyye sostoiianiia i opticheskie perekhody v tverdykh telakh [Electronic States and optical transitions in solids]*. Moscow: Nauka [in Russian].
- 2 Borodin, Y.V., Ermolaev, D.S., Pak, V., & Zhang, K. (2016). Research of nanocomposite structure of boron nitride at proton radiation. Proceedings from RTEP2016 IOP Conference Series: Materials Science and Engineering, 110, 1–4. DOI: 10.1088/1757-899X/110/1/012072.
- 3 Tsu, R., Nicollian, E.H., & Reisman, A. (1989). Passivation defects in polycrystalline superlattices and quantum well structures. *Appl. Phys. Lett.*, 55, 18, 1897–1899.
- 4 Borodin, Y.V., & Sergeev, A.N. (2008). The formation of nanocomposition structure in crystals. *Proceedings of the 3rd International Forum on Strategic Technology, IFOST*, 174–176.
- 5 Yurov, V.M., Arkhipov, V.V., Ranova, G.A., & Laurinas, V.Ch. (2019). Study of dimensional dependencies of thermodynamic characteristics of nanoparticles. *Bulletin of the University of Karaganda – Physics*, 2(94), 35–41. DOI: 10.31489/2019Ph2/35–41.
- 6 Yurov, V.M., Guchenko, S.A., Laurinas, V.Ch., & Zavatskaya, O.N. (2019). Structural phase transition in surface layer of metals. *Bulletin of the University of Karaganda – Physics*, 1(93), 50–60. DOI: 10.31489/2019Ph1/50–60.
- 7 Vereshchagin, V.I., Sergeev, M.A., Semukhin, B.S., & Borodin, Y.V. (2000). Boron nitride with packets of nanotubes for microcomposite ceramics. *Refractories and Industrial Ceramics*, 41, 11–12, 440–443.
- 8 Kauli, Dzh. (1979). *Fizika difraktsii [Physics of diffraction]*. Moscow: Mir [in Russian].
- 9 Borodin, Y.V. (2015). Low-temperature nanodoping of protonated LiNbO₃ crystals by univalent ions. *Technical Physics*, 60, 107–111.
- 10 Flugge, Z. (1974). *Zadachi po kvantovoi mekhanike [Problems in quantum mechanics]*. Moscow: Mir [in Russian].
- 11 Liubarskii, H.Ya. (1958). *Teoriia hrupp i ee primenenie v fizike [Group theory and its application in physics]*. Moscow: Nauka [in Russian].
- 12 Loktiushin, A.A. (1983). Opticheskie spektry elektronnykh tsentrov okraski [Optical spectra of electronic color centers]. *Rukopis deponirovana v VINITI 12 iulia 1983 h., № 4328–83 — Manuscript deposited at VINITI, July, 12, 1983, No. 4328–83*. Tomsk [in Russian].
- 13 Wang, Chumin, & Barrio, R.A. (1988). Theory of the Raman Response in Fibonacci Superlattices. *Phys. Rev. B.*, 61, 191.
- 14 Sushchinskii, M.M. (1969). *Spektry kombinatsionnoho rasseianiia molekul i kristallov [Spectra of Raman scattering of molecules and crystals]*. Moscow: Nauka [in Russian].
- 15 Birman, Dzh. (1978). *Prostranstvennaia simmetriia i opticheskie svoistva tverdykh tel [Spatial symmetry and optical properties of solids]*. Vol. 2. Moscow: Nauka [in Russian].

V.A. Perminov*, K.O. Fryanova

Tomsk Polytechnic University, Russia
(*E-mail: perminov@tpu.ru)

Mathematical modeling of the initiation and spread of forest fires and their impact on buildings and structures

Currently, methods of mathematical modeling are used to study processes in emergency situations. Forest fires are extremely complex and destructive natural phenomena which depend on availability of fuel, meteorological and other conditions. Mathematical model of forest fire is based on an analysis of known experimental data and using concept and methods from reactive media mechanics. In this paper the theoretical study of the problems of crown forest fire spread in windy condition and their thermal impact on the wooden building were carried out. The research was based on numerical solution of two-dimensional Reynolds equations. The boundary-value problem is solved numerically using the method of splitting according to physical processes. A discrete analogue for the system of equations was obtained by means of the control volume method. A study of forest fire spreading made it possible to obtain a detailed picture of the change of the component concentration of gases and temperature fields in forest fire and on the wall of building with time. It let to determine the limiting distances between forest fire and building for possibility of wooden walls ignition for different meteorology conditions, size of building and intensity of fire impact.

Keywords: crown fire, fire spread, forest fire, mathematical model, ignition, finite volume method, building, turbulence.

Introduction

A number of authors are studying the problem of the behavior of forest fires. Rothermal [1] and Van Wagner [2] formulated the first mathematical methods to study the behavior of forest fires. They represent semi-empirical approaches that allow one to obtain fairly reliable values of the flame front propagation velocity, depending on a given supply and moisture content of forest combustible materials, wind speed and terrain. However, in their models, the authors used parameters for specific fires based on certain data. This limitation significantly reduces the possibility of widespread use of this method in modeling various forest fires. Numerical modeling based on identical installations is used to compare the effectiveness of two main approaches based on Eulerian LSM and Lagrangian DEVS schemes in constructing forest fire models [3]. The mathematical models presented in the works [4–9] provide more detailed conditions for the spread of forest fires. A distinctively new approach to studying the behavior of forest fires by the method of mathematical modeling was proposed by Grishin. [10], which is based on the application of experimental data and the use of approaches and methods of reactive mechanics [11]. However, when studying the problem of the behavior of forest fires [10, 11], the issue of the effect of the wildland fires front on buildings and structures located near the forest zone were not studied. In the summer season of 2019, according to official data, more than 2 million hectares of timber burned out as a result of forest fires in Russia. Such large-scale forest fires carry not only an economic threat, but also a threat to human victims as a result of the transition of the flame front to urban areas. Extinguishing forest fires requires a lot of effort and cost, creating airborne teams of

firefighting specialists, engaging outside organizations and volunteer groups, etc., and, in the vast majority of cases, is ineffective or impossible. Currently, the most effective methods for studying natural fires are mathematical modeling methods using numerical methods [10–14] and modern software to solve problems.

Physical and mathematical setting

The mathematical model considered in this paper and the calculation results are used to study the interaction of forest fire fronts with wooden structures. We assume that on the ground cover there is an area of elevated temperature, that is, a center of a lower fire, which has some dimensions, at a certain height, above the forest canopy, the wind speed is set. Under the influence of this burning zone, inert heating of forest combustible materials takes place in the forest canopy, moisture evaporates, pyrolysis occurs with the release of condensed and volatile pyrolysis products, which then ignite. A combustion front is formed, which moves along the forest canopy under the influence of wind. If a building is located near the forest, then the flame front has a thermal effect on it due to the transfer of energy by radiation, convection and transfer of burning particles. As a result, ignition of this object is possible. Let us consider schematically the region of the process under consideration. The axis Ox_2 is directed perpendicular to the earth surface, and the axis Ox_1 is directed parallel to the earth surface and coincides with the direction of the wind. Figure 1 shows a scheme of this process:

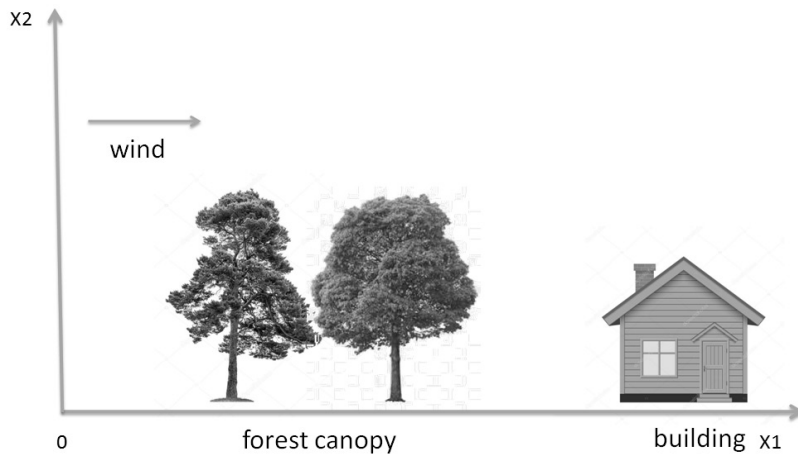


Figure 1. Forest fire propagation pattern

It is supposed that: 1) the flow is turbulence, while laminar transport is neglected, since it is not significant compared with turbulent; 2) the density of the gas-dispersed phase does not depend on pressure, due to the fact that the flow velocity is small relative to the speed of sound; 3) it is assumed that the local-thermodynamic equilibrium is taken place; 4) the wind speed is defined at height of the forest canopy; 5) the multiphase medium consist of particles of the condensed and gas phase (oxygen, gaseous combustible pyrolysis products and inert components (nitrogen, water vapor, gas products of combustion and etc.) [10, 12]. The problem given above reduces to solving the following system of differential equations:

$$\frac{\partial \rho}{\partial t} + \frac{\partial}{\partial x_i} (\rho v_i) = m, j = 1, 2, i = 1, 2; \quad (1)$$

$$\rho \frac{dv_i}{dt} = -\frac{\partial p}{\partial x_i} + \frac{\partial}{\partial x_j} (-\rho \overline{v'_i v'_j}) - \rho s c_d v_i |\vec{v}| - \rho g_i - \dot{m} v_i; \quad (2)$$

$$\rho c_p \frac{dT}{dt} = \frac{\partial}{\partial x_j} (-\rho c_p \overline{v'_j T'}) + q_s R_s - \alpha_v (T - T_s) + k_g (c U_R - 4\sigma T^4); \quad (3)$$

$$\rho \frac{dc_\alpha}{dt} = \frac{\partial}{\partial x_j} (-\rho \overline{v'_j c'_\alpha}) + R_{s\alpha} - \dot{m} c_\alpha, \alpha = \overline{1, 2}; \quad (4)$$

$$\frac{\partial}{\partial x_j} \left(\frac{c}{3k} \frac{\partial U_R}{\partial x_j} \right) - k c U_R + 4k_s \sigma T_s^4 + 4k_g \sigma T^4 = 0, k = k_g + k_s; \quad (5)$$

$$\sum_{i=1}^4 \rho_i c_{pi} \Phi_i \frac{\partial T_s}{\partial t} = q_{3w} R_{3w} - q_{2R_{2s}} - k(cU_R - 4\sigma T_s^4) + \alpha_V (T - T_s); \quad (6)$$

$$\rho_1 \frac{\partial \Phi_1}{\partial t} = -R_{1s}, \rho_2 \frac{\partial \Phi_2}{\partial t} = -R_{2s}, \rho_3 \frac{\partial \Phi_3}{\partial t} = \alpha_C R_{1s} - \frac{M_C}{M_1} R_{3w}, \rho_4 \frac{\partial \Phi_4}{\partial t} = 0; \quad (7)$$

$$\sum_{\alpha=1}^3 c_\alpha = 1, p_e = \rho RT \sum_{\alpha=1}^3 \frac{c_\alpha}{M_\alpha}, v = (v_1, v_2), g = (0, g); \quad (8)$$

$$\dot{m} = (1 - \alpha_c) R_1 + R_2 + \frac{M_c}{M_1} R_3, R_{s1} = -R_3 - \frac{M_1}{2M_2} R_5, R_{s2} = v(1 - \alpha_c) R_1 - R_5, R_{s3} = 0. \quad (9)$$

This system of equations is solved using the next initial and boundary conditions:

$$t = 0: v_i = 0, T = T_e, c_\alpha = c_{\alpha e}, T_s = T_e, \Phi_k = \Phi_{ke}, i = 1, 2; k = 1, 2; \alpha = 1, 3; \quad (10)$$

$$x_1 = -x_{1e}: v_1 = V_e(x_2), v_2 = 0, T = T_e, c_\alpha = c_{\alpha e}, -\frac{c}{3k} \frac{\partial U_R}{\partial x_1} + \frac{c U_R}{2} = 0; \quad (11)$$

$$x_1 = x_{1e}: \frac{\partial v_1}{\partial x_1} = 0, \frac{\partial v_2}{\partial x_1} = 0, \frac{\partial T}{\partial x_1} = 0, \frac{\partial c_\alpha}{\partial x_1} = 0, \frac{c}{3k} \frac{\partial U_R}{\partial x_1} + \frac{c U_R}{2} = 0; \quad (12)$$

$$x_2 = 0: v_1 = 0, (\rho v_2) = h_0 m,$$

$$T = T_s = \begin{cases} T_e + (T_0 - T_e) \exp(-((x_1 - x_{10}) / \Delta_x)^2) t / t_0, & t \leq t_0 \\ T_e + (T_0 - T_e) \exp(-(((x_1 - x_{10}) - x_f) / \Delta_x)^2), & t > t_0 \end{cases}$$

$$-\rho D_t \frac{\partial c_\alpha}{\partial x_2} + \rho v_2 c_\alpha = h_0 R_{5\alpha}, -\frac{c}{3k} \frac{\partial U_R}{\partial x_3} = \frac{\varepsilon}{2(2 - \varepsilon)} (4\sigma T_s^4 - c U_R); \quad (13)$$

$$x_2 = x_{2e}: \frac{\partial v_1}{\partial x_2} = 0, \frac{\partial v_2}{\partial x_2} = 0, \frac{\partial c_\alpha}{\partial x_2} = 0, \frac{\partial T}{\partial x_2} = 0, \frac{c}{3k} \frac{\partial U_R}{\partial x_2} + \frac{c U_R}{2} = 0, \quad (14)$$

where x_1, x_2, v_1, v_2 — coordinates and corresponding projections of the velocity vector on the axes of coordinate; R_5 and $R_{5\alpha}$ — combustion reaction rates of gaseous pyrolysis products and the appearance of α — gas dispersed phase components; c_p, ρ , — specific heat and density of the gas phase; T — the temperature of gas-dispersed phase; c_α — mass concentrations ($\alpha = 1$ — oxygen, 2 — CO, 3 — inert air components); P — pressure; U_R — radiation energy density; σ — Stefan-Boltzmann constant; k_g — absorption coefficient for gas-dispersed phases; q_i, E_i, k_i — thermal effects of the reactions, activation energies, and pre-exponents of the reaction of pyrolysis, evaporation of moisture and combustion of pyrolysis products; M_α, M — molecular weights of the components of the gas phase and air mixture; c — speed of light; α_c, v — coke number and mass fraction of combustible gases in the mass of gaseous pyrolysis products; g — gravitational constant. Indexes «o» и «e» relate to functions in the field of combustion and at a considerable distance from the fire front, respectively. Index «'» used to indicate the pulsating components of various functions [10]. The thermodynamic, thermophysical, and structural quantities used in the statement of the problem belong to forest combustible materials corresponding to the pine forest: $E_5/R = 11500$ K, $k_5 = 3 \cdot 10^{13}$, $q_5 = 10^7$ J/kg, $c_p = 1000$ J/(kg·K), $\alpha_c = 0.06$, $v = 0.7$, $\rho_e = 1.2$ kg/m³, $c_{2e} = 0$, $p_e = 10$ N/m², $T_e = 300$ K, $c_{1e} = 0.23$ [12]. Turbulent stress tensor components $\overline{\rho v' w'}$ and turbulent heat and mass fluxes $\overline{v' T'}$, $\overline{v' c'_\alpha}$ computed using middle flow gradients as follows:

$$-\overline{\rho_5 u_i u_j} = \mu_T \left(\frac{\partial u_i}{\partial x_j} + \frac{\partial u_j}{\partial x_i} \right) - \frac{2}{3} K \delta_{ij}, ; -\overline{\rho_5 u_j c_p T'} = \lambda_T \frac{\partial T}{\partial x_j}, -\overline{\rho_5 u_j c'_\alpha} = \rho_5 D_T \frac{\partial c_\alpha}{\partial x_j}, \quad (15)$$

$$\lambda_T = \mu_T c_p / Pr_T, \rho_5 D_T = \mu_T / Sc_T, \mu_T = c_\mu \rho_5 K^2 / \varepsilon, ; \mu_t = c_\mu \rho K^2 / \varepsilon, \quad (16)$$

where K — kinetic energy of turbulence, v_i and v'_i — components of the average velocity and the pulsating component of the velocity in the projection onto the axis x_i ; μ_b, λ_b, D_t — coefficients of turbulent, dynamic viscosity, turbulent thermal conductivity and diffusion; Pr_t, Sc_t — turbulent Prandtl and Schmidt numbers; δ_{ij} — Kronecker characters; $\mu_t = c_\mu \rho K^2 / \varepsilon$, where ε — dissipation rate of turbulent kinetic energy, c_μ — constant. The determination of the coefficient of turbulent dynamic viscosity has certain difficulties [10; 15], such as the arbitrariness in choosing the initial and boundary conditions for the kinetic energy equation of

turbulence, as well as the approximate closure method, which is based on the Prandtl mixing path hypothesis, which actually means the equilibrium approximation for the kinetic energy equation turbulence. In [10], the approach for the two-dimensional planar case is described in more detail. If in the case under consideration the non-stationary and convective terms and the diffusion terms of turbulent kinetic energy are neglected in the equation for the kinetic energy of turbulence, then the coefficient of turbulent dynamic viscosity and the expression for the kinetic energy of turbulence can be obtained from the right side of the equation, as described in Grishin [10]. A locally equilibrium turbulence model is used. To determine the turbulent dynamic viscosity in the two-dimensional case, the next formula was used:

$$\mu_t = \rho l^2 \left\{ 2 \left[\left(\frac{\partial v_1}{\partial x_1} \right)^2 + \left(\frac{\partial v_2}{\partial x_2} \right)^2 \right] + \left(\frac{\partial v_1}{\partial x_2} + \frac{\partial v_2}{\partial x_1} \right)^2 - \frac{2}{3} \left[\frac{\partial v_1}{\partial x_1} + \frac{\partial v_2}{\partial x_2} \right]^2 - \frac{g}{T \text{Pr}_t} \frac{\partial \theta}{\partial x_2} \right\}^{1/2}, \quad (17)$$

where $\theta = T - T_e$. The formula for the mixing path proposed by the authors of [13] has the form

$$l = z k_\tau / (1 + 2.5z \sqrt{c_d s / h}), \quad (18)$$

where $k_\tau = 0.4$ — Karman constant, h — forest canopy height.

Numerical method

For numerical integration of the original system of equations, the control volume method is used [13]. The main meaning of this method is easily understood and lends itself to direct physical explanation. We divide the computational domain into a certain number of disjoint control volumes so that each node point is contained in only one volume. In the case of a two-dimensional problem, we consider a rectangle. The second step is the integration of the differential equation for each control volume. To carry out the calculation of the integrals, profiles are used that describe the change between the nodal points of the function Φ . The discrete analogue obtained as a result of integration expresses the conservation law for the state parameter Φ in each finite control volume [13]. The discrete analogue obtained in this way expresses the conservation law Φ for a finite control volume in the same way that the differential equation expresses the conservation law for an infinitely small control volume. An important property of this method is that the control volume method contains the exact integral conservation of such quantities as mass, momentum and energy for any group of control volumes and for the entire calculation area. This feature is demonstrated for any number of nodal points, and not only in the limiting case of a large number of them. Even a coarse grid solution satisfies precise integral balances [13]. Differential equations obeying the generalized conservation law describe the processes of hydrodynamics and heat transfer, mass transfer. When denoting any desired function of the variable Φ , the generalized differential equation takes the form in tensor form [13]:

$$\frac{\partial}{\partial t} (\rho \Phi) + \frac{\partial}{\partial x_i} (\rho v_i \Phi) = \frac{\partial}{\partial x_i} \left(\Gamma_\phi \frac{\partial \Phi}{\partial x_i} \right) + S_\phi, \quad (19)$$

where, ρ is the density, t is the temporal coordinate, x_i is the spatial coordinate, v_i are the components of the velocity vector, Γ_ϕ is the transport coefficient (Γ_ϕ is the coefficient of thermal conductivity, turbulent viscosity, diffusion, etc.), S_ϕ is the source term. In special cases, the heat flux as a result of chemical reactions in the energy equation or an increase (decrease) in component concentrations during chemical reactions in the diffusion equations may enter S_ϕ . The specific form of Γ_ϕ and S_ϕ depends on the semantic load of the variable Φ . For the nodal point P the neighboring points W and E are located in the direction of the x_1 axis, points N and S (denoting north and south) — in the direction of the x_2 axis. The control volume surrounding point P is shown by lines. The volume depth in the z axis direction is assumed to be unity. Designations for distances Δx , (δx) e , etc., apply here to two dimensions. The question of the location of the faces of the control volume with respect to the nodal points remains open. You can position them exactly in the middle between adjacent points, but other methods can be applied, some of which will be discussed below. The discrete analog obtained here can be used in any such case.

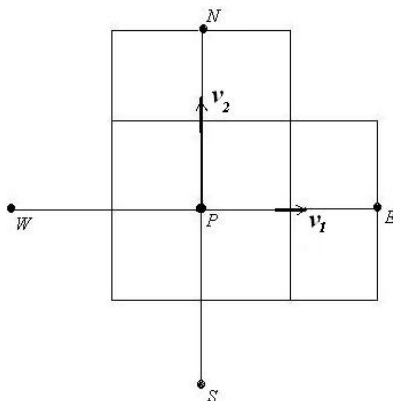


Figure 2. Control volume (shaded area) for the two-dimensional case

The calculated area is divided into a number of non-overlapping control volumes. Then we integrate the system of differential equations for each control volume [13]. As a result, we obtain a system of nonlinear algebraic equations, which is then solved numerically using the SIP method. Thus, we obtain the distributions of the sought-for functions at all points of the computational domain at different instants of time.

The results of calculations and their analysis

Using the described mathematical model, numerical calculations were carried out to determine the pattern of the ignition of a wooden structure as a result of the action of a flame front. The fields of the distribution of temperature, velocity, mass fractions of components, and volume fractions of phases were obtained numerically. The first stage is associated with an increase in the maximum temperature at the ignition site. As a result, a hotbed of flame appears. At this stage of the process, a heat flow arises above the hearth and a zone of heated wood pyrolysis products is formed, which mix with air, rise up and penetrate the tree crown. As a result, the forest canopy is heated in the crowns of trees, moisture evaporates and gaseous and dispersed pyrolysis products are formed. Ignition of gaseous pyrolysis products occurs in the next step. As a result of heating the wood, moisture evaporates, pyrolysis occurs, accompanied by the release of gaseous products, which then ignite and burn. At the time of ignition, gaseous combustible products are burned, and the oxygen concentration rapidly decreases. The temperatures of both phases reach their maximum value at the flash point. The calculation makes it possible to take into account the spread of forest fires at different wind speeds, bulk of forest fuel, and moisture of forest fuel. The influence of a forest fire on a building that is located near a forest is considered. The influence of wind speed and the distance between the forest and the building on the ignition of the building is studied numerically. The calculation results can be used to assess the thermal effect on a building located next to forest fires.

Fields of wind and temperature interact with an obstacle — construction (Fig. 3a) and b)). In Fig. 4 shows the results of modeling the wall temperature at different distances between the front of a forest fire and a wooden building (20×50×20 meters) for various values of wind speed from 3 to 15 m/s.

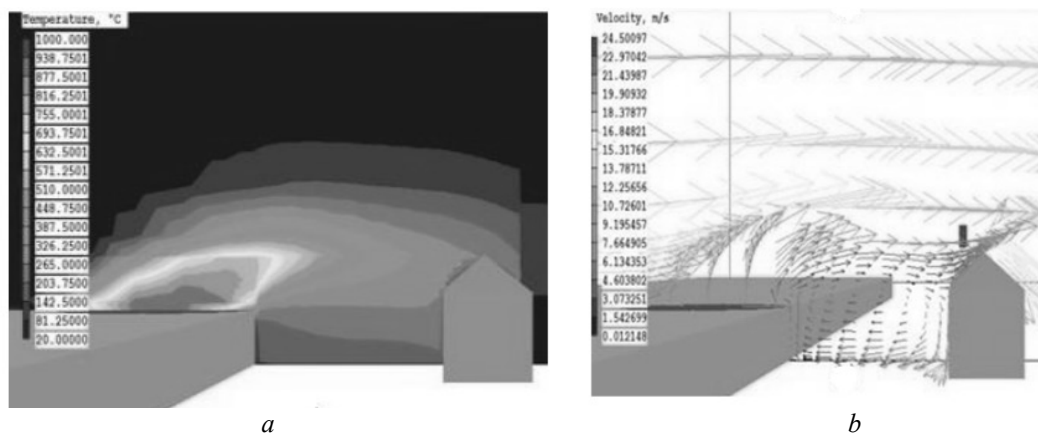


Figure 3. Distribution of temperature a) and speed b) near the building

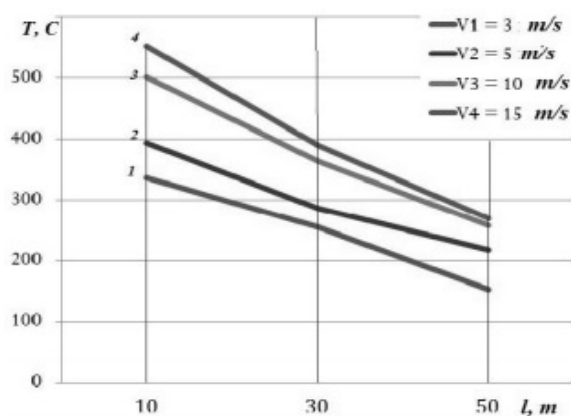


Figure 4. The temperature distribution on the wall of a wooden structure ($20 \times 50 \times 20$) for different wind speeds (3–15 m/s) and for different distances l (10–50 m)

An analysis of this relationship shows the following: 1) a wooden structure with a wind speed of 3 m/s lights up at a distance of 15–16 meters from forest fires; 2) with $v = 5$ m/s — $l \approx 26$ –27 meters; 3) $v = 10$ m/s — $l \approx 39$ –40 meters; 4) $v = 15$ m/s — $l \approx 46$ –47 meters. In Figure 5 shows the temperature dependence on the walls of a wooden house measuring $12 \times 15 \times 12$ meters for different wind speeds (3–15 m/s) for distances l (10–50 m).

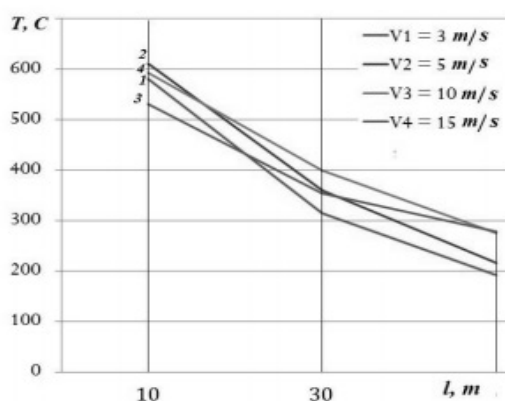


Figure 5. The temperature distribution on the wall of a wooden structure ($12 \times 15 \times 12$ m) for different wind speeds (3–15 m/s) and for different distances l (10–50 m)

An analysis of this relationship (Fig. 5) shows the following: 1) a wooden structure with a wind speed of 3 m/s lights up at a distance of 32–33 meters from forest fires; 2) $v = 5$ m/s — $l \approx 38$ –39 meters from forest fires; 3) $v = 10$ m/s — $l \approx 43$ –44 meters from forest fires; 4) $v = 15$ m/s — $l \approx 42$ –43 meters.

Conclusion

The result of solving this problem allows you to get a detailed picture of the change in speed, temperature and concentration fields of components in the wildland fire and on the near located buildings over time. This allows to study the dynamics of the impact of forest fires on wooden buildings under the influence of various external conditions, such as, meteorological conditions (air temperature, wind speed, etc.) and the type of forest combustible material and its state (bulk of forest fuel, moisture, etc.). Calculations make it possible to obtain the maximum safe distance from the forest fire front to the structures (buildings and other objects) in order to exclude the possibility of its ignition.

References

- 1 Rothermal R.C. Predicting behaviour and size of crown fires in the Northern Rocky Mountains / R.C. Rothermal // Res. Pap. INT-438. — Ogden, UT: US Department of Agriculture, Forest Service, Intermountain Forest and Range Experiment Station, 1972.

- 2 Van Wagner C.E. Conditions for the start and spread of crown fire / C.E. Van Wagner // Canadian Journal of Forest Research. — 1977. — No. 7. — P. 23–34.
- 3 Kaur I. Turbulence and fire-spotting effects into wildland fire simulators / I. Kaur, A. Mentrelli, F. Bosseur, J.-B. Filippi, G. Pagnini // Communications Nonlinear Science Numerical Simulation. — 2016. — Vol. 39. — P. 300–320.
- 4 Alexander M.E. Crown fire thresholds in exotic pine C.E. / M.E. Alexander // 10th Conference on fire and forest meteorology / D.C. MacIver, H. Auld, R. Whitewood (Eds.). — Ottawa (Ontario). — 1979. — P. 207–212.
- 5 Xanthopoulos G. Development of a wildland crown fire initiation model: PhD thesis / G. Xanthopoulos. — Montana: University of Montana, 1990.
- 6 Van Wagner C.E. Prediction of crown fire behavior in two stands of jack pine / C.E. Van Wagner // Canadian Journal of Forest Research. — 1999. — Vol. 23. — P. 445–449.
- 7 Cruz M.G. Predicting crown fire behavior to support forest fire management decision-making/ M.G. Cruz, M.E. Alexander, R.H. Wakimoto // IV International Conference on Forest Fire Research / D.X. Viegas (Eds.). — LusoCoimbra, Portugal, 2002.
- 8 Albin F. Modeling ignition and burning rate of large woody natural fuels / F. Albin, E.D. Reinhardt // International Journal of Wildland fire. — 1995. — Vol. 5, No. 2. — P. 81–91.
- 9 Scott J.H. Assessing crown fire potential by linking models of surface and crown fire behavior / J.H. Scott, E.D. Reinhardt // USDA Forest Service, Rocky Mountain Forest and Range Experiment Station: Fort Collins: RMRS-RP-29, USA. — 2001.
- 10 Grishin A.M. Mathematical modeling forest fire and new methods fighting them / A.M. Grishin. — Tomsk: Publishing House of Tomsk University, 1997.
- 11 Morvan D. Modeling the propagation of wildfire through a Mediterranean shrub using a multiphase formulation / D. Morvan, J.L. Dupuy // Combustion and Flame. — 2004. — Vol. 138. — P. 199–210.
- 12 Perminov V.A. Numerical modeling of the process of thermal impact of wildfires on buildings located near forests / V.A. Perminov, K.O. Fraynova, A. Lukianov // Materials Science Forum. — 2019. — Vol. 970. — P. 82–87.
- 13 Patankar S.V. Numerical heat transfer and fluid flow / S.V. Patankar. — London; New York; M.: CRC Press Taylor & Francis Group, 1980.
- 14 Agranat V.M. Mathematical modeling of wildland fire initiation and spread / V.M. Agranat, V.A. Perminov // Environmental Modeling & Software. — 2020. — Vol. 125.
- 15 Toleuov G. Experimental study of free turbulent jet / G. Toleuov, M.S. Isataev, Zh.K. Seidulla, A. Dosanova, Zh. Tolen // Bulletin of the University of Karaganda – Physics. — 2019. — No. 1(93). — P. 79–86.

В.А. Перминов, К.О. Фрянова

Орман өрттерінің пайда болуы мен таралуын және олардың ғимараттар мен құрылыстарға әсерін математикалық модельдеу

Қазіргі таңда төтенше жағдайлардың қозғалыстарын зерттеу үшін математикалық модельдеу әдістері қолданылады. Орманнан шығатын өрттер өте қауіпті өрттер болып саналады, олар отынның метеорологиялық және басқа жағдайлардың болуына байланысты пайда болады. Орман өртінің математикалық моделі белгілі эксперименттік мәліметтерді талдауға және реакциялық ортаның механикалық түсінігі мен әдістерін қолдануға негізделген. Зерттеу барысы желдің әсерінен орман өрттерінің таралуы мен олардың ағаш құрылымына термиялық әсері туралы теория жүзінде берілген. Зерттеу екі өлшемді Рейнольдс теңдеулерінің сандық шешіміне негізделген. Шеттік есеп физикалық қозғалыстарға бөлу әдісімен сандық түрде шешіледі. Теңдеулер жүйесіне арналған дискретті аналогы басқару көлемінің әдісі арқылы алынды. Орман өрттерінің таралуын зерттеу — орман өртінің алдындағы ғимарат қабырғасында газ тәрізді құрамдас бөліктердің және температура өрістерінің концентрациясының өзгеруінің нақты көрінісін алуға мүмкіндік береді. Бұл бізге әртүрлі метеорологиялық жағдайларда ағаш қабырғалардың тұтану мүмкіндігін, ғимараттың көлемі мен өрттің қарқындылығы үшін орман өрті мен ғимарат арасындағы ең үлкен қашықтықты анықтауға мүмкіндік береді.

Кілт сөздер: өрттің таралуы, орманның жануы, орман өрті, математикалық модель, тұтану, шектеулі көлем әдісі, құрылыс, турбуленттілік.

В.А. Перминов, К.О. Фрянова

Математическое моделирование возникновения и распространения лесных пожаров и их воздействие на здания и сооружения

В настоящее время методы математического моделирования используются для изучения процессов в чрезвычайных ситуациях. Лесные пожары являются чрезвычайно сложными и разрушительными природными явлениями, которые зависят от наличия топлива, метеорологических и других условий. Математическая модель лесного пожара основана на анализе известных экспериментальных данных и

использовании концепции и методов механики реагирующих сред. В статье теоретически исследованы проблемы распространения лесных пожаров под действием ветра и их термическое воздействие на деревянное строение. Исследование было основано на численном решении двумерных уравнений Рейнольдса. Краевая задача решена методом расщепления по физическим процессам. Дискретный аналог для системы уравнений был получен методом контрольного объема. Изучение распространения лесных пожаров позволило получить детальную картину изменения концентрации газообразных компонентов и температурных полей во фронте лесного пожара и на стене здания в различные моменты времени. Это позволило определить предельные расстояния между лесным пожаром и зданием для возможности возгорания деревянных стен при различных метеорологических условиях, размерах здания и интенсивности воздействия огня.

Ключевые слова: верховой пожар, распространение пожара, лесной пожар, математическая модель, зажигание, метод конечных объемов, здание, турбулентность.

References

- 1 Rothermal, R.C. (1972). *Predicting behavior and size of crown fires in the Northern Rocky Mountains*. Ogden: US Department of Agriculture.
- 2 Van Wagner, C.E. (1977). Conditions for the start and spread of crown fire. *Canadian Journal of Forest Research*, 7, 23–34.
- 3 Kaur, I, Mentrelli, A., Bosseur, F., Filippi, J.-B., & Pagnini, G. (2016). Turbulence and fire-spotting effects into wildland fire simulators. *Communications Nonlinear Science Numerical Simulation*, 39, 300–320.
- 4 Alexander, M.E. (1979). Crown fire thresholds in exotic pine plantations of Australasia. *PhD thesis*. Department of Forestry, Australian National University.
- 5 Xanthopoulos, G. (1990). Development of a wildland crown fire initiation model. *Doctor's thesis*. Montana.
- 6 Van Wagner, C.E. (1999). Prediction of crown fire behavior in two stands of jack pine. *Canadian Journal of Forest Research*, 23, 445–449.
- 7 Cruz, M.G., Alexander, M.E., & Wakimoto, R.H. (2002). Predicting crown fire behavior to support forest fire management decision-making. *Proceedings of the IV International Conference on Forest Fire Research*, 120–125.
- 8 Albin, F., Reinhardt, E.D. (1995). Modeling ignition and burning rate of large woody natural fuels. *International Journal of Wildland Fire*, 5, 81–91.
- 9 Scott, J.H., & Reinhardt, E.D. (2001). *Assessing crown fire potential by linking models of surface and crown fire behavior*. Fort Collins: US Department of Agriculture.
- 10 Grishin, A.M. (1997). *Mathematical modeling forest fire and new methods fighting them*. Tomsk: Publishing House of Tomsk University.
- 11 Morvan, D., & Dupuy, J.L. (2004). Modeling the propagation of wildfire through a Mediterranean shrub using a multiphase formulation, *Combustion and Flame*, 138, 199–210.
- 12 Perminov, V.A., Fraynova, K.O., & Lukianov, A. (2019). Numerical modeling of the process of thermal impact of wildfires on buildings located near forests. *Materials Science Forum*, 970, 82–87.
- 13 Patankar, S.V. (1980). *Numerical heat transfer and fluid flow*. London; New York; M.: CRC Press Taylor & Francis Group.
- 14 Agranat, V.M., Perminov, V.A. (2020). Mathematical modeling of wildland fire initiation and spread. *Environmental Modeling & Software*, 125, 1–7.
- 15 Toleuov, G., Isataev, M.S., Seidulla, Zh.K., Dosanova, A., & Tolen, Zh. (2019). Experimental study of free turbulent jet. *Bulletin of the University of Karaganda – Physics*, 1(93), 79–86.

V.P. Kovbasa¹, A.V. Solomka², A.V. Spirin^{1*},
V.Yu. Kucheruk³, D.Zh. Karabekova⁴, A.K. Khassenov⁴

¹National Agrarian University, Vinnitsa, Ukraine;

²National University of Life and Environmental Sciences of Ukraine, Kiev, Ukraine;

³Vinnitsa national technical university, Ukraine;

⁴Karaganda University of the name of academician E.A. Buketov, Kazakhstan

(*E-mail: spirinanatoly16@gmail.com)

Theoretical determination of the distribution of forces and the size of the boundaries of the contact in the interaction of the deformable drive wheel with the soil

The article presents the results of an analytical determination of the forces distribution along the length of the contact curve of the driving deformable wheel on the deformable supporting surface, and also are defined the boundaries of the contact zone. The case in a flat statement of the problem is considered. The supporting surface and the surface of the deformable wheel are represented as a continuous deformable medium. The shape of the wheel in the contact zone is represented by the circle equation, which in the contact zone is expanded in a Macloran-series. By using conditions at the boundaries of the contact zone, a system of equations is obtained from which the sizes of the contact zone are determined. The solution of these equations allows one to find expressions of the sizes of the contact zone of the deformable wheel with the deformable surface, depending on the mechanical properties of the wheel materials and the supporting surface, from the geometric dimensions of the wheel and from the loads applied to it. In addition, the results of the studies allow us to determine the analytical expression of the coefficient of rolling resistance of a deformable wheel over a deformable surface, depending on their mechanical properties, geometric parameters, and the loads applied to it.

Keywords: deformable wheel, deformable supporting surface, contact zone boundaries, applied loads, forces distribution in the contact zone, absolute deformations, medium mechanical properties, two-dimensional problem.

Introduction

Manufacturing processes in many industries involve the interaction of deformable drive wheels with deformable bearing surfaces. These processes include the movement of transport and technological means and machines during mining, in agricultural, land reclamation, construction, road and other industries. In this case, it is necessary to solve the problem of the interaction of deformable wheels with a supporting surface, which is deformed also. This is necessary to ensure the passability of the machines and provide the necessary tractive effort, the necessary adhesion of the wheels, as well as to ensure the permissible deformation of the supporting surface and for reduce the resistance to movement of the machine, etc. When solving the above problems, questions arise about the size of the contact spot of the deformable wheel and the supporting surface, and the magnitude of their deformations, and the distribution of forces in the contact zone. In this case, it is necessary to take into account the reasons for the occurrence of sliding and skidding of the wheel, as well as the distribution of stresses and deformations on the wheel surface and on the supporting surface in the contact zone itself and at a certain distance from it. It is also necessary to take into account possible violations of the continuity of the structure of the supporting surface (destruction).

By the stresses magnitude and their distributions in the supporting surface, it is possible to judge about the load-bearing capacity of the supporting surface, about change of its mechanical properties and the conditions for the occurrence of slipping of the wheel and its passability. Knowing the deformations magnitudes of the wheel surface and of supporting surface, as well as the applied loads, it is possible to determine the resistance to rolling of the wheel. In such problems, two cases of rolling the deformable wheel along the supporting surface should be distinguished: the rolling of a passive wheel to which no torque is applied, and the rolling of the drive wheel, i.e. wheel to which torque is applied. From the point of view of the mechanics of interaction, the rolling of a passive wheel is a special case of rolling of the drive wheel. Therefore, it is advisable to consider a more general case — the rolling of a drive wheel.

An analysis of known studies of this problem shows that all the results can be divided into three groups: 1) analytical studies of a fundamental and applied nature; 2) the construction of solutions using well-known models by numerical methods — mainly methods of finite elements (FEM) and finite volumes (DEM); 3) purely experimental research. It should be noted that the first group of studies can give a fairly complete picture of the physical nature of the process and the effect of wheel geometrical parameters on it, the mechanical properties of both the wheel and the supporting surface, and the loads applied to it. The relationship of these values gives the most complete picture of the process and allows you to determine the direction of their influence on the final result of such an interaction.

A significant contribution to the analytical solution of contact interaction problems belongs to A.Yu. Ishlinsky [1, 2], D.I. Zolotarevskaya [3, 4] and others. But an analysis of these works allows us to conclude that not all of these works were taken into account conditions for the application of forces, in particular torque, in addition, the solution to these problems does not give an answer to how the absolute strains are distributed in the vertical and longitudinal directions of the contact zone. In addition, in these solutions there is no clear definition of the boundaries of the contact zones and their dependence on the nature of the application of forces of geometric shapes and the stress-related properties of the contacting bodies.

More modern studies consider numerical solutions of contact problems using the FEM and DEM methods [5–8]. Unfortunately, these works do not give an answer to the question: how do the geometric parameters of the deformable wheel, of the deformable surface, and the magnitudes of the applied loads affect the magnitude of the contact patch. In addition, these results do not have generality, which does not allow us to extend them to more general cases.

It should be noted that the boundaries of the contact patch are used in solving the contact problem in the form of integration limits of potential biharmonic functions that describe solutions of the Laplace systems of equations. These systems are solutions to contact problems in the Papkovich-Neiber form. Therefore, finding the boundaries of the contact of the deformable wheel with the deformable supporting surface is an actual fundamental and applied problem.

The main part of the solving of the contact problem is the analytical determination of the distributed pressures and deformations in the contact zone of the deformable wheel with the supporting surface and the determination of the contact boundaries depending on the applied forces, from the geometric dimensions and shapes of the wheel, as well as the mechanical properties of the wheel and the supporting surface in a flat definition.

This problem definition is suitable for the case of the absence of transverse forces (the condition of linear rolling without taking into account the transverse components of the forces in the contact zone).

Experimental

To describe the contact interaction of the wheel and the surface on which it moves, it is necessary to solve the following tasks:

- deduce the functions of distributed loads in the contact zone under the action of concentrated forces and moments;
- determine the boundaries of the contact zones of the deformable wheel with the deformable surface.

In general, the procedure for solving a contact problem in an analytical form, for the case of geometric linearity of the equations, that connect stress and strain involves the search for functions that are a solution to elliptic equations.

The main types of such solutions are given in the fundamental literature on mathematical physics [9] and consist in the search for analytical biharmonic potential functions that satisfy the conditions on the surface. These are solutions equations Businesk, Cherruti, P.F. Papkovich and Neuber [10–12].

Taking into account the conditions of the problem statement, it can be assumed that there are no vertical displacements of the coordinate system xoz . In this case, one can apply analogs of the solutions of V.M. Aleksandrov, and M.I. Chebakov [13], T.I. Argatov and N.N. Dmitriev [14], as well as V.L. Popov [15], V.P. Kovbasa [16, 17] and others.

These solutions can describe the relationship of the vertical displacements of points of contact surfaces of deformable bodies under vertical and horizontal loading in the form:

$$v_p[x, 0] = M_p \int_{a_1}^a ((v_{1p}(-F_\xi + F_{m\xi}) + v_2 p F_{i\xi}) \frac{B\iota}{\iota^2 + (x + \iota - \xi)^2}) d\xi;$$

$$v_k[x, 0] = M_k \int_{a_1}^a ((v_{1k}(F_{\xi}^i - F_{m\xi}) + v_{2k}F_{i\xi}) \frac{Bt}{\iota^2 + (x + \iota - \xi)^2}) d\xi, \quad (1)$$

where $v_p[x, 0], v_k[x, 0]$ — are the displacement (or velocities displacements), depending on the mediums models, in the direction of the vertical coordinate axis of the contact between the support surface and the wheel surface along the length of the contact zone $\{a_1, a\}$ (it should be noted that the arguments in square brackets indicate that the contact surface is considered at $z = 0$ for the soil and wheel, respectively (Fig. 1); $F_{i\xi}$ — distributed propulsive pressure in the contact zone; F_{ξ} — gravity pressure caused by the mass applied to the wheel in the contact zone; $F_{m\xi}$ — distributed pressure from the vertical reaction force, which is due to

the rolling resistance moment in the contact zone $\{0, a\}$; $M_p = \frac{e^{\frac{G_p t}{\mu_p} (-1 + e^{\mu_p})}}{6G_p (1 + \nu_p)}$, $M_k = \frac{e^{\frac{G_k t}{\mu_k} (-1 + e^{\mu_k})}}{6G_k (1 + \nu_k)}$,

$\nu_{1p} = 2(-2 + \nu_p)$, $\nu_{2p} = (-1 + 5\nu_p)$, $\nu_{1k} = 2(-2 + \nu_k)$, $\nu_{2k} = (-1 + 5\nu_k)$ — stress-related complexes of wheel and supporting surface properties; $G_p, G_k, \mu_p, \mu_k, \nu_p, \nu_k$ — elastic moduli, shear strain viscosity coefficients and lateral expansion coefficients (in the first approximation, Poisson's ratios) of the supporting surface and wheel, respectively.

With prolonged deformation, the exponential functions that enter to M_p, M_k become to unit and depend only on the elastic moduli and the lateral expansion coefficients; $\iota, B = \pi/5b$ — a coefficient that eliminates the singularity of functions (4) and ensures the fulfillment of conditions at the boundary [16, 17].

These equations (1) can be used to determine the components of absolute deformations, and to determine the components of the strain rates of the wheel and the strain rates of the supporting surface in the zone of their contact.

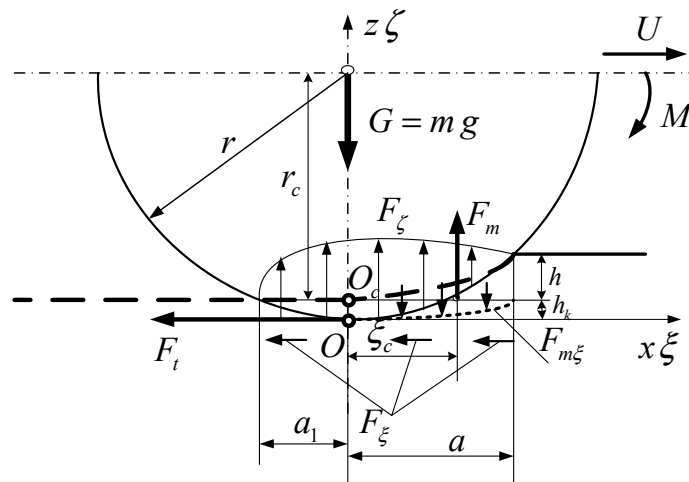


Figure 1. Scheme of interaction of deformable drive wheel with a deformable medium

We can visually represent the nature of the pressures in the contact zone from the scheme of the interaction of the active wheel with the supporting surface (Fig. 1). The fixed coordinate system is denoted as xOz . The movable coordinate system in which the deformations of the wheel and the supporting surface are described is represented as $\xi O \zeta$. In this coordinate system, the wheel surface equation is: $\zeta = r - \sqrt{r^2 - \xi^2}; \xi = r - \sqrt{r^2 - \zeta^2}$. In general, to the wheel a moment M acts, which creates a driving force, a distributed rolling resistance pressure acts and a vertical load $G = mg$.

The rolling resistance forces, on the one hand, are formed in front of the contact zone by a distributed horizontal soil reaction (reaction to a torque component relative to the rotation instantaneous center). The resistance moment to rolling is the product of the integral function of the distribution of resistance force to rolling by the coordinate of the center of its distribution with respect to the coordinates center. On the other

hand, the resistance moment to rolling is the product of the integral function of the distribution center of the vertical components in front of the contact zone and the coordinate of the rotation instantaneous center. These vertical components arise due to the reaction of the soil to the weight applied to the wheel.

If we take into account the presence of components of distributed pressures, then first of all it is necessary to determine the distribution of pressures in the contact zone. In this case, one should take into account the shape of the contact surface in the vertical-longitudinal plane. For the convenience of further transformations, the transcendental shape of the curved contact surface $\zeta = r - \sqrt{r^2 - \xi^2}$ can be represented in the form of a Maclaurin series at the contact area $a_1 - a$. Then the shape of the curve will take the form: $\zeta_n = \xi^2/2r$. The coincidence of the real curve and its expansion in a series over the length of the contact section is evidenced by the graphical presentation of these functions and their derivatives along the contact length (Fig. 2).

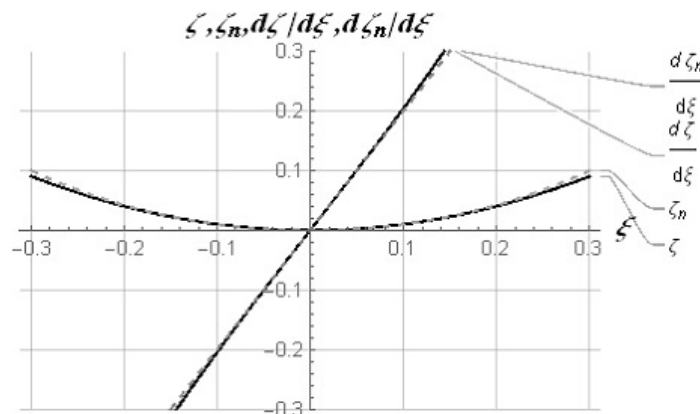


Figure 2. Comparison of the exact analytical expressions of the curve in the contact zone and its expansion into the Maclaurin series

To determine the pressure distribution along the length of the contact surface, one can take into account the properties of a curvilinear integral of the second kind. That is, the pressure distribution along the length of the contact zone $\{a_1; a\}$ can be represented by the equation:

$$\frac{d}{d\xi} \left(\int \frac{G}{(a - a_1)} d\xi \right) = \frac{d}{d\xi} \left(\int \left(F_\zeta \sqrt{1 + \left(\frac{d}{d\xi} \left(\frac{\xi^2}{2r} \right) \right)^2} \right) d\xi \right).$$

Hence, the distribution of pressure from the action of gravity per wheel is:

$$F_\zeta = \frac{G}{(a - a_1) \sqrt{1 + \frac{\xi^2}{r^2}}}. \quad (2)$$

The distribution of the propulsive force created by the torque can be determined based on the above equation:

$$\frac{d}{d\xi} \left(\int F_t d\xi \right) = \frac{d}{d\xi} \left(\int \frac{M}{r} d\xi \right) = \frac{d}{d\xi} \left(\int F_{t\xi} \sqrt{1 + \left(\frac{d}{d\xi} \left(\frac{\xi^2}{2r} \right) \right)^2} d\xi \right).$$

From here, the distributed force from the action of the torque is created by tangential tractive effort that distributed over the contact patch:

$$F_{t\xi} = \frac{M r \sqrt{1 + \frac{\xi^2}{r^2}}}{(a - a_1)(r^2 + \xi^2)}. \quad (3)$$

The distribution of the force that creates the rolling resistance moment of the wheel in the contact area $\{0; a\}$, is also determined using a curvilinear integral of the second kind:

$$\frac{d}{d\xi} \left(\int F_m d\xi \right) = \frac{d}{d\xi} \left(\int (M / (r/a)) d\xi \right) = \frac{d}{d\xi} \left(\int (-F_{m\xi} (\xi - a)^2) d\xi \right),$$

hence the distributed force due to the moment of rolling resistance will have the form:

$$F_{m\xi} = -\frac{aM}{r(a-\xi)^2}. \tag{4}$$

To determine the boundaries of the contact of the wheel with the soil with subsequent integration of these forces distributions, insurmountable difficulties will also arise. In order to prevent the complexity of integration of functions (1), expressions (2), (3), (4) were expanded into Maclaurin series within the length of the contact zone of two bodies:

$$F_n = \frac{gm(2r^2 - \xi^2)}{2(a-a_1)r^2}; F_m = \frac{M(2r^2 - \xi^2)}{2(a-a_1)r^3}; \tag{5}$$

$$F_{mn} = -\frac{M(a^2 + 2a\xi + 3\xi^2)}{a^3r},$$

here F_n — weight force pressure, which has been expanded to the Maclaurin series; F_m — propulsive force pressure, which has been expanded to the Maclaurin series; F_{mn} — rolling resistance pressure, which has been expanded to the Maclaurin series.

The adequacy of the functions expansions and their originals can be judged by their graphical interpretation (Fig. 3), the analysis of which allows us to conclude that they can be used for further solutions.

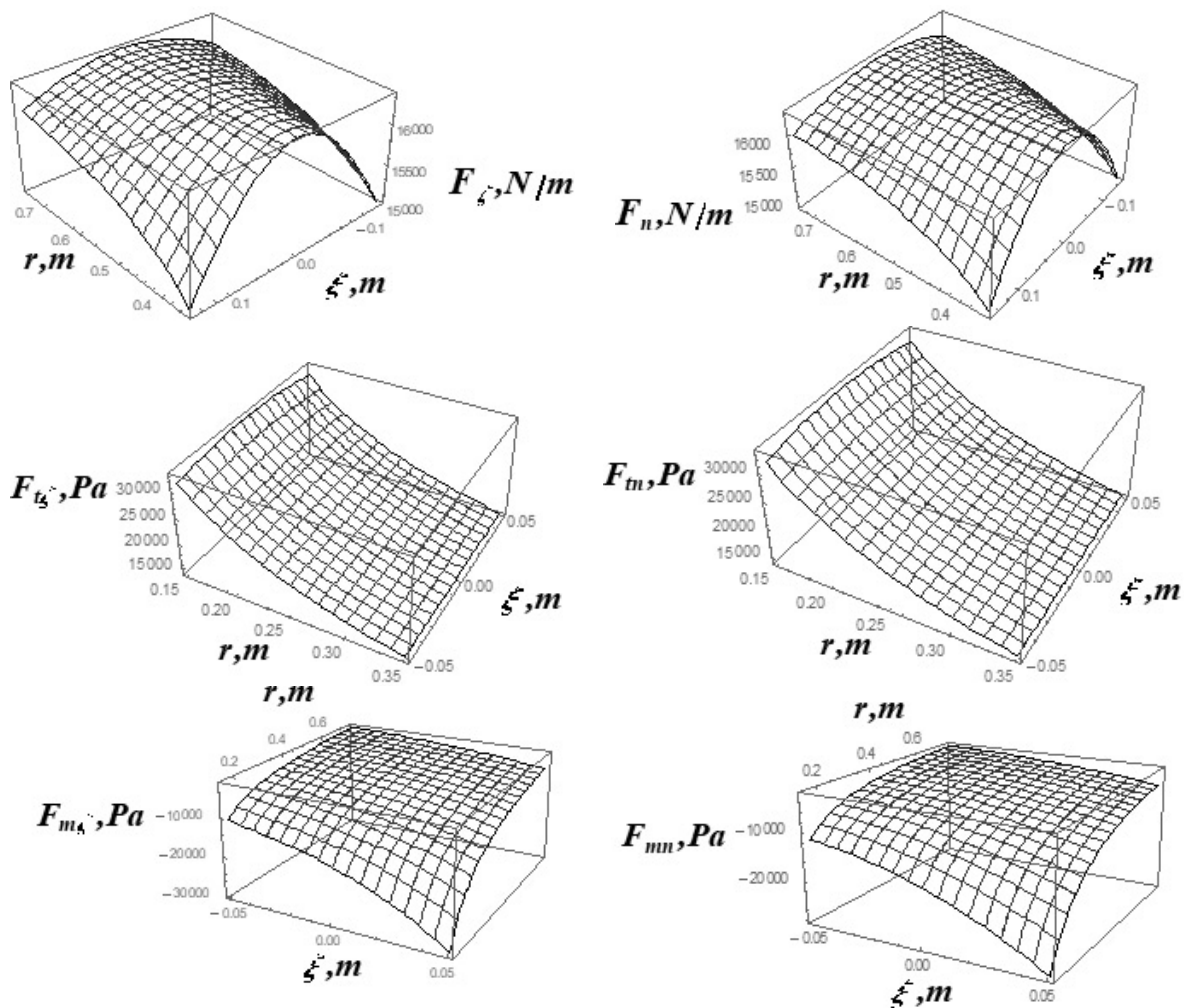


Figure 3. Pressure distribution graphs in the contact zone, plotted both by exact expressions and by their expansion to the Maclaurin series

Thus, the above functions of pressure distributions of the weight force, propulsive force, and rolling resistance, which has been expanded to the Maclaurin series, make it possible to integrate expressions (1) in a final form. Moreover, the boundaries of these integrals are arguments that designate the front and back boundaries of the contact. From the obtained expressions, the dependences of the boundaries of the contact zone can be determined.

Results and Discussion

An analysis of the expressions for the distribution of normal pressure in the contact zone (functions (2), (5)) allows us to conclude that this magnitude is directly proportional to the mass applied to the wheel and inversely proportional to the magnitude of the radius of the wheel and the length of the contact zone. A similar conclusion can be made regarding the tangent component of the pressure distribution in the contact zone (functions (3), (5)): this magnitude is also directly proportional to the propulsive force applied to the wheel in the contact zone, and inversely proportional to the length of the contact zone and the radius of the wheel. The distribution of vertical pressure from the action of rolling resistance forces (functions (3), (5)) indicates that this magnitude is also directly proportional to the torque applied to the wheel in the contact zone and inversely proportional to the length of the contact zone and the radius of the wheel.

From this it should be concluded that the determination of the size and boundaries of the contact zone have a decisive role in the study of the contact interaction of a deformable wheel with a deformable surface.

Solving the problem of the contact interaction of two deformable bodies of inconsistent geometric shape in the presence of normal and tangential pressures in the contact zone requires determining the length of the contact zone. In this case, the length of the contact zone should be determined taking into account the magnitudes of the applied loads, of the mechanical properties of the wheel and the supporting surface, as well as the wheel geometric parameters.

Finding the sizes and contact zones can be performed on the basis of solutions of equations (1) for the absolute vertical displacements of the wheel surfaces and the boundary of the supporting surface. In this case, one should consider the solutions of the system of obtained equations of vertical displacements at the contact boundaries.

The boundaries of the contact zone should be determined from the conditions at the edges of the contact boundary. At the rear contact boundary at the point a_1 the vertical displacement is equal to the deformation of the wheel surface $a_1^2/2r$. The second boundary condition is determined by the total displacement from the deformations of the wheel surface and the bearing surface at the beginning of the front contact boundary. This offset is 0. Based on these boundary conditions, a system of equations was compiled:

$$\begin{aligned} v_k|_{\{a_1, a \rightarrow 0\}} &= M_k \int_{a_1}^0 ((v_{1k}(F_\xi - F_{m\xi}) + v_{2k}F_{t\xi}) \frac{B\iota}{\iota^2 + (x + \iota - \xi)^2} d\xi - \frac{a_1^2}{2r}); \\ (v_k - v_p)|_{\{a, a_1 \rightarrow 0\}} &= \int_0^a \left(\left(M_k ((v_{1k}(F_\xi - F_{m\xi}) + v_{2k}F_{t\xi}) - \right. \right. \\ &\quad \left. \left. - M_p ((v_{1k}(F_\xi - F_{m\xi}) + v_{2k}F_{t\xi})) \frac{B\iota}{\iota^2 + (x + \iota - \xi)^2} \right) d\xi. \end{aligned} \quad (6)$$

The integration of these expressions is carried out taking into account that $x = \xi$.

The results of integration of expressions (6) include transcendental components in the form: $\text{ArcTan}[(a + \iota)/\iota], \ln[2\iota^2], \ln[\iota^2 + (a + \iota)^2]$. Given the fact that $\ln[f \rightarrow 0] \rightarrow (\approx 3/(2\pi))$, and

$\text{ArcTan}[(a + \iota)/\iota]_{\{a \gg 0.01, \iota \rightarrow 0\}} \rightarrow \frac{\pi}{2}$, then the expressions can be reduced to a form convenient for solving. In

the final form, the solutions of expressions (6) with respect to the values that determine the front and rear contact boundaries (taking into account the signs of the magnitudes of the front and rear boundaries of the contact) have the form:

$$a_1 = - \frac{\sqrt{6} \sqrt{g M_k m v_{1k} + \frac{M_k M v_{2k}}{r}}}{\sqrt{\frac{3r^2 + g M_k m r v_{1k} + M_k M v_{2k}}{r^3}}}; \quad (7)$$

$$a = \frac{\sqrt{2} \sqrt{6M_k M r^2 v_{1k} + g M_k m r^3 v_{1k} + 6M M_p r^2 v_{1p} + g m M_p r^3 v_{1p} + M_k M r^2 v_{2k} - M M_p r^2 v_{2p}}}{\sqrt{g M_k m r v_{1k} + g m M_p r v_{1p} + M_k M v_{2k} - M M_p v_{2p}}}$$

To simplify the analysis of expressions (7), their graphical interpretations are given. Analysis of the graphs (Fig. 4) indicates that the mass, which is given to the wheel, as well as the deformative properties of the wheel surface and the supporting surface, have a significant effect on the size of the rear part of the contact zone.

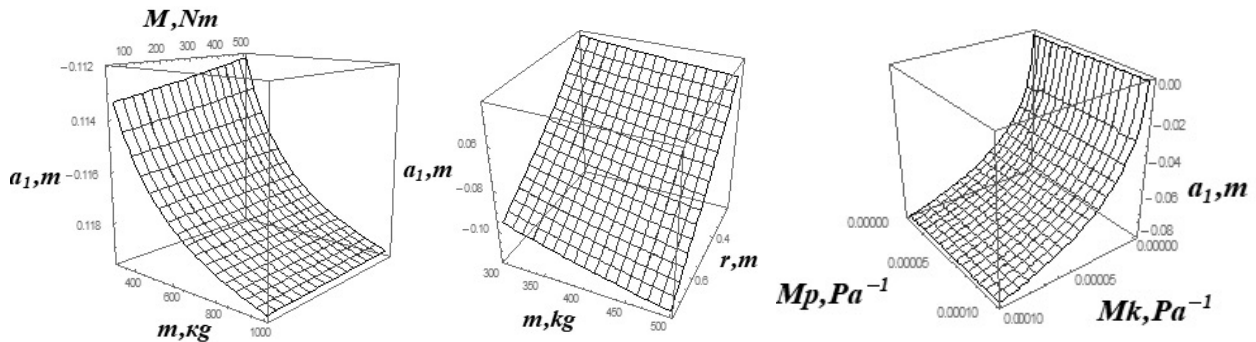


Figure 4. The plots of the dependence of the front contact zone magnitude on the wheel stress-related properties, on the mass applied to the wheel, on the the torque and wheel radius

The size of the front boundary of the contact zone also depends from the mass that applied to the wheel, as well as the deformative properties of the wheel surface and the supporting surface.

The sum magnitude of the front and back of the contact zone indicates a significant influence of the propulsive force, which is created by tangential pressure. At the same time, the mass vertical component has a smaller effect (Fig. 5–6).

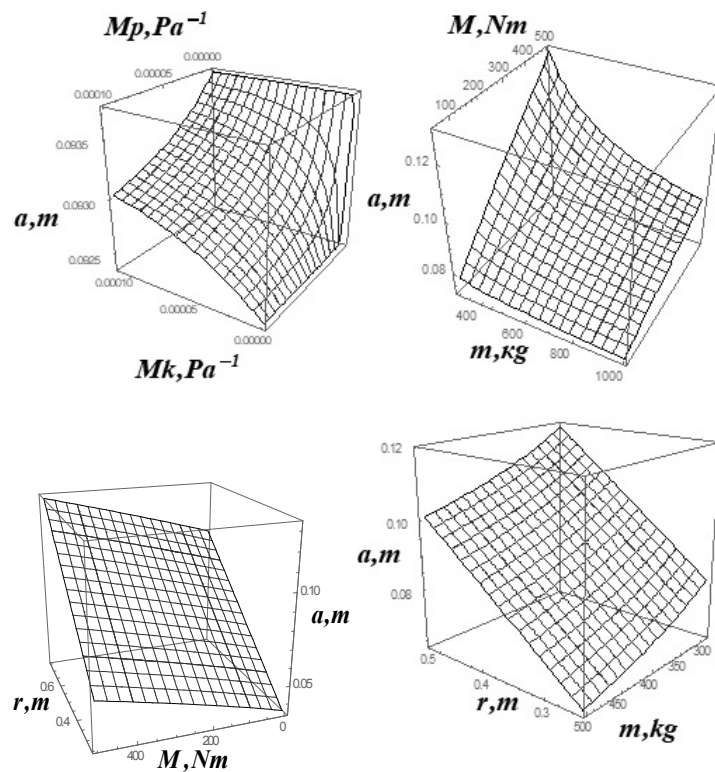


Figure 5. The plots of the dependence of the back contact zone magnitude on the wheel stress-related properties, on the mass applied to the wheel, on the the torque and wheel radius

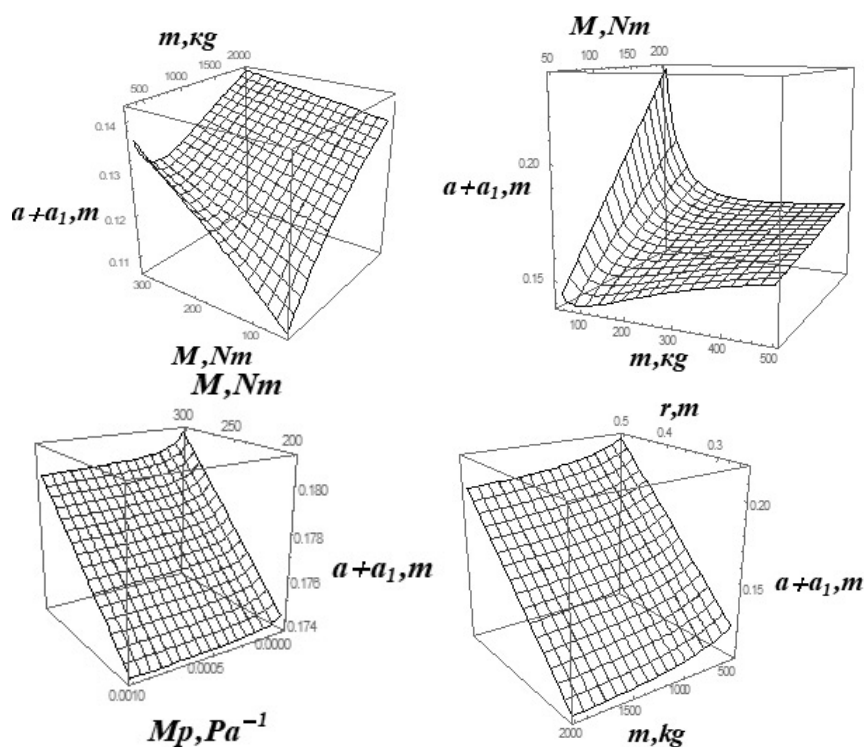


Figure 6. The plots of the dependence of the total magnitude of the contact zone on the wheel stress-related properties, on the mass applied to the wheel, on the the torque and wheel radius

Thus, the conducted studies indicate that the wheel stress-related properties the greatest influence on the size of the contact zone, in contrast to the soil stress-related properties. This may be due to less curvature of the wheel surface.

Analysis of the dependences magnitudes of front a and back a_1 contact zone of a deformable wheel with a deformable support surface allows us to draw the following conclusions:

- the size of the back boundary of the contact zone a_1 significantly depends on the deformative properties of the wheel surface M_k . The deformative properties of the supporting surface M_p do not significantly affect this magnitude;
- an increase in pressure from the propulsive force, which is created by the torque M , leads to an increase in both the front and back boundaries of the contact zone;
- an increase in the wheel geometric size r increases the size of the back and front parts of the contact zone;
- an increase of the deformative properties of the supporting surface M_p entails an increase of the front part of the contact zone;
- an increase in the mass applied to the wheel leads to an increase in the total length of the contact zone $(|a_1|+|a|)$.

Conclusions

The carried out theoretical studies made it possible to obtain analytical dependences of the influence of the wheel geometric parameters, of the mechanical properties of the supporting surface and the wheel, as well as of the dynamic loads applied to it, on the dimensions and magnitudes of the boundaries of the contact zone between the deformable wheel and the deformable support surface.

The analytical functions of the magnitudes of contact zone boundaries of the deformable wheel with the deformable supporting surface are the limits of integration of biharmonic potential functions in the Papkovitch-Neiber equations for solving this contact problem.

The obtained analytical functions can be used in the design of wheeled propulsions of various technological machines and vehicles, as well as road-building equipment.

In addition, the functional dependencies of the relationship between the dimensions of the contact zone with the parameters and loading modes of the wheel propulsion, which are presented in the work, are the initial ones for the deepening analytical studies of the contact interaction of deformable bodies of inconsistent geometric shape.

References

- 1 Ишлинский А.Ю. О качении жестких и пневматических колес по деформируемому грунту. Прикладные задачи механики. Кн. 1 / А.Ю. Ишлинский. — М.: Наука, 1986. — С. 293–314.
- 2 Ишлинский А.Ю. Математическая теория пластичности / А.Ю. Ишлинский, Д.Д. Ивлев. — М.: Физматлит, 2003. — 704 с.
- 3 Золотаревская Д.И. Взаимосвязь различных математических моделей деформирования почвы / Д.И. Золотаревская // Механизация и электрификация сельского хозяйства. — 1983. — № 5. — С. 10–16.
- 4 Золотаревская Д.И. Основы теории и методы расчета уплотняющего воздействия на почву колесных движителей мобильной сельскохозяйственной техники: дис. ... д-ра техн. наук: 05.20.01 — «Технологии и средства механизации сельского хозяйства» / Д.И. Золотаревская. — М., 1997. — 432 с.
- 5 Junlong Guoa. Linear normal stress under a wheel in skid for wheeled mobile robots running on sandy terrain / Junlong Guoa, Haibo Gaoa, Liang Ding, Tianyou Guob, Zongquan Deng // Journal of Terramechanics. — 2017. — Vol. 70. — P. 49–57.
- 6 Wanshen Xiao. Design of manned lunar rover wheels and improvement in soil mechanics formulas for elastic wheels in consideration of deformation / Wanshen Xiao, Yan Zhang // Journal of Terramechanics, — 2016. — Vol. 65. — P. 61–71.
- 7 Wang Yang. Prediction for Tire-Pavement Contact Stress under Steady-State Conditions based on 3D Finite Element Method / Wang Yang, Sun Tiecheng, Lu Yongjie, Si Chundi // Journal of Engineering Science and Technology. — 2016. — Review 9(4). — P. 17–25.
- 8 Guthrie A.G. 3D contact patch measurement inside rolling tyres / A. Glenn Guthrie, Theunis R. Botha, P. Schalk Els // Journal of Terramechanics. — 2017. — Vol. 69. — P. 13–21.
- 9 Полянин А.Д. Справочник по линейным уравнениям математической физики / А.Д. Полянин. — М.: Физматлит, 2001. — 576 с.
- 10 Новацкий В. Теория упругости / В. Новацкий. — М.: Мир, 1975. — 872 с.
- 11 Папкович П.Ф. Теория упругости / П.Ф. Папкович. — Л.; М.: Оборонпром, 1939. — 639 с.
- 12 Партон В.З. Механика упругопластического разрушения / В.З. Партон, Е.М. Морозов. — М.: Наука, 1985. — 504 с.
- 13 Александров В.М. Введение в механику контактных взаимодействий / В.М. Александров, М.И. Чебаков. — М.; Ростов н/Д., 2007. — 114 с.
- 14 Аргатов И.И. Основы теории упругого дискретного контакта / И.И. Аргатов, Н.Н. Дмитриев. — СПб.: Политехника, 2003. — 233 с.
- 15 Попов В.Л. Механика контактного взаимодействия и физика трения / В.Л. Попов. — М.: Физматлит, 2013. — 352 с.
- 16 Ковбаса В.П. Механіко-технологічні основи взаємодії робочих органів з ґрунтом / В.П. Ковбаса. — Киев; Нежин, 2016. — 298 с.
- 17 Гуцол О.П. До визначення фізичних рівнянь пружно-пластичного середовища з умовою руйнування за модифікованим критерієм Кулона-Мора / О.П. Гуцол, В.П. Ковбаса, В.П. Курка // Праці ТДАТУ. — Мелитополь, 2011. — Вып. 11, Т. 2. — С. 161–174.

В.П. Ковбаса, А.В. Соломка, А.В. Спирин,
В.Ю. Кучерук, Д.Ж. Карабекова, А.К. Хасенов

Деформацияланатын жетек доңғалағының топырақпен әрекеттесуі кезінде күштердің таралуы мен байланыс шекараларының мөлшерін теориялық анықтау

Мақалада деформацияланатын тірек бетіндегі деформацияланатын жетек доңғалағының байланыс қисығының ұзындығы бойынша күштердің таралуын аналитикалық анықтау нәтижелері келтірілген және оның байланыс аймағының шекаралары анықталған. Мәселенің тегіс тұжырымындағы жағдай қарастырылған. Деформацияланатын доңғалақтың тірек беті мен беті серпімді модульдермен және Пуассон коэффициенттерімен сипатталатын үздіксіз деформацияланатын орта ретінде ұсынылған. Доңғалақ оған берілген салмақ күшімен және байланыс аймағында қозғалмалы күш тудыратын моментпен жүктеледі. Мұндай өндіріс жалпы болып табылады және пассивті доңғалақтың жанасуы үшін қолданылуы мүмкін. Байланыс аймағындағы доңғалақтың пішіні шеңбер теңдеуімен ұсынылған, ол байланыс аймағында Маклорен қатарына бөлінеді, бұл шешімнің нәтижесіне айтарлықтай әсер етпейді. Контакт аймағының шекарасындағы шарттарды қолдана отырып, теңдеулер жүйесі алынған, оның көмегімен контакт аймағы өлшемдерінің шамалары анықталған. Бұл теңдеулер жүйесін шешу

доңғалақтың материалдары мен тірек бетінің Пуассонының серпімділік модульдері мен коэффициенттеріне, оған қоса берілген доңғалақ пен жүктемелердің геометриялық өлшемдеріне байланысты деформацияланатын доңғалақтың деформацияланатын бетімен байланыс аймағының өлшемдерін көрсетті. Зерттеу нәтижелері бойынша доңғалақ беті мен тірек бетінің абсолютті және салыстырмалы деформацияларын, байланыс аймағынан тыс контактілі денелердегі кернеулердің таралуын анықтауға негіз болып табылады, сонымен қатар деформацияланатын доңғалақтың деформацияланатын бетке айналу кедергісі коэффициентінің аналитикалық көрінісін олардың механикалық қасиеттеріне, геометриялық параметрлеріне және қолданылатын жүктемелеріне байланысты анықтауға мүмкіндік береді.

Кілт сөздер: деформацияланатын доңғалақ, деформацияланатын тірек беті, байланыс аймағының шекаралары, қолданылатын жүктемелер, байланыс аймағында қысымның таралуы, абсолютті деформациялар.

В.П. Ковбаса, А.В. Соломка, А.В. Спирин,
В.Ю. Кучерук, Д.Ж. Карабекова, А.К. Хасенов

Теоретическое определение распределения сил и размера границ контакта при взаимодействии деформируемого приводного колеса с почвой

В статье представлены результаты аналитического определения распределения сил по длине кривой контакта приводного деформируемого колеса на деформируемой опорной поверхности и определены границы зоны его контакта. Рассмотрен случай в плоской постановке задачи. Опорная поверхность и поверхность деформируемого колеса даны как сплошная деформируемая среда, которая характеризуется модулями упругости и коэффициентами Пуассона. Колесо нагружено силой веса, приведенной к нему, и крутящим моментом, который создает в зоне контакта движущую силу. Такая постановка является общей и может быть применена также для контакта пассивного колеса. Форма колеса в зоне контакта представлена уравнением окружности, которое разложено в ряд Маклорана в зоне контакта, что не оказывает существенного влияния на результат решения. С использованием условий на границе зоны контакта получена система уравнений, из которой определены величины размеров зоны контакта. Решение этой системы уравнений дало выражение размеров зоны контакта деформируемого колеса с деформируемой поверхностью в зависимости от модулей упругости и коэффициентов Пуассона материалов колеса и опорной поверхности, геометрических размеров колеса и нагрузок, приложенных к нему. Результаты проведенных исследований являются основой для определения абсолютных и относительных деформаций поверхности колеса и опорной поверхности, распределения напряжений в контактирующих телах за пределами зоны контакта, а также позволяют определить аналитическое выражение коэффициента сопротивления перекатывания деформируемого колеса по деформируемой поверхности в зависимости от их механических свойств, геометрических параметров и приложенных нагрузок.

Ключевые слова: деформируемое колесо, деформируемая опорная поверхность, границы зоны контакта, приложенные нагрузки, распределение давления в зоне контакта, абсолютные деформации.

References

- 1 Ishlinskiy, A.Yu. (1986). *O kachenii zhestkikh i pnevmaticheskikh koles po deformiruемому hruntu. Prikladnye zadachi mekhaniki. Knizha 1 [About rolling hard and pneumatic wheels on deformable soil. Applied problems of mechanics. Book 1]*. Moscow: Nauka [in Russian].
- 2 Ishlinskiy, A. Yu., & Ivlev, D.D. (2003). *Matematicheskaya teoriya plastichnosti [Mathematical Theory of Plasticity]*. Moscow: Fizmatlit [in Russian].
- 3 Zolotarevskaya, D.I. (1983). *Vzaimosvyez razlichnykh matematicheskikh modelei deformirovaniya pochvy [The relationship of various mathematical models of soil deformation]*. *Mekhanizatsiya i elektrifikatsiya selskogo khoziaistva — Mechanization and electrification of agriculture*, 5, 10–16 [in Russian].
- 4 Zolotarevskaya, D.I. (1997). *Osnovy teorii i metody rascheta uplotniayushchego vozdeystviya na pochvu kolesnykh dvizhitelei mobilnoi selskokhoziaistvennoi tekhniki [Fundamentals of the theory and methods of calculating the sealing effect on the soil of wheeled movers of mobile agricultural machinery]*. *Doctor's thesis*. Moscow [in Russian].
- 5 Junlong Guoa, Haibo Gaoa, Liang Ding, Tianyou Guob, & Zongquan Deng (2017). *Linear normal stress under a wheel in skid for wheeled mobile robots running on sandy terrain*. *Journal of Terramechanics*, 70(4), 49–57.
- 6 Wanshen Xiao, & Yan Zhang (2016). *Design of manned lunar rover wheels and improvement in soil mechanics formulas for elastic wheels in consideration of deformation*. *Journal of Terramechanics*, 65(6), 61–71.
- 7 Wang Yang, Sun Tiecheng, Lu Yongjie, & Si Chundi (2016). *Prediction for Tire-Pavement Contact Stress under Steady-State Conditions based on 3D Finite Element Method*. *Journal of Engineering Science and Technology*, 9(4), 17–25.

- 8 Guthrie, A.G., Botha, T.R., & Els, P.S. (2017). 3D contact patch measurement inside rolling tyres. *Journal of Terramechanics*, 69(2), 13–21.
- 9 Polyinin, A.D. (2001). *Spravochnik po lineinym uravneniiam matematicheskoi fiziki [Handbook of linear equations of mathematical physics]*. Moscow: Fizmatlit [in Russian].
- 10 Novatskiy, V. (1975). *Teoriia uprugosti [Elasticity theory]*. Moscow: Mir [in Russian].
- 11 Papkovich, P.F. (1939). *Teoriia uprugosti [Elasticity theory]*. Leningrad; Moscow: Oboronprom [in Russian].
- 12 Parton, V.Z., & Morozov, E.M. (1985). *Mekhanika upruhoplasticheskoho razrusheniia [Mechanics of Elastoplastic Destruction]*. Moscow: Nauka [in Russian].
- 13 Aleksandrov, V.M., & Chebakov, M.I. (2007). *Vvedenie v mekhaniku kontaktnykh vzaimodeistvii [Introduction to the Mechanics of Contact Interactions]*. Moscow [in Russian].
- 14 Argatov, I.I., & Dmitriev, N.N. (2003). *Osnovy teorii uprugoho diskretnogo kontakta [Fundamentals of the theory of elastic discrete contact]*. Saint Petersburg: Politekhnik [in Russian].
- 15 Popov, V.L. (2013). *Mekhanika kontaktnoho vzaimodeistviia i fizika treniia [Contact mechanics and physics of friction]*. Moscow: Fizmatlit [in Russian].
- 16 Kovbasa, V.P. (2016). *Mekhaniko-tehnologichni osnovi vzayemodiyi robochih orhaniv z hruntom [Mechanical and technological bases of interaction of tools with soil]*. Kyiv; Nezhyn [in Ukrainian].
- 17 Gucol, O.P., Kovbasa, V.P., & Kurka V.P. (2011). Do viznachennia fizichnih rivnyan pruzhnov'yazko-plastichnogo seredovischa z umovoyu ruynuvannia za modifikovanim kriteriem Kulona-Mora [On the determination of the physical equations of an elastic-viscous-plastic medium with the condition of destruction by the modified Coulomb-Mohr criterion] *Praci Tavriiskoho derzhavnoho ahrotehnologichnogo universitetu — Proceedings of the Tavria State Agrotechnological University*, 11(2), 161–174 [in Ukrainian].

A.P. Sarode^{1*}, O.H. Mahajan²

¹*Dr. A.G.D. Bendale Girls College, Jalgaon, India;*

²*M.J. College, Jalgaon, India*

(*E-mail: abhijitsarode@yahoo.com)

Theoretical aspects of transient temperature on cubic crystal surface in a photoacoustic effect

In photoacoustic effect, the solid sample absorbs a fraction of the radiation falling upon it and excitation process occurs. The type of excitation depends on the energy of the incident radiation. The relaxation processes, which are also popularly known as non-radiative de-excitation processes generally take place. The light – matter interaction is responsible for the generation of heat within the solid sample. The temperature of the sample changes due to absorption and non-radiative relaxation by the atoms. The pressure fluctuations will be generated due to the heating and cooling of the sample. Today, crystalline solids are widely studied due to their wide scientific and industrial applications. Temperature is one of the important parameter to be studied regarding artificial preparation of large crystals. In this paper, transient translational temperature on the surface of a homogeneous isotropic cubic crystal kept in a photoacoustic cell is calculated theoretically. For a simple cubic homogeneous crystal kept in a photoacoustic cell, an airy stress function is determined based on laser interaction with surface of the crystal. By applying the finite Marchi-Fasulo integral transform method within the crystal size limitations, transient translational temperature is exactly determined.

Keywords: airy stress function, cubic crystal, energy transfer, light – matter interaction, Marchi-Fasulo transform, non-radiative de-excitation, photoacoustic cell, photoacoustic effect, transient temperature,

Introduction

Photoacoustic effect is a phenomenon in which electromagnetic radiation is absorbed by molecules of sample material. In 1880–1881, Alexander Graham Bell [1] found the interaction of light with solid. When mechanically chopped sunlight incident on a thin disk, sound waves were generated. This effect is called as Photoacoustic effect. The conversion of an optical signal into an acoustic signal takes place in photoacoustic effect [2]. The solid sample absorbs a fraction of the radiation falling upon it and excitation process occurs. The type of excitation depends on the energy of the incident radiation. The relaxation processes, which are also popularly known as non-radiative de-excitation processes generally, take place. The light – matter interaction is responsible for the generation of heat within the solid sample [3].

Rosencwaig initiated theoretical explanation of temperature of solids during photoacoustic interaction [4]. Rosencwaig and Gersho presented a one dimensional model regarding heat flow and temperature [5]. McDonald and Wetsel presented temperature calculations of photoacoustic interaction in three dimensional model with restrictions on thermal waves in transverse direction [2]. Quimby and Yen primarily calculated the surface heat conductance in temperature estimation [6]. Chow developed a three dimensional model in a general way without any restrictions on sample size in photoacoustic cell [7]. In the recent years, Merzadinova et. al calculated ambient temperature of a solid in thermal diffusivity determination of structurally inhomogeneous, multilayer and composite solids in photoacoustic interaction [8].

In this paper, an attempt has been made to calculate transient translational temperature on the surface of a homogeneous isotropic cubic crystal kept in a photoacoustic cell. Determination of transient translational temperature will be helpful in the development of a methodology of stress determination in photoacoustic problems.

Situation of the crystal

Consider a cubic crystal placed in a photoacoustic cell. The crystal is isotropic and homogeneous in nature. This crystal is placed in a cylindrical cavity of a photoacoustic cell where it produces a photoacoustic signal.

The Photoacoustic effect is directly related with on heating of the sample due to the phenomenon of optical absorption [9, 10]. Periodic processes of heating and cooling of the solid sample are necessary because it will develop pressure fluctuations should be generated in the cell [11]. These fluctuations can be detected by a sensitive sensor.

In the schemes of modulated excitation, sources of radiation are used in which intensity periodically fluctuates [12–16]. These intensity fluctuations are in the form of a sine wave or a square wave. This is similar to mechanical chopping of a radiation source. This method can be overcome by modulating the phase of the optical signal instead of its amplitude [17–19]. The most common sources in Photoacoustic analysis are the use of modulated continuous wave lasers.

Two level system model

To describe the absorption of light, consider a two level system, in which energy transfers take place, as shown in Figure 1. These energy transfers are radiative and non-radiative. Let us consider two states i and j . Also, consider the coefficients r_{ij} and c_{ij} . The radiative transition rate is r_{ij} and non-radiative transition rate is c_{ij} . The coefficient c_{ij} is also called collision-induced energy transfer. Now, introduce Einstein coefficients for stimulated and spontaneous emission, B_{ij} and A_{ij} . Consider that ρ_ω be the spectral energy density for the corresponding frequency of the transition between E_0 and E_6 . Einstein coefficients can be expressed as

$$r_{ij} = \rho_\omega B_{ij} + A_{ij} \tag{1}$$

The quantity ρ_ω measures the radiant energy per volume per unit frequency and can be expressed in terms of units JS/m^3 .

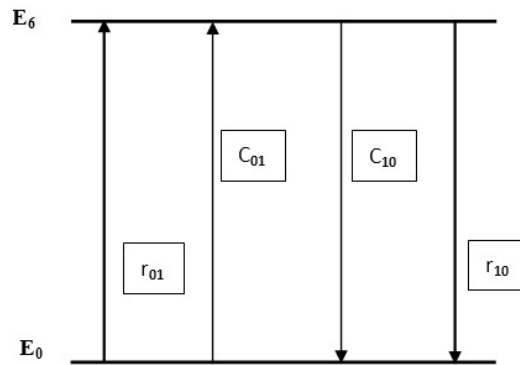


Figure 1. A schematic representation of a two level system

Note that $B_{ij} = B_{ji}$ so that $B_{06} = B_{60}$. But $A_{06} = 0$ because spontaneous emission from a state of lower energy to that of higher energy does not exist. Hence $r_{06} = \rho_\omega B_{06}$. Again, the probability of excitation due to collision from E_0 to E_6 is very low, Therefore, approximately we can say, $c_{06} \sim 0$.

Let us determine the rate of transition. For this calculation, we must distinguish the population densities of absorbing molecules in the ground and excited states. Consider these population densities as n_0 and n_6 , respectively corresponding to energies E_0 and E_6 . To calculate the rate of change of population in upper state, we must consider the difference between the number of molecules entering and leaving the excited state:

$$\begin{aligned} \dot{n}_6 &= (r_{06} + c_{06})n_0 - (r_{60} + c_{60})n_6 \\ \dot{n}_6 &= \rho_\omega B_{06}n_0 - (\rho_\omega B_{06} + A_{60} + c_{60})n_6 \\ \dot{n}_6 &= \rho_\omega B_{06}(n_0 - n_6) - (A_{60} + c_{60})n_6 \end{aligned} \tag{2}$$

Let the radiative and collisional time constants be $\tau_r = 1/A_{60}$ and $\tau_c = 1/c_{60}$ respectively.

The total time constant is, then addition of radiative and collisional time constants:

$$\tau = \tau_r + \tau_c.$$

Mathematical formulation

Assume that the cubic crystal placed in the cell is occupying the space. This space is defined mathematically, as

$$D: -a \leq x \leq a, -a \leq y \leq a, -a \leq z \leq a.$$

Consider a Cartesian co-ordinate system, in which the displacement components are u_x, u_y, u_z in the x, y, z direction respectively. These displacement components can be expressed in the integral form as

$$u_x = \int \left[\frac{1}{Y} \left(\frac{\partial^2 U}{\partial y^2} + \frac{\partial^2 U}{\partial z^2} - \nu \frac{\partial^2 U}{\partial x^2} \right) + \lambda T \right] dx; \quad (2.1)$$

$$u_y = \int \left[\frac{1}{Y} \left(\frac{\partial^2 U}{\partial z^2} + \frac{\partial^2 U}{\partial x^2} - \nu \frac{\partial^2 U}{\partial y^2} \right) + \lambda T \right] dy; \quad (2.2)$$

$$u_z = \int \left[\frac{1}{Y} \left(\frac{\partial^2 U}{\partial x^2} + \frac{\partial^2 U}{\partial y^2} - \nu \frac{\partial^2 U}{\partial z^2} \right) + \lambda T \right] dz. \quad (2.3)$$

Where Y, ν and λ are the Young modulus, the poisson ratio and the coefficient of linear thermal expansion of the material of the crystal respectively. Consider that $U(x, y, z, t)$ is the Airy stress function which satisfies the differential equation.

$$\left(\frac{\partial^2}{\partial x^2} + \frac{\partial^2}{\partial y^2} + \frac{\partial^2}{\partial z^2} \right)^2 U(x, y, z, t) = -\lambda Y \left(\frac{\partial^2}{\partial x^2} + \frac{\partial^2}{\partial y^2} + \frac{\partial^2}{\partial z^2} \right)^2 T(x, y, z, t). \quad (2.4)$$

Here $T(x, y, z, t)$ denotes the temperature of the crystal satisfying the following differential equation,

$$\frac{\partial^2 T}{\partial x^2} + \frac{\partial^2 T}{\partial y^2} + \frac{\partial^2 T}{\partial z^2} + \frac{\theta(x, y, z, t)}{k} = \frac{1}{\alpha} \frac{\partial T}{\partial t}, \quad (2.5)$$

where k is thermal conductivity and α is the thermal diffusivity of the material of the crystal.

Let $\theta(x, y, z, t)$ is heat generated within the crystal for $t > 0$ subject to initial conditions

$$T(x, y, z, 0) = F(x, y, z). \quad (2.6)$$

The boundary conditions are

$$\left[T(x, y, z, t) + k_1 \frac{\partial T(x, y, z, t)}{\partial x} \right]_{x=-a} = F_1(y, z, t); \quad (2.7)$$

$$\left[T(x, y, z, t) + k_2 \frac{\partial T(x, y, z, t)}{\partial x} \right]_{x=a} = F_2(y, z, t); \quad (2.8)$$

$$\left[T(x, y, z, t) + k_3 \frac{\partial T(x, y, z, t)}{\partial y} \right]_{y=-a} = F_3(x, z, t); \quad (2.9)$$

$$\left[T(x, y, z, t) + k_4 \frac{\partial T(x, y, z, t)}{\partial y} \right]_{y=a} = F_4(x, z, t); \quad (2.10)$$

$$\left[T(x, y, z, t) + k_5 \frac{\partial T(x, y, z, t)}{\partial z} \right]_{z=-a} = f_1(x, y, t); \quad (2.11)$$

$$\left[T(x, y, z, t) + k_6 \frac{\partial T(x, y, z, t)}{\partial z} \right]_{z=a} = f_2(x, y, t). \quad (2.12)$$

The components in term of $U(x, y, z, t)$ are given by

$$\sigma_{xx} = \left(\frac{\partial^2 U}{\partial y^2} + \frac{\partial^2 U}{\partial z^2} \right); \quad (2.13)$$

$$\sigma_{yy} = \left(\frac{\partial^2 U}{\partial z^2} + \frac{\partial^2 U}{\partial x^2} \right); \tag{2.14}$$

$$\sigma_{zz} = \left(\frac{\partial^2 U}{\partial x^2} + \frac{\partial^2 U}{\partial y^2} \right). \tag{2.15}$$

The equations (2.1) to (2.15) constitute the mathematical formulation of the conditions of the crystal under consideration.

Mathematical solution

The finite Marchi-Fasulo integral transform of $f(z)$, within limitations $-h < z < h$ is defined to be

$$\bar{F} = \int_{-h}^h f(z) P_n(z) dz. \tag{3.1}$$

Then at each point of $(-h, h)$ at which $f(z)$ is continuous.

Also the inverse finite Marchi-Fasulo transform is defined as

$$f(z) = \sum_{n=1}^{\infty} \frac{\bar{F}(n)}{\lambda_n} P_n(z), \tag{3.2}$$

where

$$\begin{aligned} P_n(z) &= Q_n \cos(a_n z) - W_n \sin(a_n z); \\ Q_n &= a_n (\alpha_1 + \alpha_2) \cos(a_n h) + (\beta_1 - \beta_2) \sin(a_n h); \\ W_n &= (\beta_1 + \beta_2) \cos(a_n h) + (\alpha_1 - \alpha_2) a_n \sin(a_n h); \\ \lambda_n &= \int_{-h}^h P_n^2(z) dz = \\ &= h [Q_n^2 + W_n^2] + \frac{\sin(2a_n h)}{2a_n} [Q_n^2 - W_n^2]. \end{aligned}$$

The Eigen values a_n are the solutions of the equation

$$\begin{aligned} [\alpha_1 a \cos(ah) + \beta_1 \sin(ah)] \times [\beta_2 \cos(ah) + \alpha_2 a \sin(ah)] &= [\alpha_2 a \cos(ah) - \beta_2 \sin(ah)] \times \\ &\times [\beta_1 \cos(ah) - \alpha_1 a \sin(ah)] \end{aligned} \tag{3.3}$$

Where $\alpha_1, \alpha_2, \beta_1, \beta_2$ are constants.

By applying the finite Marchi-Fasulo transform three times to equation (2.5) and their inverses, we obtain

$$\frac{d\bar{T}^*}{dt} + \infty q^2 \bar{T}^* = \infty \left(\emptyset + \frac{\bar{\theta}^*}{k} \right), \tag{3.4}$$

where $\emptyset = P_m(a)F_2 - P_m(-a)F_1 + P_n(b)F_4 - P_n(-b)F_3 + P_l(h)f_2 - P_l(-h)f_1$

$$\text{and } q^2 = a_m^2 + a_n^2 + a_l^2 \text{ is Eigen value.} \tag{3.5}$$

Equation (3.4) is first order differential equation and has solution

$$\bar{T}^*(m, n, l, t) = e^{-\infty q^2 t} \left[\int_0^t \infty \left(\emptyset + \frac{\bar{\theta}^*}{k} \right) e^{\infty q^2 t' dt'} + c, c = \bar{F}^*(m, n, l) \right]; \tag{3.6}$$

$$\bar{T}^*(m, n, l, t) = \int_0^t \infty \left(\emptyset + \frac{\bar{\theta}^*}{k} \right) e^{\infty (a_m^2 + a_n^2 + a_l^2)(t-t') dt'} + e^{-\infty (a_m^2 + a_n^2 + a_l^2)t} \bar{F}^*(m, n, l). \tag{3.7}$$

Applying inverse finite Marchi- Fasulo Transform three times with boundary conditions, we get

$$T(x, y, z, t) = \sum_{m, n, l=1}^{\infty} \left[\frac{P_m(x)}{\lambda_m} \right] \left[\frac{P_n(y)}{\mu_n} \right] \left[\frac{P_l(z)}{\nu_l} \right] \left\{ \int_0^t \infty \left(\varnothing + \frac{\bar{\theta}^*}{k} \right) e^{\infty(a_m^2 + a_n^2 + a_l^2)(t-t')dt'} + e^{-\infty(a_m^2 + a_n^2 + a_l^2)t} F^*(m, n, l) \right\}. \quad (3.8)$$

Conclusion

An exact expression for the transient translational temperature on the surface of a cubic crystal in a photoacoustic cell is mathematically determined using Marchi-Fasulo method in terms of thermal conductivity of material of the crystal.

The result obtained will be helpful in the study of cubic crystals, and their various properties such as elasticity, stress, strain, etc. in photoacoustic cell. The elastic parameters of the crystals are studied more than only academic interest. Crystals of better quality and large size are synthetically prepared in application point of view. Transient translational temperature determination will provide a base for surface behavior of crystals of different materials in laser interactions in Photoacoustic effect. This work will also be useful in research for scientific and industrial applications in future.

References

- 1 Bell A. Photoacoustic imaging and spectroscopy / A. Bell // American Journal of Science. — 1980. — Vol. 20. — P. 305–324.
- 2 McDonald F. Generalized theory of the photoacoustic effect / F. McDonald, G. Wetsel // Journal of Applied Physics. — 1978. — Vol. 49. — P. 2313–2322.
- 3 Markushev D. The surface recombination velocity and bulk lifetime influences on photogenerated excess carrier density and temperature distributions in n-type silicon excited by a frequency-modulated light source / D. Markushev, S. Galovic, S. Aleksic, D. Pantic, D. Todorovic // DM FU Elect Energy. — 2018. — Vol. 31, No. 2. — P. 313–328.
- 4 Rosencwaig A. Photoacoustic spectroscopy of solids / A. Rosencwaig // Physics Today. — 1975. — Vol. 28, No. 9. — P. 23–30.
- 5 Rosencwaig A. Theory of the photoacoustic effect with solids / A. Rosencwaig, A. Gersho // Journal of Applied Physics. — 1976. — Vol. 47. — P. 64–68.
- 6 Quimby R. Photoacoustic theory including energy migration / R. Quimby, W. Yen // Journal of Applied Physics. — 1980. — Vol. 51. — P. 4985–4990.
- 7 Chow H. Theory of three-dimensional photoacoustic effect with solids / H. Chow // Journal of Applied Physics. — 1980. — Vol. 51. — P. 4053–4056.
- 8 Merzadinova G. Laser photoacoustics method for determination of the coefficients of thermal conductivity and thermal diffusivity of materials / G. Merzadinova, K. Sakipov, D. Sharifov, A. Mirzo, A. Bekeshev // Eurasian Physical Technical Journal. — 2019. — Vol. 16, No. 1(31). — P. 94–98.
- 9 Sigrist M. Photoacoustic spectroscopy, method and instrumentation / M. Sigrist // Encyclopedia of spectroscopy and spectrometry. — 1999. — Vol. 3. — P. 1810–812.
- 10 Djordjevic K. Photoacoustic measurements of the thermal and elastic properties of n-type silicon using neural networks / K. Djordjevic, D. Markushev, Z. Cojbasic // Silicon. — 2020. — Vol. 12, No. 6. — P. 1289–1300.
- 11 Carslaw H. Conduction of heat in solids / H. Carslaw, J.C. Jaeger. — Oxford: Oxford Clarendon Press, 1959.
- 12 Zheng H. Single-tube on-beam quartz-enhanced photoacoustic spectroscopy / H. Zheng, L. Dong, A. Sampaolo, H. Wu, P. Patimisco, X. Yin, et al. // Optics Letters. — 2016. — Vol. 41. — P. 978–981.
- 13 Nosaka Y. Pulsed photoacoustic spectroscopy for powder suspension using a flash lamp / Y. Nosaka, R. Igarashi, H. Miyama // Analytical Chemistry. — 1985. — Vol. 57, No. 1. — P. 92–94.
- 14 Zhou S. Demonstration of a highly sensitive photoacoustic spectrometer based on a miniaturized all-optical detecting sensor / S. Zhou, M. Slaman, D. Iannuzzi // Opt. Express. — 2017. — Vol. 25. — P. 17541–17548.
- 15 Mikkonen T. Broadband cantilever-enhanced photoacoustic spectroscopy in the mid-IR using a supercontinuum / T. Mikkonen, C. Amiot, A. Aalto, K. Patokoski, G. Genty, J. Toivonen // Optics Letters. — 2018. — Vol. 43. — P. 5094–5097.
- 16 Salikhov T. To the theory of generation of photoacoustic signal by solid state samples / T. Salikhov, N. Melikkhudza, Y. Khodzhaev, I. Khodzhaev // Докл. АН Республики Таджикистан. — 2017. — Т. 60, № 11, 12. — С. 569–574.
- 17 Agilar C. Photoacoustic Spectroscopy in the Optical Characterization of Foodstuff: A Review / C. Agilar, A. Pachec // Hindawi Journal of Spectroscopy. — 2019. — Vol. 2019. — P. 1–34.
- 18 Zhou M. A noise reduction method for photoacoustic imaging *in vivo* based on EMD and conditional mutual information / M. Zhou, H. Xia, H. Zhong // IEEE Photonics Journal. — 2019. — Vol. 11, No. 1. — P. 99–107.
- 19 Pan Y. Cavity-enhanced photoacoustic sensor based on a whispering-gallery-mode diode laser / Y. Pan, L. Dong, H. Wu, W. Ma // Atmospheric Measurements Techniques. — 2019. — Vol. 12. — P. 1905–1911.

А.П. Сарод, О.Х. Махаджан

Фотоакустикалық әсердегі текше кристалдың бетіндегі өтпелі температураның теориялық аспектілері

Фотоакустикалық әсер кезінде қатты үлгі оған түсетін сәулеленудің бір бөлігін жұтады және қозу процесі жүреді. Қозу түрі түскен сәулеленудің энергиясына байланысты. Түссізденудің радиациялық емес процестер ретінде де белгілі релаксация процестері өз орынын алады. Жарық пен заттың өзара әрекеттесуі қатты үлгінің ішінде жылу шығаруға жауап береді. Үлгінің температурасы атомдардың жұтылуына және радиациялық емес релаксациясына байланысты өзгереді. Қысымның ауытқуы үлгіні қыздыру мен салқындатуға байланысты пайда болады. Бүгінгі таңда кристалды қатты заттар олардың кең ғылыми және өнеркәсіптік қолданылуына байланысты кеңінен зерттелуде. Температура — үлкен кристалдарды жасанды түрде алу кезінде зерттелетін маңызды параметрлердің бірі. Жұмыста фотоакустикалық ұяшықта сақталатын біртекті изотропты текше кристалдың бетіндегі өтпелі аудармалы температура теориялық тұрғыдан есептелген. Фотоакустикалық ұяшықтағы қарапайым текше біртекті кристалл үшін кристалл бетімен лазерлік өзара әрекеттесуге негізделген Эйри кернеуінің функциясы анықталған. Марки-Фасулоның ақырғы интегралдық түрлендіру әдісін кристалл мөлшерінің шектеулері аясында қолдана отырып, өтпелі аударма температурасын дәл анықтауға болады.

Кілт сөздер: Эйри кернеуінің функциясы, текше кристалл, энергияны тасымалдау, жарық пен заттың өзара әрекеттесуі, Марки-Фасулоның түрленуі, радиациялық емес қозу, фотоакустикалық жасуша, фотоакустикалық әсер, өтпелі температура.

А.П. Сарод, О.Х. Махаджан

Теоретические аспекты переходной температуры на поверхности кубического кристалла в фотоакустическом эффекте

При фотоакустическом эффекте твердый образец поглощает часть падающего на него излучения и происходит процесс возбуждения. Тип возбуждения зависит от энергии падающего излучения. Релаксационные процессы, которые также широко известны как нерадиационные процессы высвечивания, обычно имеют место. Взаимодействие света и вещества ответственно за генерацию тепла внутри твердого образца. Температура образца подвергается изменению за счет поглощения и нерадиационной релаксации атомами. Колебания давления будут генерироваться из-за нагрева и охлаждения образца. Сегодня кристаллические твердые тела широко изучаются благодаря их широкому научному и промышленному применению. Температура является одним из важных параметров, подлежащих изучению при искусственном получении крупных кристаллов. В настоящей работе теоретически рассчитана переходная поступательная температура на поверхности однородного изотропного кубического кристалла, удерживаемого в фотоакустической ячейке. Для простого кубического однородного кристалла, содержащегося в фотоакустической ячейке, определяется функция напряжения Эйри, основанная на лазерном взаимодействии с поверхностью кристалла. Применяя метод конечных интегральных преобразований Марки-Фасуло в рамках ограничений размера кристалла, можно точно определить переходную поступательную температуру.

Ключевые слова: функция напряжения Эйри, кубический кристалл, перенос энергии, взаимодействие света и вещества, преобразование Марки-Фасуло, нерадиационное де-возбуждение, фотоакустическая ячейка, фотоакустический эффект, переходная температура.

References

- 1 Bell, A. (1980). Photoacoustic imaging and spectroscopy. *American Journal of Science*, 20, 305–324.
- 2 McDonald, F., & Wetsel, G. (1978). Generalized theory of the photoacoustic effect. *Journal of Applied Physics*, 49, 2313–2322.
- 3 Markushev, D., Galovic, S., Aleksic, S., Pantic, D., & Todorovic D. (2018). The surface recombination velocity and bulk lifetime influences on photogenerated excess carrier density and temperature distributions in n-type silicon excited by a frequency-modulated light source. *DM FU Elect Energy*, 31(2), 313–328.
- 4 Rosencwaig, A. (1975). Photoacoustic spectroscopy of solids. *Physics Today*, 28(9), 23–30.
- 5 Rosencwaig, A., & Gersho, A. (1976). Theory of the photoacoustic effect with solids. *Journal of Applied Physics*, 47, 64–68.
- 6 Quimby, R., & Yen, W. (1980). Photoacoustic theory including energy migration. *Journal of Applied Physics*, 51, 4985–4990.
- 7 Chow, H. (1980). Theory of three-dimensional photoacoustic effect with solids. *Journal of Applied Physics*, 51, 4053–4056.

- 8 Merzadinova, G., Sakipov, K., Sharifov, D, Mirzo, A., & Bekeshev, A. (2019). Laser photoacoustics method for determination of the coefficients of thermal conductivity and thermal diffusivity of materials. *Eurasian Physical Technical Journal*, 16, 1(31), 94–98.
- 9 Sigrist, M. (1999). Photoacoustic spectroscopy, method and instrumentation. *Encyclopedia of spectroscopy and spectrometry*, 3, 1810–812.
- 10 Djordjevic, K., Markushev, D., & Cojbasic, Z. (2019). Photoacoustic Measurements of the Thermal and Elastic Properties of n-Type Silicon Using Neural Networks. *Silicon*, 12(6), 1289–1300.
- 11 Carslaw H., & Jaeger, J.C. (1959). *Conduction of heat in solids*. Oxford: Oxford Clarendon Press.
- 12 Zheng, H., Dong, L., Sampaolo, A., Wu, H., Patimisco, P., & Yin, X., et al. (2016). Single-tube on-beam quartz-enhanced photoacoustic spectroscopy. *Optics Letters*, 41, 978–981.
- 13 Nosaka, Y., Igarashi, R., & Miyama, H. (1985). Pulsed photoacoustic spectroscopy for powder suspension using a flash lamp. *Analytical Chemistry*, 57(1), 92–94.
- 14 Zhou, S., Slaman, M., & Iannuzzi, D. (2017). Demonstration of a highly sensitive photoacoustic spectrometer based on a miniaturized all-optical detecting sensor. *Opt. Express*, 25, 17541–17548.
- 15 Mikkonen, T., Amiot, C., Aalto, A., Patokoski, K., Genty, G., & Toivonen, J. (2018). Broadband cantilever-enhanced photoacoustic spectroscopy in the mid-IR using a supercontinuum. *Optics Letters*, 43, 5094–5097.
- 16 Salikhov, T., Melikkhudza, N., Khodzhaev, Y., & Khodzhakhonov, I. (2017). To the theory of generation of photoacoustic signal by solid state samples. *Doklady Akademii nauk Respubliki Tadjikistan — Reports of the Academy of Sciences of the Republic of Tajikistan*, 60(11–12), 569–574.
- 17 Agilar, C., & Pachec, A. (2019). Photoacoustic Spectroscopy in the Optical Characterization of Foodstuff: A Review. *Hindawi Journal of Spectroscopy*, 2019, 1–34.
- 18 Zhou, M., Xia, H., & Zhong, H. (2019). A noise reduction method for photoacoustic imaging *in vivo* based on emd and conditional mutual information. *IEEE Photonics Journal*, 11(1), 99–107.
- 19 Pan, Y., Dong, L., Wu, H., & Ma, W. (2019). Cavity-enhanced photoacoustic sensor based on a whispering-gallery-mode diode laser. *Atmospheric Measurements Techniques*, 12, 1905–1911.

Yu.A. Udovytska¹, S.V. Luniov^{1*}, V.T. Maslyuk², I.G. Megela²

¹*Lutsk National Technical University, Ukraine;*

²*Institute of electronic physics NAS of Ukraine, Uzhgorod, Ukraine*

(*E-mail: luniovser@ukr.net)

Influence of electron irradiation on mechanical properties of epoxy polymers

The effect of different absorbed doses of electron irradiation with the energy of 12 MeV and heat treatment on the mechanical properties of ED-20 epoxy-dianic resin with hardener PEPA (11, 12 and 13 parts by weight per 100 parts by weight of epoxy resin) was investigated. Heat treatment of irradiated epoxy resin samples was performed in two modes: before or after electron irradiation. It is shown that the optimal choice of the content of hardener PEPA and using electron irradiation with the energy of 12 MeV in the integrated combination with heat treatment allow significantly improve the mechanical properties of epoxy-dianic resin. It was established that for the content of the hardener 12 parts by weight and absorbed doses of 10–20 kGy, the boundary of strength increases in 3 times, and additional heat treatment both before and after irradiation reduces this figure through the thermal destruction. Only for the content of hardener 11 and 13 parts by weight and these absorbed doses heat treatment of irradiated samples of epoxy resin leads to an increase in the boundary of strength. In doing so, the hardness increases regardless of the content of hardener for the absorbed doses greater than 50 kGy.

Key words: electron irradiation, heat treatment, epoxy-dianic resin, PEPA hardener, boundary of strength, hardness, mechanical properties, absorbed dose.

Introduction

Approximately 50 years have elapsed since the researchers first began to study the effect of ionizing radiation on polymeric materials and discovered, under its influence, the formation of additional chemical bonds and other beneficial effects in these materials [1]. The obtaining and application of composite materials, their radiation modification and stability have always been a pressing problem of science and technology [2–5]. Radiation-modified polymer materials are widely used in electronic, cable, electrochemical industries [4, 5]. The irradiation technologies used for the treatment of polymers contain a variety of techniques and sources of radiation. In particular, known methods of solidifying polymer-composite materials using magnetic fields and irradiation [6–9] are known. Today there is significant commercialization, which is aimed at treatment polymers by radiation. Important new products, obtaining which have become available due to radiation technologies, continue to enter the market, and interesting innovations in the application of radiation for high molecular weight materials are under research around the world.

Therefore, an important scientific and applied task of modern materials science is the search of methods of radiation treatment of polymeric materials to improve their physico-chemical and operating properties. In particular, establishing optimal conditions for electron irradiation and heat treatment will enhance the mechanical properties of epoxy polymers, which can be used for the creation of high quality structural and anti-friction materials for mechanical engineering and instrumentation, which will have lower cost, lower weight, durability, increased resistance to aggressive environments. Obtaining such materials requires the study of the effect of various modes of electron irradiation and heat treatment on the mechanical properties of epoxy polymers, which is the main purpose of this work.

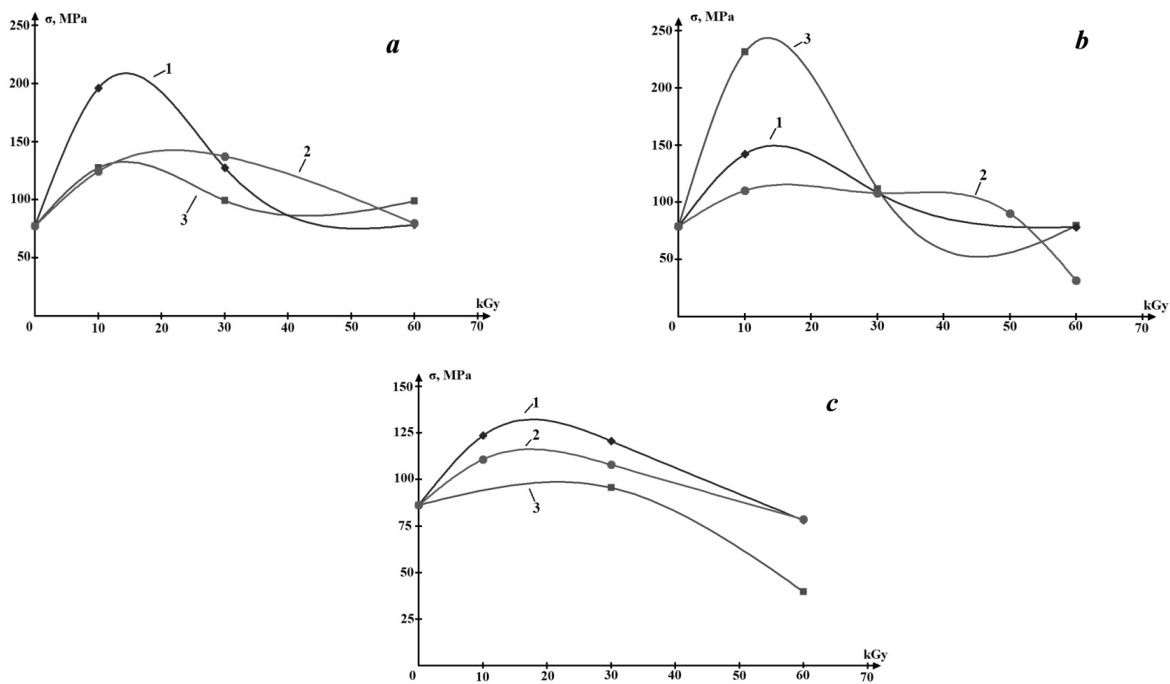
Experimental

The effect of irradiation with different doses of electrons with the energy of 12 MeV on the mechanical properties of ED-20 epoxy-dianic resin with hardener polyethylene polyamine (PEPA) (11, 12, 13 parts by weight per 100 parts by weight of epoxy resin) was investigated. The composition was poured into special forms, resulting in the samples of a cylindrical shape with a height $h=1.5$ cm and a diameter $d=1$ cm and parallelepiped shape samples measuring $1 \times 1.5 \times 1.5$ cm for researching of the boundary of strength and hardness, respectively. Three methods of curing the epoxy polymer were used. The initial curing process in all three modes continued for 24 hours under normal conditions. The samples of the first group were irradiated with different electron doses. The samples of the second group after irradiation were further heat treated. The samples of the third group before irradiation were heat treated. The heat treatment was a stepwise drying process in a furnace at temperatures of 70... 130 °C for 6 hours. The samples of the epoxy resin were irradiated at the Institute of Electronic Physics on the microtron M-30 by the electron energy of 12 MeV and doses from 5 to 60 kGy. To ensure the stability of the room temperature of irradiation, which was recorded by a copper-constant differential thermocouple, the test samples were blown with nitrogen vapour. The compressive strength in conditions of normal separation was determined according to GOST 14759–69. The research was carried out on the UMM-5 breaking machine for the speed of movement of the lower traverse of 2 mm/min. In the studies of hardness, the samples were made in the form of a parallelogram with a smooth surface. In this case, a steel ball with a diameter of 5 mm was pressed into the surface of the tested material with an appropriate load for 60 seconds. The effort was chosen so that there remained a visible imprint whose diameter is smaller than the diameter of the ball. To determine the hardness, a table of the dependence of the hardness value on the diameter of the imprint, which was determined using a magnifying glass with a scale, was used.

Results and discussion

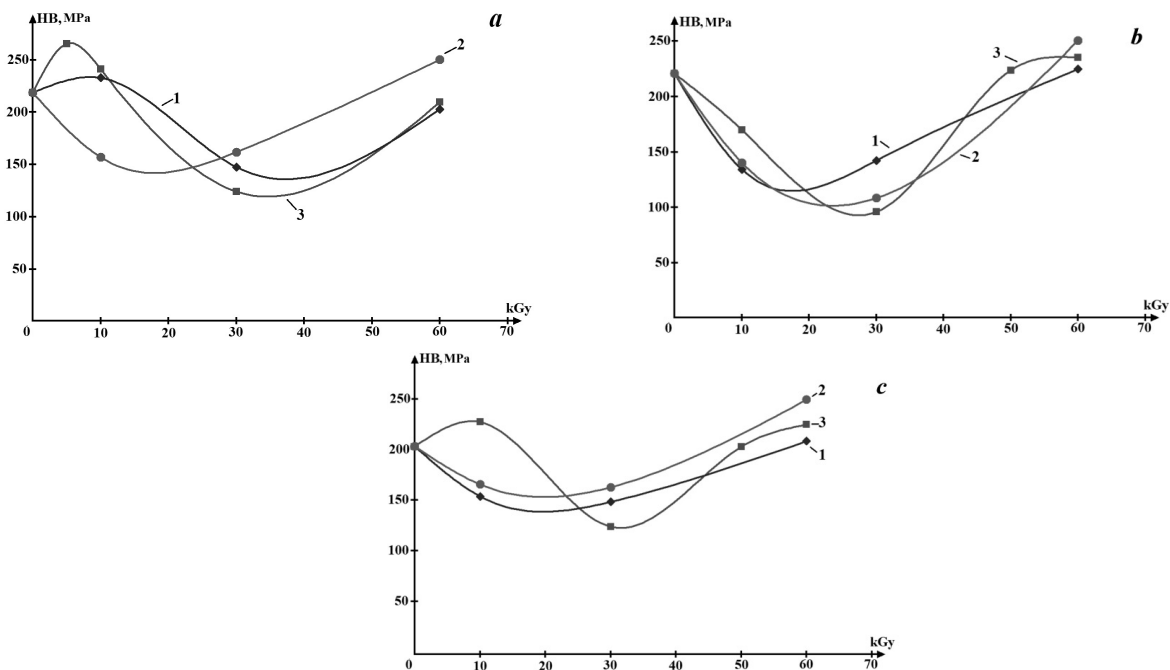
Figure 1 shows the dependencies of the boundary of strength for epoxy-dianic resin on the absorbed doses of electron irradiation. As can be seen from Figure 1, the strength of the epoxy polymer, which is obtained by different methods, increases for irradiation doses up to 10–20 kGy, and then monotonically decreases with increasing dose. In polymeric materials, the processes of excitation and ionization of polymer molecules take place under the action of irradiation resulting in the chemical bonds be torn in the polymer macromolecule and free radicals are forming [10]. The interaction of free radicals with the chains of polymer macromolecules leads to the formation of additional intermolecular bonds («cross-linking» of the polymer) and in process of their accumulation — spatial networks. The Young modulus and therefore strength and hardness for the polymer increase with increasing the number of such bonds. The destruction of intermolecular bonds under the action of irradiation leads to the destruction of the polymer matrix and, accordingly, to the reduction of the strength and hardness of the polymer. The probability of these two mechanisms of chemical transformations in polymers determines their physico-mechanical properties. As is known from the theory of material resistance [11], the critical mechanical stress of the material's destruction is directly proportional to Young's modulus. Therefore, such specific dependencies of the boundary of strength on the absorbed dose for samples of epoxy polymers are associated with changes in the value of the Young modulus under irradiation. Two processes are happening in polymers under the influence of electron irradiation: transverse «cross-linking» and destruction [10, 12]. The transverse «cross-linking» resulting in macromolecules of the polymer through creating transverse chemical bonds between linear macromolecules. The volatile products and macromolecules of less length are formed under the destruction of macromolecules. Also, the destruction of polymer molecules could be happening due to additional heat treatment. Besides, creating of microcracks, the size and depth of which depends on the irradiation dose are possible in the volume of polymers under the electron irradiation with the energy $E > 2$ MeV [13].

The maximum relative increase of the boundary of strength is equal to 3 (see Fig. 1 b) for the content of hardener 12 parts by weight at the electron irradiation without heat treatment. In this case, additional heat treatment, both before and after irradiation, reduces the strength due to thermal destruction. Only additional thermal treatment of irradiated epoxy polymers with the content of hardener of 11 and 13 parts by weight by the doses of 10–20 kGy leads to the increasing boundary of strength. According to the results of our previous work [14], the boundary of strength for epoxy-dianic resin with the content of hardener 12 parts by weight, which was irradiated by the electrons with an energy of 10 MeV and much greater doses (about 0.2 MGy), increases less than 2 times.



a — 11 parts by weight; *b* — 12 parts by weight; *c* — 13 parts by weight;
 1 — samples of epoxy polymer, which initially were irradiated, followed by additional heat treatment;
 2 — samples of epoxy polymer, which initially exposed the additional heat treatment before irradiation;
 3 — the same irradiated samples without additional heat treatment

Figure. 1. The dependencies of the boundary of strength on the absorbed doses of electron irradiation for an epoxy-dianic resin with different content of PEPA hardener



a — 11 parts by weight; *b* — 12 parts by weight; *c* — 13 parts by weight;
 1 — samples of epoxy polymer, which initially exposed the additional heat treatment before irradiation;
 2 — samples of epoxy polymer, which initially were irradiated, followed by additional heat treatment;
 3 — the same irradiated samples without additional heat treatment

Figure 2. The dependencies of the hardness on the absorbed doses of electron irradiation for an epoxy-dianic resin with different content of PEPA hardener

The maximum increase of the boundary of strength for an epoxy-dianic resin at doses of 10–20 kGy may be related to the dominant role of transverse intermolecular «cross-linking». Processes of radiation destruction and creating of microcracks, which lead to the reduction boundary of strength, are becoming effective for doses of more than 20 kGy. Also, the mass fraction of hardener in the epoxy resin significantly affects the magnitude of the boundary of strength of the obtained samples of epoxy polymer. Similar considerations can be made regarding the obtained results of hardness for irradiated samples of epoxy resin (Fig. 2).

However, a distinctive feature of the dependencies the hardness of the epoxy resin is their increasing at irradiation doses greater than 30 kGy, and the additional heat treatment of the irradiated samples by such electron doses leads to an increase of the hardness. In this case, the formation of microcracks can make a secondary contribution to reducing the material hardness than the boundary of strength.

Conclusions

Conducted studies of the influence of heat treatment and high-energy electron irradiation on the mechanical properties of epoxy-dianic resin made it possible to establish the optimum technological conditions for obtaining this epoxy polymer with elevated values of the boundary of strength and hardness. Peculiarities of the formation of the structure and mechanical properties of epoxy resin under the action of electron irradiation and heat treatment are determined by the different relative contribution of the mechanisms of cross-linking, radiation destruction and the formation of microcracks. The obtained results can find their practical use in nuclear power, instrument making, mechanical and aircraft engineering for the creation of lighter, cheaper coatings and structural materials based on epoxy resin.

The study performed in this work was financed under the project «Development of a complex of managed properties of many-valley semiconductors and polymer composite materials for operation in extreme conditions of operation», State registration number 0117U000630.

References

- 1 Clough R. High-energy radiation and polymers: A review of commercial processes and emerging applications / R.L. Clough // Nuclear Instruments and Methods in Physics Research Section B: Beam Interactions with Materials and Atoms. — 2001. — Vol. 185, No. 1–4. — P. 8–33. DOI: 10.1016/S0168–583X(01)00966–1.
- 2 Ахмедов Ф.И. Влияние гамма-облучения на электропроводность полимерных композитов полипропилена с оксидами алюминия и железа / Ф.И. Ахмедов, А.Д. Кулиев, Р.Б. Ахвердиев, А.С. Самедова, М.Б. Гусейнова // Электронная обработка материалов. — 2013. — № 6. — С. 94–97.
- 3 Пинчук Т.Н. Радиационная модификация физико-механических свойств изотактического полипропилена с многостенными углеродными нанотрубками / Т.Н. Пинчук и др. // Вопросы атомной науки и техники. — 2009. — № 4. — С. 275–278.
- 4 Джур Є.О. Полімерні композиційні матеріали в ракетно-космічній техніці: підручник / Є. О. Джур, Л.Д. Кучма, Т.А. Манько, Т.А. Ситало. — Київ: Вища освіта, 2003. — 399 с.
- 5 Wypych G. Handbook of polymers / G. Wypych. — Elsevier, 2016. — 399 p.
- 6 Sadovnichii D.N. Radiation-induced conductivity of polymer composites filled by finely divided oxides / D.N. Sadovnichii et al. // High Energy Chemistry. — 2003. — Vol. 37, No. 6. — P. 389–394. DOI: 10.1023/B: HIEC.0000003397.26349.63
- 7 Magerramov A.M. Radiothermoluminescence of γ -irradiated composites of polypropylene and dispersed oxides / A.M. Magerramov, M.A. Nuriev, F.I. Akhmedov, I.M. Ismailov // Surface Engineering and Applied Electrochemistry. — 2009. — Vol. 45, No. 5. — P. 437. DOI: 10.3103/S1068375509050184
- 8 Демура А.Л. Використання електромагнітного поля надвисокої частоти в технологічному процесі виготовлення виробів з полімерних композиційних матеріалів / А.Л. Демура // Вісник двигунобудування. — 2006. — № 4. — С. 76–79.
- 9 Shubhra Q.T.H. Study on the mechanical properties, environmental effect, degradation characteristics and ionizing radiation effect on silk reinforced polypropylene/natural rubber composites / Q.T.H. Shubhra et al. // Composites Part A: Applied Science and Manufacturing. — 2010. — Vol. 41, No. 11. — P. 1587–1596. DOI: 10.1016/j.compositesa.2010.07.007
- 10 Головина Е.А. Основы радиационного материаловедения: учеб. пос. / Е.А. Головина, В.Б. Маркин. — Барнаул: Изд-во АлГТУ, 2008. — 145 с.
- 11 Піскунов В.Г. Опір матеріалів з основами теорії пружності й пластичності: підручник для студ. буд. і транспорт. спец. вузів: [у 2 ч.]. — 5. кн. / В. Г. Піскунов. — Київ: Вища шк., 1994. — 260 с.
- 12 Козлов Н.А. Физика полимеров: учеб. пос. / Н.А. Козлов, А.Д. Митрофанов. — Владимир: Изд-во Владимир. гос. ун-та, 2001. — 345 с.
- 13 Павленко В.И. Воздействие высокоэнергетических пучков быстрых электронов на полимерные радиационно-защитные композиты / В.И. Павленко, Р.Н. Ястребинский, О.Д. Едаменко, Д.Г. Тарасов // Вопросы атомной науки и техники. — 2010. — № 1. — С. 129–134.
- 14 Удовицька Ю.А. Вплив електронного опромінення на механічні та експлуатаційні властивості полімерів на основі епоксидної смоли / Ю.А. Удовицька, С.В. Луньов, В.П. Кашицький, П.П. Савчук, В.Т. Маслюк // Перспективні технології та прилади. — 2017. — № 11. — С. 138–141.

Ю.А. Удовицкая, С.В. Лунёв, В.Т. Маслюк, И.Г. Мегела
**Эпоксиполимерлердің механикалық қасиеттеріне
электронды сәулеленудің әсері**

ПЭПА қатайтқышы бар (11, 12 және 13 мас. с. бөліктері 100 мас.с. бөлікке эпоксидті шайыр) ЭД-20 маркалы эпоксидті-диан шайырының механикалық қасиеттеріне 12 МэВ энергиясы бар электронды сәулеленудің және термиялық өңдеудің әртүрлі жұтылған дозаларының әсері зерттелген. Эпоксидті шайырдың сәулеленген үлгілерінің термиялық өңдеуі екі режимде жүргізілді: сәулеленуден бұрын немесе электрондармен сәулеленуден кейін. ПЭПА қатайтқышының құрамын оңтайлы таңдауы және 12 МэВ энергиясы бар электронды сәулеленуді термиялық өңдеумен кешенді түрде қолдану эпоксидті-диан шайырының механикалық қасиеттерін едәуір жақсартатыны көрсетілген. Қатайтқыш құрамы 12 мас. с. және 10–20 кГр жұтылған дозалар үшін беріктік шегі 3 есе артатыны, ал қосымша термиялық өңдеу кезінде, сәулеленуге дейін және одан кейін, термиялық деструкцияға байланысты көрсеткішті төмендететіні анықталған. Эпоксидті шайырдың сәулеленген үлгілерінің термиялық өңдеуі 10–20 кГр жұтылған дозаларда тек 11 және 13 мас. с. қатайтқыш құрамы үшін олардың беріктік шегінің өсуіне әкеледі. Сонымен бірге қаттылық 50 кГр аса үлкен мөлшерде жұтылған дозаларда қатайтқыштың құрамына қарамастан артады.

Кілт сөздер: электронды сәулелену, термиялық өңдеу, эпоксидті шайыр, қатайтқыш, беріктік шегі, қаттылық, механикалық қасиеттер, жұтылған доза.

Ю.А. Удовицкая, С.В. Лунёв, В.Т. Маслюк, И.Г. Мегела
**Влияние электронного облучения
на механические свойства эпоксиполимеров**

Исследовано влияние различных поглощенных доз электронного облучения с энергией 12 МэВ и термообработки на механические свойства эпоксидно-диановой смолы марки ЭД-20 с отвердителем ПЭПА (11, 12 и 13 мас. ч. на 100 масс. ч. эпоксидной смолы). Термообработка облученных образцов эпоксидной смолы проводилась в двух режимах: до и после облучения электронами. Показано, что оптимальный выбор содержания отвердителя ПЭПА и использование электронного облучения с энергией 12 МэВ в комплексном сочетании с термообработкой позволяют значительно улучшить механические свойства эпоксидно-диановой смолы. Было установлено, что для содержания отвердителя 12 мас. ч. и поглощенных доз 10–20 кГр предел прочности возрастает в 3 раза, а дополнительная термообработка, как до, так и после облучения, снижает данный показатель за счет термической деструкции. Термическая обработка облученных образцов эпоксидной смолы приводит к росту их предела прочности только для содержания отвердителя 11 и 13 мас. ч. при поглощенных дозах 10–20 кГр. При этом твердость возрастает, независимо от содержания отвердителя при поглощенных дозах, больших за 50 кГр.

Ключевые слова: электронное облучение, термообработка, эпоксидная смола, отвердитель, граница прочности, твердость, механические свойства, поглощенная доза.

References

- 1 Clough, R.L. (2001). High-energy radiation and polymers: A review of commercial processes and emerging applications. *Nuclear Instruments and Methods in Physics Research Section B: Beam Interactions with Materials and Atoms*, 185(1–4), 8–33.
- 2 Ahmedov, F.I., Kuliev, A.D., Ahverdiev, R.B., Samedova, A.S., & Guseynova, M.B. (2013). Vlianie hamma-oblucheniia na elektroprovodnost polimernykh kompozitov polipropilena s oksidami aliuminiia i zheleza [Influence of gamma-irradiation on the electrical conductivity of polypropylene polymer composites with aluminum and iron oxides]. *Elektronnaiia obrabotka materialov — Electronic material processing*, 6, 94–97 [in Russian].
- 3 Pinchuk, T.N. (2009). Radiatsionnaia modifikatsiia fiziko-mekhanicheskikh svoystv izotakticheskoho polipropilena s mnohostennymi uhlernodnymi nanotrubbkami [Radiation modification of physical and mechanical properties of isotactic polypropylene with multi-walled carbon nanotubes]. *Voprosy atomnoi nauki i tekhniki — Atomic science and technology issues*, 4, 275–278 [in Russian].
- 4 Dzhur, E.O., Kuchma, L.D., Manko, T.A., & Sytalo, T.A. (2003). Polimerni kompozitsiini materiali v raketno-kosmichnii tekhnitsi [Polymer composite materials in rocket and space technology]. Kyiv: Vyshcha osvita [in Ukrainian].
- 5 Wypych, G. (2016). *Handbook of polymers*. Elsevier.
- 6 Sadovnichii, D.N. et al. (2003). Radiation-induced conductivity of polymer composites filled by finely divided oxides. *High Energy Chemistry*, 37(6), 389–394.

- 7 Magerramov, A.M., Nuriev, M.A., Akhmedov, F.I., & Ismailov, I.M. (2009). Radiothermoluminescence of γ -irradiated composites of polypropylene and dispersed oxides. *Surface Engineering and Applied Electrochemistry*, 45(5), 437.
- 8 Demura, A.L. (2006). Viktoristannia elektromahnitnoho polia nadvisokoi chastoti v tekhnolohichnomu protsesi vihotovlennia virobiv z polimernikh kompozitsiynikh materialiv [Using of the electro-magnetic field of the above-high frequency in the technological process of preparing products from composite materials]. *Visnik dvigunobuduvannia — Bulletin of engine building*, 4, 76–79 [in Ukrainian].
- 9 Shubhra, Q.T.H. et al. (2010). Study on the mechanical properties, environmental effect, degradation characteristics, and ionizing radiation effect on silk reinforced polypropylene/natural rubber composites. *Composites Part A: Applied Science and Manufacturing*, 41(11), 1587–1596.
- 10 Holovyna, E.A., & Markin, V.B. (2008). Osnovy radiatsionnoho materialovedeniia [Fundamentals of radiation materials science]. Barnaul: Altai State Techn. Univ. Publ. [in Russian].
- 11 Piskunov, V.H. (1994). Opir materialiv z osnovami teorii pruzhnosti i plastichnosti [Resistance of materials with the basics of the theory of elasticity and plasticity] (in 5 books). Kiyv: Vyscha shkola, 260 [in Ukrainian].
- 12 Kozlov, N.A., & Mitrofanov, A.D. (2001). Fizika polimerov [Polymer Physics]. Vladimir: Vladimir State Univ. Publ. [in Russian].
- 13 Pavlenko, V.I., Yastrebinskyi, R.N., Edamenko, O.D., & Tarasov, D.H. (2010). Vozdeistvie vysokoenerheticheskikh puchkov bystrykh elektronov na polimernye radiatsionno-zashchitnye kompozity [Influence of high-energy of fast electrons on polymer radiation-protective composites]. *Voprosy atomnoi nauki i tekhniki — Atomic science and technology issues*, 1, 129–134 [in Russian].
- 14 Udovitska, Yu.A., Luniov, S.V., Kashytskyi, V.P., Savchuk, P.P., & Masliuk, V.T. (2017). Vpliv elektronnoho oprominennia na mekhanichni ta ekspluatatsiini vlastivosti polimeriv na osnovi epoksidnoi smoli [Include of electronic irradiation on mechanical and exploitation of polymers based on epoxy resin]. *Perspektivni tekhnologii ta priladi — Advanced technologies and devices*, 11, 138–141 [in Ukrainian].

S. Zinchenko^{1*}, A. Ben¹, P. Nosov¹, I. Popovych², V. Mateichuk¹, O. Grosheva¹

¹*Kherson State Maritime Academy, Kherson, Ukraine;*

²*Kherson State University, Kherson, Ukraine*

(*E-mail: srz56@ukr.net)

The vessel movement optimisation with excessive control

The article discusses the issues of automatic control of the vessel's movement using excessive control, which allows to organize the movement of the vessel without a drift angle, to reduce the hydrodynamic resistance and fuel consumption. Issues of reducing energy consumption and fuel economy on board, as well as related issues of reducing emissions and improving the environment are especially relevant at the present time. A brief review of literature devoted to improving the energy efficiency of ships was carried out. As a result of the analysis, it was found that the issues of improving energy efficiency are solved in various ways, for example, constructively, by reducing weight, hydrodynamic and aerodynamic drag of the hull, using a sail, creating more advanced power plants, however, the authors have not found methods and algorithms for reducing hydrodynamic drag and fuel consumption through the use of excessive control. It is concluded that the development of such systems is relevant. Mathematical, algorithmic, and software have been developed for an on-board controller simulator of a vessel's motion control system with excessive control, the operability and efficiency of which has been verified by numerical simulation in a closed circuit with a mathematical model of the control object for various types of vessels, navigation areas and weather conditions. The experiments have confirmed the efficiency and effectiveness of the developed method, algorithmic and software, and allow us to recommend them for practical use in the development of mathematical support for vessel control systems with excessive control.

Keywords: excessive control, sufficient control, optimal control, distribution of control, control quality criterion, minimization of fuel consumption.

Introduction

Issues of reducing energy and fuel consumption on board, as well as related issues of reducing emissions and improving the environment are especially relevant at present [1]. Ways to solve these issues are different, but most often these are constructive solutions to reduce weight [2], hydrodynamic [3], use a sail [4] or improve power plants. Fuel economy is also possible due to proper route planning, psychological preparation [5–7], the use of decision support systems (DSS) [8–12]. However, the presence of the human factor in both manual control systems and DSS systems excludes control optimization due to the impossibility of a quick and accurate assessment of the situation, the presence of delays in the transmission of information, tiredness and other factors. This article discusses the optimization of energy costs for moving a ship in automatic control systems through the use of sufficient or excessive control structures, organizing with their help the movement of the ship along a route without a drift angle, with less hydrodynamic resistance. In addition, redundant structures can further reduce energy costs for management due to the optimal redistribution of control within the structure itself. Traditionally, control redundancy is used to increase maneuverability, redundancy and reliability [13–15] and much less frequently for optimal control [16–19]. By control redundancy is understood the difference between the number of independent controls and the number of degrees of freedom to be controlled. In article [20], the authors analyzed the redundancy of control for some types of vessels for various purposes.

For most transport vessels, such as Bulk carrier 6 (Dis. 44081t), Crude Oil Tanker 4, Car Carrier 2 (Dis. 19587t), MSC container ship 1 (Dis. 32025t), Shuttle tanker 1 (Dis. 160529t), Container ship 22 (Dis. 191000t), River-sea ship 3 «Sormovsky», etc., the number of which is more than 85 % of the total number of all vessels, the redundancy in the control at the transition is equal to $IU = U - S = -1$ (insufficient control), where $U = 2$ is the number of independent control (power plant and aft steering wheel), and $S = 3$ — the number of degrees of freedom to be controlled (longitudinal, lateral and angular movement in the yaw channel). On ships with insufficient control, the lateral effect of wind and current, as well as the moments from the effect of wind and current, can only be compensated by a corresponding turn of the vessel in the direction of external influence. But in this case, the ship will move with a drift angle, which increases the hydrodynamic resistance and fuel consumption. In the maneuvering mode, the Car Carrier 2 (Dis. 19587t), MSC con-

tainer ship 1 (Dis. 32025t), Shuttle tanker 1 (Dis. 160529t) vessels have sufficient control ($IU = 0$) due to the additional use of the bow thruster.

Passenger ships Passenger cruise ship 10 Common DP, Passenger cruise ship 10 have redundancy at the transition $IU = 5 - 3 = 2$, but in maneuverable mode $IU = 7 - 3 = 4$. Offshore vessels OSV 11, OSV 11 Common DP, OSV 11 Navis DP, OSV 11 AH, OSV 11 AH Common DP, OSV 11 AH Navis DP have redundancy at the transition $IU = 4 - 3 = 1$, and in maneuverable mode $IU = 6 - 3 = 3$.

The Semisubmersible 1AH, Semisubmersible 1AH Common, Semisubmersible 1AH Navis, Semisubmersible 1AH Common DP, Semisubmersible 1AH Navis DP oil platforms have redundancy in the transition and in maneuverable mode $IU = 8 - 3 = 5$. For ships with sufficient and redundant control, the external influence from wind and current can be compensated by the total control vector so that the ship itself can move without a drift angle, with less hydrodynamic resistance and lower fuel consumption.

As can be seen in the examples of passenger, offshore vessels and oil platforms, control redundancy is usually used to increase maneuverability, as well as to increase reliability. In open sources, the authors were not able to find methods of using redundancy for control to reduce energy costs for moving the vessel. Therefore, the solution of this issue is an urgent scientific and technical problem.

The object of the research is the process of automatic vessel movement control with sufficient or excessive control structure, which allows to reduce energy costs for moving the vessel and save fuel by organizing the movement of the vessel without a drift angle.

The subject of the study is the methods and algorithms, implemented in the software of the onboard controller of the control system, and allowing to reduce energy costs for moving the vessel and save fuel.

The purpose of the Article is the development of methods and algorithms of automatic vessel movement control with sufficient or excessive control structure, which allows to reduce energy costs for moving the vessel and save fuel by organizing the movement of the vessel without a drift angle.

Problem statement

A mathematical model of a controlled object (own ship) is set in the form of a system of nonlinear differential equations

$$\begin{aligned} \frac{d\mathbf{X}}{dt} &= \mathbf{f}(\mathbf{X}, \mathbf{U}, \mathbf{W}), \\ \mathbf{X} &= (V_x, V_y, \omega_z, \psi, \Delta X, \Delta Y), \\ \mathbf{W} &= \mathbf{f}_w(t), \end{aligned} \quad (1)$$

there $\mathbf{f}(\bullet)$ — mathematical model of the control object; \mathbf{X} — state vector of the control object; $V_x, V_y, \omega_z, \psi, \Delta X, \Delta Y$ — components of the state vector, respectively, longitudinal speed, lateral speed, yaw rate, yaw angle, longitudinal and lateral displacement; \mathbf{W} — vector of external influences from wind and current.

It is required to synthesize such control $\mathbf{U}(\mathbf{X})$ that would ensure minimum energy consumption and fuel consumption for moving the vessel in the presence of external influences $\mathbf{W} = \mathbf{f}_w(t)$.

Literature review

The article [2] presents research to reduce energy consumption and increase the environmental friendliness of a vessel by reducing the weight of a ship's structure made of fiber-reinforced plastic. A method was proposed for optimizing the weight of a structure, based on the algorithm of an artificial bee colony. The method was tested on the example of optimizing the design of a fishing vessel. The simulation results showed the possibility of reducing the weight of the structure by 8.31 %.

In article [3] there were considered the issues of improving the resistance characteristics and the quality of the vessel's trail field due to the optimization of contours. A decrease in resistance is directly related to a decrease in energy consumption for moving a ship and a decrease in fuel consumption. The shape of the contours was optimized by selecting 9 design variables using numerical methods. Model tests of the optimized form showed that the resistance and quality of the track field of the vessel were improved by 1.59 % and 17.8 %, respectively.

In article [4] there were considered issues of increasing the energy efficiency of a ship with a sail. The design of a rigid sail was optimized using the aerodynamic profile parameterization method and particle swarm optimization algorithm. The performance of optimized airfoil has been verified by multi-point theory,

computational fluid dynamics examination, and energy efficiency design index calculation. The maximum lift-to-drag ratio of optimized airfoil has increased by 10 % than that of the arc-shaped sail.

The work [5, 6] explores the issues of psychological training for skippers, which indirectly, through the application of good maritime practice, can also improve the management of the ship and fuel economy.

In article [7] there were conducted psychological studies during the training «Master Pilot» of active sailors in the training center of the Kherson State Maritime Academy. The training is aimed at improving the professional training of acting sailors, as well as improving communication skills between the captain and the pilot, which helps to optimize the management of the vessel.

In articles [8–12] there were investigated the issues of the influence of the human factor on the vessel control processes, as well as ways to reduce this effect through the use of decision support systems (DSS). Using DSS allows to control not only the parameters of the vessel's movement and the operation of the power plant, but also the psychological state of the skipper, who is on duty, to recognize critical situations in time and to generate an alarm.

A number of works are also devoted to optimization of control due to redundancy. Traditionally, control redundancy has been used to increase maneuverability and reliability. However, both indirectly optimize control processes and also lead to lower energy costs.

So, in article [13] there were considered the issues of software control of reserving an attack submarine of the US Navy Sea Wolf. Policies and procedures for detecting and isolating faults, as well as reconfiguring equipment, are discussed.

In article [14] there are studied the influence of excess control on the power and vibration of the main axis of the rotor of a helicopter. By changing the rotor speed and the differential transverse step, which are redundant controls, it was possible to determine the state of low power and low vibration.

In article [15] there is described a fault-tolerant control method that minimizes the influence of error due to a change in the system control law when a failure is detected. The method evaluates the state of the system using analytical relationships, which allows to calculate faulty states of the system without using an observer.

In article [16] there was studied the distribution of the thrust force of an autonomous underwater vehicle engine between an excess number of propulsors using the presented redundancy resolution scheme. At the same time, an excessive number of propulsors was also used to increase the reliability of the system as a whole due to parry failures. The results are confirmed by computer simulation.

In article [17], the author considers the control of the angular position of the spacecraft using the excess structure of power gyroscopes. The presence of redundancy allows not only to increase the reliability of actuators as a whole, but also to optimize control in accordance with the selected quality function.

In article [18] there were considered the issues of controlling the unloading of flywheels of a control system for the angular orientation of a spacecraft. For a minimally redundant system of flywheels and electromagnetic executive equipment of the unloading system that create an additional external moment, control algorithms are synthesized that guarantee asymptotic stability to the zero solution of model equations describing the movement of the flywheels. The operability of the proposed algorithms and the features of the unloading process are investigated by the example of the controlled motion of a spacecraft while stabilizing the triaxial orbital orientation.

In article [19] there was considered the use of angular redundancy for planning and optimizing the path of movement of a welding torch in various complex media. Efficiency strategies have been introduced, such as a heuristic domain sampling strategy, a collision verification strategy. The proposed algorithm is effective in solving complex planning problems when the weld passes in tight places. The experiment confirmed that the algorithm proposed by the authors can not only find a path free from collisions with obstacles in various complex environments, but also optimize the angle of the welding torch according to the established criterion.

Material and method

Expand system (1) in the vicinity of the equilibrium state point for two control schemes $\mathbf{U} = (\theta, \delta_1)$ (insufficient control) and $\mathbf{U} = (\theta, \delta_1, \delta_2, \dots, \delta_n)$ (excessive control).

For a circuit with insufficient control, system (1) takes the form

$$\begin{aligned} (m + \lambda_{11}) \frac{dV_x}{dt} &= \frac{dP}{d\theta} \theta - \frac{dF_x}{dV_x} V_x - \frac{dF_x}{d\beta} \beta - \frac{dF_x}{d\delta_1} \delta_1 + W_x, \\ (m + \lambda_{22}) \frac{dV_y}{dt} &= \frac{dF_y}{d\theta} \theta - \frac{dF_y}{dV_y} V_y + \frac{dF_y}{d\beta} \beta + \frac{dF_y}{d\delta_1} \delta_1 + W_y, \\ (I_z + \lambda_{66}) \frac{d\omega_z}{dt} &= \frac{dF_y}{d\theta} l \theta - \frac{dM_z}{d\omega_z} \omega_z + \frac{dF_y}{d\delta_1} \delta_1 l + \frac{dM_z}{d\beta} \beta + W_z. \\ \frac{d\psi}{dt} &= \omega_z, \frac{d\Delta X}{dt} = V_x, \frac{d\Delta Y}{dt} = V_y, \end{aligned} \quad (2)$$

For a scheme with redundant control $\mathbf{U} = (\theta, \delta_1, \delta_2, \dots, \delta_n)$, system (1) takes the form

$$\begin{aligned} (m + \lambda_{11}) \frac{dV_x}{dt} &= \frac{dP}{d\theta} \theta - \frac{dF_x}{dV_x} V_x - \frac{dF_x}{d\beta} \beta - \frac{dF_x}{d\delta_1} \delta_1 - \frac{dF_x}{d\delta_2} \delta_2 - \dots - \frac{dF_x}{d\delta_n} \delta_n + W_x, \\ (m + \lambda_{22}) \frac{dV_y}{dt} &= \frac{dF_y}{d\theta} \theta - \frac{dF_y}{dV_y} V_y + \frac{dF_y}{d\beta} \beta + \frac{dF_y}{d\delta_1} \delta_1 + \frac{dF_y}{d\delta_2} \delta_2 + \dots + \frac{dF_y}{d\delta_n} \delta_n + W_y, \\ (I_z + \lambda_{66}) \frac{d\omega_z}{dt} &= \frac{dF_y}{d\theta} l \theta - \frac{dM_z}{d\omega_z} \omega_z + \frac{dF_y}{d\delta_1} \delta_1 l_1 + \frac{dF_y}{d\delta_2} \delta_2 l_2 + \dots + \frac{dF_y}{d\delta_n} \delta_n l_n + \frac{dM_z}{d\beta} \beta + W_z, \\ \frac{d\psi}{dt} &= \omega_z, \frac{d\Delta X}{dt} = V_x, \frac{d\Delta Y}{dt} = V_y, \end{aligned} \quad (3)$$

where m — vessel mass; I_z — Inertia moment of the vessel; $\lambda_{11}, \lambda_{22}, \lambda_{66}$ — attached masses of water; $\frac{dF_x}{dV_x}, \frac{dF_x}{d\beta}, \frac{dF_y}{dV_y}, \frac{dF_y}{d\beta}, \frac{dM_z}{d\omega_z}, \frac{dM_z}{d\beta}$ — hydrodynamic characteristics of the vessel; $\frac{dP}{d\theta}, \frac{dF_x}{d\delta_1}, \frac{dF_x}{d\delta_2}, \dots$, $\frac{dF_x}{d\delta_n}, \frac{dF_y}{d\theta}, \frac{dF_y}{d\delta_1}, \frac{dF_y}{d\delta_2}, \dots, \frac{dF_y}{d\delta_n}$ — control characteristics of the vessel; $\theta, \beta, \delta_1, \delta_2, \dots, \delta_n$ — telegraph deflection angle, drift angle and steering angles; l, l_1, l_2, \dots, l_n — arms from the propeller and rudders to the center of rotation; P — screw force; $\mathbf{W} = (W_x, W_y, W_z)$ — components of external influences of wind and current.

For steady state $\left(\frac{dV_x}{dt} = 0, \frac{dV_y}{dt} = 0, \frac{d\omega_z}{dt} = 0, \frac{d\psi}{dt} = 0, \frac{d\Delta X}{dt} = 0, \frac{d\Delta Y}{dt} = 0 \right)$ the system of equations (2) takes the form

$$\begin{aligned} \frac{dF_x}{dV_x} V_x &= \frac{dP}{d\theta} \theta - \frac{dF_x}{d\beta} \beta - \frac{dF_x}{d\delta_1} \delta_1 + W_x, \\ \frac{dF_y}{d\beta} \beta + \frac{dF_y}{d\delta_1} \delta_1 &= -\frac{dF_y}{d\theta} \theta - W_y, \\ \frac{dM_z}{d\beta} \beta - \frac{dF_y}{d\delta_1} l \delta_1 &= -\frac{dF_y}{d\theta} l \theta - W_z, \\ \psi &= \text{const}, V_x = \text{const}, V_y = \text{const}. \end{aligned} \quad (4)$$

From the second and third equations of system (4) it follows that in the steady state, in the presence of external influences from the wind and the current, the drift angle and the rudder angle are not equal to zero ($\beta \neq 0, \delta_1 \neq 0$). Moreover, due to the presence of lateral force and the moment from the rotation of the screw, which are also disturbances, even in the absence of external influences from wind and current, the drift angle and the rudder angle will also not be zero.

For steady state $\left(\frac{dV_x}{dt} = 0, \frac{dV_y}{dt} = 0, \frac{d\omega_z}{dt} = 0, \frac{d\psi}{dt} = 0, \frac{d\Delta X}{dt} = 0, \frac{d\Delta Y}{dt} = 0 \right)$ the system of equations (3) takes the form

$$\begin{aligned} \frac{dF_x}{dV_x} V_x &= \frac{dP}{d\theta} \theta - \frac{dF_x}{d\beta} \beta - \frac{dF_x}{d\delta_1} \delta_1 - \frac{dF_x}{d\delta_2} \delta_2 - \dots - \frac{dF_x}{d\delta_n} \delta_n + W_x, \\ \frac{dF_y}{d\beta} \beta + \frac{dF_y}{d\delta_1} \delta_1 + \frac{dF_y}{d\delta_2} \delta_2 + \dots + \frac{dF_y}{d\delta_n} \delta_n &= -\frac{dF_y}{d\theta} \theta - W_y, \\ \frac{dM_z}{d\beta} \beta + \frac{dF_y}{d\delta_1} l_1 \delta_1 + \frac{dF_y}{d\delta_2} l_2 \delta_2 + \dots + \frac{dF_y}{d\delta_n} l_n \delta_n &= -\frac{dF_y}{d\theta} l \theta - W_z, \\ \psi &= \text{const}, V_x = \text{const}, V_y = \text{const}. \end{aligned} \tag{5}$$

From the second and third equations of system (5) it follows that the drift angle can be reduced to zero even in the presence of external influences from wind, current and screw due to the appropriate choice of controls $\mathbf{U} = (\theta, \delta_1, \delta_2, \dots, \delta_n)$. At the same time, the minimum required number of independent controls that can provide a zero drift angle of the vessel is 2, $\mathbf{U} = (\theta, \delta_1, \delta_2)$.

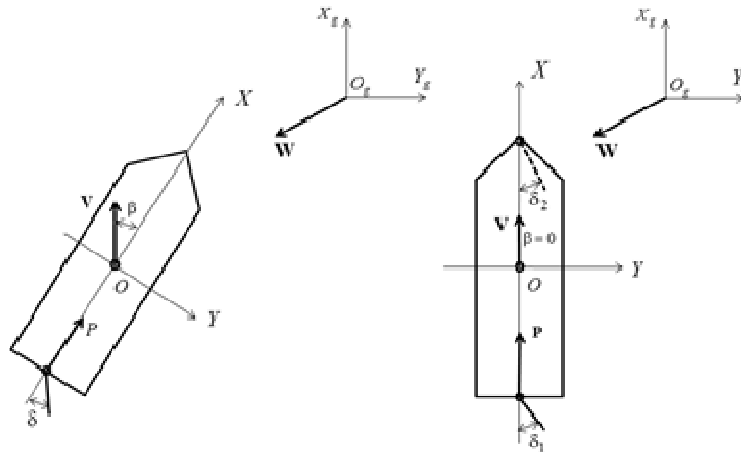


Figure 1. Steady state of ships with insufficient and sufficient control under external influences from wind and current

Thus, in contrast to the control circuit (4), which cannot ensure the movement of the vessel without a drift angle in the presence (and even in the absence) of external disturbances from wind and current, the control circuit (5) allows to control the vessel without a drift angle by compensating for external disturbances by the controls. The absence of a drift angle reduces the hydrodynamic resistance to the movement of the vessel, reduces fuel consumption and reduces emissions.

Figure 1 shows the steady state of ships with insufficient $\mathbf{U} = (\theta, \delta_1)$ and sufficient $\mathbf{U} = (\theta, \delta_1, \delta_2)$ control under external influences from wind and current.

To bring the control object to state (5) with a zero drift angle, we use the PID controller and the subsequent splitting of the control into two controls $\mathbf{U} = (\delta_1, \delta_2)$ [20].

$$\begin{aligned} \theta &= V_x^* \frac{\pi}{2V_{\max}}, \\ \sigma_1 &= k_y V_y + k_y \Delta Y + k_{f_y} \int \Delta Y dt, \\ \sigma_2 &= k_\omega \omega_z + k_\psi \psi + k_{f_\psi} \int \psi dt, \\ \delta_1 &= \sigma_1 - \sigma_2, \\ \delta_2 &= -\sigma_1 - \sigma_2, \end{aligned} \tag{6}$$

where V_x^*, V_{\max} — respectively, the required and maximum speed of the vessel; $k_y, k_y, k_{f_y}, k_\omega, k_\psi, k_{f_\psi}$ — PID gain.

Experiments

To test the operability and effectiveness of the method and algorithms for controlling ship schemes with sufficient and excessive control (3), comparing them with the traditional scheme with insufficient control (2), mathematical modeling of the vessel motion in a closed circuit with a control system was carried out.

For the scheme (3), the control and splitting law (6) was used, and for the scheme (2) the control law (7) was used

$$\theta = V_x^* \frac{\pi}{2V_{\max}},$$

$$\sigma_1 = k_y V_y + k_y \Delta Y + k_{\int y} \int \Delta Y dt, \quad (7)$$

$$\delta_1 = \sigma_1.$$

The results of mathematical modeling are presented in the form of time variation graphs of the longitudinal velocity (V_{xg}), lateral velocity (V_{yg}), yaw rate (W_z), course (F_i), longitudinal displacement (X_g), lateral displacement (Y_g), telegraph deflection angle (teta), rudder deflection angles (delta1, delta2).

Figure 2 shows the results of mathematical modeling of a control circuit $U = (\theta, \delta_1)$ with control (7) for the values of the lateral component of wind speed and current $W = (1, 2, 3, 3.5)$ m/s. A further increase in the lateral component of wind speed and current leads to loss of control. As can be seen from the above graphs, control (7) ensures that the vessel is kept on the route (lateral mismatch and lateral mismatch speed is reduced to zero), however, the course (F_i) differs from the required value ($F_i = 0$) by the drift angle, which in this case, for the maximum lateral component of wind speed and current $W = 3.5$ m/s, it is 4° .

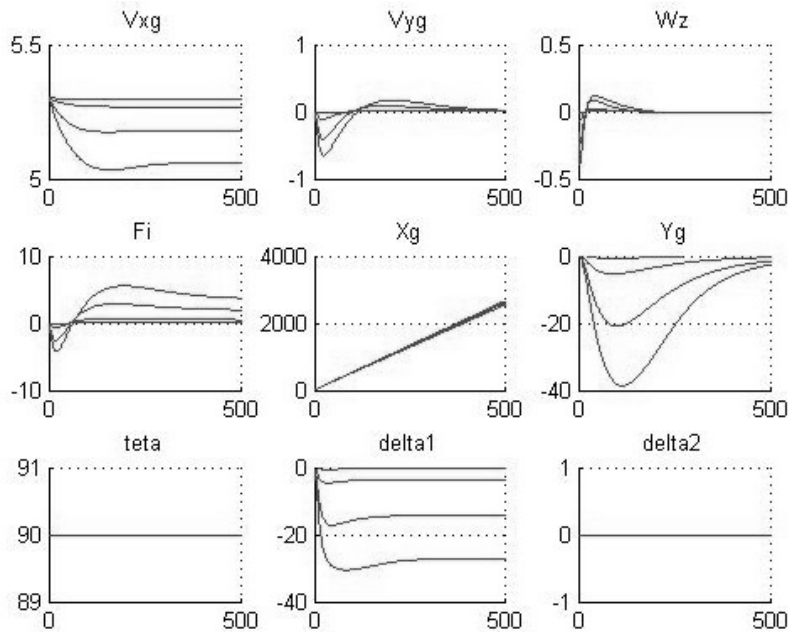


Figure 2. Results of mathematical modeling of the vessel movement with insufficient control

Figure 3 shows the results of mathematical modeling of a control circuit with control (6) for the values of the lateral component of wind speed and current = (1, 2, 3, 4, 4.5) m/s. A further increase in the lateral component of wind speed and current leads to loss of control. As can be seen from the above graphs, control (6) provides not only the retention of the vessel along the route (lateral mismatch and lateral mismatch speed is reduced to zero), but also maintaining a given course ($F_i = 0$) with a zero drift angle.

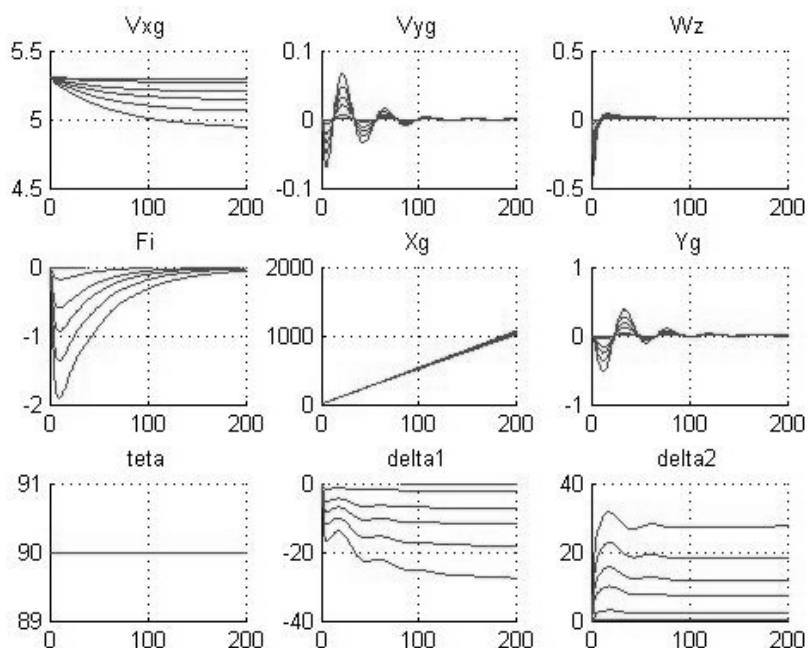


Figure 3. Results of mathematical modeling of the vessel movement with sufficient control

In addition, from the above results of mathematical modeling it also follows that the control circuit with control (6) is able to maintain control for large values of the lateral component of wind speed and current, transient processes in this control circuit also pass 5 times faster.

Table 1 shows the fuel consumption [kg] per 5 km of track for two control schemes.

Table 1

Fuel consumption [kg] per 5 km of track for two control schemes

Control scheme	Lateral wind speed [m/s]	Fuel consumption [kg] per 5 km
The scheme $U = (\theta, \delta_1)$	1	63.89
	2	64.227
	3	65.310
	3.5	66.826
	4	The system is not controllable
The scheme $U = (\theta, \delta_1, \delta_2)$	1	63.89
	2	64.200
	3	65.012
	3.5	65.716
	4	66.758
	4.5	68.315
	5	The system is not controllable

As follows from the presented results of comparing fuel consumption, the circuit $U = (\theta, \delta_1, \delta_2)$ is more economical than the circuit $U = (\theta, \delta_1)$. So, for the same lateral component of wind speed $W = 3.5$ m/s, the circuit $U = (\theta, \delta_1, \delta_2)$ consumes 1.111 kg less fuel for every 5 km of the track. With an increase in the lateral component of wind speed, fuel economy also increases.

From the above simulation results, it can be seen that in the presence of external influences:

- transition processes in scheme with sufficient control proceed several times faster than in scheme with insufficient control;
- the scheme with insufficient control ensures that the vessel is kept on the route, but does not provide a zero drift angle;

- the scheme with sufficient control ensures the retention of the vessel on the route with a zero drift angle;
- the scheme with sufficient control provides control for higher values of crosswind than a scheme with insufficient control;
- the scheme with sufficient control is more economical in comparison with the scheme with insufficient control; the amount of fuel saved increases with increasing lateral component of the wind speed;
- the scheme with sufficient control is more reliable due to redundancy of control channels.

Conclusions

There were proposed a method and algorithm for controlling a vessel with a sufficient and redundant control scheme, which allows to reduce fuel consumption at the transition by providing movement with a zero drift angle.

The scientific novelty of the results obtained is that for the first time a method and algorithms are proposed that provide fuel economy during the transition due to the organization of the movement of the vessel with a zero drift angle in the presence of transverse components of the external effects of wind and current. This is achieved through the use of ship control circuits with sufficient or excessive control, periodic, with the on-board controller clock cycle, measuring the parameters of the vessel's movement in the channels of longitudinal, lateral and angular movement, calculating the deviation of the measured parameters from their program values, and forming using the PID controller control signals in the channels of longitudinal, lateral and angular movement, splitting the received control signals into control of individual actuating control structures.

The practical value of the obtained results lies in the fact that the developed method and algorithms are implemented in the control system software and investigated in a closed circuit with the control object by numerical simulation in the MATLAB environment for various types of vessels, navigation areas and weather conditions.

Further research will be related to the development of a method and algorithms for control redundant structures with optimization of the quality control function.

Acknowledgements

The work was carried out in the framework of the research «Development of software solutions for dynamic functions of dynamically positioning systems of marine vessels», (state registration number 0119U100948), Department of Navigation and Electronic Navigation Systems of Kherson State Maritime Academy.

References

- 1 Vidoza J.A. Design and optimization of power hubs for Brazilian off-shore oil production units / J.A. Vidoza, J.G. Andreassen, F. Haglind, M. Reis, W. Gallo // *Energy*. — 2019. — Vol. 176, No. 1. — P. 656–666. DOI: 10.1016/j.energy.2019.04.022
- 2 Kai L. Research on structural optimization method of FRP fishing vessel based on artificial bee colony algorithm / L. Kai, Y. Yanyun, W. Yunlong, H. Zhenwu // *Advances in Engineering Software*. — 2018. Vol. 121. — P. 250–261. DOI: 10.1016/j.advengsoft.2018.03.011
- 3 Feng Y. Multidisciplinary optimization of an offshore aquaculture vessel hull form based on the support vector regression surrogate model / Y. Feng, Z. Chen, Y. Dai, F. Wang, J. Cai, Z. Shen // *Ocean Engineering*. — 2018. — Vol. 166. — P. 145–158. DOI: 10.1016/j.oceaneng.2018.07.062
- 4 Ma Y. Hard sail optimization and energy efficiency enhancement for sail-assisted vessel / Y. Ma, H. Bi, M. Hu, Y. Zheng, L. Gan // *Ocean Engineering*. — 2019. — Vol. 173, No. 1. — P. 687–699. DOI: 10.1016/j.oceaneng.2019.01.026
- 5 Popovych I.S. Research of Relationship between the Social Expectations and Professional Training of Lyceum Students studying in the Field of Shipbuilding / I.S. Popovych, O.Ye. Blynova, M.I. Aleksieieva, P.S. Nosov, N.Ye. Zavatska, O.O. Smyrnova // *Revista Espacios*. — 2019. — Vol. 40, No. 33. — P. 21–34.
- 6 Popovych I. Constructing a Structural-Functional Model of Social Expectations of the Personality [E-Reader Version] / I. Popovych, A. Borysiuk, L. Zahrai, O. Fedoruk, P. Nosov, S. Zinchenko, V. Mateichuk // *Revista Inclusiones*. — 2020. — 7-num Especial. — P. 154–167. — Retrieved from <http://ekhsuir.kspu.edu/handle/123456789/10471>
- 7 Popovych I.S. Experimental Research of Effective «The Ship's Captain and the Pilot» Interaction Formation by Means of Training Technologies / I.S. Popovych, V.V. Cherniavskiy, S.V. Dudchenko, S.M. Zinchenko, P.S. Nosov, O.O. Yevdokimova, O.O. Burak, V.M. Mateichuk // *Revista Espacios*. — 2020. — Vol. 41, No. 11. — P. 30. — Retrieved from <http://www.revistaespacios.com/a20v41n11/20411130.html>

- 8 Nosov P.S. Diagnostic system of perception of navigation danger when implementation complicated maneuvers / P.S. Nosov, S.M. Zinchenko, I.S. Popovych, A.P. Ben, Y.A. Nahrybelnyi, V.M. Mateichuk // Radio Electronics, Computer Science, Control. — 2020. — No. 1. — P. 146–161.
- 9 Nosov P.S. Identification of «Human error» negative manifestation in maritime transport / P.S. Nosov, A.P. Ben, V.N. Mateichuk, M.S. Safonov // Radio Electronics, Computer Science, Control. — 2018. — Vol. 4, No. 47. — P. 204–213. DOI: 10.15588/1607–3274–2018–4–20.
- 10 Nosov P. Approaches going to determination periods of the human factor of navigators during supernumerary situations / P. Nosov, A. Ben, A. Safonova, I. Palamarchuk // Radio Electronics, Computer Science, Control. — 2019. — Vol. 2, No. 49. — P. 140–150. DOI: 10.15588/1607–3274–2019–2–15
- 11 Nosov P. Development of means for experimental identification of navigator attention in ergatic systems of maritime transport / P. Nosov, I. Palamarchuk, S. Zinchenko, I. Popovych, Y. Nahrybelnyi, H. Nosova // Bulletin of the University of Karaganda – Physics. — 2020. — No. 1(97). — P. 58–69. DOI: 10.31489/2020Ph1/58–69
- 12 Zinchenko S.M. Automatic collision avoidance system with multiple targets, including maneuvering ones / S.M. Zinchenko, P.S. Nosov, V.M. Mateichuk, P.P. Mamenko, I.S. Popovych, O.O. Grosheva // Bulletin of the University of Karaganda – Physics. — 2019. — No. 4(96). — P. 69–79. DOI: 10.31489/2019Ph4/69–79
- 13 Sims J.T. Redundancy management software services for Seawolf ship control system / J.T. Sims // Proceedings of IEEE 27th International Symposium on Fault Tolerant Computing. — 1997, June. DOI: 10.1109/FTCS.1997.614114.
- 14 Jacobellis G. Using Control Redundancy for Power and Vibration Reduction on a Coaxial Rotor Helicopter at High Speeds / G. Jacobellis, F. Gandhi, M. Floros // Journal of the American Helicopter Society. — 2019. — Vol. 64, No. 3. — P. 1–15. DOI: 10.4050/JAHS.64.032008
- 15 Mohammadi A. An Active Actuator Fault-Tolerant Control of a Quadrotor Based on Analytical Redundancy Relations / A. Mohammadi, A. Ramezani // Iranian journal of science and technology — transactions of electrical engineering. — 2020. — Vol. 44. — P. 1069–1079. DOI: 10.1007/s40998–019–00292–6
- 16 Tarun K.P. Fault-tolerant control of an autonomous underwater vehicle under thruster redundancy / K.P. Tarun, S. Nilanjan // Robotics and Autonomous Systems. — 2001. — Vol. 34, No. 1. — P. 39–52.
- 17 Земляков А.С. Управление угловым положением космического аппарата с избыточной структурой гиродинов / А.С. Земляков // Вестн. Казан. гос. техн. ун-та им. А.Н. Туполева. — 2001. — Т. 4. — С. 56–62.
- 18 Lebedev D.V. Momentum unloading excessive reaction-wheel system of a spacecraft / D.V. Lebedev // Journal of Computer and Systems Sciences International. — 2008. — Vol. 47, No. 4. — P. 613–620.
- 19 Wenxiang G. Automatic motion planning for complex welding problems by considering angular redundancy / G. Wenxiang, T. Qing, Y. Jin, Y. Yaru // Robotics and Computer-Integrated Manufacturing. — 2020. — P. 62. DOI: 10.1016/j.rcim.2019.101862
- 20 Zinchenko S.M. Control redundancy as a quantitative measure of ship maneuverability / S.M. Zinchenko, P.S. Nosov, P.P. Mamenko, O.O. Grosheva, V.M. Mateichuk // Advanced Information and Innovative Technologies for Transport (MINT — 2019): Materials of the XII International Scientific and Practical Conference. — Kherson State Maritime Academy, Kherson, Ukraine, 2019, May. — P. 97–99.

С. Зинченко, А. Бень, П. Носов, И. Попович, В. Матейчук, О. Грошева

Кеме қозғалысын шамадан тыс басқаруды оңтайландыру

Мақалада шамадан тыс басқару көмегімен кемеңіз қозғалысын автоматты түрде басқару, гидродинамикалық кедергі мен отын шығынын азайту, кемеңіз қозғалысын көлбеу бұрышсыз ұйымдастыруға мүмкіндік беретін мәселелер талқыланды. Қазіргі уақытта бортта энергия тұтынуды және отын үнемдеуді азайту мәселелері, сондай-ақ шығарындыларды азайту және қоршаған ортаны жақсарту мәселелері өзекті болып отыр. Кемелердің энергия тиімділігін арттыруға арналған әдебиеттерге қысқаша шолу жасалған. Талдау нәтижесінде энергия тиімділігін арттыру мәселелері әртүрлі жолдармен шешілетіні, мысалы, корпусың салмағы, гидродинамикалық және аэродинамикалық сүйреуі, парусты пайдалану, дамыған электр станцияларын құру, алайда авторлар гидродинамикалық сүйреу мен отын шығынын шамадан тыс бақылауды азайту әдістері мен алгоритмдерін тапқан жоқ. Мұндай жүйелердің дамуы өзекті болып табылады. Шамадан тыс бақылауы бар кемеңіз қозғалысын басқару жүйесінің борттық контроллері үшін математикалық, алгоритмдік және бағдарламалық жасақтама жасалды, оның жұмыс қабілеттілігі және тиімділігі басқару объектісінің математикалық моделімен жабық тізбектегі сандық модельдеумен тексерілді, кемелердің әртүрлі түрлеріне, навигациялық аймақтарға және ауа-райына байланысты жүргізілген тәжірибелер әзірленген әдістің, алгоритмдік және бағдарламалық жасақтаманың жұмысқа қабілеттілігі мен тиімділігін растады және оларды шамадан тыс басқарумен кемеңіз басқару жүйелеріне математикалық қолдау жасауда практикалық қолдануға ұсынуға мүмкіндік береді.

Кілт сөздер: шамадан тыс бақылау, жеткілікті бақылау, оңтайлы бақылау, бақылауды бөлу, бақылау сапасының өлшемі, отын шығынын азайту.

С. Зинченко, А. Бень, П. Носов, И. Попович, В. Матейчук, О. Грошева

Оптимизация движения судна с избыточным управлением

В статье рассмотрены вопросы автоматического управления движением судна с использованием избыточного управления, что позволяет организовать движение судна без угла дрейфа, снизить гидродинамическое сопротивление и расход топлива. Вопросы сокращения энергопотребления и экономии топлива на борту, а также связанные с ними вопросы сокращения выбросов и улучшения состояния окружающей среды особенно актуальны в настоящее время. Проведен краткий обзор литературных источников, посвященных повышению энергоэффективности судов. В результате проведенного анализа выявлено, что вопросы повышения энергоэффективности решаются различными способами, например, конструктивно, путем снижения веса, гидродинамического и аэродинамического сопротивления корпуса, с помощью паруса, создания более совершенных силовых установок. Однако авторами не найдены методы и алгоритмы уменьшения гидродинамического сопротивления и расхода топлива за счет использования избыточного управления. Сделан вывод об актуальности разработки таких систем. Разработано математическое, алгоритмическое и программное обеспечение для имитатора бортового контроллера системы управления движением судна с избыточным управлением, работоспособность и эффективность которых проверена численным моделированием в замкнутой схеме с математической моделью объекта управления для различных типов судов, районов плавания и погодных условий. Проведенные эксперименты подтвердили работоспособность и эффективность разработанного метода, алгоритмического и программного обеспечения и позволяют рекомендовать их для практического использования при разработке математического обеспечения систем управления судами с избыточным управлением.

Ключевые слова: избыточное управление, достаточное управление, оптимальное управление, распределение управления, критерий качества управления, минимизация расхода топлива.

References

- 1 Vidoza, J.A., Andreasen, J.G., Haglind, F., Reis, M., & Gallo, W. (2019). Design and optimization of power hubs for Brazilian off-shore oil production units. *Energy*, 176(1), 656–666. DOI: 10.1016/j.energy.2019.04.022
- 2 Kai, L., Yanyun, Y., Yunlong, W., & Zhenwu, H. (2018). Research on structural optimization method of FRP fishing vessel based on artificial bee colony algorithm. *Advances in Engineering Software*, 121, 250–261. DOI: 10.1016/j.advengsoft.2018.03.011
- 3 Feng, Y., Chen, Z., Dai, Y., Wang, F., Cai, J., & Shen, Z. (2018). Multidisciplinary optimization of an offshore aquaculture vessel hull form based on the support vector regression surrogate model. *Ocean Engineering*, 166, 145–158. DOI: 10.1016/j.oceaneng.2018.07.062
- 4 Ma, Y., Bi, H., Hu, M., Zheng, Y., & Gan L. (2019). Hard sail optimization and energy efficiency enhancement for sail-assisted vessel. *Ocean Engineering*, 173(1), 687–699. DOI: 10.1016/j.oceaneng.2019.01.026
- 5 Popovych, I.S., Blynova, O.Ye., Aleksieieva, M.I., Nosov, P.S., Zavatska, N.Ye., & Smyrnova, O.O. (2019). Research of Relationship between the Social Expectations and Professional Training of Lyceum Students studying in the Field of Shipbuilding. *Revista Espacios*, 40(33), 21–34.
- 6 Popovych, I., Borysiuk, A., Zahrai, L., Fedoruk, O., Nosov, P., Zinchenko, S., & Mateichuk, V. (2020). Constructing a Structural-Functional Model of Social Expectations of the Personality [E-Reader Version]. *Revista Inclusiones*, 7-num Especial, 154–167. Retrieved from <http://ekhsuir.kspu.edu/handle/123456789/10471>
- 7 Popovych, I.S., Cherniavskiy, V.V., Dudchenko, S.V., Zinchenko, S.M., Nosov, P.S., & Yevdokimova, O.O. et al. (2020). Experimental Research of Effective «The Ship’s Captain and the Pilot» Interaction Formation by Means of Training Technologies. *Revista Espacios*, 41(11), 30. Retrieved from <http://www.revistaespacios.com/a20v41n11/20411130.html>
- 8 Nosov, P.S., Zinchenko, S.M., Popovych, I.S., Ben, A.P., Nahrybelnyi, Y.A., & Mateichuk, V.M. (2020). Diagnostic system of perception of navigation danger when implementation complicated maneuvers. *Radio Electronics, Computer Science, Control*, 1, 146–161.
- 9 Nosov, P.S., Ben, A.P., Mateichuk, V.N., & Safonov, M.S. (2018). Identification of «Human error» negative manifestation in maritime transport. *Radio Electronics, Computer Science, Control*, 4(47), 204–213. DOI: 10.15588/1607–3274–2018–4–20.
- 10 Nosov, P., Ben, A., Safonova, A., & Palamarchuk, I. (2019). Approaches going to determination periods of the human factor of navigators during supernumerary situations. *Radio Electronics, Computer Science, Control*, 2(49), 140–150. DOI: 10.15588/1607–3274–2019–2–15
- 11 Nosov, P., Palamarchuk, I., Zinchenko, S., Popovych, I., Nahrybelnyi, Y., & Nosova, H. (2020). Development of means for experimental identification of navigator attention in ergatic systems of maritime transport. *Bulletin of the University of Karaganda – Physics*, 1(97), 58–69. DOI: 10.31489/2020Ph1/58–69
- 12 Zinchenko, S.M., Nosov, P.S., Mateichuk, V.M., Mamenko, P.P., Popovych, I.S., & Grosheva, O.O. (2019). Automatic collision avoidance system with multiple targets, including maneuvering ones. *Bulletin of the University of Karaganda – Physics*, 4(96), 69–79. DOI: 10.31489/2019Ph4/69–79
- 13 Sims, J.T. (1997, June). Redundancy management software services for Seawolf ship control system. *Proceedings of IEEE 27th International Symposium on Fault Tolerant Computing*. DOI: 10.1109/FTCS.1997.614114.

14 Jacobellis, G., Gandhi, F., & Floros, M. (2019). Using Control Redundancy for Power and Vibration Reduction on a Coaxial Rotor Helicopter at High Speeds. *Journal of the American Helicopter Society*, 64(3), 1–15. DOI: 10.4050/JAHS.64.032008

15 Mohammadi, A., & Ramezani, A. (2020). An Active Actuator Fault-Tolerant Control of a Quadrotor Based on Analytical Redundancy Relations. *Iranian journal of science and technology — transactions of electrical engineering*, 44, 1069–1079. DOI: 10.1007/s40998-019-00292-6

16 Tarun, K.P., & Nilanjan, S. (2001). Fault-tolerant control of an autonomous underwater vehicle under thruster redundancy. *Robotics and Autonomous Systems*, 34(1), 39–52.

17 Zemlyakov, A.S. (2001). Upravlenie uhlovyim polozheniem kosmicheskogo apparata s izbytochnoi strukturoi hirodinov [Controlling the angular position of a spacecraft with a redundant gyrodine structure]. *Vestnik Kazanskoho gosudarstvennogo tekhnicheskogo universiteta imeni A.N. Tupoleva — Bulletin of Kazan State Technical University named after A.N. Tupolev*, 4, 56–62 [in Russian].

18 Lebedev, D.V. (2008). Momentum unloading excessive reaction-wheel system of a spacecraft. *Journal of Computer and Systems Sciences International*, 47(4), 613–620.

19 Wenxiang, G., Qing, T., Jin, Y., & Yaru, Y. (2020). Automatic motion planning for complex welding problems by considering angular redundancy. *Robotics and Computer-Integrated Manufacturing*, 62. DOI: 10.1016/j.rcim.2019.101862

20 Zinchenko, S.M., Nosov, P.S., Mamenko, P.P., Grosheva, O.O., & Matejchuk, V.M. (2019, May). Control redundancy as a quantitative measure of ship maneuverability. Proceedings from Advanced Information and Innovative Technologies for Transport (MINT-2019): *XII International Scientific and Practical Conference*. (pp. 97–99). Kherson State Maritime Academy, Kherson, Ukraine.

АВТОРЛАР ТУРАЛЫ МӘЛІМЕТТЕР СВЕДЕНИЯ ОБ АВТОРАХ INFORMATION ABOUT AUTHORS

- Ben, A.** — Associate Professor, PhD, vice-rector for research, professor of navigation and electronic navigation systems department, Kherson State Maritime Academy, Kherson, Ukraine.
- Borodin, Y.V.** — PhD of Engineering Sciences, Associate Professor of School of Non-Destructive Testing, Tomsk Polytechnic University, Tomsk, Russia.
- Dmitriyeva, E.A.** — Candidate of physical and mathematical sciences, leading researcher, Institute of Physics and Technology, Almaty, Kazakhstan.
- Fedosimova, A.I.** — 3d year PhD student, researcher, Institute of Physics and Technology, Almaty, Kazakhstan.
- Frolova, O.A.** — Candidate of philological sciences, associate professor, MIREA — Russian Technological University, Moscow, Russia.
- Fryanova, K.O.** — PhD student, School of Non-Destructive Testing, Tomsk Polytechnic University, Tomsk, Russia.
- Grosheva, O.** — Senior lecturer of ship handling department, Kherson State Maritime Academy, Kherson, Ukraine.
- Grushevskaya, E.A.** — 2nd year PhD student, junior researcher, Institute of Physics and Technology, Almaty, Kazakhstan.
- Ibrayev, N.Kh.** — Doctor of Physics and Mathematical Sciences, Professor, Director of the Institute of Molecular Nanophotonics, Karagandy University named after academician E.A. Buketov, Kazakhstan.
- Jiang Xiao Hong** — Professor, Head of The international Chinese-Belarusian scientific laboratory on vacuum-plasma technologies, Nanjing University of science and technology (People's Republic of China).
- Karabekova, D.Zh.** — PhD, Associate Professor, Karagandy University named after academician E.A. Buketov, Kazakhstan.
- Khassenov, A.K.** — PhD, Associate Professor, Karagandy University named after academician E.A. Buketov, Kazakhstan.
- Kovbasa, V.P.** — Professor, Dr. Sci. Tech.; Professor of the Department of General Technical Disciplines and Labor Protection; Vinnitsa National Agrarian University, Vinnitsa, Ukraine.
- Kucheruk, V.Yu** — Vinnitsa national technical university, Ukraine.
- Kulesh, E.A.** — Junior Researcher Scientist, F. Scorina Gomel State University; International Chinese-Belarusian Scientific Laboratory by Vacuum-Plasma Technologies, Republic Belarus.
- Lebedev, I.A.** — Doctor of physical and mathematical sciences, head of laboratory, Institute of Physics and Technology, Almaty, Kazakhstan.
- Luchnikov, A.P.** — Research Scientist, MIREA — Russian Technological University, Moscow, Russia.
- Luniov, S.V.** — Candidate of Physical and Mathematical Sciences, Associate Professor, Department of Basic Sciences, Lutsk National Technical University, Lutsk, Ukraine.
- Mahajan, O.H.** — Associate Professor at M.J. College, affiliated to K.B.C. North Maharashtra University, Jalgaon, India.
- Maslyuk, V.T.** — Doctor of Physical and Mathematical Sciences, Professor, Head of the Department of Photonuclear Processes, Institute of Electronic Physics, NAS, Uzhgorod, Ukraine.

- Mateichuk, V.** — Senior lecturer of ship handling department, head of the electronic simulators laboratory, Kherson State Maritime Academy, Kherson, Ukraine.
- Megela, I.G.** — Leading Engineer of the Department of Photonuclear Processes, Institute of Electronic Physics, NAS, Uzhgorod, Ukraine.
- Murzalynov, D.O.** — PhD, senior lecturer of the department «Physics and Chemistry», Kazakh Agrotechnical University named after S. Seifullin, Nursultan, Kazakhstan.
- Nosov, P.** — Associate Professor, PhD, Associate professor of navigation and electronic navigation systems department, Kherson State Maritime Academy, Kherson, Ukraine.
- Omarova, G.S.** — 3rd year PhD student, Karagandy University named after academician E.A. Buketov, Kazakhstan.
- Perminov, V.A.** — Doctor of physical and mathematical sciences, Professor of School of Non-Destructive Testings, Tomsk Polytechnic University, Tomsk, Russia
- Pilipstou, D.G.** — PhD (Eng.), Associate Professor, International Chinese-Belarusian Scientific Laboratory on Vacuum-Plasma Technology, Francisk Skorina Gomel State University, Republic Belarus.
- Popovych, I.** — Full professor, Doctor of psychological sciences, Professor of general and social psychology department, Kherson State University, Kherson, Ukraine.
- Rande, V.R.** — Master of Science student, School of Non-Destructive Testing, Tomsk Polytechnic University, Tomsk, Russia.
- Rogachev, A.A.** — Doctor of technical sciences, Professor, Belarusian State University of transport, Gomel, Republic Belarus.
- Rogachev, A.V.** — Dr. Sc. (Chem.), Professor, Head of Department, International Chinese-Belarusian scientific Laboratory on Vacuum-Plasma Technology, Francisk Skorina Gomel State University, Republic Belarus.
- Rudnikov, A.S.** — PhD (Eng.), Associate Professor, International Chinese-Belarusian Scientific Laboratory on Vacuum-Plasma Technology, Francisk Skorina Gomel State University Gomel, Republic Belarus.
- Sarode, A.P.** — Associate Professor and Head of Physics Department at Dr. A.G.D. Bendale Girls College, affiliated to K.B.C. North Maharashtra University, Jalgaon, India.
- Seliverstova, E.V.** — Senior researcher, PhD Physics, Institute of molecular nanophotonics, Karagandy University named after academician E.A. Buketov, Kazakhstan.
- Serikkanov, A.S.** — Candidate of physical and mathematical sciences, Institute Director, Institute of Physics and Technology, Almaty, Kazakhstan.
- Serikov, T.M.** — Doctor PhD, Senior Lecturer, Department of Physics and Nanotechnology, Karagandy University named after academician E.A. Buketov, Kazakhstan.
- Solomka, A.V.** — PhD in Technical Sciences; Assistant of the Department of Tractors, Automobiles and Bioenergy Systems; National University of Life and Environmental Sciences of Ukraine, Kiev, Ukraine.
- Spirin, A.V.** — Associate Professor, PhD in Technical Sciences; Associate Professor of the Department of General Technical Disciplines and Labor Protection, Vinnitsa National Agrarian University, Vinnitsa, Ukraine.
- Starý, O.** — PhD, Professor Assistant, Czech Technical University in Prague, Prague, Czech Republic.
- Surzhikov, A.P.** — Doctor of physical and mathematical sciences, Professor, Senior Researcher, Tomsk Polytechnic University, School of Non-Destructive Testing, Tomsk, Russia.
- Sysolov, K.V.** — Master of Science student, School of Non-Destructive Testing, Tomsk Polytechnic University, Tomsk, Russia.
- Temiraliyev, A.T.** — Candidate of physical and mathematical sciences, Senior researcher, Institute of Physics and Technology, Almaty, Kazakhstan.
- Temirbayeva, D.A.** — 2nd year PhD student, Karagandy University named after academician E.A. Buketov, Kazakhstan.

Tompakova, N.M. — 2nd year PhD student, junior researcher, Institute of Physics and Technology, Almaty, Kazakhstan.

Udovytska, Yu.A. — Young Researcher, Lutsk National Technical University, Lutsk, Ukraine.

Vavilova, G.V. — PhD of Engineering Sciences, Associate Professor of School of Non-Destructive Testing, Tomsk Polytechnic University, Tomsk, Russia.

Yarmolenko, M.A. — Candidate of technical sciences, Associate professor, Francisk Skorina Gomel State University, Gomel, Republic Belarus.

Zinchenko, S. — PhD, senior lecturer of ship handling department, head of the electronic simulators laboratory, Kherson State Maritime Academy, Kherson, Ukraine.